NASA Technical Memorandum 82501

Space and Planetary Environment Criteria Guidelines for Use in Space Vehicle Development, 1982 Revision (Volume II)

JUNE 1983

25th Anniversary
1958-1983

NASA

NASA Technical Memorandum 82501

Space and Planetary Environment Criteria Guidelines for Use in Space Vehicle Development, 1982 Revision (Volume II)

Robert E. Smith and George S. West, *Compilers*
George C. Marshall Space Flight Center
Marshall Space Flight Center, Alabama

National Aeronautics
and Space Administration

**Scientific and Technical
Information Branch**

1983

FOREWORD

This document, NASA TM-82501, entitled "Space and Planetary Environment Criteria Guidelines for Use in Space Vehicle Development, 1982 Revision," provides information relative to the natural environment for Jupiter, the Satellites of Jupiter, Saturn, Uranus, Neptune, Pluto, the Asteroids, Comets, and Interplanetary Dust. NASA TM-82501 is a compendium of up-to-date information on the physical characteristics of bodies in the solar system and a guide to recent scientific literature. It is intended for NASA engineers, for scientists who design spacecraft and space experiments, and for teachers and others interested in the space program and is a companion document to NASA TM-82478, both of which are follow-ons to NASA TM-78119, which is the 1977 revision on this subject.

Figures and tables reprinted from copyrighted material are included with permission of copyright holder.

As mentioned above, this document is a follow-on to the 1977 publication NASA TM-78119. However, NASA TM-78119 is still considered to be of use and of interest to scientists and engineers in some areas, but any conflict in the data will be resolved by using the values in this new NASA TM- 82501. Further, there is no intent to automatically change any references to previous documents in contract Scopes of Work by the issuance and acquisition of either of the TMs (NASA TM-82473, NASA TM-82478, or NASA TM-82501).

This document, TM-82501, is recommended as a tool for use in the development of space vehicles and associated equipment, and the information presented is based on data and models currently considered to be accurate. However, an environment specialist should be consulted in critical design interface applications for the most current information and scientific interpretation.

Sections on the Sun, Terrestrial Space, the Moon, Mercury, Venus, and Mars constitute Volume I (TM-82478). Volume II (TM-82501) contains chapters on Jupiter, Saturn, Uranus, Neptune, Pluto, Comets, Asteroids, and Interplanetary Dust.

Various programs of NASA's Office of Space Flight, Office for Aeronautics and Space Technology, and Office for Space Science and Applications provided resources required for the preparation of this document.

TABLE OF CONTENTS

TABLE OF CONTENTS (Continued)

TABLE OF CONTENTS (Concluded)

ACKNOWLEDGMENTS

Many individuals participated in the project compiling information, writing, and reviewing. Overall Project Director was M. H. Davis, Universities Space Research Association (USRA). Melanie A. Cook, USRA, contributed to the writing, much of the editing, the assembly, and final checking. Special recognition is due to Duncan Steel of the University of Canterbury, New Zealand; and Chris McKay, Ames Research Center.

INTRODUCTION – William Vaughan, NASA, Marshall Space Flight Center
Robert E. Smith, NASA, Marshall Space Flight Center
George S. West, NASA, Marshall Space Flight Center

SUMMARY – Robert E. Smith, NASA, Marshall Space Flight Center

The following individuals assembled information and wrote sections of the document (institutional affiliations are given for the purpose of identification only):

SECTION	TITLE	PRINCIPAL AUTHOR	OTHER CONTRIBUTORS
SECTION 7.	JUPITER	Henry B. Garrett, Jr. JPL	Carol Stoker U. of Colo.
SECTION 7A.	JUPITER SATELLITES	Thomas Meyer Independent	–––
SECTION 8.	SATURN	Hugh Anderson S.A.I./Seattle	Gene Amarrell Independent
SECTION 9.	URANUS	Duncan Steel U. of Canterbury, NZ	–––
SECTION 10.	NEPTUNE	Duncan Steel	–––
SECTION 11.	PLUTO	Duncan Steel	–––
SECTION 12.	ASTEROIDS	Chris McKay NASA/Ames	–––
SECTION 13.	COMETS	Chris McKay	M. H. Davis
SECTION 14.	INTERPLANETARY DUST	Duncan Steel	–––

T. Neil Divine, JPL, contributed valuable comments and corrections.

Editorial and biliographic services were provided by:

Melanie A. Cook, USRA
Carter Emmart
Sheri Harms, Document Control
Judy Maples
Sylvia Pigors
Margaret Rothermel

SUMMARY

This document, Volume II, provides a consolidated presentation of space and planetary natural environment data for use as design criteria guidelines in space vehicle development programs.

Specifically, information is provided in the disciplinary areas of atmospheric and ionospheric properties, radiation, magnetic field, astrodynamic constants, interplanetary space, and the atmospheres and surfaces (when available) of the outer planets of this solar system.

INTRODUCTION

A knowledge of environment parameters is necessary for the establishment of design requirements for space vehicles and associated equipment. Such data are required to define the design condition for fabrication, storage, transportation, test, preflight, in-flight, and on-orbit design conditions and should be considered for both the whole system and the components which make up the system. The purpose of this document is to provide guideline data on space and planetary environmental conditions relative to various disciplinary areas which are applicable to the design of space vehicles and associated equipment for NASA.

Good engineering judgment must be exercised in the application of the environment data to space vehicle design analysis. Consideration must be given to the overall vehicle mission and performance requirements. Knowledge still is lacking on the relationships between some of the environment variates which are required as inputs to the design of space vehicles. Also, interrelationships between space vehicle parameters and environment variables cannot always be clearly defined. Therefore, a close working relationship and team philosophy should exist between the design/operational engineer and the respective organization's environment scientists. Although a space vehicle design should accommodate all expected operational environment conditions, it is neither economically nor technically feasible to design space vehicles to withstand all extremes. For this reason, consideration should be given to protection of space vehicles or critical subsystem for some extremes. This document does not specify how the designer should use the data in regard to a specific space vehicle design. Such specifications may be established only through analysis and study of a particular design problem.

Assessment of the natural environment in early stages of a space vehicle development program will be advantageous in developing a space vehicle with a minimum operational sensitivity to the environment. For those areas of the environment that need to be monitored prior to and during tests and operations, this early planning will permit development of the required measuring and communication systems for accurate and timely monitoring of the environment.

The environment criteria data presented in this document were formulated based on discussions and requests from engineers involved in space vehicle development and operations; therefore, they represent responses to actual engineering problems and are not just a general compilation of environmental data. This report is used extensively by various government and private space vehicle development organizations in design and operational studies. Inquiries may be directed through appropriate organizational channels for subsequent communications to the Atmospheric Sciences Division, Marshall Space Flight Center, Alabama 35812.

Based on known and projected user requirements, it was decided that it is more advantageous to present the natural environment parameters grouped according to spatial regions rather than scientific disciplinary areas. These spatial areas are interplanetary space and those surrounding the individual planets. The outer limits depend upon the component of the environment being discussed. For clarity in discussion, limits have been arbitrarily taken to be 10 radii above the surface of the planet or Moon. In the discussion of the meteoroid environment, however, the limits extend to a point where the gravitational attraction of the planet or Moon becomes negligible.

Some of the space and planetary environmental data available today are speculative and will remain so until additional satellites, planetary probes, and manned space flights provide more information. Therefore, care must be used in the interpretation and use of available space environment data for a specific design decision. Although the data in this document provide valuable guides for preliminary design studies and analyses, their use for final program decisions depends upon the specific design problem involved. This report was prepared primarily for use in NASA space vehicle development and advanced study projects. The data contained in this document are reviewed on a continuing basis, and revision or amendments will be published as necessary. The numbers given in brackets refer to references given at the end of each section.

This document does not include the subject of environmental test procedures. Reference should be made to Department of Defense MIL-STD-810C Environmental Test Methods (1975)* available from the National Technical Information Service, Springfield, Virginia, 22161. This document covers procedures for: Low Pressure (Altitude), High and Low Temperature, Temperature Shock, Temperature Altitude, Solar Radiation, and Space Simulations (Unmanned Test). An excellent comparison of the various international environmental testing standards may be found in the Journal of Environmental Sciences, Vol. XXIV, Number 2, March/April 1981.

*Revision being considered by DOD.

SECTION 7. JUPITER

7.1 INTRODUCTION

As the god Jupiter was the first among the gods, so the planet Jupiter is the first among the planets. If Jupiter were only 10 times larger, nuclear burning would have originated in its core, and it would have become a star and a rival to the Sun itself. Not only is it the largest of the planets but its retinue of moons, which resembles a miniature solar system, has proven to be of spectacular beauty and interest. Much is now known of the Jovian system and, with the recent appearance of several books and journal reviews, a fairly detailed account can be rendered of this king of planets and its environs.

Although Jupiter and its motions were well known in ancient times, the beginning of the detailed scientific study of the planet can be placed in 1610 with the discovery of the four Jovian (or Galilean) moons, Io, Europa, Ganymede, and Callisto, by Galileo. The discovery of these moons provided strong support for the Copernican theory and led in 1675, to a determination of the speed of light by the Danish astronomer, Romer, through careful timings of their transits. More recently, the discovery of radio emissions from Jupiter helped give birth to the field of radio astronomy. The flybys of the Pioneer and Voyager spacecraft, through their spectacular photos of the Great Red Spot and of the volcanoes of Io, have inspired a new generation of young scientists and engineers. Jupiter, therefore, has been and will be an important test bed for scientific ideas and deserves careful and continuing scrutiny.

Research enthusiasm was greatly intensified in the last few years by the passage of the two Pioneer and two Voyager spacecraft through the Jovian system. Pioneer 10 passed by Jupiter on December 4, 1973, followed a year later by Pioneer 11 on December 3, 1974. More recently Voyager 1 and Voyager 2 passed through the Jovian system on March 5 and July 9, 1979 [7-1]. The twin Voyager spacecrafts were three-axis stabilized and provided long integration times and the advantage of highly selective viewing for spectroscopic and imaging experiments. The large number of high resolution images of the Jovian system returned by this mission (over 18,000 from Voyager 1 alone) provide a detailed look at this giant among planets and of its satellites. Although most of the discussion will be drawn from this huge data base, it should be noted that valuable data are still being obtained from Earth-based telescopes – data which will allow much longer timeline studies of the Jovian system than the spectacular but brief fly-by missions.

7.1.1 General References

In compiling this short review, two data sources stand out. These are the 1976 book JUPITER (edited by Gehrels) [7-2], which details the findings of the Pioneer 10 and 11 missions, and the 1981 September special issue of THE JOURNAL OF GEOPHYSICAL RESEARCH, which details the accomplishments of the Voyager mission to Jupiter. Other useful, though less detailed sources are to be found in issues of NATURE [7-3] and SCIENCE [7-4,7-5]. Numerous individual scientific papers are to be found in the literature along with periodic general reviews (e.g., SCIENTIFIC AMERICAN [7-6]).

7.2 DYNAMIC PROPERTIES

Jupiter is the fifth planet from the Sun and is separated from the orbits of the four inner-terrestrial planets by the asteroid belt. Its mean distance from the Sun is 5.2 AU or 7.78×10^8 km;

its orbital eccentricity is 0.05, midway between that of the Earth and Mars. This eccentricity leads to a difference of about 7.6×10^7 km between perihelion and aphelion. When in opposition to the Sun, Jupiter is about 6.0×10^8 km from the Earth, whereas, at conjuction, this distance is about 9.6×10^8 km. The sidereal period is 11.86 years, and the Jovian synodic period is 399 days. The mean orbital velocity is 13.06 km sec^{-1}. Details of the orbit are summarized in Table 7-1 [7-7].

TABLE 7-1. PHYSICAL DATA AND DYNAMIC PROPERTIES

Distance from sun	$r = 5.20 \pm 0.25$ AU
Period of revolution about sun	$T = 11.862$ years
Mass of planet, excluding satellites	$M_J = (1.899 \pm 0.002) \times 10^{30}$ g
Equatorial radius	$R_J = 71398 \pm 200$ km
Mean density	$\bar{\rho} = 1.32 \pm 0.01$ g/cm^3
Flattening (dynamical)	$\epsilon = 0.0645 \pm 0.0008$
Period of rotation	$T_o = 9^h\ 55^m\ 29.^s73 \pm 0.^s04$
Rotational angular velocity	$\omega_o = (1.758531 \pm 0.000002) \times 10^{-4}$ rad/s
Angular momentum	$C\omega_o = (4.3 \pm 0.2) \times 10^{45}$ g-cm^2/s
Celestial coordinates of North Pole	$\alpha_R = 17^h52^m\ 0.^s84 + 0.^s247$ (t-1919.0)
	$\delta_R = +64°\ 33'34"\ 6 - 0.60"$ (t-1910.0)
Moment of inertia about rotational axis	$C = (2.4 \pm 0.1) \times 10^{49}$ g-cm^2
Moment of inertia about equatorial axes	$A = (2.25 \pm 0.1) \times 10^{49}$ g-cm^2
Gravitational parameter	$GM = 1.267076 \times 10^8$ km^3/s^2
Semi-major axis of orbit	$a = 5.202803$ AU
Synodic period	$S = 398.88$ days
Eccentricity	$e = 0.04845$ (1970)
Inclination to ecliptic	$i = 1°18'17"$ (1970)
Mean longitude of ascending node	$\Omega = 99°26'30"$
Perihelion longitude	$\varpi = 12°43'15"$
Escape velocity	$(2GM/R)^{1/2} = 61$ km/s
Semi-diameter at 1 AU (equatorial)	$D(1\ AU) = 98.37"$
Semi-diameter at opposition	$D(Opp) = 23.43"$

7.2.1 Comments

Although the mass (1.9×10^{30} gm) of Jupiter is only 0.001 of the Sun's, its gravitational attraction is felt throughout the Solar System. Effects include perturbations to the orbits of the other planets, the trapping of the Trojan asteroids at the Lagrange points, and significant alterations in the orbits of all comets traversing the Jovian orbit. Jupiter exerts a profound influence on the asteroid belt where there are several marked orbital voids (called Kirkwood's gaps) corresponding to the orbits which would be commensurate with the orbital period of Jupiter. Finally, as exemplified by the Pioneer and Voyager missions, the gravity well represented by Jupiter (paragraph 7.3.1) can be used to carry out significant orbital adjustments in a spacecraft's orbit. The Pioneer 11 and both Voyager missions made use of this effect to allow them to approach near to Saturn.

7.3 PHYSICAL DATA

7.3.1 Mass, Figure, and Other Physical Properties

Table 7-1 also summarizes the current estimates of the mass and figure of Jupiter. By way of comparison, the volume of Jupiter is about 1300 times that of the Earth whereas its mass is 317.8 that of the Earth (thus the density of Jupiter is 1.32 $g\text{-}cm^{-3}$ or roughly that of the Sun). Jupiter's rotation rate, the highest of the planets, leads to the pronounced oblateness in its figure indicated by Table 7-1.

7.3.2 Mapping Permanent Features

With the possible exception of the Great Red Spot, which has been observed for 300 years [7-8], Jupiter has no "permanent" features in the true sense of the word. Careful observations over the years have, however, allowed a division of the features observable from the Earth into "zones" and "belts." The zones are light colored bands interspersed with darker regions called belts. A more detailed description of these features will be given later. Figure 7-1 and Table 7-2 illustrate the approximate belt structure. The details as to exact latitude and width of these features can change on a monthly time scale as evidenced by the Pioneer and Voyager pictures.

In the past, features in the Jovian atmosphere were used to define map coordinate systems. Jupiter's rotation rate, based on cloud features visible from the Earth, varies, however, from 9 hr 50 min at the equator to 9 hr 56 min near the poles. The arbitrariness thus introduced has led to the abandonment of cloud-based systems and the adoption of a new coordinate system, System III, based on the mean rotational period of decametric and decimetric radio sources. This system, which is presumably tied to more viscous regions in Jupiter's interior, was defined by the International Astronomical Union in 1962 to have a rotation period of 9 hr 55 min 29.37 sec. There have been subsequent modifications to this (Table 7-1), and the reader is referred to Reference 7-11 for the most recent update. Unless otherwise noted, wind and cloud velocities will be referred to this system throughout.

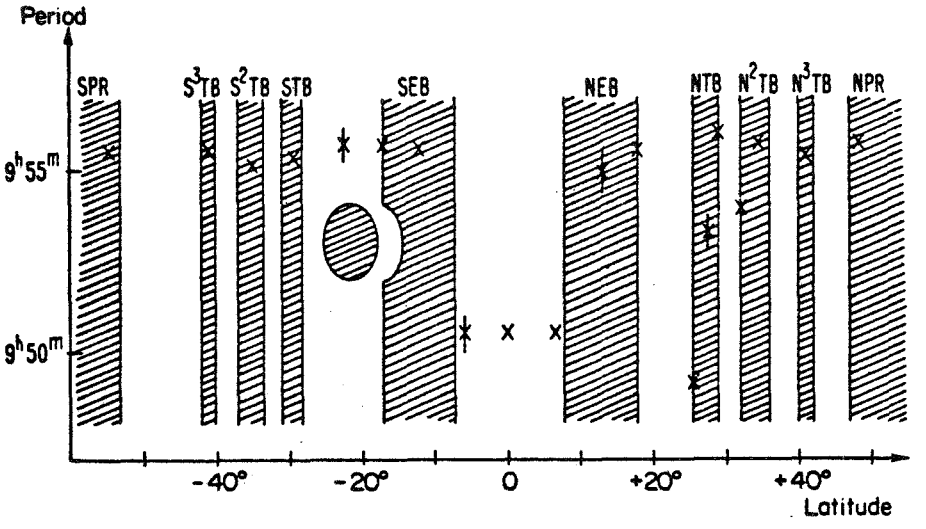

Figure 7-1. Jupiter's belts and periods of rotation [7-9]. S = South, N = North, PR = Polar Region, E = Equatorial, B = Belt, and T = Temperate. The brighter intervening zones have a similar nomenclature. (By permission.)

TABLE 7-2. MEAN ZENOGRAPHIC LATITUDES OF JUPITER'S BELTS (1960 TO 1970) (Fig. 7-1) (Adapted from [7-10].)

Feature	Mean latitude (deg)	Range of apparitional means (deg)	
NPB	+ 56.0	+ 59.5	+ 54.3
NNNTB	+ 44.8	+ 45.9	+ 44.3
NNTB	+ 37.1	+ 38.0	+ 35.9
N. edge NTB	+ 31.3	+ 31.6	+ 31.0
NTB	+ 27.8	+ 28.7	+ 26.9
S. edge NTB	+ 24.3	+ 25.8	+ 22.8
N. edge NEB	+ 19.9	+ 21.4	+ 16.9
S. edge NEB	+ 7.4	+ 8.6	+ 6.6
EB	− 0.4	+ 0.2	− 1.2
N. edge SEBn	− 6.9	− 5.8	− 7.6
S. edge SEBn	− 11.0	− 10.6	− 11.4
N. edge SEBs	− 16.0	− 14.5	− 17.9
S. edge SEBs	− 20.9	− 19.9	− 21.7
N. edge STB	− 26.3	− 24.8	− 27.6
STB	− 29.9	− 29.3	− 31.0
S. edge STB	− 33.6	− 32.9	− 34.5
STZB	− 38.3	− 37.6	− 38.8
SSTB	− 44.4	− 43.1	− 46.3
SSSTB	− 55.9	− 54.9	− 58.0
SPB	− 65.9	− 64.9	− 67.4

7.3.3 Gravity Field

Accurate knowledge of the Jovian gravity field allows a determination of the bulk properties of Jupiter which are the starting point for models of the interior of Jupiter. Values based on an analysis of Doppler data from the Pioneer 10 and 11 missions are listed in Table 7-3 (the radius of Jupiter was assumed to be 71,398 km for these calculations) [7-12]. These values are consistent with independent estimates based on the orbits of the Jovian satellites.

TABLE 7-3. JUPITER GRAVITY HARMONICS FROM PIONEERS 10 AND 11 [7-12].
(Jovian equatorial radius is assumed to be 71,398 km.)

Coefficient × 10^6	Pioneer 10	Pioneer 11
J_2	14,720 ± 40	14,750 ± 50
J_3	< 150	10 ± 40
J_4	− 650 ± 150	− 580 ± 40
J_6	Assumed Zero	50 ± 60

7.3.4 Magnetic Field and Magnetosphere

The magnetic field of Jupiter is strong and of complex structure. The Earth's magnetic field strength is about 0.3 G at 1 Earth radius while that of Jupiter is 4.2 G at 1 Jovian radius. Its effects are felt as far away as Saturn [7-13]. Long before the Pioneer and Voyager missions, radio observations gave some hint of the strength of this field and showed that it is in the opposite sense to that of the Earth (Section 7.11). The subsequent spacecraft missions give a complex picture of Jupiter's field and how it influences and is influenced by the plasma environment surrounding the planet. The data that will be presented are based primarily on the helium vector magnetometers flown on Pioneer 10 and 11 [7-14] and the fluxgate magnetometers flown on Pioneer 11 and Voyager 1 and 2 [7-15 through 7-17].

In Tables 7-4a and 7-4b the components for several of the most popular magnetic field models are listed [7-18, 7-19]. The two most used are referred to as D4 [7-19] and 04 [7-18,7-20]. Of these, the 04 (or Octupole) model is the more detailed. The D4 [7-19] (or Offset Tilted Dipole [7-18] model is, however, adequate for most practical purposes and represents a significant savings in computation time. In this model, the magnetic field strength is given by

$$B = (M/R_m^3)\,[1 + 3\,(\sin \lambda_m)^2]^{1/2} \qquad (7\text{-}1)$$

where

B = magnetic field strength

M = dipole moment (Table 7-4) [7-19]

λ_m = latitude relative to the magnetic dipole (Table 7-4) [7-19]

R_m = radial distance from the magnetic dipole .

TABLE 7-4a. DIPOLE TERMS IN DIFFERENT MATHEMATICAL REPRESENTATIONS [7-18]. (Entries in the last column are for the 04 model. See also D-4 representation in [7-19].)

	Highest Term in the Expansion			
	Dipole	OTD	Quadrupole	Octupole
Dipole moment, G R_J^3				
g_1^0	4.31	4.29	4.30	4.22
g_1^1	−0.258	−0.402	−0.424	−0.442
h_1^1	+0.584	+0.598	+0.613	+0.562
Moment	4.36	4.35	4.36	4.28
Tilt from Z axis	8.4°	9.5°	9.8°	9.6°
Longitude (λ_{III})	246°	236°	235°	232°
Offset, R_J				
X_0	NA	−0.0618	NA	NA
Y_0	NA	+0.0239	NA	NA
Z_0	NA	−0.0148	NA	NA
Residual vector rms, G	0.021	0.011	0.011	0.0085

Table 7-4b. HIGHER-ORDER SPHERICAL HARMONICS COEFFICIENTS FOR 04 MODEL [7-18]

n	*m*	*g*	*h*
2	0	−0.203	...
2	1	−0.871	−0.037
2	2	+0.331	−0.402
3	0	−0.233	...
3	1	−0.357	−0.463
3	2	+0.506	+0.096
3	3	−0.292	+0.233

For distances greater than 20 R_J (Jovian radii; 1 R_J = 71,398 km), the magnetic field strengths measured by the Pioneer and Voyager magnetometers commonly exceeded those predicted by equation (7-1). To approximately model those data, it is recommended that the field strength be taken as the larger of values computed using equation (7-1) and equation (7-2) from Reference 7-21:

$$B = B_0 \left(1 - (b/2) \exp\left[-((R\lambda_0 - Z)/H)^2\right)\right] (R_0/R_J)^b \qquad (7\text{-}2)$$

where

$B_0 = 53\ \gamma$

$b = 1.6$

$R_0 = 20\ R_J$

$Z = (3.8\ R_J)\ (\cos\ [L + 0.9R\text{-}39])$

λ_0 = Jovicentric latitude (in radians)

R = Jovicentric radial distance from Jupiter (in R_J)

L = West longitude (degrees)

H = 1 R_J .

The presumed source of deviations from the simple offset tilted dipole model is an azimuthal current sheet [7-18]. A consistent model of such effects has been developed but, due to its complexity, is not included here [7-22].

The magnetic field models presented thus far are primarily intended to represent the inner Jovian magnetic field. As yet no comprehensive quantitative model exists (aside perhaps from that of Reference 7-22), although two types of models are being considered at this time. Models of the first type are known as magnetodisc models [7-23,7-24]. They assume that at distances from Jupiter greater than a few R_J, any anomalies in the main field can be ignored and the field can be assumed to be dipolar. The dynamic behavior of particles and fields is then interpreted entirely by references to the rotation of a tilted dipole and its interaction with the solar wind. The principal structures within the Jovian magnetosphere are assumed to be formed by magnetic field lines that are highly stretched out, implying a disc-like azimuthal current sheet and associated plasma sheet. In Figure 7-2 are typical magnetic data from Voyager 1 showing the pronounced periodic variations observed in the Jovian magnetosphere. The magnetodisc models account for these variations in terms of geometrical and temporal variations introduced by the periodic motions of the current sheet as Jupiter rotates. In a departure from this model, Dessler, Vasyliunas, and their collaborators [7-24] have proposed the "magnetic-anomaly" model. This model makes the fundamental assumption that the surface magnetic anomaly (marked by a pronounced weakness in the field), which lies in the northern hemisphere and is centered at a longitude 230 deg, exerts a significant influence on the outer Jovian magnetosphere. At present there has been no way to observationally distinguish between these two quite different concepts of the Jovian magnetic field.

In addition to the details of the inner magnetosphere and the controversy over the importance of magnetic asymmetries, the structure of Jupiter's magnetic tail and the magnetosheath have received a great deal of attention. The stand-off distance of the bow shock and magnetopause apparently varied between 70 and 85 R_J and 55 and 70 R_J respectively between the two Voyager missions [7-25]. Typical magnetosheath magnetic field values were approximately 2 to 6 nT, whereas immediately within the Jovian magnetosphere typical values were approximately 10 nT or larger (these are to be compared with solar wind fields of 1 nT or less). Although the exact shape of the Jovian magnetopause and bow shock are not known, they are assumed to be somewhat similar to those of the Earth as illustrated in Figure 7-3. The shape of the Jovian magnetotail is even less well known but may extend in some form as far as the orbit of Saturn [7-13].

7.4 INTERIOR

7.4.1 General Considerations

As one cannot see into a planet's interior, knowledge of its structure and composition can only be inferred. In the case of Jupiter, however, several circumstances do allow reliable inferences to be made of its interior. First, as for any planet, the interior structure may be studied by precisely measuring the gravity field. In the case of Jupiter, with its extreme oblateness, such a procedure works quite

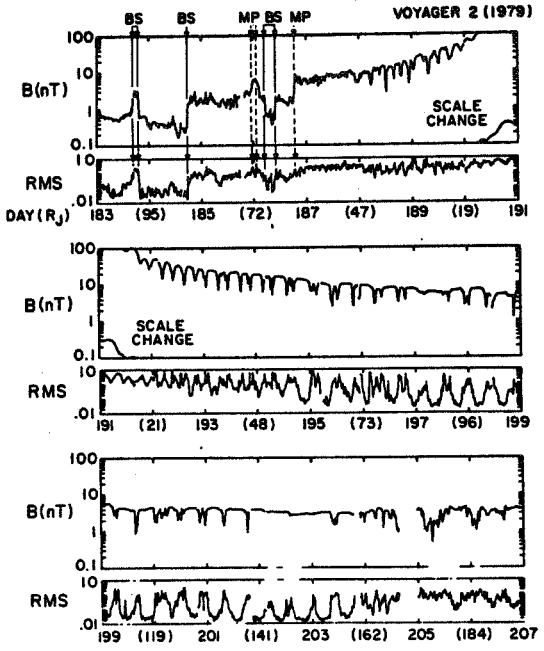

Figure 7-2. Magnetic field magnitude (B) and mean RMS deviations near closest approach for Voyager 2 [7-17]. BS = Bowshock, MP = Magnetopause, "(119)" = R_J, "199" = Day of Year.

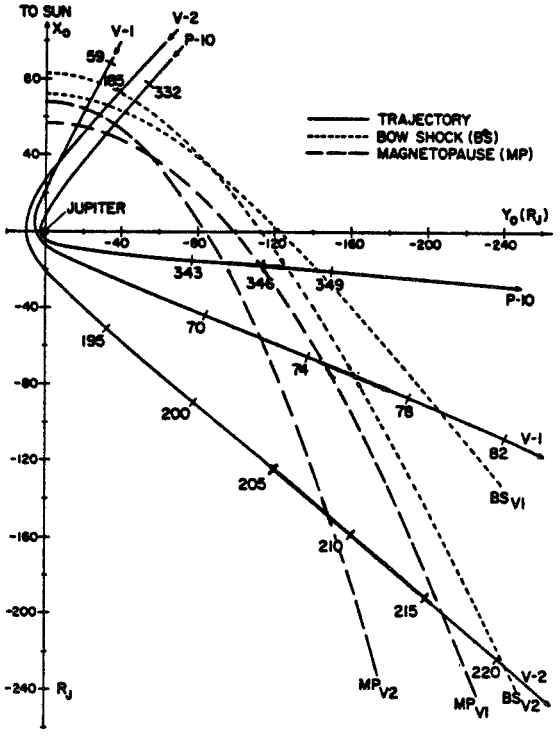

Figure 7-3. Approximate locations of the bow shock and magnetopause as observed by Pioneer 10 and Voyager 1 and 2 [7-25].

well, though the results are not unique. Secondly, the very high gravity of Jupiter means that little if any of the helium and hydrogen have ever escaped. It is therefore reasonable to assume that their ratio resembles that of the Sun since Jupiter and the Sun were formed from the same primordial cloud. Thirdly, the pronounced magnetic field of Jupiter provides a probe of the interior. Present theories of how such fields are generated imply that Jupiter must have an electrically conductive interior. Further, Jupiter is observed to emit twice as much heat as it receives from the Sun implying an internal source of heat. Finally, Jupiter, like the Sun, is made primarily of hydrogen and helium whose properties are probably the best understood theoretically of all materials. Thus it is possible to develop detailed equations of state for the interior. The ways that these factors contribute to present understanding of the interior structure of Jupiter are described in the following paragraphs.

7.4.2 Core

Most pre-Pioneer models of Jupiter assumed that it had approximately the same heavy element abundances as the Sun. Models based on this assumption gave values of the helium to hydrogen abundance ratio for the observed density and mass of Jupiter that are nearly twice the Solar value [7-26]. This posed serious cosmological consequences [7-27]. A simple way out of these difficulties is to assume that, whereas the Jovian helium to hydrogen ratio is the same as for the Sun, the excess Jovian mass is made up by a core consisting of a higher concentration of heavier elements than for the Sun. Models have been developed based on this assumption [7-28]. Hubbard and Slattery [7-29] showed that both this type of model and one based on the assumption that the excess mass is distributed uniformly throughout Jupiter can account for the Pioneer observations. (Note: it is not possible to prove the existence of a core by means of gravitational studies alone). Typical interior models assume something in between these extremes with about 10 to 15 Earth masses (3 to 10 percent of the Jovian mass) of SiO_2, MgO, Fe, and Ni concentrated in a central rocky core and an additional 30 Earth masses of H_2O, CH_4, or NH_3 mixed in the surrounding envelope [7-30]. Under these assumptions the temperature in the core is approximately 20,000 to 30,000°K, the density is 26 to 27 g-cm^{-3}, and the central pressure 10 to 100 megabar [7-31]. Numerous interior models and their assumptions are reviewed in Reference 7-31.

7.4.3 Shell Structure

In Figure 7-4 is plotted a crude cross section of Jupiter's inferred internal structure (from Reference 7-6, as adapted from References 7-29 and 7-32). As shown the inner rocky core of Jupiter is envisioned as being surrounded by a shell of liquid metallic hydrogen extending out to about 46,000 km. The great pressure, in excess of 3 megabar, forces hydrogen into a liquid metallic state in which the hydrogen molecules are dissociated into atoms. The resulting fluid is electrically conducting in agreement with magnetic dynamo theories. The outer layer, consisting primarily of liquid hydrogen in its molecular form, extends to about 70,000 km. Above this layer is what is considered to be the Jovian atmosphere. If this model is correct, the excess heat given off by Jupiter is simply a remnant of the heat generated when Jupiter was formed (earlier models evoked either nuclear heating as a source – too small or gravitational collapse – impossible, since Jupiter's interior is virtually incompressible). A final prediction of such liquid planet models is that Jupiter's interior is stirred by large convection currents – currents which could generate the Jovian magnetic fields. In support of this, the strong quadrupole and octupole moments contribute much more to the surface magnetic field of Jupiter than would be the case if all the field were generated deep in the core [7-20].

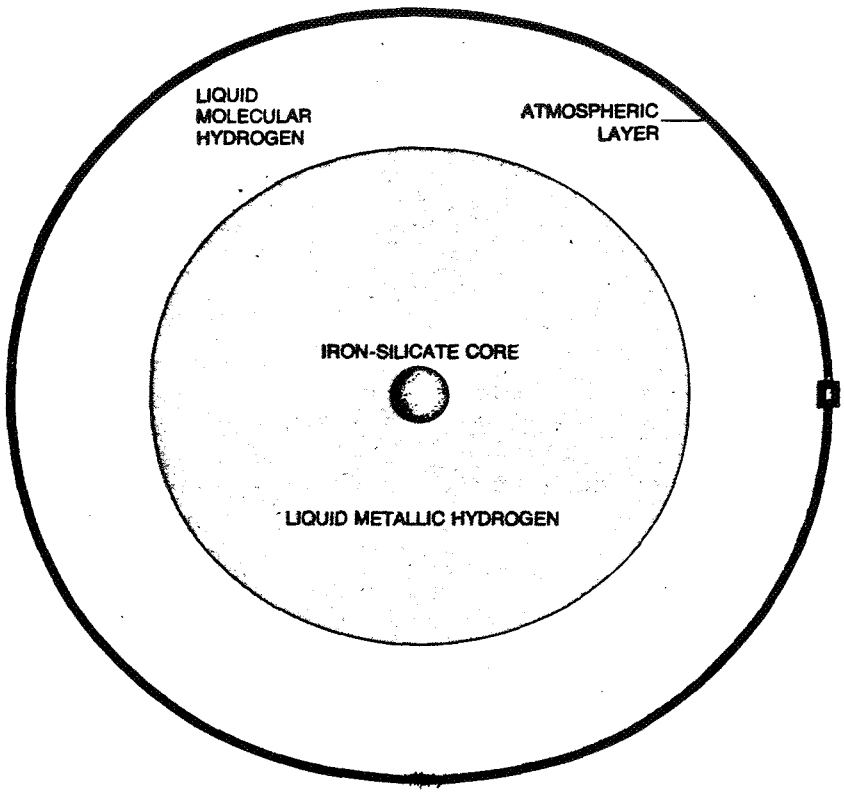

Figure 7-4. Model of the Jovian interior demonstrating the shell structure [7-6]. A portion of the atmospheric layer (corresponding to the small box) is enlarged in Figure 7-7.

Major concerns for interior models are the hydrogen to helium abundance ratio and whether that ratio changes in the interior. Recent evidence from infrared and radio measurements by Voyager place the helium mass fraction between 0.19 and 0.21 [7-33] which is equal to the Solar value. Table 7-5 is a tabulation of estimates of the helium abundance for various determinations. The results apply to the outer layer of Jupiter, and although they are consistent with the assumption of a uniform mix of helium and hydrogen in Jupiter's interior, separation of the hydrogen and helium cannot be ruled out. In fact, recent models [7-34], which make use of improved equations of state, indicate that liquid hydrogen and helium may become separated at the temperatures in the Jovian interior. These models imply that there is no need to require that additional heavy elements be mixed in the outer shells of the Jovian interior and partly account for the excess heat flux by the progressive separation of helium-rich and helium-poor components in the interior [7-35].

7.5 ATMOSPHERE

7.5.1 Global Structure

By studying the characteristics of the reflection, emission, and scattering spectra of Jupiter at different wavelengths, it is possible to penetrate to varying depths through the cloud cover. Occultation experiments (i.e., observing the scattering, absorption, and differential refraction of a spacecraft radio signal or the light of a star as the source passes behind Jupiter) have allowed measurements of the vertical thermal and density profiles. Taken together, these data have allowed the development of global atmospheric models. The general features of the Jovian atmosphere and the details of the various atmospheric regions and the Great Red Spot are discussed in the following paragraphs.

TABLE 7-5. VARIOUS ESTIMATES OF THE HELIUM MASS FRACTION (Y) AND THE HYDROGEN MOLE FRACTION (q) FOR JUPITER, THE SUN, AND THE PRIMORDIAL NEBULA [7-33]

Determination	q	Y
	Jupiter	
Aircraft	0.89 ± 0.11	$0.20^{+0.16}_{-0.20}$
	$0.88^{+0.12}_{-0.06}$	$0.21^{+0.09}_{-0.21}$
Pioneer 11	0.88 ± 0.06	$0.21^{+0.09}_{-0.10}$
Voyager IRIS (inversion)	0.897 ± 0.030	0.19 ± 0.05
Voyager IRIS radio occultation (egress)	0.880 ± 0.036	0.21 ± 0.06
	Solar	
Helium emission lines	0.88 ± 0.02	0.21 ± 0.03
Cosmic rays	0.89 ± 0.02	0.20 ± 0.04
Standard interior models (initial abundance)	$0.86 - 0.88$	$0.22 - 0.24$

7.5.1.1 Energy Balance

The precise measurement of the emitted thermal energy and absorbed Solar flux is critical to a complete understanding of Jovian dynamics and structure. Most of the thermal emission occurs at wavelengths between 10 and 100 μm. Combining the Voyager and Pioneer estimates gives a Jovian Bond albedo of 0.343 ± 0.032 and a thermal emission of $1.359 \pm 0.014 \times 10^{-3}$ W cm^{-2} corresponding to a blackbody temperature of 124.4 ± 0.3°K [7-36]. The internal Jovian heat flux is estimated [7-36] to be $5.444 \pm 0.425 \times 10^{-4}$ W cm^{-2} which gives an energy balance ratio of 1.668 ± 0.085 (i.e., ratio of emitted thermal to absorbed Solar energy).

7.5.1.2 Globally Averaged Thermal Profile

The vertical temperature profile for Jupiter can be obtained from infrared data either by comparing observed and model thermal infrared spectra or by performing a numerical inversion of the observed thermal spectrum [7-37]. The radio occultation data can be used to determine profiles in height of the gas refractivity, molecular number density, pressure, temperature, and microwave absorption in the Jovian troposphere and stratosphere at latitudes ranging from 0 to 70 deg south [7-38]. A mean thermal profile for Jupiter based on these methods is presented in Figure 7-5 [7-39]. A recent tabulation of equatorial temperature, density, and pressure profiles is found in Reference 7-40 from which a nominal profile is presented in Table 7-6. The atmospheric regions illustrated in Figure 7-5 are discussed in the following paragraphs (unless otherwise indicated, the discussion parallels that of Reference 7-39).

The lowest region, the troposphere, is rapidly stirred by a combination of free convection and the vertical component of large scale atmospheric circulation. Below the tropopause, which is defined as the level of minimum temperature, the temperature gradient is expected to be very close to the adiabatic value of -1.9 K km^{-1}. The temperature at 1 bar is 170°K and the tropopause occurs at a temperature minimum of 110°K.

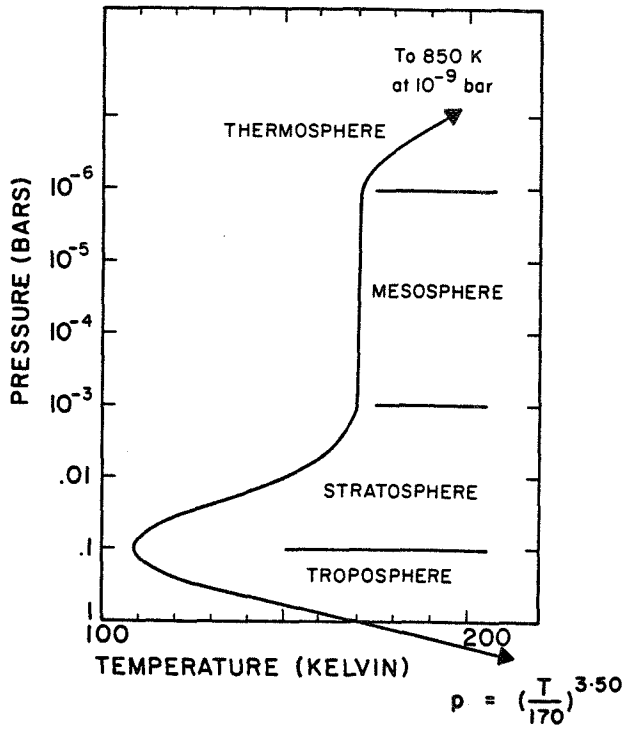

Figure 7-5. Temperature profile and nomenclature of layers in the Jovian atmosphere [7-39].

TABLE 7-6. NOMINAL VERTICAL PROFILE OF THE JOVIAN ATMOSPHERE AT THE EQUATOR FOR MOLAR FRACTIONS OF 0.888 (HYDROGEN), 0.112 (HELIUM), 1.7 x 10^{-3} (METHANE) AND 2.2 x 10^{-4} (AMMONIA) [7-40]

A	B	C	D	E	F	G	H
1	-273	1.00E+02	662	4.12E-03	2.20E-02	3.42	1.41
7	-150	2.51E+01	441	1.55E-03	5.53E-03	3.40	1.42
14	-57	5.01E+00	274	4.99E-04	1.10E-03	3.33	1.43
21	0	1.00E+00	166	1.65E-04	2.20E-04	3.06	1.48
28	34	2.00E-01	114	4.78E-05	5.68E-08	2.77	1.56
35	63	3.98E-02	123	8.84E-06	6.88E-09	2.83	1.55
42	98	7.94E-03	152	1.42E-06	1.37E-09	3.00	1.50
49	138	1.58E-03	163	2.64E-07	2.74E-10	3.05	1.49
56	181	3.16E-04	169	5.90E-08	5.46E-11	3.08	1.48
63	225	6.31E-05	175	9.81E-09	1.09E-11	3.10	1.48
70	279	1.26E-05	181	1.89E-09	2.17E-12	3.12	1.47
77	318	2.51E-06	187	3.66E-10	4.34E-13	3.15	1.47
84	367	5.01E-07	202	6.75E-11	8.66E-14	3.20	1.46
91	425	1.00E-07	246	1.11E-11	1.73E-14	3.30	1.44
98	495	2.00E-08	296	1.83E-12	3.45E-15	3.35	1.42
105	578	3.98E-09	346	3.13E-13	6.88E-16	3.38	1.42
112	674	7.94E-10	396	5.45E-14	1.37E-16	3.39	1.42
119	788	1.58E-10	521	8.28E-15	2.74E-17	3.40	1.42
126	954	3.16E-11	744	1.16E-15	5.46E-18	3.43	1.41

(Column A corresponds to the level, B to the altitude (km), C to pressure (bar), D to Temperature (K), E to density (g-cm^{-3}), F to partial pressure of NH3 (bar), G to C_p/R and H to C_p/C_v.)

Above the tropopause, in the stratosphere, radiative transport is the dominant mode of heat transport. Planetary and Solar radiation are absorbed by molecular species in this region. The energy is subsequently reradiated to space at infrared wavelengths. Temperature increases with height because of the rapidly decreasing ability of He and H_2 to radiate absorbed Solar flux. The stratopause is taken to occur at a pressure of approximately 1 mbar and a temperature of 180°K. This is somewhat arbitrary as, unlike for the Earth, the stratosphere on Jupiter does not exhibit a pronounced temperature maximum.

The Jovian mesosphere arises from Solar heating in the 3.3 μm band of CH_4 with subsequent reradiation in the 7.7 μm band. On Jupiter, the neutral atmosphere temperature gradient in the mesosphere between 1 mbar and 10 μbar is uncertain, but a temperature of 170°K at 10 μbar is likely. The absence of any plausible candidate for an additional heat source in the mesosphere has led to the assumption of an approximately isothermal mesosphere. The mesopause boundary is taken to correspond to the point at which insufficient collisions exist between molecules to maintain local thermodynamic equilibrium. Above the mesopause (at about 1.0 μbar), molecules no longer radiate a significant fraction of the energy absorbed at infrared wavelengths.

The final atmospheric region, the thermosphere, overlaps the ionosphere and is heated by photoionization and photodissociation processes. The heating is balanced at the lower boundary by downward conduction. The temperature rises steeply in the thermosphere reaching 850°K at 10^{-9} bar [7-41] and cannot be accounted for by Solar ultraviolet heating alone. Voyager data indicate the possibility of even higher temperatures (1300°K). This heating deficit will be discussed further in paragraph 7.6 on ionospheres.

7.5.1.3 Global Thermal Variations

A striking finding of the Pioneer and Voyager missions is that there is little difference between the effective temperature at the equator and at the poles of Jupiter. The expected difference, due to Solar heating, should be 20 K for the 3 deg inclination of Jupiter [7-42]. The Solar heating averaged in longitude is about 9×10^{-4} W cm^{-2} at the equator and nearly zero at the poles. Further, Pioneer observations implied that the nightside temperatures were comparable to the dayside values. These factors suggest that the Jovian atmosphere has an enormous heat capacity and that internal heating plays an important role in Jovian atmospheric dynamics [7-6,7-42].

In contrast to the uniform temperature between the poles and equator, Pioneer observations showed that the effective temperature of the belts is 3 to 4°K greater than the zones [7-42]. This provides compelling evidence that the zones are higher in the Jovian atmosphere and regions of rising gas in contrast to the belts which are probably regions of descending gas. Voyager observations supported this finding, and because of the greater degree of horizontal resolution of the infrared and radiometry experiments, revealed additional thermal information [7-43,7-44]:

a) Strong spatial variations are observed in the upper troposphere, the tropopause, and the stratosphere.

b) The tropopause is found to be warmest and lowest at approximately -15 deg latitude, becoming cooler and higher at high latitudes.

c) The upper stratosphere is, on the average, cooler at high southern latitudes than at high northern latitudes. This structure suggests a pole to pole meridional circulation in the upper stratosphere similar to the behavior of the terrestrial mesosphere.

7.5.1.4 Global Neutral Composition Profile

Observations show that, besides H_2 (67 km atm) and He (34 km atm), the upper atmosphere of Jupiter consists of CH_4 (45 km atm), C_2H_2 (2 x 10^{-6} m atm), and C_2H_6 (10^{-4} m atm). (C_2H_2 and C_2H_6 are known to exist, but their abundances are uncertain.) [7-45] Approximate abundances relative to H_2 are listed in Table 7-7 [7-48]. Three typical neutral composition profiles for Jupiter are presented in Figure 7-6 [7-45].

TABLE 7-7. COMPOSITION OF THE JOVIAN ATMOSPHERE AS DETERMINED FROM IR MEASUREMENTS. (Adapted from [7-48].)

Gas	Abundance relative to H_2	Region (μm) where detected
1. Identification firm		
H_2	1	0.8
HD	2×10^{-5}	0.7
He	.05 – .15	–
CH_4	7×10^{-4}	0.7
CH_3D	3×10^{-7}	5.0
$C^{13}H_4$	$C^{12}/C^{13} \sim 110 \pm 35$	1.1
NH_3	2×10^{-4}	0.7
H_2O	1×10^{-6}	5.0
C_2H_6	$\sim 4 \times 10^{-4}$	10.0
2. Recent reports		
CO	2×10^{-9}	5.0
GeH_4	7×10^{-10}	5.0
HCN	1×10^{-7}	5.0
C_2H_2	$\sim 8 \times 10^{-5}$	10.0
PH_3	4×10^{-7}	10.0

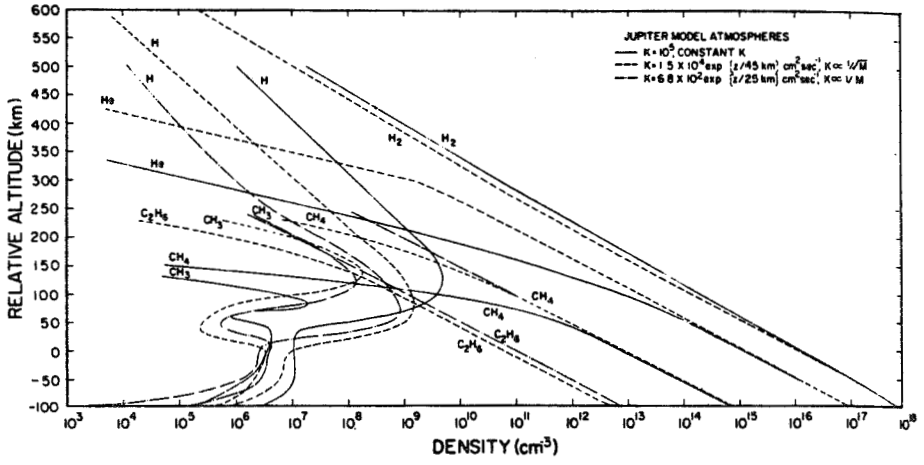

Figure 7-6. Models of the Jovian neutral atmosphere for various values of the eddy diffusion coefficient K and a constant thermospheric temperature of 150° [7-45]. (The height scale refers to altitude above a level where the density is 10^{16} cm^{-3}.) (By permission.)

7.5.2 Jovian Cloud Structure and Color

The colorful, pastel appearance of the lower atmosphere of Jupiter is due to its varied cloud structure. Typical colors of such clouds range from pastels of red, red orange, and brown to blue, gray, and yellow [7-46]. One of the most striking features of the Voyager pictures is the sharp boundaries between these different colored cloud systems. Given knowledge of the vertical temperature profile and a model for the neutral composition, it is possible through basic thermochemical considerations to construct plausible models of the vertical cloud structure by predicting the altitudes at which constituents condense out. One such model is presented in Figure 7-7 [7-47]. In this model the top most clouds are ammonia ice, the middle clouds are ammonium hydrosulfide ice, and the lowest clouds are a combination of water ice and a dilute solution of ammonia in liquid water.

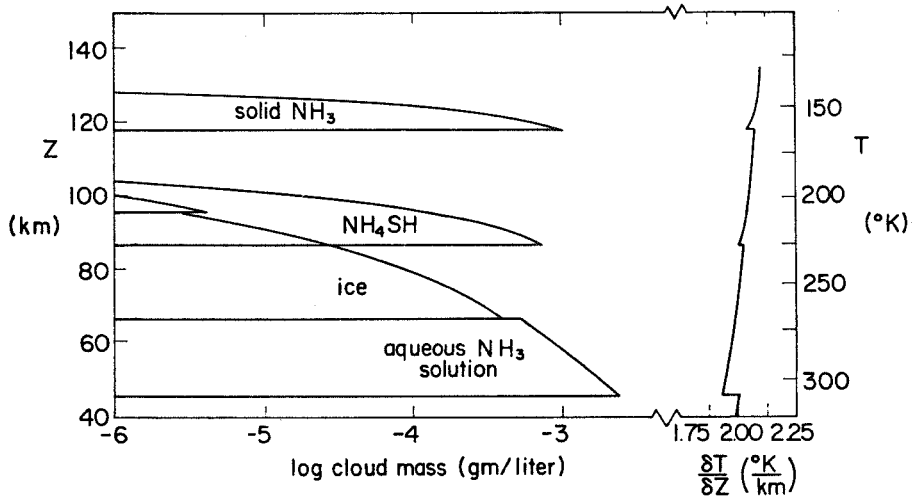

Figure 7-7. Schematic of the Jovian outer layer and atmosphere [7-47]. Cloud mass and the wet adiabatic lapse rate are shown as functions of altitude and temperature for NH_3-H_2O and NH_3-H_2S clouds.

Although latitude, altitude, and dwell time are all critical factors in determining cloud color, the source of the many pastel colors exhibited by Jovian clouds remains a mystery. The white of the zones is probably the result of frozen ammonia which condenses as the temperature in rising air parcels in the zones reaches the condensation point. The darker belts, as they are regions of sinking motions, are not obscured by the ammonia clouds and allow a glimpse down to deeper, warmer layers in the atmosphere [7-49,7-50]. In descending order, there are the white clouds, the light brown or tawny clouds (ammonium hydrosulfide and/or monosulfide), a dark brown belt present only at some latitudes, and the blue-gray "hot spots" of the equatorial region [7-50]. The polar reigons are covered with high, very dark ultraviolet-absorbing material [7-51].

Two chemical theories, organic and inorganic, have been advanced to explain the pastel hues observed in Jupiter. The organic theory [7-52] assumes that photolytic reactions in the Jovian atmosphere could produce organic compounds with colored species. In support of this theory, laboratory simulations, in which mixtures of hydrogen, methane, and ammonia were illuminated by UV or subjected to an electrical discharge, have produced complex organic compounds such as acetylene, ethane, and cyanides [7-53 through 7-56]. Deep orangish-brown and red-brown polymers were also produced. On the other hand, the production rates are not known for these substances and hydrogen atoms readily destroy them. Vertical mixing could carry the organic compounds to altitudes where they would be

destroyed by pyrolitic processes. In the inorganic hypothesis, however, this vertical mixing is an important element as it can carry compounds to altitudes where sulfur and phosphorous may be produced by photolysis in sufficient quantities to act as chromophores. Phosphine [7-48], which can be readily dissociated into phosporus, has been detected. It may be the source of the red color of the Great Red Spot [7-57].

7.5.3 Atmospheric Dynamics and Morphology

Because of Jupiter's internal heating and rapid rotation, it is little wonder that the atmosphere is very active dynamically. Even a cursory examination of the time lapse photographs returned by the Voyager spacecraft attest to this activity. The visible Jovian surface reveals a rolling, turbulent atmosphere with a variety of colorful features, both short and long-lived. Although no review can adequately address all these, a few of the more obvious of the dynamic patterns and features will be described in the following paragraphs.

7.5.3.1 Zonal Currents

Careful observations of individual cloud features larger than 130 km allow a determination of the horizontal velocities in the Jovian atmosphere. Figure 7-8 is a plot of Voyager 1 zonal velocities for February 1979 and Voyager 2 velocities for July 1979 [7-58]. Although some changes in the velocities can be observed, the constancy (to 1.5 percent) of the zonal currents between the two missions is remarkable. This is particularly true when it is realized that every major type of zonal flow observed from the Earth in the last 100 years was observed in just one 10-hr segment of Voyager observations [7-59]. Further, the north/south symmetry of these winds is in marked contrast to the north/south asymmetry of the cloud features for the same region.

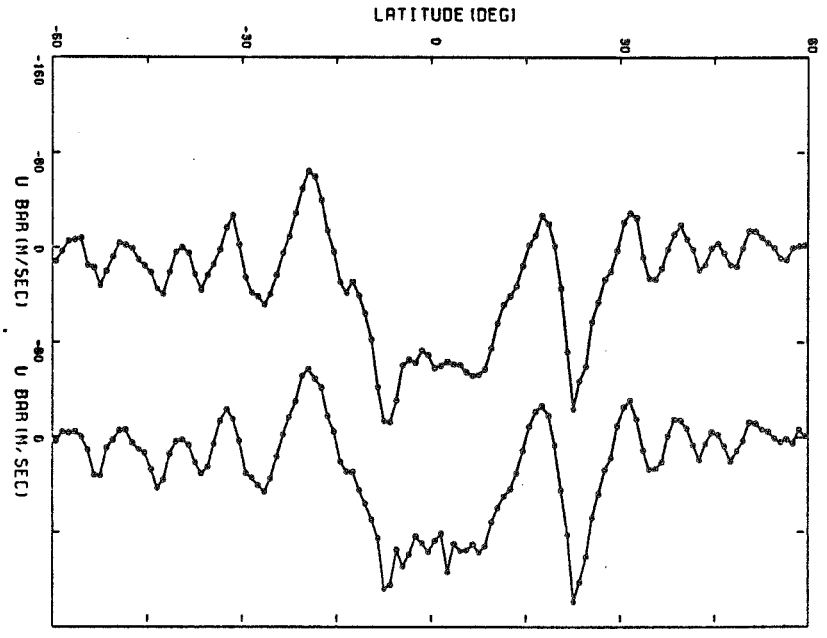

Figure 7-8. Comparison of the zonal velocities in late February 1979 (Voyager 1, left) and those for early July 1979 (Voyager 2, right) [7-58].

7.5.3.2 The Great Red Spot

As Jupiter is a planet of visual superlatives, so the Great Red Spot is the most striking of these visual features. It has been observed from the Earth for 300 years [7-8] and, by way of comparison, is nearly twice the diameter of the Earth. It is immersed within the south tropical zone at about 22 deg south and bounded by the eastward jet associated with the south equatorial belt to the north and bounded by the westward jet associated with the south tropical zone in the south [7-10]. It tends to vary in size (it measured 26,200 km in length and 13,800 km in width in 1975, while it was 22,000 by 11,000 km in 1979) and color. (The deep orange-red hue changes with time.) The color variations seem to be linked to the south equatorial belt – disturbances of the belt, characterized by outbursts of bright and dark spots which spread out in longitude until the entire belt is in turmoil, are often followed by a slow fading in the color of the Great Red Spot until it disappears altogether [7-10]. (At those times when it disappears visually, its effects on the south equatorial belt show that it is still there.) Dynamically, the Great Red Spot is an anticyclonic feature (clockwise rotation in the southern hemisphere) rotating in an anticyclonic shear zone. The period of rotation is six days, suggesting a vorticity of 2.5×10^{-5} sec^{-1} and a Rossby number of 0.2 [7-60]. It exhibits a zonal oscillation with an average peak-to-peak amplitude of 1800 km and a period of 89.95 days [7-10] along with more random long-term wanderings.

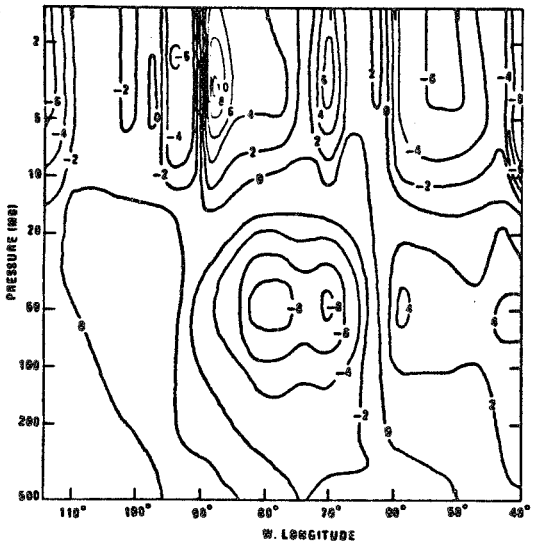

Figure 7-9a. East-west vertical cross section of the temperature across the Great Red Spot [7-61]. The temperatures are deviations in K from an average temperature profile.

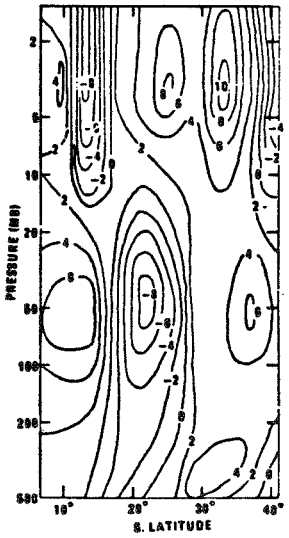

Figure 7-9b. North-south vertical cross section of the temperature across the Great Red Spot [7-61].

Figures 7-9a and 7-9b show the temperature profile associated with the Great Red Spot compared with the surrounding zone. The upper troposphere and lower stratosphere above the Great Red Spot are colder than in the surrounding regions, with a maximum horizontal temperature difference at the tropopause of 5 to 7°K [7-10]. The Great Red Spot also appears brighter in photographs at 8900 Å. These two facts, taken together, indicate that the Great Red Spot is higher than the surrounding cloud layers.

Many theories have been proposed to explain the Great Red Spot. It has been suggested [7-62] that the Great Red Spot is a Taylor column, but the longitudinal wanderings and the absence of an underlying solid surface argue against this hypothesis. Golistyn [7-63] suggested that the Great Red Spot is a long-lived eddy. The idea appears unlikely, however, since the radiative and dynamical time scales in the Jovian atmosphere range from 10 days to a few years [7-64]; much shorter than the period during which the Spot has been observed. Others [7-65] have suggested solitary waves (solitons) as a possible explanation. Again, the model fails to account for the longevity of the feature. To summarize, any model of the Great Red Spot must account for the following [7-66]:

a) Its long lifetime.

b) Its oscillatory latitudinal motions

c) Its longitudinal motion. (The Spot has wandered through more than 1000 deg in 50 years.)

d) Its temperature structure and the evidence that it is higher in the atmosphere than the surrounding region.

e) Its variable color.

7.5.3.3 Southern Hemispheric Features

Aside from the remarkably cyclic variations in wind speed from east to west in the southern hemisphere, large oblong cyclones with folded filament morphologies are observed to alternate longitudinally with more clearly defined smaller elliptical anticyclonic features. These have been observed primarily at latitudes of 14 deg south, 31 deg south, and 40 deg south [7-67]. The larger of the elliptical features, called the "white ovals," are long-lived features, having been first observed in 1939 [7-8].

High resolution images of the white ovals and of the smaller elliptical spots at 41 deg south indicate that they are dynamically similar to the Great Red Spot. These features all have similar morphologies, are characterized by anticyclonic motion, and produce disturbances to their west [7-68]. Typical values for the vorticities and Rossby numbers of the white ovals are 3.0×10^{-5} sec^{-1} and 0.16, respectively, and 2.0×10^{-5} sec^{-1} and 0.09 for the small spots at 41 deg. These are quite similar to the values for the Great Red Spot. The major differences between the Great Red Spot and these features appear to be color, size, and lifetime.

7.5.3.4 Equatorial Features

In contrast to the long-lived features of the southern hemisphere, changes in the equatorial zone (between roughly ±9 deg) occur very rapidly – in some cases on the time scale of a single rotation. At the time of the Voyager 1 encounter, the northern edge of the equatorial region was characterized by a wave pattern formed in the strong eastward jet of the equatorial zone. These features, indicative of vertical shear, are thought to be plumes trailing behind (to the west of) small bright centers of rising motion and are not observed on the southern border. Voyager observations showed rapid brightenings followed by spreading of the bright material, with time constants of 50 to 100 hr, in the region of the plume heads [7-67]. At the time of Voyager 1 encounter, 13 plumes were visible with four plume heads actively spreading material. By the time of the Voyager 2 encounter, only 11 plumes were seen and only one of these had an active bright nucleus [7-68]. Generally, the plume heads are

uniformly bright over scales of 200 km. Small (100 to 200 km) puffy features within the plume heads resemble terrestrial cumulus clouds. This had led to the association of these features with mesoscale convection [7-68].

7.5.3.5 Northern Hemispheric Features

In marked contrast to the southern hemisphere, the northern hemisphere is characterized by a lack of large-scale (greater than 1000 km), longitudinally dependent structures. The smaller northern hemispheric features, such as the white ovals, are, however, often morphologically similar to their southern counterparts though their time scales for change are more rapid. There is, for example, a wedge-shaped pattern between 40 deg west and 100 deg west of highly folded light and dark filaments rolling cyclonically much like the area west of the Great Red Spot, only with no visible feature to the west or east [7-67].

An interesting type of feature indigenous to the northern hemisphere is the dark brown cigar shaped clouds or "barges" in the north equatorial belt. These features are associated with high infrared emission levels at 5 μm suggesting that they are holes in the clouds through which darker, deeper, and hence warmer levels may be seen. This view is supported by Voyager 2 observations of one such feature which shows a white cloud intruding over a portion of the dark feature. A whispy cloud veil apparently overlays the dark cloud itself [7-68].

7.5.3.6 Polar Region Features

The high latitude regions have a mottled appearance, superficially suggestive of convection [7-51]. High resolution images, however, show the features actually to be spiral spots rotating anti-cyclonically. The belt-zone pattern of east-to-west velocity was also found from these images to extend much higher in latitude (±60 deg) than previously thought. The polar regions of Jupiter appear to be darker and exhibit less contrast than the midlatitudes. Ultraviolet observations at 2400 Å show strong absorption at this wavelength by an unknown molecular or particulate constituent. The absorption is enhanced northward of 45 deg north up to the polar regions.

7.6 IONOSPHERE

Radio occultation observations from Pioneer and Voyager spacecraft have been used to probe the Jovian ionsophere. A typical electron profile determined from Pioneer 11 observations near 79 deg south is presented in Figure 7-10 [7-41]. At the time of the Pioneer 11 observations, the vertical thickness of the ionosphere was between 3500 and 4000 km. The scale height of the topside ionosphere (L1 in Fig. 7-10) was 540 ± 60 km. As already discussed for the neutral atmosphere, the temperature of this region, if it is assumed to be composed primarily of H^+ [7-41], reaches about 850 ± 100°K which is considerably in excess of what would be expected from solar ultraviolet alone and requires an additional heating source if it is to be explained.

Numerous models of the ion composition and structure have been developed. The pre-Voyager models are reviewed in References 7-45 and 7-69 through 7-71. Table 7-8 is a summary of the more important reactions in the ionosphere of Jupiter [7-45]. The results of a typical model calculation based on these reactions, an assumption of photochemical equilibrium, and a neutral atmosphere model (i.e., Fig. 7-6) are presented in Figure 7-11. This model is only adequate in fitting the Pioneer data up

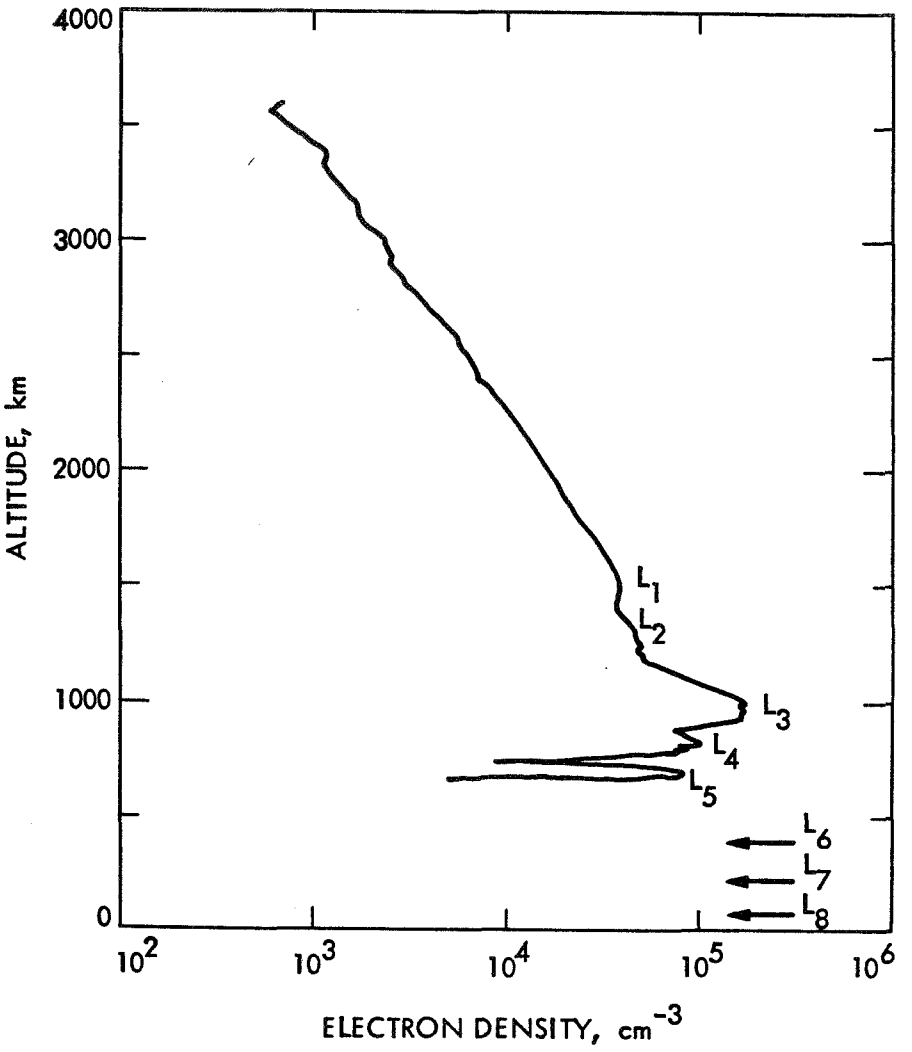

Figure 7-10. Electron density as a function of height above the level where the lower neutral atmosphere has a refractivity of 1. For a pure H_2 atmosphere this corresponds to a density of 2×10^{17} molecule cm^{-3} (roughly 3 mbar level). [7-41] (By permission.)

to about the L5 layer. To bring the ionospheric models into agreement with observations above this altitude requires the assumption of a "hot thermosphere" as discussed in the previous paragraph.

Although the ionosphere observed by the Pioneers near solar minimum was surprisingly intense, it pales in comparison with the ionospheric conditions observed by the Voyagers near solar maximum. For example, the vertical thickness of the ionosphere in 1979 was 6000 km as compared to 4000 km in 1973 [7-72]. Voyager 1 measurements (Fig. 7-12) of the peak afternoon electron density (12 deg south) at 1600 km gave a value of 2.2×10^5 cm^{-3} [7-73], five times the Pioneer values at the same height. Similar differences were seen in the topside scale heights. These ranged from 960 km at high altitudes during the day and night for Voyager 1 (consistent with a neutral atmospheric temperature of 1300°K, an eddy diffusion coefficient at the turbopause of $1 - 3 \times 10^5$ cm^2 sec^{-1} and a rate of ionization in sunlight of 26 protons cm^{-3} sec^{-1} – an order of magnitude larger than the Pioneer observations) to 880 km for morning and 1040 km for evening for Voyager 2 (corresponding to plasma temperatures of 1200 and 1600°K, respectively). These differences between the Pioneer and Voyager data can be

TABLE 7-8. MAJOR REACTIONS IN THE JOVIAN IONOSPHERE (Adapted from [7-45].)

Reaction	Rate Constant[a]
Ion Production:	
$H_2 + h\nu \rightarrow H_2^+ + e$	
$\rightarrow H^+ + H + e$	
$H_2 + e \rightarrow H_2^+ + 2e$	
$\rightarrow H^+ + H + 2e$	
$H + h\nu \rightarrow H^+ + e$	
$H + e \rightarrow H^+ + 2e$	
$He + h\nu \rightarrow He^+ + e$	
$He + e \rightarrow He^+ + 2e$	
Ion Exchange:	
$H_2^+ + H_2 \rightarrow H_3^+ + H$	2.0×10^{-9}
$H_2^+ + H \rightarrow H^+ + H_2$	$\sim 1.0 \times 10^{-10}$
$He^+ + H_2 \rightarrow H_2^+ + He$ (sum)	$\lesssim 20\%$
$\rightarrow HeH^+ + H$ (sum)	1.0×10^{-13}
$\rightarrow H^+ + H + He$ (sum)	$\gtrsim 80\%$
$He^+ + CH_4 \rightarrow CH^+ + H_2 + H + He$	2.4×10^{-10}
$\rightarrow CH_2^+ + H_2 + He$	9.3×10^{-10}
$\rightarrow CH_3^+ + H_2 + He$	6.0×10^{-11}
$\rightarrow CH_4^+ + He$	4.0×10^{-11}
$H^+ + H_2 + H_2 \rightarrow H_3^+ + H_2$	3.2×10^{-29}
$H^+ + CH_4 \rightarrow CH_3^+ + H_2$	2.3×10^{-9}
$\rightarrow CH_4^+ + H$	1.5×10^{-9}
$HeH^+ + H_2 \rightarrow H_3^+ + He$	1.85×10^{-9}
$H_3^+ + CH_4 \rightarrow CH_5^+ + H_2$	2.4×10^{-9}
$CH^+ + H_2 \rightarrow CH_2^+ + H$	1.0×10^{-9}
$CH_2^+ + H_2 \rightarrow CH_3^+ + H$	7.2×10^{-10}
$CH_3^+ + CH_4 \rightarrow C_2H_5^+ + H_2$	8.9×10^{-10}
$CH_4^+ + CH_4 \rightarrow CH_5^+ + CH_3$	1.11×10^{-9}
$CH_4^+ + H_2 \rightarrow CH_5^+ + H$	4.1×10^{-11}
Ion Removal/Electron-Ion Recombination:	
$H_3^+ + e \rightarrow H_2 + H$	3.8×10^{-7}
$H_2^+ + e \rightarrow H + H$	$< 1.0 \times 10^{-8}$
$HeH^+ + e \rightarrow He + H$	$\sim 1.0 \times 10^{-8}$
$H^+ + e \rightarrow H + h\nu$	6.6×10^{-12}
$He^+ + e \rightarrow He + h\nu$	6.6×10^{-12}
$CH_5^+ + e \rightarrow$ neutral products	1.9×10^{-6}
$C_2H_5^+ + e \rightarrow$ neutral products	1.9×10^{-6}

[a]The rate constants are in units of $cm^3\ sec^{-1}$ for two-body reactions, and $cm^6\ sec^{-1}$ for three-body reactions

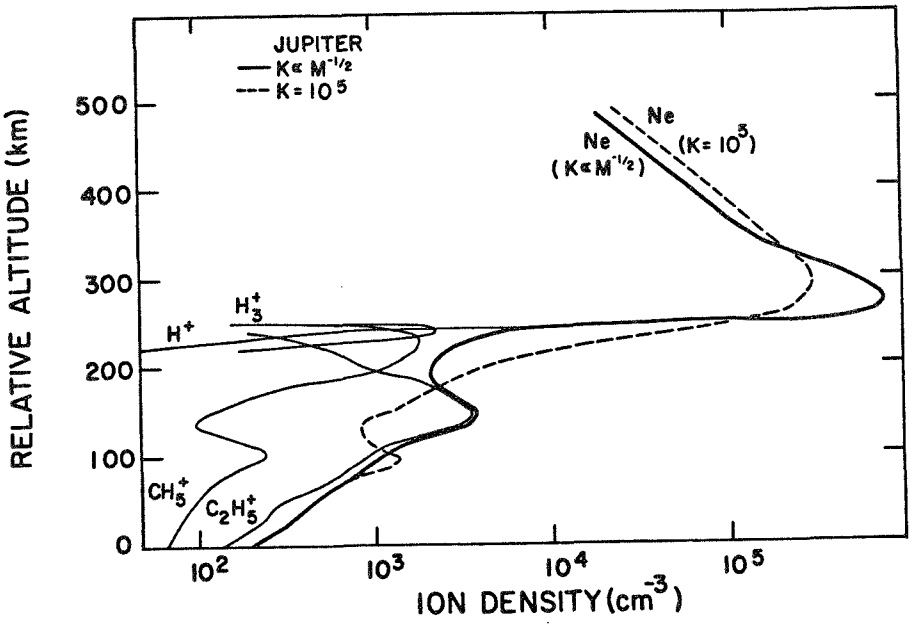

Figure 7-11. Modeled ion and electron (Ne) density profiles [7-45]. The height scale is the same as Figure 7-6. (Note: The H+ profile overlaps Ne at high altitudes.) (By permission.)

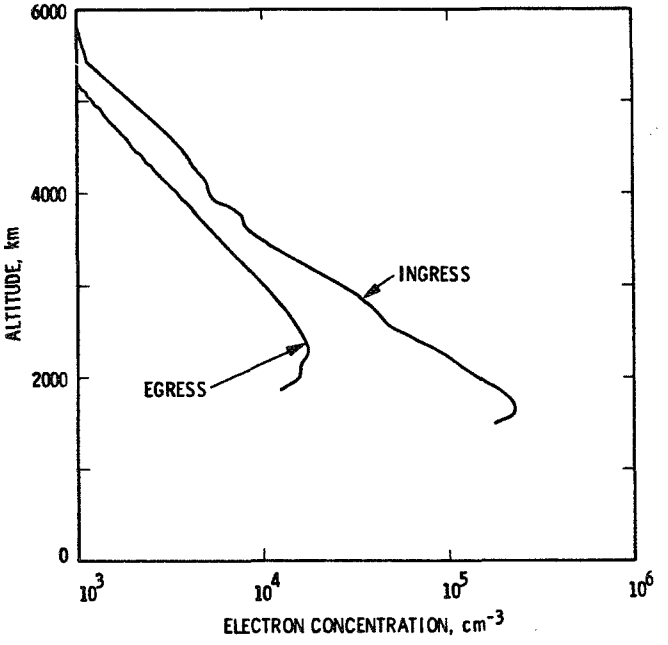

Figure 7-12. Upper ionospheric electron density profiles from Voyager 1 occultation data at about 12 deg south (ingress near afternoon) and 1 deg north (egress near predawn) [7-73]. Height scale is the same as for Figure 7-10.

explained in part by a 2.5 increase in the solar ionizing flux and by an apparent increase in the hydrogen abundance since 1973 to 1974 [7-74]. Variations in the Jovian magnetosphere and the Io plasma torus may also be related.

7.7 THE JOVIAN MAGNETOSPHERIC PLASMA ENVIRONMENT

Like the other features of Jupiter, its magnetospheric plasma environment is undoubtedly the most interesting in the solar system. Jovian magnetospheric effects have been detected as far away from the Sun as Saturn, and recent observations of high energy particles even indicate that Jovian particles have been observed in the vicinity of the Earth. As will be discussed, the high energy particles circulating in Jupiter's magnetic field are the primary source of the intense radio signals given off by Jupiter. It is, in fact, this strong Jovian magnetic field, the extremely high rotation rate of Jupiter, and the Io torus that dominate Jovian plasma dynamics and place them in a unique category. In the following the more interesting aspects of those dynamics will be described in terms of three energy ranges: 0 eV to 1 keV (the low energy environment), 1 to 30 keV (the medium energy environment), and 30 keV and higher energies (the high energy environment).

The primary measurements of the low energy Jovian plasma environment come from the Voyager Plasma Science experiment [7-75]. This experiment consisted of four modulated grid Faraday cups which returned measurements of the electrons and ions in the energy range 10 eV to 6 keV from four different directions. Review reference 7-76 for information on the ions and Reference 7-77 for the electrons. Sample electron and ion spectra and variations in charge and mass density are presented in Figures 7-13 through 7-15 for the Voyager data. The ion spectra in Figure 7-14 also show model fits [7-21]. The large corotation velocity imparts a common velocity to all ions which are then observed at different characteristic energies due to mass differences as illustrated in Figure 7-14. The high energy data are available from both the Pioneer and Voyager missions. There is little or no information, however, on the 1 to 30 keV energy range although some data are available from Voyager (review References 7-76 and 7-77 for energies up to 6 keV and Reference 7-78 for energies between 15 and 30 keV). The comprehensive, though rudimentary, descriptions of the different Jovian plasma regions presented in the following paragraphs are based on these data and taken from a model which appears in unpublished work by Divine [7-21].

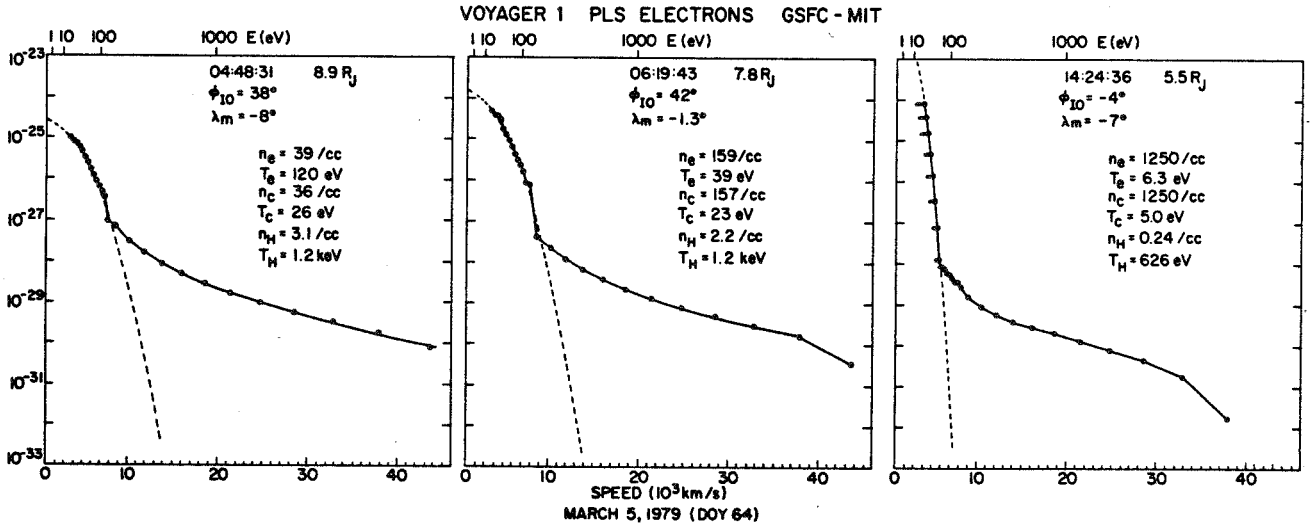

Figure 7-13. Representative low energy electron phase-space distribution functions (s^3 cm^{-6}) versus velocity and energy for 3 locations of Voyager 1 with model fits and parameter values [7-77]. (For explanation of units, review Reference.)

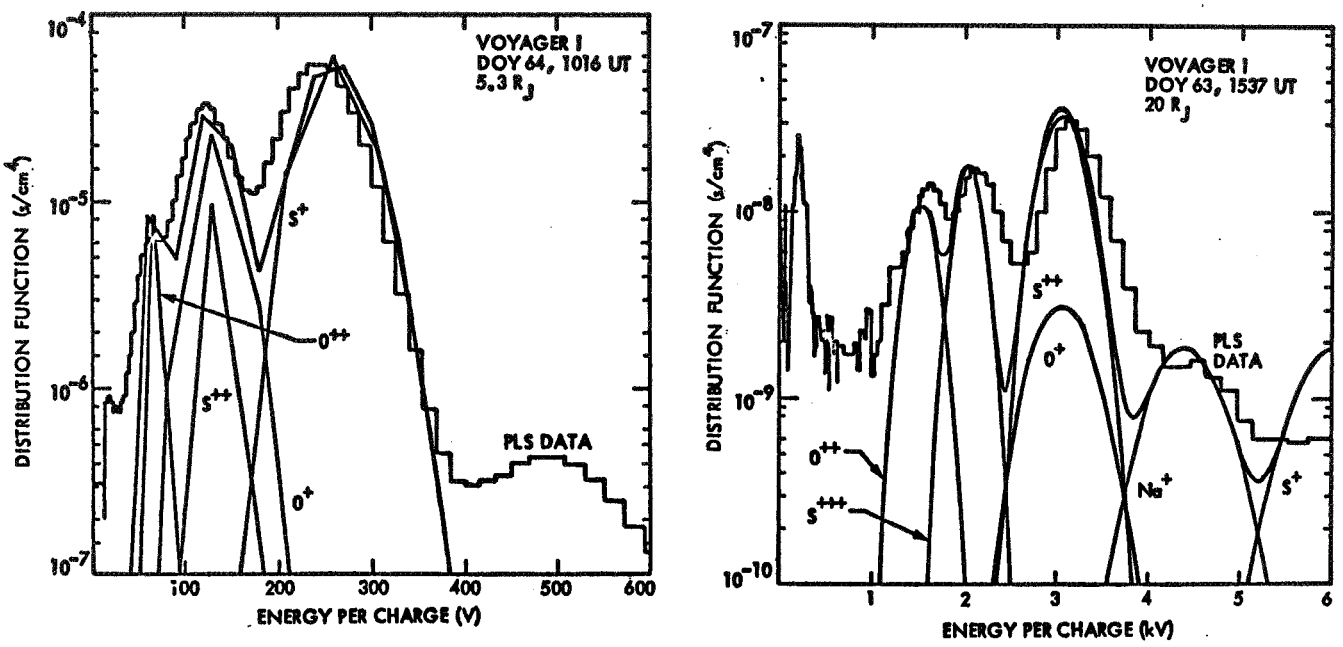

Figure 7-14. Representative low energy (reduced) ion distribution functions (s-cm^{-4}) for Voyager 1 [7-76]. [Note the change in energy scale reflecting the differences between the Torus (5.3 R_J) and outer disc (20 R_J)]. The PLS data are approximated by the sum of distributions for the indicated ions. (For explanation of units, review Reference.)

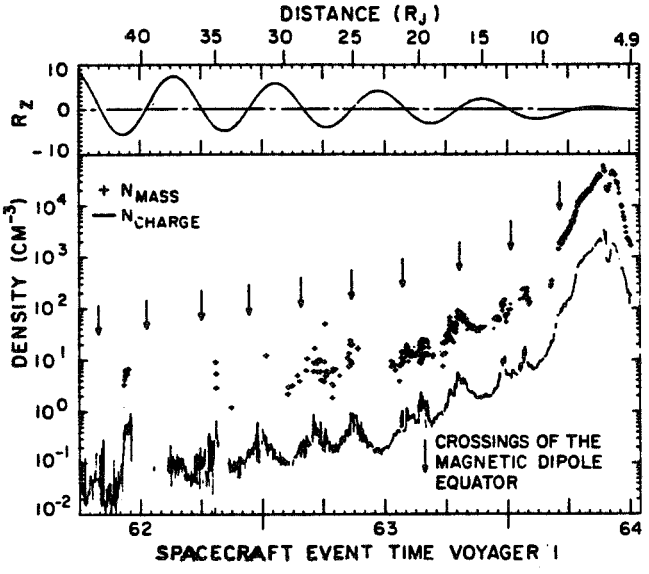

Figure 7-15. Estimates of the total mass (amu-cm^{-3}) and charge densities of positive ions as functions of distance (R_J) for Voyager 1 [7-76]. The oscillations are associated with plasma sheet encounters. Rz is the distance of Voyager 1 from the magnetic dipole plane.

7.7.1 Low Energy Plasmas

Although the dynamics of the source and loss mechanisms are not fully understood, it is clear from Earth-based observations of neutral sodium and potassium and by in-situ measurements from voyager that Io generates a pronounced torus of plasma and neutral gas (paragraph 7.12) [7-79]. The plasma of this ring, centered roughly on the orbit of Io (i.e., at 5.9 R_J), dominates the low energy Jovian plasma population. The dynamics of this plasma are, however, dominated by the Jovian magnetic field and the tremendous centrifugal force generated by Jupiter's rotation (this imparts a velocity of 12.6 (R/R_J) km sec^{-1}; at 6 R_J, a proton is moving at 75.6 km sec^{-1} which corresponds to an energy of 30 eV). The mass of the torus and the centrifugal force are sufficient to distort the Jovian magnetic field. The bulk of the low energy plasma stays trapped near the centrifugal plane (e.g., the theories of Hill, Dessler, and Michel [7-80,7-81]). The interchange of magnetic flux tubes, with the more filled tubes moving outwards from Jupiter, is believed to be the main means of outward diffusion of the low energy torus plasma.

The Voyager electron and ion observations can be summarized in model form as follows. First, the plasma density falls off rapidly away from the equatorial region (specifically, the centrifugal rather than the magnetic equator where the centrifugal equator has the same center and line of nodes with respect to the rotational equator as does the magnetic equator, but only two-thirds of the inclination or 7.2 deg [7-81]) with a typical scale height between 0.2 R_J and 1 R_J. Moving outwards from the planet the inner plasmasphere is located between 1 and 3.8 R_J; a region which is not well observed. One model has temperatures, assumed to be the same for electrons and ions, on the order of 50 eV. The charge density varies from a value typical of the ionosphere (10^4 cm^{-3}) with the major heavy ions being O^+, O^{++}, S^+, and S^{++} (refer to Table 7-9 for relative densities) to about 40 cm^{-3} at 3.8 R_J. Although no observational estimates of the H^+ content exist, it is probably consistent with that of the ionosphere.

TABLE 7-9. APPROXIMATE ION SPECIES NUMBER DENSITIES (IN TERMS OF PERCENTAGE OF ELECTRON DENSITIES) FOR MODEL PLASMA DISTRIBUTION [7-21]

SPECIES	IONIZATION STATE	RELATIVE DENSITY* $1.0<r<5.5R_J$	$5.5<r<7.9R_J$	$7.9<r<170R_J$
O	+1	0.20	0.06	0.07
	+2	0.02	0.08	0.06
S	+1	0.70	0.24	0.06
	+2	0.03	0.25	0.26
	+3	0.0	0.01	0.06
Na	+1	0.0	0.01	0.05

*Density of e^- is 1.00

The next region, the Io torus proper, is actually divided into two regions – the cool, inner torus which resembles the plasmasphere in composition but has temperatures of less than 1 eV and is characterized by a steep gradient in the density associated with the inward diffusion of torus plasma (Fig. 7-17) and the warm torus which extends from 5.5 to 7.9 R_J. Plasma densities in the warm torus, which are associated with outward diffusion of plasma, have been observed by both in-situ and Earth-based observations to be as high as 3000 cm^{-3}. The density varies erratically in the inner part of the region, dropping exponentially to about 150 cm^{-3} at 7.9 R_J. The temperature, however, is warm only in a relative sense – varying from less than 1 eV to 50 eV at 7.9 R_J. The heavy ion population is O^+, O^{++}, S^+, S^{++}, S^{+++}, and Na^+ (Table 7-9). Although observed [7-76], H^+ densities are not available for this region.

The region outside the torus is referred to loosely as the disc region (paragraph 7.3.4) [7-23].. In the inner disc (7.9 to 20 R_J), the plasma, which is observed to be strictly corotating with Jupiter within 7.9 R_J, slows from strict corotation so that by 20 R_J (the outer disk region) it is rotating at only 200 km sec^{-1} (or 80 percent of the corotation velocity). The temperature is assumed constant with radius in the disc (15 eV at the equator) but increases away from the equator to 100 eV. The density falls exponentially from about 150 to 0.001 cm^{-3} at 100 R_J. The few H^+ observations that exist in the 8 to 100 R_J range imply densities of about 5 cm^{-3} at 10 R_J and 0.001 cm^{-3} at 80 R_J and temperatures equal to those of the other ion species.

The model presented above [7-21] (as adapted in part from Reference 7-82) is graphically presented in Figures 7-16 and 7-17 for the electrons (note: the ion profiles would not differ greatly). Figure 7-16 demonstrates how the number density and energy vary in the centrifugal equatorial plane (remember: the centrifugal axis is inclined by about 7.2 deg from the spin axis). Figure 7-17 presents

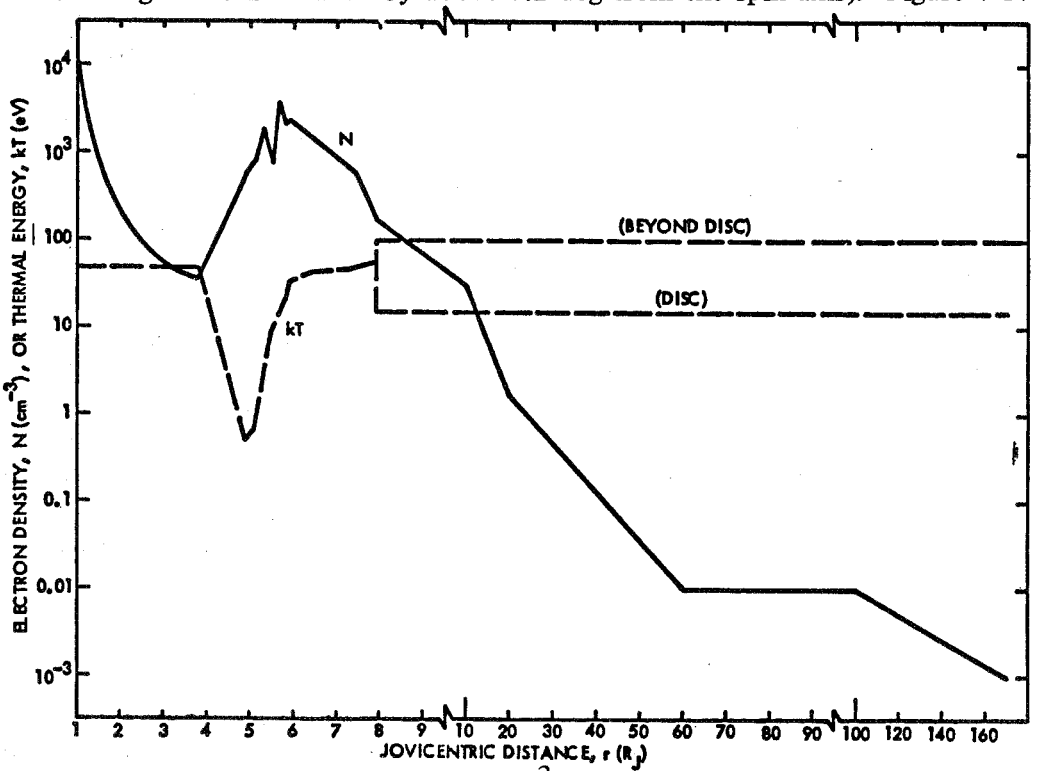

Figure 7-16. Low energy electron density, N (cm^{-3}), and thermal energy, KT (eV), as functions of Jovicentric distance in the equatorial plane [7-21].

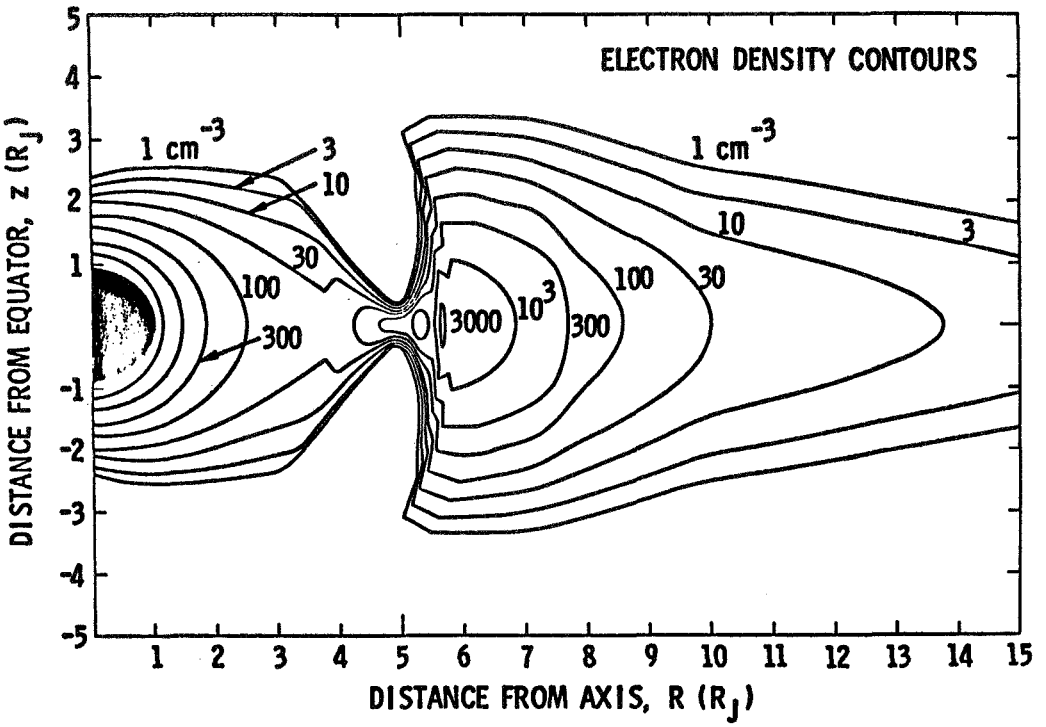

Figure 7-17. Meridional cross-section showing low energy electron density contours [7-21].

contours of constant number density for a meridional cross section. In all cases the flux is assumed to be omnidirectional in the rest frame of the plasma. The model is compared with actual ion data at 5.3 and 20 R_J in Figure 7-14. Note that the corotation energy is a significant fraction of the energy. (Voyager can be assumed to be in a roughly inertial frame relative to the plasma frame for these calculations so that the data are offset by the corotation energy in the plasma detector look direction which was into the flow).

7.7.2 Medium Energy Plasma

Unlike the low energy and high energy plasmas, the medium energy plasma is poorly defined for the Jovian environment. What is available is summarized in Figure 7-18 [7-21] where the density for the electrons and H^+ appear, according to the observations, to fall off roughly exponentially. In terms of a Maxwellian temperature, the electron temperature varies between a few 100 eV and 3 KeV [7-77] with a median value of 1 KeV. The H^+ (other ions undoubtedly exist but have yet to be identified in this energy range) temperatures vary between 20 and 60 KeV with a median of about 30 KeV [7-78]. There is no apparent variation with latitude in either population although this may be an artifact of the paucity of data.

7.7.3 The High Energy Plasma Environment

Long before the Pioneer and Voyager encounters with Jupiter, it was known from radio observations that Jupiter possessed a pronounced radiation belt (pre-Voyager findings are reviewed in Reference 7-83). The Pioneer and Voyager encounters have more than verified the existence of this radiation belt

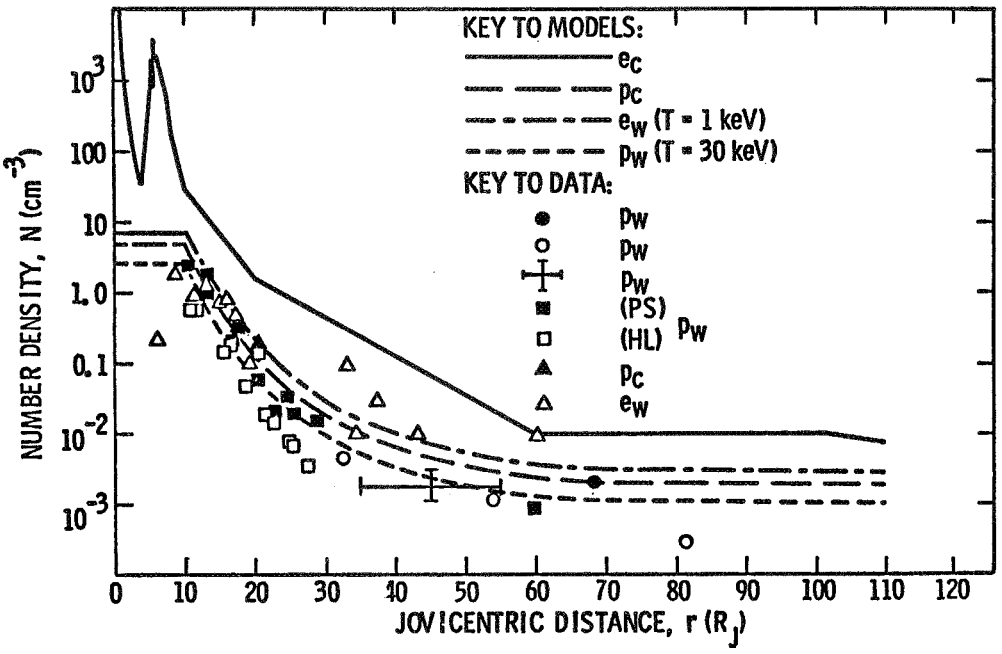

Figure 7-18. Comparison between actual density data and an approximate fit to the data for the cold protons (Pc), warm electrons (Ec), warm protons (Pw) [7-21]. Also shown is the equatorial low energy electron density for comparison. (PS stands for plasma sheet measurements and HL stands for high latitude measurements.)

as will be detailed in the following. Unlike the low energy plasmas, the high high-energy plasma is well organized in terms of the Jovian magnetic field in a manner analogous to the Earth (i.e., B-L coordinates can be used to organize data). This is illustrated in Figure 7-19 which is an overview figure of the electron and ion count rates from the Voyager 2 encounter. The sharp spikes at 10 hr intervals mark encounters with the magnetic equator (this is what led in part to the formulation of the magnetodisc model, discussed in paragraph 7.3.4, in which most of the Jovian plasma is confined by the magnetic field to a relatively thin disc). As in the case of the Earth, the fluxes of both electrons and ions are pitch angle dependent – particles having small pitch angles are lost into the Jovian atmosphere [7-84].

The observation that B-L coordinates can be used to organize Jovian observations to first order simplifies the task of modeling. Here the results of one such model for the inner magnetosphere will be discussed [7-21,7-85]. Data from the Pioneer [7-2] and Voyager [7-78] missions have been fitted to give a model dependent on B, L, and pitch angle. The general results of the model are summarized in Figures 7-20 and 7-21 for the electrons between L values of 1 and 16 (roughly 1 and 16 R_J) and for protons between 1 and 12. The electron energy range is for energies greater than 0.06 MeV and the proton energy range for energies greater than 0.6 MeV. The electrons show a minimum near 7 R_J (somewhat outside the orbit of Io) whereas the protons show a dip at the orbit of Io (such perturbations in the high energy electron and ion data have been used to locate moonlets). Sample intensity spectra as functions of energy are included with each figure for selected L values and magnetic latitudes.

Beyond 15 R_J the intrinsic variability of the fluxes (Fig. 7-19) makes modeling difficult. Not only are the particles modulated strongly by the magnetic field but there were pronounced time and position (local time) variations between missions. For reference, however, peak flux estimates for the omnidirectional electron fluxes in the outer magnetosphere are tabulated in Table 7-10 [7-85] (note:

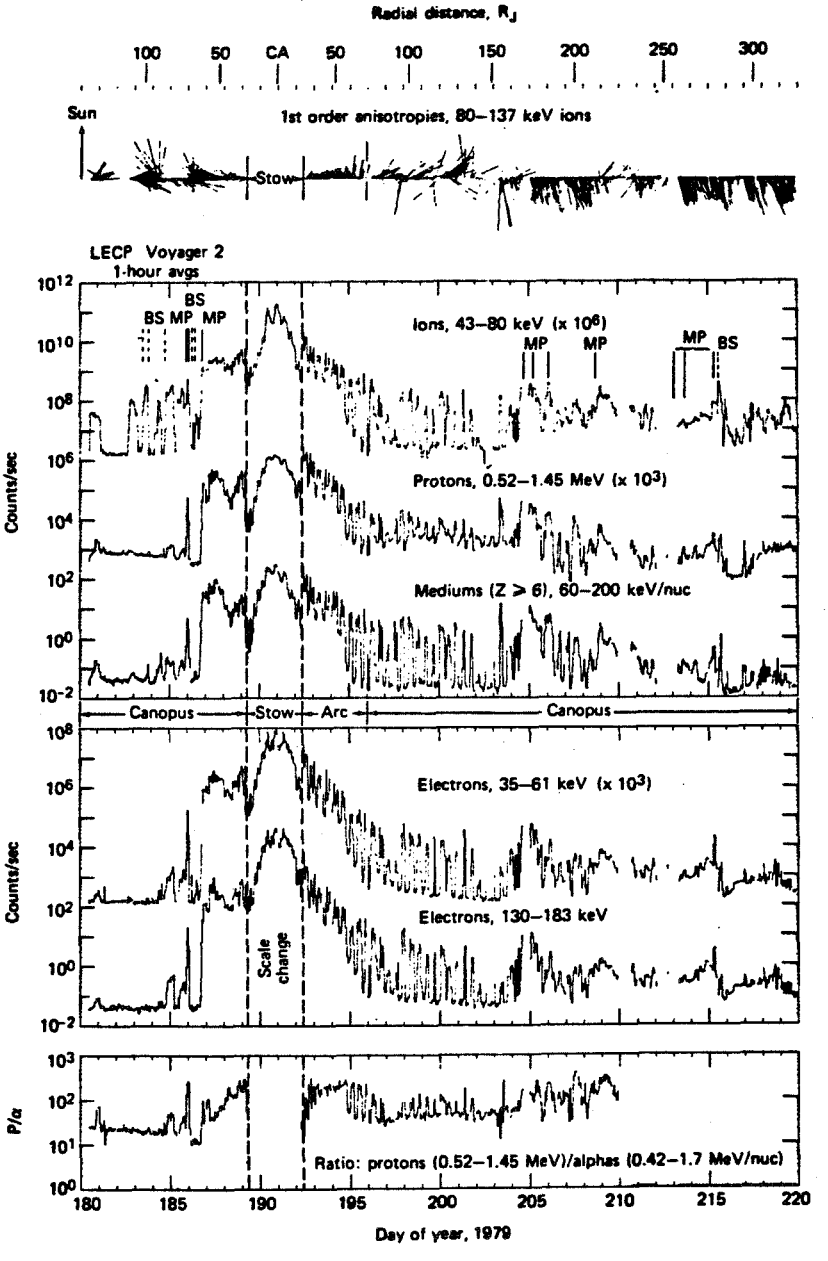

Figure 7-19. Overview of the high energy plasma measurements for Voyager 2 [7-78]. The apparent noise between 40 and 150 R_j is real and the result of encounters with the Jovian magnetic equator.

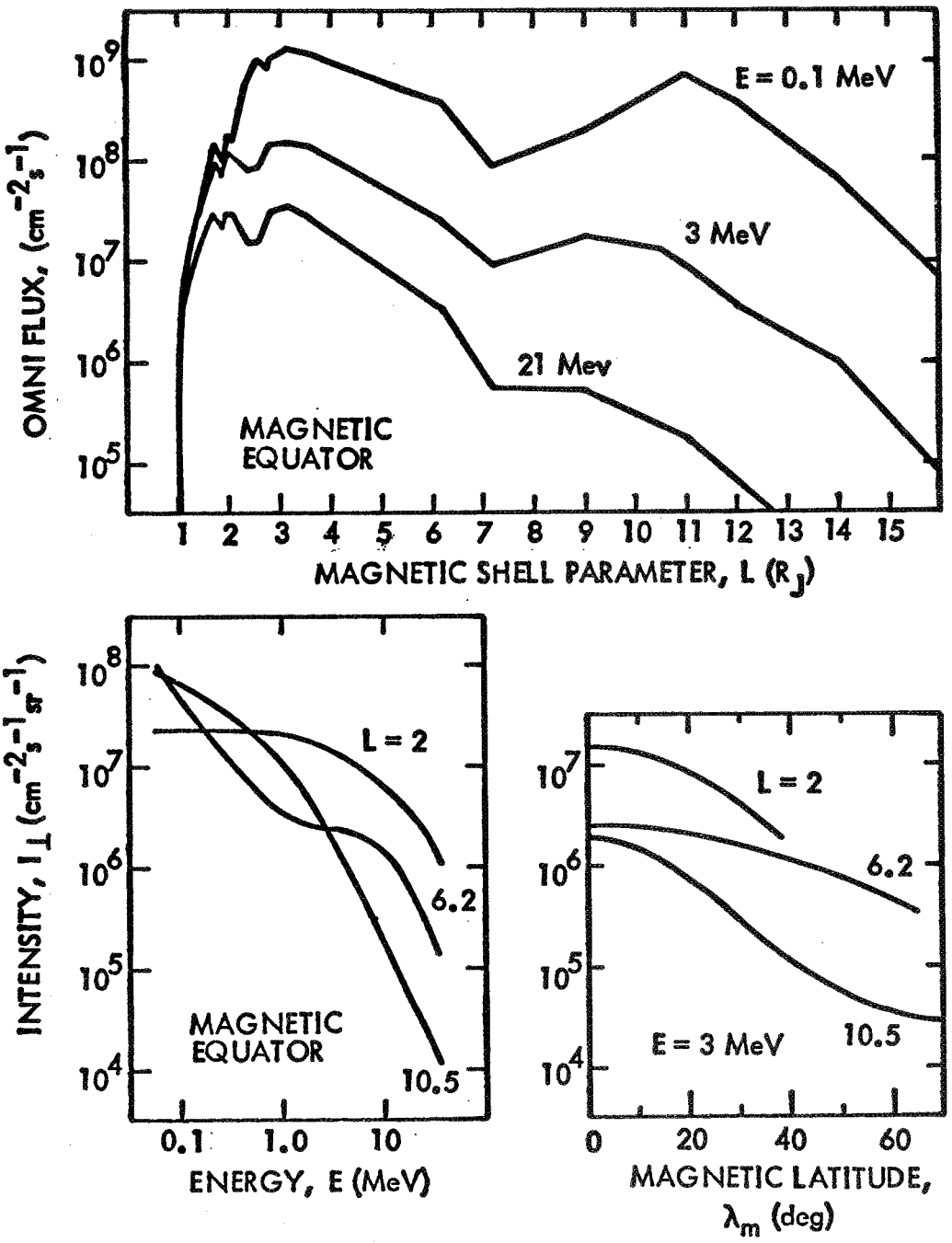

Figure 7-20. Model predictions [7-21] of the high energy electron omnidirectional fluxes as functions of magnetic L values, intensity perpendicular to the magnetic field as a function of energy for different L values, and intensity at different magnetic latitudes for various L values.

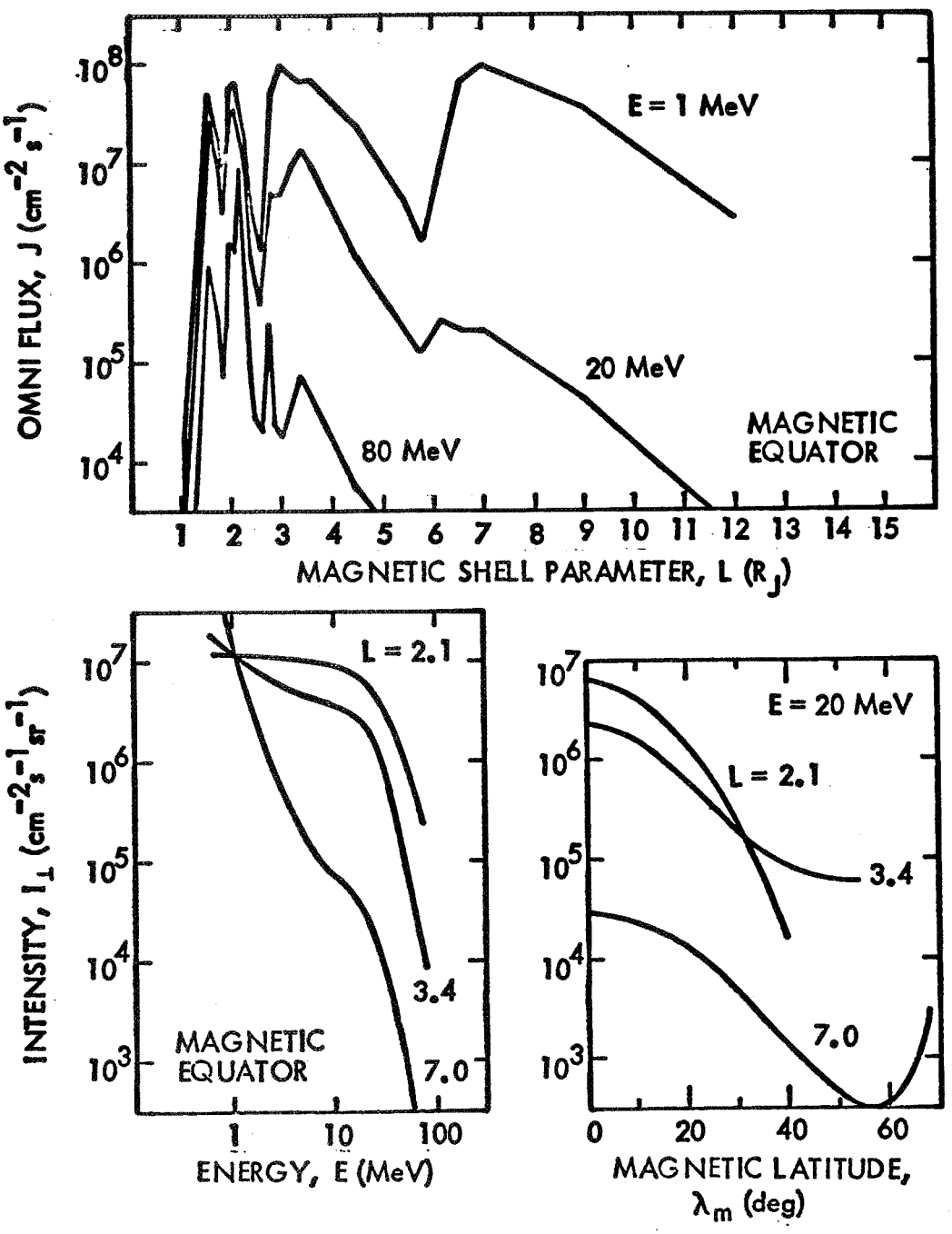

Figure 7-21. Model predictions [7-21] of the high energy proton omnidirectional fluxes as functions of magnetic L values, intensity perpendicular to the magnetic field as a function of energy for different L values, and intensity at different magnetic latitudes for various L values.

TABLE 7-10. EXPECTED VALUES FOR PEAK OMNIDIRECTIONAL ELECTRON FLUXES AT SIX VALUES OF JOVICENTRIC DISTANCE (PARENTHESES INDICATE POWERS OF TEN) [7-85]

ELECTRON ENERGY	OMNIDIRECTIONAL ELECTRON FLUX J_o ($cm^{-2}s^{-1}$)					
E_e (MeV)	15 R_J	25 R_J	35 R_J	50 R_J	75 R_J	100 R_J
0.40	1.0 (7)	4.4 (5)	2.2 (5)	1.0 (5)	4.3 (4)	2.3 (4)
0.63	7.0 (6)	2.7 (5)	1.4 (5)	6.7 (4)	2.9 (4)	1.6 (4)
1.0	3.2 (6)	1.5 (5)	7.9 (4)	4.0 (4)	1.8 (4)	1.0 (4)
1.6	1.3 (6)	6.7 (4)	3.8 (4)	2.1 (4)	1.0 (4)	5.8 (3)
2.5	4.5 (5)	2.9 (4)	1.7 (4)	9.6 (3)	4.9 (3)	3.0 (3)
4.0	1.4 (5)	1.1 (4)	6.8 (3)	3.9 (3)	2.1 (3)	1.3 (3)
6.3	4.5 (4)	4.5 (3)	2.7 (3)	1.6 (3)	8.4 (2)	5.4 (2)
10	1.4 (4)	1.7 (3)	1.0 (3)	6.0 (2)	3.2 (2)	2.1 (2)
16	5.0 (3)	6.4 (2)	3.8 (2)	2.2 (2)	1.2 (2)	7.9 (1)
25	1.8 (3)	2.5 (2)	1.5 (2)	8.8 (1)	4.8 (1)	3.1 (1)
40	8.0 (2)	9.3 (1)	5.6 (1)	3.3 (1)	1.8 (1)	1.2 (1)

these are peak fluxes). These values vary with the Jovian 10-hr period and may change as much as two orders of magnitude in one cycle.

Not considered in the above are the composition and anisotropy of the ions. As an example, for Voyager 1 and 2, at 1 MeV/nucleon the major constituents of the ion population were H, He, C, O, Na, S, and the hydrogen molecules H_2 and H_3 [7-86]. Relative to He, the abundance of H and H_3 at equal energy/nucleon was highest in the outer magnetosphere, the abundances of O, Na, and S were highest in the inner magnetosphere, and the abundance of C constant throughout [7-86]. Indications are that there are approximately equal numbers of O, S, and He ions, with the abundance of H ions being 15 times higher. Ion anisotropies in the outer Jovian magnetosphere are, like those of the low energy ions, the result of high corotation velocities [7-87]. In contrast to the low energy particles, evidence implies that the plasma corotates out to about 58 R_J beyond which the plasma moves slower than corotation. Beyond 130 R_J on the nightside the anisotropies indicate flow of particles away from Jupiter in a magnetospheric wind.

7.8 JOVIAN AURORAL OBSERVATIONS

Limb photographs by Voyager 1 in visible light have revealed active auroras on the nightside of Jupiter [7-60]. Unambiguous detection of auroras in the extreme ultraviolet by means of the UV spectrometers on Voyager 1 [7-74] and Voyager 2 [7-88] has also been made. The Voyager 2 observations showed that the southern auroras were 40 percent brighter than the northern auroras while for Voyager 1 the opposite was true. The auroras appear to be located on magnetic field lines which intersect the Io torus. This suggests that the Io torus is the source of the precipitating electrons assumed to be producing

the auroras. The auroras appear to occur at two levels – 500 and 1700 km above the Jovian haze layer (the layer is apparently a high altitude haze that extends up to pressures of 3.5 mbar) [7-89]. If the visible emission is assumed to lie in the 4000 to 5000°A region, the slant intensity is about 20 kR [7-89]. The UV observations imply that a power of 1.7×10^{11} W is required if the source is precipitating electrons [7-88].

7.9 JOVIAN LIGHTNING

Another curious feature of the Jovian nightside is lightning [7-60]. Lightning strokes appear to be uniformly distributed over the planet. Their intensity is comparable to terrestrial superbolts observed near tops of thunderstorms. The energy of such bolts is about 10^{10} Joules per bolt.

7.10 THE JOVIAN RING

Jupiter's ring was discovered in a photographic image of the area halfway between the satellite Amalthea and the limb of Jupiter during the closest approach of Voyager 1 [7-60,7-68] and was determined subsequently to correspond to an absorption feature observed in the high energy electron profiles from Pioneer II. The ring has been found to consist of three major components: the bright ring, the faint sheet, and the out-of-plane halo [7-90]. The outer radius of the bright ring is 1.81 ± 0.01 R_J (well within the Roche limit of 2.4 R_J), the inner radius is 1.72 R_J, and the eccentricity not greater than 0.003. The normal optical depth of the bright ring is 3.0×10^{-5}. A faint sheet extends from the inner edge of the bright ring to the surface of Jupiter and has an optical depth of 7.0×10^{-5}. A halo of small (less than 0.5 μm) charged particles is believed to envelope the ring. Possible sources of ring particles include micrometeorites from the interplanetary medium, micrometeorite impact erosion from Amalthea or 1979 JI, magnetically swept "dust" from the plumes on Io, or erosion from larger bodies in the ring [7-90].

7.11 JOVIAN RADIO EMISSIONS

An astonishing feature of Jupiter is that it emits 100 times as much radio power per unit area as does the quiet Sun. These powerful radio emissions were discovered quite unexpectedly in 1955 at 22.2 MHz [7-91]. Subsequent to these early observations, ground-based measurements in the 3 to 40 MHz range [decametric (DAM) radiation] and in the GHz range [decimetric wavelength radiation), supplemented by satellite measurements in the hectometer (HOM) and kilometer (KOM) wavelength range, have revealed a number of important facts about Jupiter and its magnetosphere. The analysis of Jovian radio emissions has since become a major field of study for which a few of the more important areas are discussed below. Review References 7-92 through 7-94 for more details.

7.11.1 Decameter, Hectometer, and Kilometer Radio Emissions

Early observations of the DAM radiation coming from Jupiter gave extremely high values for the effective temperature of Jupiter (10^{12}°K at 20 MHz). The high temperatures implied that much of the Jovian radiation is not thermal. For the low frequencies the most interesting aspect is this nonthermal component. The nonthermal component is polarized to a much greater extent than for other astronomical sources which suggested the existence of a strong magnetic field. Further, the sporadic bursts

which are characteristic of the nonthermal component appear statistically to be correlated with the locations of Io and System III longitude (there are, however, non-Io related sources which are tied to specific ranges of Jovian longitudes). Spectra of the DAM radio emissions show several distinct patterns. One of the most pronounced patterns is the arc – a feature which appears as a C-shaped structure on a frequency versus time plot where signal strength is proportional to the increasing shading. A plot from Voyager 1 is illustrated in Figure 7-22 (the change at 1.3 MHz in structure is an instrumental artifact). Several types of arcs, corresponding perhaps to different sources [7-95], have been observed by Voyager [7-93]. Multiple Alfven wave reflections excited by Io have been proposed as one such source [7-79]. HOM emissions (below 1.3 MHz) were extensively studied by the Voyagers and appear to come from two sources near longitudes of 120 and 240 deg and are not controlled by Io. HOM may, however, represent in part the low-frequency extension of DAM arcs. A composite peak flux density spectrum from several Earth-based sources is presented in Figure 7-23a.

At the low frequency end of the Jovian radio spectrum lies the newly discovered KOM emissions. The KOM is divided up into two types – bKOM and nKOM. The bKOM component is the more intense of the two and extends upwards from the lowest frequency of the Voyager instrument (20 kHz). It is highly variable in intensity and the polarization is dependent on observer location (the dayside was apparently LH polarized while the nightside was the opposite). bKOM is observed to occur when the north magnetic pole is pointing toward the observer (i.e., when the observer is at 200 deg longitude). A possible source of bKOM is the magneto-ionic ordinary mode generated in Jupiter's auroral ionsophere [Green and Gurnett, 1980]. nKOM occupies a much narrower bandwidth (40 to 80 kHz) than bKOM. The emission lasts for minutes to hours and is typically at 100 kHz. In contrast to bKOM, the source of nKOM does not appear to be fixed in longitude.

7.11.2 Decimeter and Shorter Radio Emissions

Decimeter wavelength (or microwave; i.e., 1 GHz to 600 GHz) radio emissions have been particularly useful in studying the Jovian environment from Earth. These high frequency components, like the lower frequencies, give high values for the Jovian thermal temperature, again implying major nonthermal sources. A range of Jovian integrated flux density measurements in the microwave range is given in Figure 7-23b. The microwave radiation is dominated by thermal emissions at high frequencies as indicated by low, realistic estimates of Jovian temperatures in this range whereas at the lower frequencies, synchrotron emissions (i.e., the electromagnetic waves emitted by a relativistic electron undergoing acceleration) from the Jovian radiation belts dominate. The first published suggestion of synchrotron radiation as a source was apparently that of Reference 7-97. Synchrotron emission by a relativistic electron moving in a magnetic field gives a characteristic non-isotropic, quasi-continuum of frequencies. The signal is polarized relative to the magnetic field. Because of this polarization, beaming, and dependence on short term processes, the nonthermal emission is of considerable observational interest. The thermal data are consistent with thermal emissions by molecular hydrogen and are, by comparison, of little interest except in the determination of the thermal spectrum. Although there is little information on the angular structure of the thermal component which is apparently uniform across the Jovian disk, there are numerous maps of the nonthermal component.

The polarization of the nonthermal synchrotron component varies in time along with its amplitude. These variations have been shown to be the results of beaming from relativistic electrons trapped in a dipolar magnetic field. A map of the brightness distribution over Jupiter at a wavelength of 10.4 cm [7-98] is presented in Figure 7-24. It was possible from these and related measurements to show that the magnetic field of Jupiter had the opposite sense to that of the Earth and to estimate the strength of the field and the density of the particles. The time variations and polarization changes gave

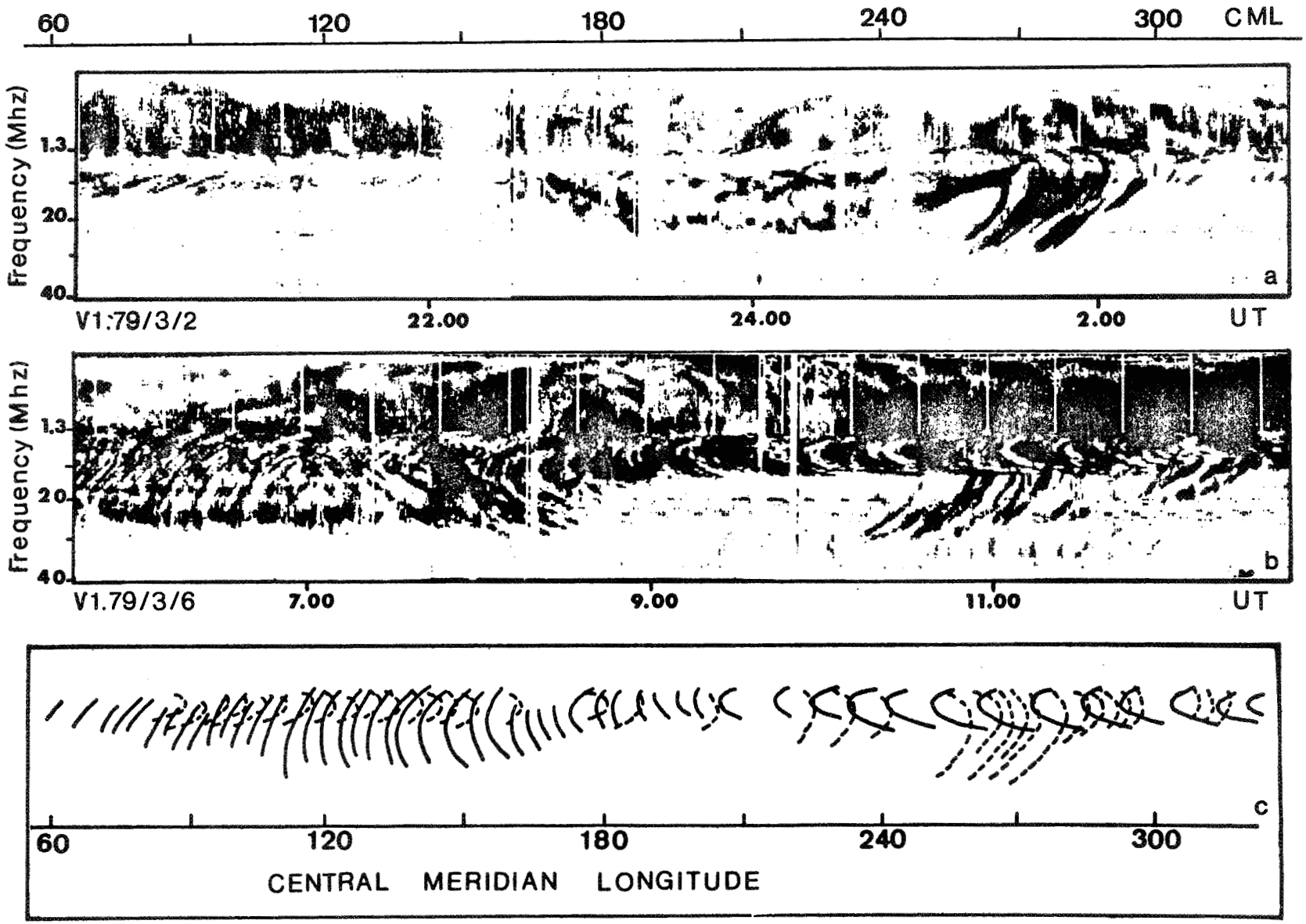

Figure 7-22. Dynamic spectra of Jovian DAM emissions observed by Voyager 1 [7-96]. The arcs consist of 2 types: arcs that open toward increasing time (the solid lines) and arcs that open toward decreasing time (the dashed lines). At the bottom is a schematic view of the two types of arcs and their dependence on CML.

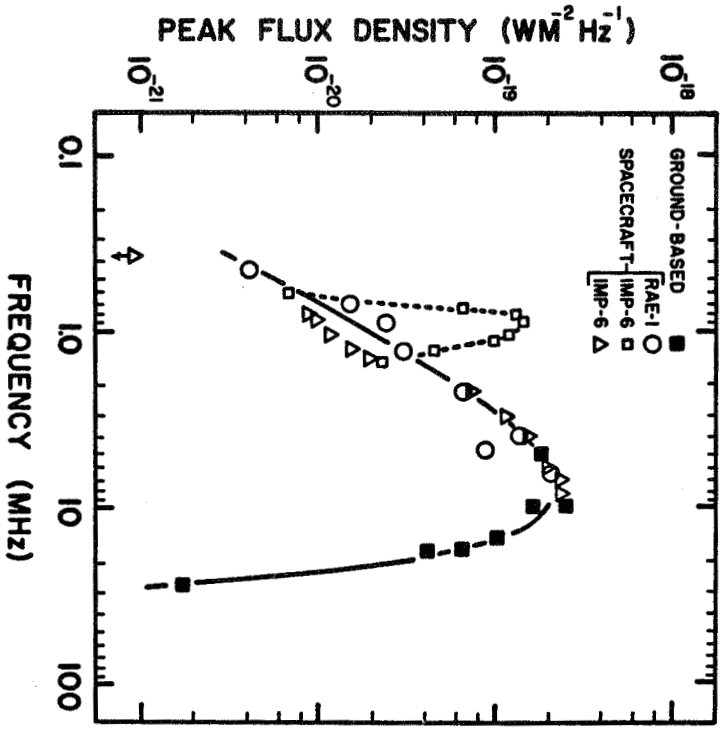

Figure 7-23a. Peak flux density spectrum of DAM and HOM combining ground-based and spacecraft data [7-94]. (By permission.)

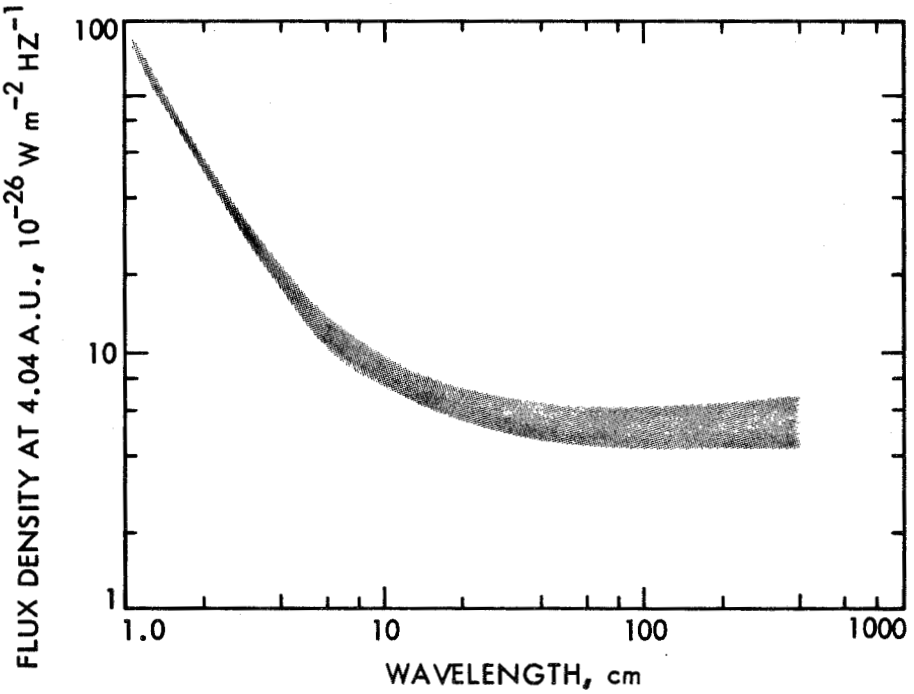

Figure 7-23b. Plot of the Jovian microwave spectrum from ICM to 300 cm. (Shading represents the range of the data over the last decade. From 1 cm to 1 mm, the flux density is given by $S\alpha \lambda^{-2}$.)

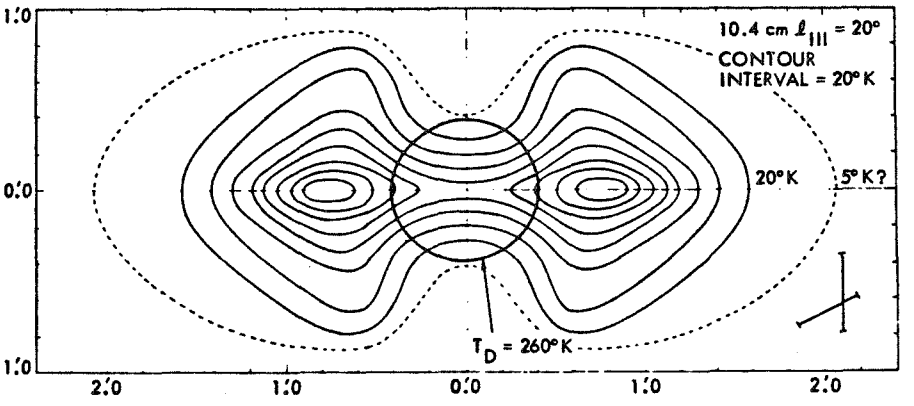

Figure 7-24. Map of the radio brightness of Jupiter at 10.4 cm [7-98]. The contours are at 20°K intervals and the central meridian longitude (system III – 1957.0) is 20°K. A background disk component of 260°K has been subtracted.

additional information on the tilt of the magnetic field and on the rotation rate of Jupiter. As discussed, subsequent in-situ measurements have amply born out these estimates.

7.12 THE Io TORUS

Earth-based observations in the early 1970s revealed the existence of a sodium cloud associated with the orbit of Io. Specifically, Na emissions indicate that the Na forms a partial torus centered on Io. The cloud consists of an inner, optically thick region close to Io and an optically thin emission region extending about 60 arc sec from Io in the orbital plane. A neutral potassium component has also been identified in the torus region.

Besides the neutral torus, several ion constituents have also been identified which make up a plasma ring around Jupiter. This dense plasma ring, according to Voyager EUV observations, consists primarily of sulfur (S^{+++}, S^{++++}, and S^{+++++}) and oxygen (O^{++} and O^{+++}). Ionized K and Na have also been identified. Table 7-9 lists some of the ions identified by the in-situ Voyager plasma measurements in the torus. As noted earlier, the plasma torus divides into two distinct regions (Fig. 7-17) – a cold, low density inner torus ($n \simeq 150$ cm^{-3}; $T \simeq 1$ eV) and a warm, high density outer torus ($n \simeq 1000$-3000 cm^{-3}; $T \simeq 50$ eV).

The source of the Io torus is uncertain. Although the Ionian volcanos would seem the obvious source, their effluents are apparently gravitationally trapped. The more likely source is sputtering. In sputtering, fast ions from the torus or the Jovian magnetosphere strike atmospheric and surface atoms transferring sufficient energy for them to escape Io. SO_2 in the Ionian atmosphere, for example, is a likely source for the sulfur and oxygen ions which dominate the torus [7-99].

7.13 CONCLUSION

As outlined in the preceding, our knowledge of the complex Jovian environment has expanded greatly over the last decade. Although much has been learned of that environment from Earth-based observations, the in-situ measurements by the Pioneer and Voyager missions have been the main source of knowledge about this king of the planets. From the surprising diversity and complexity of its magnetosphere to the subtle complexities of the Great Red Spot, Jupiter and its environs have proven to be of great beauty and scientific interest. Even so, much more remains unexplained about Jupiter than explained. As should be evident, most of our knowledge is statistical or descriptive in nature. Ultimately, it is hoped that the Galileo entry probe and orbiter planned for launch in the late 1980s will provide the in-situ data base necessary to develop a firm theoretical understanding. Until that time, we must be content with the memorable photographs and tantalizing, but brief in-situ measurements of the Pioneers and Voyagers – our first Jovian explorers.

REFERENCES

7-1. Stone, E. C.: The Voyager Mission Through the Jupiter Encounters. J. Geophys. Res., vol. 86, 1981, pp. 8123-8124.

7-2. Gehrels, T. (ed.): Studies of the Interior, Atmospheres, Magnetosphere and Satellites. Jupiter, The University of Arizona Press, Tucson, Arizona, 1976.

7-3. Nature, vol. 280, 1979, pp. 725-806.

7-4. Science, vol. 204, 1979, pp. 911-1008.

7-5. Science, vol. 206, 1979, pp. 925-996.

7-6. Wolfe, J. H.: Jupiter. Scientific American, vol. 233, 1975, pp. 118-126.

7-7. West, G. S., Wright, J., and Euler, H. C. (eds.): Space and Planetary Environment Criteria Guidelines for Use in Space Vehicle Development, 1977 Revision. NASA TM-78119, 1977, pp. 8-33 to 8-36.

7-8. Peek, R. G.: The Planet Jupiter. Faber and Faber, London, 1958.

7-9. Stone, P. H.: The Meteorology of the Jovian Atmosphere. Jupiter, T. Gehrels (ed.), The University of Arizona Press, Tucson, Arizona, 1976, pp. 586-618.

7-10. Smith, B. A. and Hunt, G. E.: Motions and Morphology of Clouds in the Atmosphere of Jupiter. Jupiter, T. Gehrels (ed.), The University of Arizona Press, Tucson, Arizona, 1976, pp. 564-585.

7-11. Seidelman, P. K. and Divine, N.: Evaluation of Jupiter Longitudes in System III (1965). Geophysical Research Ltre., vol. 4, 1977, pp. 65-68.

7-12. Null, G. W., Anderson, J. D., and Wong, S. K.: The Gravity Field of Jupiter from Pioneer II Tracking Data. Science, vol. 188, 1975, pp. 476-477.

7-13. Scarf, et al., 1981.

7-14. Smith, E. J., Connor, B. V., and Foster, G. T., Jr.: Measuring the Magnetic Fields of Jupiter and the Outer Solar System. IEEE Trans. on Magnetics, Mag-11, 1975, pp. 962-980.

7-15. Acuna, M. H. and Ness, N. F.: The Pioneer XI High Field Fluxgate Magnetometer. Space Sci. Inst., vol. 1, 1975, pp. 177-188.

7-16. Ness, N. F., Acuna, M. H., Lepping, R. P., Burlaga, L. F., Behannon, K. W., and Neubauer, F. M.: Magnetic Field Studies at Jupiter by Voyager 1: Preliminary Results. Science, vol. 204, 1979, pp. 982-987.

7-17. Ness, N. F., Acuna, M. H., Lepping, R. P., Burlaga, L. F., Behannon, K. W., and Neubauer, F. M.: Magnetic Field Studies at Jupiter by Voyager 2: Preliminary Results. Science, vol. 206, 1979, pp. 966-972.

7-18. Acuna, M. H. and Ness, N. F.: The Main Magnetic Field of Jupiter. J. Geophys. Res., vol. 81, 1976, p. 2917.

7-19. Smith, E. J., Davis, L., Jr., and Jones, D. E.: Jupiter's Magnetic Field and Magnetosphere. Jupiter, T. Gehrels (ed.), The University of Arizona Press, Tucson, Arizona, 1976, pp. 788-829.

7-20. Acuna, M. H. and Ness, N. F.: Results from the GSFC Magnetometer on Pioneer II. Jupiter, T. Gehrels (ed.), The University of Arizona Press, Tucson, Arizona, 1976, pp. 830-847.

7-21. Divine, N. and Garrett, H. B.: Charged Particle Distributions in Jupiter's Magnetosphere. JPL IOM, July 23, 1981, pp. 5137-81-83.

7-22. Connerney, J. E. P., Acuna, M. H., and Ness, N. F.: Modeling the Jovian Current Sheet and Inner Magnetosphere. J. Geophys. Res., vol. 86, 1981, pp. 8370-8384.

7-23. Goertz, C. K.: The Jovian Magnetodisc. Space Sci. Rev., vol. 23, 1979, pp. 319-343.

7-24. Vasyliunas, V. M. and Dessler, A. J.: The Magnetic-Anomaly Model of the Jovian Magnetosphere: A Post-Voyager Assessment. J. Geophys. Res., vol. 86, 1981, pp. 8435-8446.

7-25. Lepping, R. P., Burlaga, L. F., Klein, L. W., Jessen, J. M., and Goodrich, C. C.: Observations of the Magnetic Field and Plasma Flow in Jupiter's Magnetosheath. J. Geophys. Res., vol. 86, 1981, pp. 8141-8155.

7-26. Hubbard, W. B. and Smoluchowski, R.: Structure of Jupiter and Saturn. Space Sci. Rev., vol. 14, 1973, pp. 599-662.

7-27. Cameron, A. G. W.: Abundances of the Elements in the Solar System. Space Sci. Rev., vol. 15, 1973, pp. 121-146.

7-28. Podolak, M. and Cameron, A. G. W.: Models of the Giant Planets. Icarus, vol. 22, 1974, pp. 123-148.

7-29. Hubbard, W. B. and Slattery, W. L.: Interior Structure of Jupiter: Theory of Gravity Sounding. Jupiter, T. Gehrels (ed.), The University of Arizona Press, Tucson, Arizona, 1976, pp. 176-194.

7-30. Cameron, A. G. W. and Pollack, J. B.: On the Origin of the Solar System and of Jupiter and Its Satellites. Jupiter, T. Gehrels (ed.), The University of Arizona Press, Tucson, Arizona, 1976, pp. 61-84.

7-31. Smoluchowski, R.: Origin and Structure of Jupiter and Its Satellites. Jupiter, T. Gehrels (ed.), The University of Arizona Press, Tucson, Arizona, 1976, pp. 3-21.

7-32. Anderson, J. D., Hubbard, W. B., and Slattery, W. L.: Structure of the Jovian Envelope from Pioneer 10 Gravity Data. Astrophys. J., vol. 193, 1974, p. L149.

7-33. Gautier, D., Conrath, B., Flaser, M., Hanel, R., Kunde, V., Chedin, A., and Scott, N.: The Helium Abundance of Jupiter from Voyager. J. Geophys. Res., vol. 86, 1981, pp. 8713-8720.

7-34. Stevenson, D. J. and Salpeter, E. E.: Interior Models of Jupiter. Jupiter, T. Gehrels (ed.), The University of Arizona Press, Tucson, Arizona, 1976, pp. 85-112.

7-35. Salpeter, E.: On Convection and Gravitational Layering in Jupiter and in Stars of Low Mass. Astrophys. J., vol. 181, 1973, pp. L83-L86.

7-36. Hanel, R. A., Conrath, B. J., Herath, L. W., Kunde, V. G., and Pirraglia, J. A.: Albedo, Internal Heat, and Energy Balance of Jupiter: Preliminary Results of the Voyager Infrared Investigation. J. Geophys. Res., vol. 86, 1981, pp. 8705-8712.

7-37. Wallace, L.: The Thermal Structure of Jupiter in the Stratosphere and Upper Troposphere. Jupiter, T. Gehrels (ed.), The University of Arizona Press, Tucson, Arizona, 1976, pp. 284-303.

7-38. Lindal, G. F., Wood, G. E., Levy, G. S., Anderson, J. D., Sweetnam, D. N., Hotz, H. B., Buckles, B. J., Holmes, D. P., Doms, P. E., Eshleman, V. R., Tyler, G. L., and Croft, T. A.: The Atmosphere of Jupiter: An Analysis of the Voyager Radio Occultation Measurements. J. Geophys. Res., vol. 86, 1981, pp. 8721-8727.

7-39. Hunten, D. M.: Atmospheres and Ionospheres. Jupiter, T. Gehrels (ed.), The University of Arizona Press, Tucson, Arizona, 1976, pp. 22-31.

7-40. Orton, G. S.: Atmospheric Structure in the Equatorial Region of Jupiter. NASA/JPL, 1981, pp. 1625-125.

7-41. Fjeldbo, G., Kliore, A., Seidel, B., Sweetnam, D., and Woiceshyn, P.: The Pioneer II Radio Occultation Measurements of the Jovian Ionosphere. Jupiter, T. Gehrels (ed.), The University of Arizona Press, Tucson, Arizona, 1976, pp. 238-246.

7-42. Ingersoll, A. P.: Pioneer 10 and 11 Observations and the Dynamics of Jupiter's Atmosphere. Icarus, vol. 29, 1976, pp. 245-253.

7-43. Hanel, R., Conrath, B., Flasar, M., Kunde, V., Lowman, P., Maguire, W., Pearl, J., Pirraglia, J., Samuelson, R., Gautier, D., Gierasch, P., Kumar, S., and Ponnamperuma, C.: Infrared Observations of the Jovian System from Voyager 1. Science, vol. 204, 1979, pp. 973-976.

7-44. Hanel, R., Conrath, B., Flasar, M., Herath, L., Kunde, V., Lowman, P., Maguire, W., Pearl, J., Pirraglia, J., Samuelson, R., Gautier, D., Gierasch, P., Horn, L., Kumar, S., and Ponnamperuma, C.: Infrared Observations of the Jovian System from Voyager 2. Science, vol. 206, 1979, pp. 952-956.

7-45. Atreya, S. K. and Donahue, T. M.: Model Ionospheres of Jupiter. Jupiter, T. Gehrels (ed.), The University of Arizona Press, Tucson, Arizona, 1976, pp. 304-318.

7-46. Sill, G. T.: The Chemistry of the Jovian Cloud Colors. Jupiter, T. Gehrels (ed.), The University of Arizona Press, Tucson, Arizona, 1976, pp. 372-383.

7-47. Lewis, J. S.: The Clouds of Jupiter and the NH3-H2O and NH3-H2S Systems. Icarus, vol. 10, 1969, pp. 365-378.

7-48. Ridgway, S. T., Larson, H. P., and Fink, U.: The Infrared Spectrum of Jupiter. Jupiter, T. Gehrels (ed.), The University of Arizona Press, Tucson, Arizona, 1976, pp. 384-417.

7-49. Terrile, R. J. and Westphal, J. A.: The Vertical Cloud Structure of Jupiter from 5 μm Measurements. Icarus, vol. 30, 1977, pp. 274-281.

7-50. Owen, T. and Terrile, R. J.: Colors of Jupiter. J. Geophys. Res., 1981, pp. 8797-8814.

7-51. Hord, C. W., West, R. A., Simmons, K. E., Coffeen, D. L., Sato, M., Lane, A. L., and Bergstralh, J. T.: Photometric Observations of Jupiter at 2400 Angstroms. Science, vol. 206, 1979, pp. 956-959.

7-52. Urey, H. C.: The Planets. Yale University Press, New Haven, Ct., 1952.

7-53. Khare, B. N. and Sagan, C.: Red Clouds in Reducing Atmospheres. Icarus, vol. 20, 1973, pp. 311-321.

7-54. Khare, B. N. and Sagan, C.: S8: A Possible Infrared and Visible Chromophore in the Clouds of Jupiter. Science, vol. 189, 1975, pp. 722-723.

7-55. Sagan, C. and Khare, B. N.: Experimental Jovian Photochemistry: Initial Results. Astrophys. J., vol. 168, 1971, pp. 563-569.

7-56. Woeller, F. and Ponnamperuma, C.: Organic Synthesis in a Simulated Jovian Atmosphere. Icarus, vol. 10, 1969, pp. 386-392.

7-57. Prinn, R. G. and Owen, T.: Chemistry and Spectroscopy of the Jovian Atmosphere. Jupiter, T. Gehrels (ed.), The University of Arizona Press, Tucson, Arizona, 1976, pp. 319-371.

7-58. Ingersoll, A. P., Beebe, R. F., Mitchell, J. L., Garneau, G. W., Yagi, G. W., Yagi, G. M., and Muller, J. A.: Interaction of Eddies and Mean Zonal Flow on Jupiter as Inferred from Voyager 1 and 2 Images. J. Geophys. Res., vol. 86, 1981, pp. 8733-8743.

7-59. Ingersoll, A. P., Beebe, R. F., Collins, S. A., Hunt, G. E., Mitchell, J. L., Muller, J. P., Smith, B. A., and Terrile, R. J.: Zonal Velocity and Texture in the Jovian Atmosphere Inferred from Voyager Images. Nature, vol. 280, 1979, pp. 773-775.

7-60. Smith, B. A., Soderblom, L. A., Johnson, T. V., Ingersoll, P., Collins, S. A., Shoemaker, E. M., Hunt, G. E., Masursky, H., Carr, M. H., Davies, M. E., Cook, A. F., II, Boyce, J., Danielson, G. E., Owen, T., Sagan, C., Beebe, R. F., Veverka, J., Strom, R. G., McCauley, J. F., Morrison, D., Briggs, G. A., and Suomi, V. E.: The Jupiter System through the Eyes of Voyager 1. Science, vol. 204, 1979, pp. 951-972.

7-61. Flaser, F. M., Conrath, B. J., Pirraglia, J. A., Clark, P. C., French, R. G., and Gierasch, P. J.: Thermal Structure and Dynamics of the Jovian Atmosphere 1. The Great Red Spot. J. Geophys. Res., vol. 86, 1981, pp. 8759-8767.

7-62. Hide, R.: Origin of Jupiter's Red Spot. Nature, vol. 190, 1960, pp. 885.

7-63. Golistyn, G. S.: A Similarity Approach to the General Circulation of Planetary Atmospheres. Icarus, vol. 13, 1970, p. 1.

7-64. Stone, P. H.: The Dynamics of the Atmospheres of the Major Planets. Space Sci. Rev., vol. 14, 1973, pp. 444.

7-65. Maxworthy, T. and Redekopp, L. G.: Solitary Waves in the Jovian Atmosphere and a New Theory of the Great Red Spot. Nature, vol. 260, 1976, p. 509.

7-66. Hunt, G. E.: The Atmospheres of the Outer Planets. Advances in Physics, vol. 25 (5), 1976, pp. 455-487.

7-67. Mitchell, J. L., Terrile, R. J., Smith, B. A., Muller, J. P., Ingersoll, A. P., Hunt, G. E., Collins, S. A., and Beebe, R. F.: Jovian Cloud Structure and Velocity Fields. Nature, vol. 280, 1979, pp. 776-778.

7-68. Smith, B. A., Beebe, R., Boyce, J., Briggs, G., Carr, M., Collins, S. A., Cook, A. F., II, Danielson, G. E., Davies, M. E., Hunt, G. E., Ingersoll, A., Johnson, T. V., Masursky, H., McCauley, J., Morrison, D., Owen, T., Sagan, C., Shoemaker, E. M., Strom, R., Suomi, V. E., and Veverka, J.: The Galilean Satellites and Jupiter: Voyager 2 Imaging Science Results. Science, vol. 206, 1979, pp. 927-950.

7-69. Atreya, S. K., Donahue, T. M., and McElroy, M. B.: Jupiter's Ionospheres: Prospects for Pioneer 10. Science, vol. 184, 1974, pp. 154-156.

7-70. Hunten, D. M.: The Upper Atmosphere of Jupiter. J. Atmos. Sci., vol. 26, 1969, pp. 826-834.

7-71. McElroy, M. B.: The Ionosphere of the Major Planets. Space Sci. Rev., vol. 14, 1973, pp. 460-473.

7-72. Atreya, S. K., Donahue, T. M., and Waite, J. H., Jr.: An Interpretation of the Voyager Measurements of Jovian Electron Density Profiles. Nature, vol. 280, 1979, pp. 795-796.

7-73. Eshleman, V. R., Tyler, G. L., Wood, G. E., Lindal, G. F., Anderson, J. D., Levy, G. S., and Croft, T. A.: Radio Science with Voyager 1 at Jupiter: Preliminary Profiles of the Atmosphere and Ionosphere. Science, vol. 204, 1979, pp. 976-978.

7-74. Broadfoot, A. L., Belton, M. J. S., Takacs, P. Z., Sandel, B. R., Shemansky, D. E., Holdberg, J. B., Ajello, J. M., Atreya, S. K., Donahue, T. M., Moos, H. W., Bertaux, J. L., Blamont, J. E., Strobel, D. F., McConnell, J. C., Dalgarno, A., Goody, R., and McElroy, M. B.: Extreme Ultraviolet Observations from Voyager 1 Encounter with Jupiter. Science, vol. 204, 1979, pp. 979-982.

7-75. Bridge, H. S., Belcher, J. W., Butler, R. J., Lazarus, A. M., Mavretic, A. M., Sullivan, J. D., Siscoe, G. L., and Vasyliunas, V. M.: The Plasma Experiment on the 1977 Voyager Mission. Space Sci. Rev., vol. 21, 1977, p. 259.

7-76. McNutt, R. L., Jr., Belcher, J. W., and Bridge, H. S.: Positive Ion Observations in the Middle Magnetosphere of Jupiter. J. Geophys. Res., vol. 86, 1981, pp. 8319-8342.

7-77. Scudder, J. D., Sittler, E. C., Jr., and Bridge, H. S.: A Survey of the Plasma Electron Environment of Jupiter: A View from Voyager. J. Geophys. Res., vol. 86, 1981, pp. 8157-8179.

7-78. Krimigis, S. M., Carbary, J. F., Keath, E. P., Bostrom, C. O., Axford, W. I., Gloeckler, G., Lanzerotti, L. J., and Armstrong, T. P.: Characteristics of Hot Plasma in the Jovian Magnetosphere: Results from the Voyager Spacecraft. J. Geophys. Res., vol. 86, 1981, pp. 8227-8257.

7-79. Gurnett, D. A. and Goertz, C. K.: Multiple Alfven Wave Reflections Excited by Io: Origin of the Jovian Decametric Arcs. J. Geophys. Res., vol. 86, 1981, pp. 717-722.

7-80. Hill, T. W. and Michel, F. C.: Heavy Ions from the Galilean Satellites and the Centrifugal Distortion of the Jovian Magnetosphere. J. Geophys. Res., vol. 81, 1976, pp. 4561-4565.

7-81. Hill, T. W., Dessler, A. J., and Michel, F. C.: Configuration of the Jovian Magnetosphere. Geophys. Research Ltrs., vol. 1, 1974, pp. 3-6.

7-82. Sentmann, D. D. and Goertz, C. K.: Whistler Mode Noise in Jupiter's Inner Magnetosphere. J. Geophys. Res., vol. 83, 1978, pp. 3151-3165.

7-83. Schulz, M.: Jupiter's Radiation Belts. Space Sci. Rev., vol. 23, 1979, p. 277.

7-84. Simpson, J. A., Hamilton, D. C., McKibben, R. B., Morgo-Campero, A., Pyle, K. R., and Tuzzolino, A. H.: The Protons and Electrons Trapped in the Jovian Dipole Magnetic Field Region and Their Interaction with Io. J. Geophys. Res., vol. 79, 1974, pp. 3522-3544.

7-85. Divine, N.: Distribution of Electron Flux Spectra for Analysis of Galileo Optical Navigation Near Jupiter. JPL IOM, 5137-81-120, September 25, 1981.

7-86. Hamilton, D. C., Gloeckler, G., Krimigis, S. M., and Lanzerotti, L. J.: Composition of Nonthermal Ions in the Jovian Magnetosphere. J. Geophys. Res., vol. 86, 1981, pp. 8301-8318.

7-87. Carbary, J. F., Krimigis, S. M., Keath, E. P., Gloeckler, G., Axford, W. I., and Armstrong, T. P.: Ion Anisotropies in the Outer Jovian Magnetosphere. J. Geophys. Res., vol. 86, 1981, pp. 8285-8299.

7-88. Sandel, B. R., Shemansky, D. E., Broadfoot, A. L., Belton, M. J. S., Ajello, J. M., Holberg, J. B., Atreya, S. K., Donahue, T. M., Moos, H. W., Strobel, D. F., McConnell, J. C., Dalgarno, A., Goody, R., McElroy, M. D., and Takacs, P. Z.: Extreme Ultraviolet Observations from Voyager 2 Encounter with Jupiter. Science, vol. 206, 1979, pp. 962-966.

7-89. Cook, A. F., II, Jones, V., and Shemansky, D. E.: Visible Aurora in Jupiter's Atmosphere. J. Geophys. Res., vol. 86, 1981, pp. 8793-8796.

7-90. Jewitt, D. C. and Danielson, G. E.: The Jovian Ring. J. Geophys. Res., vol. 86, 1981, pp. 8691-8687.

7-91. Burke, B. F. and Franklin, K. L.: Observations of a Variable Radio Source Associated with the Planet Jupiter. J. Geophys. Res., vol. 60, 1955, pp. 213-217.

7-92. Berge, G. L. and Gulkis, S.: Earth-based Radio Observations of Jupiter: Millimeter to Meter Wavelengths. Jupiter, T. Gehrels (ed.), The University of Arizona Press, Tucson, Arizona, 1976, pp. 621-692.

7-93. Bioschot, A., Lecacheux, A., Kaiser, M. L., Desch, M. D., and Alexander, J. K.: Radio Jupiter after Voyager: An Overview of the Planetary Radio Astronomy Observations. J. Geophys. Res., vol. 86, 1981, pp. 8213-8226.

7-94. Carr, T. D. and Desch, M. D.: Recent Decametric and Hectometric Observations of Jupiter. Jupiter T. Gehrels (ed.), The University of Arizona Press, Tucson, Arizona, 1976, pp. 693-737.

7-95. Warwick, J. W.: Models for Jupiter's Decametric Arcs. J. Geophys. Res., vol. 86, 1981, pp. 8585-8592.

7-96. Leblanc, Y.: On the Arc Structure of the DAM Jupiter Emission. J. Geophys. Res., vol. 86, 1981, pp. 8546-8560.

7-97. Field, G. B.: The Source of Radiation from Jupiter at Decimeter Wavelengths. J. Geophys. Res., vol. 64, 1959, pp. 1169-1177.

7-98. Berge, G. L.: An Interferometric Study of Jupiter's Decimeter Radio Emission. Astrophys. J., vol. 146, 1966, pp. 767-798.

7-99. Eshleman, V. R., Tyler, G. L., Wood, G. E., Lindal, G. F., Anderson, J. D., Levy, G. S., and Croft, T. A.: Radio Science with Voyager at Jupiter: Initial Voyager 2 Results and a Voyager 1 Measure of the Io Torus. Science, vol. 206, 1979, pp. 959-962.

SECTION 7A. THE SATELLITES OF JUPITER

7A.1. INTRODUCTION

Jupiter has 16 known satellites, 4 of which were discovered by Galileo in 1610 and are large enough to be seen with a small telescope. The Galilean satellites range from 3 to 5 thousand kilometers in diameter, while the other 12 vary from less than 40 to about 270 km. Comparatively little was known about the Jovian system until encounters by the Pioneer and Voyager spacecrafts (1973 to 1974 and 1979) returned a wealth of data and pictures. Voyager enabled the discovery of three new moons of Jupiter and returned astounding pictures of the Galilean satellites, including pictures of erupting volcanos on Io.

Historically, Galileo's discovery was the focal point of a significant development in human civilization. On the surface it invalidated the Ptolemaic view of an Earth-centered universe held by the Roman Church and supported the Copernican theory of a heliocentric universe. But the real issue which brought Galileo to the Holy Roman Inquisition was the philosophic conflict over whether man's source of knowledge about nature derived from religious authority and subjective experience or from observation and measurement [7A-1, 7A-2]. Although he was suppressed and imprisoned by the Church, Galileo became the father of our modern scientific method along with Kepler who simultaneously and independently formulated the same principle. From this time on, the scientific method rapidly became understood and accepted, resulting in the exponential growth of scientific knowledge and technology. Our present day space probes are among the most sophisticated results of this historic development, and it is a fitting tribute that the 1985 space mission to the Jovian system be named GALILEO.

With the exception of the four Galilean satellites, all other satellites of Jupiter are comparatively small. The outermost four, Sinope, Pasiphae, Carme, and Ananke, have retrograde (clockwise) orbits of high inclination and circle Jupiter about once in two Earth years. They lie at distances of 20 to 24 million kilometers and measure less than 50 km in diameter. It is probable that they are captured asteroids.

Moving towards Jupiter, the next four satellites, Elara, Lysithea, Himalia, and Leda, are clustered between 11 and 12 million kilometers. These also have orbits of high inclination, but they move in the normal prograde (counterclockwise) direction about the Sun. The largest two, Elara (80 km) and Himalia (170 km), are known to have a rocky appearance with low albedo.

At just under 2 million kilometers is Callisto, the first of the four Galilean satellites. This is followed by Ganymede at 1 million kilometers, Europa at 670 thousand kilometers, and Io at about 420 thousand kilometers. Ganymede is the largest of the satellites of Jupiter and is nearly as large as Mars; while Europa, the smallest of the Galilean satellites, is a little smaller than our Moon.

In the approximate vicinity of Io's orbit, a plasma torus containing oxygen and sulphur ions is found to be corotating with Jupiter's magnetic equator. The torus has a diameter of about one Jupiter radius and Io's orbit wanders within it.

Inside the orbit of Io are four additional small satellites. 1979 J2, as it is tentatively called, is one of the three discovered by Voyager. It measures about 80 km in diameter and lies at 222 thousand kilometers from Jupiter. Next is diamond-shaped Amalthea at 180 thousand kilometers, which measures 270 by 155 km. Both 1979 J2 and Amalthea are dark, red, and believed to be covered with sulphur compounds originally erupted from Io's volcanos.

Continuing inward is 1979 J1 at 129 thousand kilometers, followed by 1979 J3 at 127,600 kilometers (innermost of the 16 satellites). Both are less than 40 km in diameter and circle Jupiter faster than the rotation rate of Jupiter itself.

All four satellites travel deep within Jupiter's magnetosphere where they are continuously bombarded with energetic electrons, protons, and ions. They also lie well within and react with Jupiter's magnetosphere, which extends out to 100 R_j (Jupiter radii) or 7 million kilometers. Io in particular, exhibits a strong interaction with Jupiter's magnetosphere. Not only does Io's orbit lie within the plasma torus corotating with Jupiter, but Io also has a major magnetic flux tube linking it with Jupiter.

Voyager also discovered a faint ring of material around Jupiter about 30-km wide. The outer edge is about 129 thousand kilometers from Jupiter's center and appears to have an inner edge at about 121 thousand kilometers (a small amount of material may continue all the way to the top of Jupiter's atmosphere). The orbit of 1979 J1 is at the outer edge of the ring and the orbit of 1979 J3 lies within the ring.

Also associated with Jupiter are the one thousand or more Trojan asteroids at the L4 and L5 LaGrangian points in Jupiter's orbit. The two groups respectively maintain a constant average distance (778 million kilometers) ahead (L4) and behind (L5) Jupiter and form equilateral triangles with Jupiter and the Sun (Tables 7A-1 and 7A-2).

7A.2 SINOPE, PASIPHAE, CARME, AND ANANKE

The outermost of the 16 known satellites of Jupiter is Sinope, followed by Pasiphae, Carme, and Ananke in nearby orbits. Their respective semimajor axes are 23.7, 23.3, 22.35, and 20.7 million kilometers. They measure less than 50 km in diameter. All have retrograde orbits of high inclination and circle Jupiter about once in 2 years. The remaining 12 known satellites of Jupiter move in the normal prograde direction. Because of their small size, very few observations have been made of the outer satellites beyond the photographs used for their discoveries and orbit computations [7A-4, 7A-10].

7A.3 ELARA, LYSITHEA, HIMALIA, AND LEDA

A second group also travel in closely spaced orbits. Their semimajor axes are 11.74, 11.71, 11.47, and 11.11 million kilometers, respectively. They have orbits of high inclination and move in the normal prograde directions. The largest two, Elara (80 km) and Himalia (170 km), are known to have a rocky appearance with low albedo. The other two are small and of uncertain size (Lysithea 6 to 32 km and Leda 2 to 14 km). It is possible that the outer eight satellites are captured Trojan asteroids. However, this point is in dispute because of the lack of observed brightness variations associated with the irregular shape of asteroids and unusual photometric color of Himalia (B-V = 0.68, U-B = 0.46) which is unique in the solar system and unlike that of the Trojan asteroids [7A-4, 7A-10].

7A.4 CALLISTO

Callisto is the outermost and least dense of the four Galilean satellites. It has a diameter of 4840 km and a semimajor axis of 1.88 million kilometers.

TABLE 7A-1. DYNAMIC PROPERTIES

Name	Discovered By	Year of Discovery	Siderial Period (days)	Semimajor Axis (X1000 km)	Semimajor Axis (Jupiter radii)	Eccenricity	Inclination (deg)
Sinope	Nicholson	1914	758	23,700	333	0.28	153(R)
Pasiphae	Melotte	1908	735	23,300	327	0.38	145(R)
Carme	Nicholson	1938	692	22,350	314	0.21	164(R)
Ananke	Nicholson	1951	617	20,700	617	0.17	147(R)
Elara	Perrine	1904	260.1	11,740	165	0.207	24.8
Lysithea	Nicholson	1938	260	11,710	164	0.130	29.0
Himalia	Perrine	1904	250.6	11,470	161	0.158	27.6
Leda	Kowal	1974	240	11,110	156	0.146	26.7
Callisto	Galileo	1610	16.689	1,880.0	26.33	0.01	0.2
Ganymede	Galileo	1610	7.155	1,070.0	14.99	0.001	0.2
Europa	Galileo	1610	3.551	670.9	9.40	0.000	0.5
Io	Galileo	1610	1.769	421.6	5.90	0.000	0.0
1979 J2	Synnott	1980	0.675	222.4	3.12	.	.
Amalthea	Barnard	1892	0.489	181.3	2.54	0.003	0.4
1979 J1	Jewett	1979	0.298	129.0	1.81	.	.
1979 J3	Synnott	1980	0.295	127.6	1.79	.	.

Jupiter period of rotation: 0.4135 days
Jupiter radius R_j = 71,398 km [7A-3]

(R) inclination greater than 90 deg indicates retrograde orbit.

All data from Reference 7A-4 except Callisto, Ganymede, Europa, Io, and Amalthea from Reference 7A-5 and 1979 J1, 1979 J2, and 1979 J3 from Reference 7A-6.

TABLE 7A-2. PHYSICAL DATA

Name	Diameter (km)	Density (gm/cc)	Mass (X10[23]g)	Albedo	Mean Opposition Visual Magnitude	Reduced Visual Magnitude*
Sinope	6 to 36				18.3	+11.6
Pasiphae	8 to 46				17.7	+11.0
Carme	8 to 40				18.0	+11.3
Ananke	6 to 28				18.9	+12.2
Elara	80 ± 20			0.03	16.4	+9.3
Lysithea	6 to 32				18.4	+11.7
Himalia	170 ± 20			0.03	14.8	+8.0
Leda	2 to 14				20	+13.3
Callisto	4,840	1.8	1074	0.17	5.6	-1.05
Ganymede	5,270	1.9	1490	0.43	4.6	-2.09
Europa	3,130	3.0	487	0.64	5.3	-1.41
Io	3,640	3.5	891	0.63	5.0	-1.68
1979 J2	80					
Amalthea	270 × 155			0.05	13.0	+6.3
1979 J1	40			0.05		
1979 J3	40			0.05		
Jupiter	143,000	1.3		0.51		
Earth	12,756	5.52		0.39		
Moon	3,476	3.34		0.07		
Mars	6,800	3.9		0.15		

*Visual magnitude at zero phase reduced to 1 AU from both Earth and Sun; it does not include the opposition surge exhibited by the Galilean satellites.

All data from Reference 7A-4 except diameter and mass of Galilean satellites from Reference 7A-7, Amalthea diameter from Reference 7A-8, and 1979 J1, 1979 J2, and 1979 J3 from Reference 7A-6. For mapping information review Reference 7A-9.

7A.4.1 Appearance

Callisto is dark (albedo 0.17) and its features have little contrast. Measurements in the infrared show contrast differences of less than 1 percent [7A-11]. The entire surface has a high density of craters several tens of kilometers in diameter and larger, plus two large ring structures [7A-8]. Of these, the most striking is a very large multi-ring structure named Valhalla, whose central area measures 300 km across with a series of approximately 10 equally spaced rings extending out about 1500 km from the center. Unlike similar structures on the Moon and Mercury, the central area is not a basin. No radially lineated ejecta can be seen, and there are no ring mountains. Both the flatness of this feature and its unusual ring spacing are believed to be due to the material properties of Callisto's ice-rich crust and contrast multi-ring basins on the Moon and Mercury which have a silicate crust. The reduced topographic relief is believed to be due to viscous flow during or subsequent to the impact event leaving only a broad, bright albedo feature in place of the former basin. The lack of heavy cratering in the center of this feature and an increasing crater density gradient which approaches the average density for the surface of the satellite at the outer rings indicates that the multi-ringed structure was formed relatively late in the period of heavy cratering [7A-12].

7A.4.2 Composition

Callisto has a density of 1.79 g cm^{-3} which suggests that it has a large proportion of water (perhaps 50 percent) in its bulk composition [7A-12], and cratering evidence indicates it had a soft icy crust early in its history [7A-8]. Beneath a thin surface layer about 1-mm thick, the thermal inertia of Callisto is about twice that of the Moon or about 2×10^{-3} cal cm^{-2} k^{-1} $sec^{-½}$ which suggests a more consolidated subsurface than has the Earth's Moon. This is probably due to refusion of ice materials [7A-13].

7A.4.3 Age

Callisto is the oldest and most heavily cratered object thus far observed in the solar system. It appears to be a tectonically dead body whose surface shows no history of geologic activity. It shows no cracks, no volcanos, and no mountains. This suggests that it has never seen sufficient internal heating to initiate geologic activity. The ancient crust has apparently remained unchanged over geologic time, except by the innumerable meteor impact craters estimated to date back about 4 billion years to the late torrential bombardment period [7A-8, 7A-14]. Callisto has a great deficiency of large craters ($D > 10$ km) compared to the Moon or Mercury suggesting a difference in population of impacting bodies between the inner and outer regions of the solar system [7A-15, 7A-16].

7A.4.4 Surface Temperature

Low latitude surface temperatures on Galilean satellites range from 155°K during the day (the subsolar point measured on Callisto) to 80°K at night [7A-5, 7A-13].

7A.5 GANYMEDE

Ganymede is Jupiter's largest moon. It has an orbital semimajor axis of 1.07 million kilometers and a diameter of 5270 km which is about 22 percent smaller than Mars. Ganymede has an albedo of 0.43, which is slightly brighter than the Earth (albedo 0.39) and much brighter than Callisto (albedo 0.17).

7A.5.1 Appearance

In the infrared, Ganymede shows contrast differences of less than 1 percent as do Callisto and Europa [7A-11]. The polar caps on Ganymede appear to be bluish-white and are possibly covered with a superficial frost layer which does not seem to alter the appearance of the topography [7A-8]. Optical wavelength photometry used to determine the surface microstructure of Ganymede shows that its surface is more porous than Callisto. This roughness is probably due to micrometeoroids [7A-17].

7A.5.2 Composition

Ganymede's density is only about 1.9 g cm^{-3}, which suggests it has a bulk composition of about 50 percent water by weight [7A-12]. Approximately half of Ganymede's surface is exposed water-ice and half is darker rock. Ice is exposed near large craters and to a lesser extent in the grooved terrains [7A-7]. Evolutionary models of the internal structure imply differentiation into a silicate-rich core, an ice crust, and either a liquid water mantle or a solid warm convecting ice mantle [7A-12]. Its appearance suggests that Ganymede had a soft icy crust early in its history [7A-8].

7A.5.3 Tectonic Activity

Ganymede is physically similar to its neighbor Callisto. It is 8 percent larger and slightly more dense than Callisto (1.92 versus 1.81 gm/cc) but their respective appearances suggest that they have had different geologic histories. Ganymede's surface shows a complex terrain, a global system of grooves and ridges, faulting, and other evidence of crustal activity. By contrast, Callisto appears to have never seen sufficient internal heating to initiate geologic activity and shows no cracks, mountains, volcanos, or structural variations [7A-7].

A global network of grooves and ridges is exhibited on Ganymede, many of which occur in families of as many as 20 grooves and ridges running side by side for tens or hundreds of kilometers [7A-18]. There are numerous examples of apparent classic parallel faults, some aligned side by side in swaths more than 100-km wide. In some places these swaths are broken and laterally offset by what appears to be transverse faulting. This evidence suggests that Ganymede may have seen crustal tectonic activity similar to that on Earth, the only other planet known to exhibit plate motions [7A-7]. Unlike Earth, however, there do not appear to be signs of emergence and subduction where new crustal material rises while older plates are driven into and beneath one another. This might be explained by the theory that Ganymede is blanketed with hundreds of kilometers of ice [7A-18].

7A.5.4 Terrain Types

Four distinct terrain types have been identified on Ganymede which imply differing periods of geologic activity.

7A.5.4.1 Cratered Terrain

The first terrain type is a dark, heavily cratered terrain of polygonal shape separated by bright bands and containing bright rayed impact craters. This is the most ancient of the terrain types [7A-8]. The largest dark area is about as large as the continental United States and contains remnants of a concentric ring structure similar in some respects to the giant ring structures on Callisto [7A-7, 7A-8]. The dark cratered terrain shows numerous, predominantly shallow craters ranging from a few to more than 50 km in diameter. These are probably as old as the Moon craters (4 billion years) [7A-12].

7A.5.4.2 Grooved Terrain

The second terrain type is the grooved terrain which appears as bright bands of diverse patterns and ages separating the polygons of dark heavily cratered terrain [7A-8]. Some parts of the grooved terrain have as many craters as the dark cratered terrain, while other areas have only about one-tenth as many craters with densities similar to the 3.5 billion year old lunar plains [7A-7]. This suggests that Ganymede had a mobile active crust in its early history [7A-12]. The grooved terrain consists of a mosaic of systems of grooves with one system ending abruptly at another. The systems are closely spaced shallow grooves which form interwoven networks, suggesting that the entire crust has been under tension due to global tectonic processes [7A-5, 7A-12]. In some cases, the systems transect one another, suggesting that Ganymede experienced a series of mountain building events [7A-7]. Typically, the mountain ridges are 10 to 15 km across and about 1000-m high, appearing to be similar in scale to the Appalachian Mountains in the Eastern United States [7A-7]. No higher relief exists. The topography of large and medium craters and basins appears to have been reduced, possibly by viscous flow [7A-8].

7A.5.4.3 Impact Craters

A third terrain type consists of young, rugged impact craters and ejecta blankets which are superimposed over both the grooved and ancient cratered terrain. These craters have exposed fresh bright materials which are most likely water-ice. In most, but not all of the bright patches, the original crater and its rim have all but disappeared, leaving only a smooth bright surface which interrupts the older cratered terrain. These smooth bright patches are called palimpsests [7A-8].

7A.5.4.4 Smooth Terrain

A fourth type of terrain is the young, smooth terrain which replaces or floods the older grooved terrain. It occurs in patches which locally obscure older terrains and is lightly cratered [7A-8].

A large dome about 260-km wide which rises about 2.5 km above Ganymede's surface has been noted. It has been proposed that this may be caused by water rising through a major fissure [7A-19].

7A.5.5 Age

Ancient dark heavily cratered terrain is the oldest terrain on Ganymede and is estimated to date back at least 4 billion years to the late torrential bombardment period [7A-8, 7A-14]. The formation of the grooved terrain started during this torrential period and probably lasted several hundred million years. Some of the oldest grooved terrain appears to be as old as the dark cratered terrain, while other areas have only a tenth as many craters with densities similar to the 3.5 billion year-old lunar plains [7A-7, 7A-16]. (The same deficiency of large craters noted on Callisto also exists for Ganymede.)

7A.5.6 Surface Temperatures

Voyager observations of Ganymede between 11 and 24 hr local time recorded surface temperatures at low latitudes ranging from 85 to 145°K [7A-13].

7A.5.7 Atmosphere

The presence of exposed water-ice on Ganymede suggests that there might be a tenuous atmosphere. However, Voyager 1 ultraviolet spectrometer measurements did not detect water vapor, oxygen, or carbon dioxide; thus yielding an upper limit of 10^{-11} bar for these gases [7A-7].

7A.5.8 Magnetosphere

A complex magnetosphere interaction with Ganymede was observed in the magnetic field, plasma, and energetic particles up to about 200,000 km from the satellite [7A-5]. (Review discussion of Jupiter's magnetosphere, Section 7, paragraph 7.7.)

7A-6 EUROPA

Europa, the smallest of the four Galilean satellites, is about 10 percent smaller than the Moon. It measures 3130 km in diameter and has a density of 3 g cm^{-3}. Its orbital semimajor axis is 671,000 km, and its albedo of 0.64 is the highest of the satellites of Jupiter.

7A.6.1 Appearance

Europa has a smooth surface covered with highly complex fracture patterns which show little or no relief except for numerous, thin, bright ridges superimposed one upon another of perhaps a few hundred meters high and with very regular widths of about 10 km [7A-8]. These ridges are best seen at low Sun angles and tend to disappear at higher angles. The ridges are very unusual in that instead of being straight they form scallops or cusps, with smooth curves that repeat regularly on a scale of one hundred to several hundred kilometers. Nothing similar to them has been seen on any other body [7A-7].

The surface consists of slightly mottled terrain and a smooth uniformly bright terrain crossed by darker linear markings and ridges. The dark bands are about 10 percent darker than the adjacent smooth terrain and vary in width from several to 70 km and in length from several hundred to several thousand kilometers [7A-5, 7A-8]. Europa has contrast differences in the infrared of less than 1 percent [7A-11]. The dark linear markings show little or no relief, possibly less than a few tens of meters [7A-8]. Many follow great or small circles, but others are curved or irregular [7A-7]. This implies crustal rifting or global tectonic processes possibly induced either externally by tidal despinning or internally by convection [7A-12, 7A-14]. There may also be tidal heating as in the case of Io, but probably an order of magnitude less heating than on Io [7A-12, 7A-20]. Europa shows no obvious basin structures and very few impact basins [7A-12].

7A.6.2 Composition

Europa's density of 3 g cm^{-3} suggests that it has a primarily silicon bulk composition with a small admixture of lighter materials, possibly 20 percent water. By comparison, neighboring Io, which is believed to have no water, has a density of 3.5 g cm^{-3} [7A-21]. It has been suggested that Europa may, in fact, have a thick ice crust floating on liquid water ocean [7A-7]. Groundbased radar indicates that there are large amounts of exposed water on Europa, probably as ice [7A-22]. Models indicate that if

all of the water were on the surface, a water and water-ice outer shell as thick as 100 km is possible [7A-12]. The mottled terrain, however, may be evidence that the silicate core is actually much closer to the surface (within 10 km). If this is the case, then the core probably still contains significant amounts of volatiles, mainly water [7A-8].

7A.6.3 Age

Only three impact craters about 20 km in diameter have been identified on Europa [7A-8], however, small craters may exist in the mottled terrain below the limit of resolution of the Voyager 2 photos (about 4 km). The lack of craters implies that either the surface is relatively young compared to Callisto and Ganymede (but probably at least several hundred million years old) [7A-8] or that craters are not preserved for long in the icy crust [7A-7]. Models indicate that the apparent absence of mountains or large craters may be partly due to cold flow of a fairly thin, stiff crust [7A-23]. Evidence also suggests that a significant amount of water-ice sputtering has occurred over geologic time, causing from tens of meters to kilometers of erosion.

7A.6.4 Surface Temperature

Voyager measurements of Europa indicate that the diurnal maximum equatorial temperature reaches about 125°K [7A-13].

7A.7 IO

Io is the innermost and most dense of the Galilean satellites. It has a distinctly orange color and an albedo of 0.63. It lies at a distance of 422 thousand kilometers from Jupiter and has a diameter of 3640 km (slightly larger than the Moon). Io has been dominated over geologic time by a powerful heating mechanism caused by modulation of Jupiter's intense tidal force by the orbital resonances of Europa and the other Galilean satellites. This has resulted in extensive long-term volcanic activity continuously resurfacing the planet. Io's surface is estimated to be on the order of about 1 million years old. Appearance and high density (3.5 g cm^{-3}) suggest that most of the lighter volatiles such as water and carbon dioxide have been driven off; while the heavier, less volatile compounds such as sulphur and sulphur-dioxide have been volcanically recycled into the crust, coloring much of the surface bright yellow, orange, red, and white [7A-24].

7A.7.1 Appearance

The most widespread terrain on the surface is comprised of plains deposits that lie between volcanic vents [7A-25]. Hundreds of calderas are visible up to 200 km across, much larger than those found on Earth. There are two types of calderas, those with flows and those without. Those without flows are the most common and generally show no albedo markings. Those with flows have diffuse halos or bright and dark patterns. The flows vary from black to complexly colored with reds, yellows, violets, and browns in about half of the calderas. The flow patterns show little discernible relief, implying low viscosity flows [7A-12].

Intervolcanic regions consist of featureless smooth plains which occur at various stratigraphic levels separated by scarps of unusually uniform relief [7A-12]. Topographically, the plains are featureless and smooth, but occasional mountains appear in the smooth terrain [7A-25].

Complex regions show collapse pits, scarps, faults, and layered terrains [7A-25]. Irregular or fretted scarps on Io are similar to those on Earth and Mars, but since there is probably no water on Io to facilitate erosion, a sapping mechanism involving liquid SO_2 has been proposed to explain the complex eroded terrains [7A-26]. Voyager images show a number of liquid sulphur flow fronts and frozen rivers [7A-27].

Spectral reflectance studies indicate no water absorbing features [7A-12]. Contrast differences in the infrared exceed 5 percent, suggesting dust above the surface or exposed bulk (nonpulverized) material. This compares with contrast differences of less than 1 percent for Europa, Ganymede, and Callisto [7A-11] and is consistent with the idea that considerable volcanic material has snowed back onto the surface.

7A.7.2 Composition

The fact that there are randomly distributed volcanic vents and a lack of visible regional fractures suggests that Io does not contain strongly patterned convection cells which would lead to plates with detectable margins. This is consistent with the model of Peale and others that Io has a thin (<20 km), tidally heated crust [7A-25, 7A-28]. Io has a density (3.5 g cm^{-3}) which is very close to that of the Moon and probably has a silicate interior [7A-25]. Possible geological models suggest that Io's crust may be either predominantly a layer of volatiles of S_2/SO_2 (<10-km thick) [7A-29], or alternatively, it may have a crust composed primarily of silicate magmas enriched by only minor amounts of sulphur [7A-28]. Evidence suggests that both types of flows have occurred. Mountains with relief as high as 10 km are probably composed of silicates, while extensive features of low relief exhibit the colorations and structural appearance of sulphur and sulphur compounds [7A-30].

Absorption features in Io's reflectance spectrum suggest that frozen SO_2 molecules are present on the surface as free frost [7A-31]. The infrared reflection spectrum of laboratory grown SO_2 frost, grown at a low pressure at 140°K, provides an excellent match to Io's spectrum in the 1.0 to 4.5 μm range [7A-32]. Pervasive outgassing has occurred throughout Io's history. Many of the lighter volatiles such as water probably have been lost to space, leaving only the heavier volatiles such as sulphur and sulphur dioxide remaining at the surface [7A-30].

7A.7.3 Color

Deposition from the vapor phase is believed to be the dominant process producing the composition and texture of Io's optical surface. It has been suggested that Io's reflectance spectrum from 0.25 to 5.0 μm can be explained by an optical surface layer consisting of fine-grained particles of sublimated alkali sulphides and free sulphur on which is absorbed a substantial component of H_2S and/or SO_2 [7A-33].

Four plains units may be distinguished on Io. The first is white-to-bluish-white material which may be surface deposits of SO_2 frost or the orthorhombic crystal form of sulphur. The second plains unit shows red, orange, and yellow hues which may be various forms of sulphur sublimates or sulphur alteration. The third plains unit lies largely in the polar regions and is brown or black. The fourth plains unit is very dark brown to black and appears as diffuse deposits around some vents [7A-25].

Great diversity in color and albedo can be seen in the hemisphere facing away from Jupiter which shows bright orange-red at the equatorial region, mottled by large irregular whitish patches. The poles are darker [7A-12]. Dark reddish material has been observed to be concentrated in the equatorial latitudes on the trailing hemisphere throughout the past 50 years of observations. In light of the rapid resurfacing rates that have been observed which might be expected to alter or erase such differences, this asymmetry remains to be explained [7A-34].

7A.7.4 Heating Mechanism

Io is presumed to have had a high level of volcanic activity for much of its history. This is consistent with the idea that the volcanos are probably driven by tidal heating [7A-30]. Orbital resonances of the outer Galilean satellites, especially Europa, induce forced eccentricities in Io's orbit which cause variations in the enormous tides induced by Jupiter. This model is believed to account for considerable tidal energy dissipation resulting in a molten core and a thin mantle or crust. Runaway heating in the core is stabilized when the crust becomes sufficiently thin to conduct away all of the tidally generated heat. Based on calculations from this model by Peale, et al., volcanic activity was predicted on Io. This result was published only days before Voyager 1 discovered erupting volcanos [7A-20].

7A.7.5 Volcanos

Io is the only body in the solar system other than Earth known to have active volcanism [7A-35]. More than 300 suspected vents have been identified on moderate to low resolution Voyager photographs. The vents average 40 km across and the largest is about 250 km. Complex digitate patterns radiate outward from many vents [7A-25].

Voyager 1 observed eight active volcanos on March 5, 1979. Voyager 2 observed 7 of the 8 erupting volcanos seen by Voyager 1 about 18 weeks later; 6 of these were still erupting. The largest plume had ceased activity and the next largest had increased in complexity and doubled in size [7A-8]. Associated with it was a large hot spot approximately 150°K warmer than surrounding surface [7A-14]. An additional plume appeared to have been active between the two encounters [7A-8]. All but one of the active volcanos observed lies within 30 deg of the equator [7A-25].

7A.7.6 Plumes

The largest plume observed was 280-km high and 1000 km in diameter. The morphology of the plumes seems to be related to the dimensions and geometry of the eruption event. Very diffuse plumes with no discernible central fountain, or with very broad fountains, are probably associated with long fissure eruptions and symmetrical, umbrella-shaped plumes with relatively narrow central fountains may be related to short fissure or pipe vent eruptions [7A-36].

The plume heights observed by Voyager ranged from 70 to 280 km above Io's surface [7A-29]. They consist of material of low albedo and the edges of the plumes appear to be particulate matter [7A-12]. Plume regimes contain roughly equal mounts of solid and vapor. Photos suggest there are variable rates of injection of some substance, possibly sulphur droplets, into a steady gaseous flow of sulphur dioxide [7A-37]. Evidence suggests that plumes may contain particles on the order of a micron in diameter [7A-8]. Eruption velocities of several hundred meters to 1 km/sec have been observed

[7A-12], but the escape velocity on Io is about 2.56 km/sec and, therefore, eruptions are not believed to be a direct cause of the loss of volatiles [7A-38]. Typical ballistic flight times for solids in the plumes are about 1000 sec [7A-27]. H_2S may have been an early constituent of the plume effluents, but since it is easily photodissociated and hydrogen has a very low freezing point, it can escape efficiently from Io by a process of Jeans escape (the normal atmospheric escape mechanism) or magnetospheric sweeping [7A-27].

7A.7.7 Resurfacing

The rapid rate at which volcanic material is being deposited on the surface has profound implications for its bulk chemical evolution [7A-29]. Both plume material and volcanic flows appear to be responsible for resurfacing [7A-38]. The color patterns observed on Io indicate extensive surface flows of quenched molten sulphur. The sulphur flows and effluents are quenched at the ambient temperature of about 135°K [7A-27]. Flows up to 300-km long have been noted [7A-30].

It is probable that the sustained tidal energy dissipation over geologic time has contributed to the early loss of volatiles from Io's bulk composition. Those with high vapor pressures, such as water, probably have been lost to space; while those with low vapor pressures, such as sulphur and sulphur dioxide, have survived in the continuously recycling crust; therefore, a very young surface is expected [7A-29]. Assuming a lunar size frequency spectrum and rate of cratering, an estimate of the resurfacing rate or minimum rate of burial or erosion required to remove craters over a period of a million years so that none is now visible is 10^{-2} cm/year. This is consistent with estimates of deposition rates of volcanic plume material from observations of current volcanic activity [7A-38]. A conservative estimate of the deposition rate of volcanic plume material based on observations of current volcanic activity (eight volcanos) is about 3.5×10^{-4} cm/year. This estimate neglects large plume particles, recondensation of the gaseous component of the eruptions, volcanic flow activity, and what appear to be numerous smaller gas/particulate venting features below the level detectable as plumes. Therefore, a resurfacing rate of 10^{-1} cm/year is believed to be a reasonable nominal value [7A-38].

7A.7.8 Age

Io's surface is believed to be the youngest and most dynamically active in the entire solar system [7A-8]. No visible craters have been observed down to 1-km resolution, which implies a young surface estimated to be less than a million years old [7A-12]. Over the 18 weeks between Voyager 1 and 2, several large-scale changes had occurred consistent with surface deposition rates of 10^{-2} cm/year deduced for plume areas [7A-5]. The average renewal time for color and albedo features (but not topographic features) has been estimated to be less than 10^3 years [7A-27].

7A.7.9 Atmosphere

Gaseous SO_2 with an abundance of 0.2 cm atm has been identified in the Io atmosphere by Voyager. This is consistent with an atmosphere in equilibrium with solid SO_2 at the local surface equilibrium temperature. Upper limits have been determined for the abundance of several gases which indicate that Io is apparently depleted in hydrogen, carbon, and nitrogen [7A-39]. Stellar occulations indicate Io has a very tenuous atmosphere which is estimated to be 10^{-6} bar [7A-40]. This implies that

nearly all of the volatiles produced by the volcanos return to the surface, and only minor amounts are escaping [7A-38]. The bulk of Io's atmosphere is believed to be protected from Jupiter's corotating plasma, either by a magnetosphere of Io or by a slowing down of the plasma in a comet-like interaction. But above the magnetopause (or ionopause), scavenging rates are high enough to require continuous replenishment by volcanic activity, otherwise the atmosphere would rapidly disappear. Estimates of the supply rate of SO_2 to the plasma torus is about two orders of magnitude less than the total gas outflux of Io's volcanos [7A-41].

7A.7.10 Flux Tube

A flux tube linking Jupiter and Io with an electrical current of 5 million amperes flowing in it has been observed by Voyager [7A-14]. The power dissipation implied in the current loop set up by Io's interaction with the Jovian magnetosphere suggests a Joule heating of Io of about 10^{12} W [7A-42]. (The flux tube is treated at greater length in Section 7 on Jupiter.)

7A.7.11 Plasma Torus

A plasma torus through which Io's orbit wanders has been observed to be corotating with Jupiter at about 6 R_j (Jupiter radii). Voyager observed a cold plasma with ions: O^+, O^{++}, S^{++}, and S_2^+ or SO_2^+. Ultraviolet emissions from S^{++}, S^{+++}, and O^{++} were also observed in the torus, indicating a hot (10^5°K) plasma which was not present during the Pioneer 10 encounter (December 1973). Plasma electron densities exceeding 4500 cm^{-3} were measured in some regions of the Io plasma torus [7A-14]. The magnetic field magnitude in the vicinity of Io's orbit is on the order of a micro-Tesla, although Io itself perturbs this field [7A-42].

Losses from the observed SO_2 atmosphere on Io may account for the sulfur and oxygen observed in the torus. The apparent depletion of hydrogen, carbon, and nitrogen in the Io atmosphere is consistent with the absence of these materials in the plasma torus [7A-39]. Auroral hiss has been detected on the inner edge of the plasma torus. This noise provides evidence for the existence of aurora-like charged particle beams on magnetic field lines through the inner edge of the torus. These beams probably consist of low-energy electrons and may be associated with field-aligned currents linking the plasma torus to the Jovian ionosphere [7A-43]. The plasma torus is treated at greater length in Section 7 on Jupiter.

7A.8 1979 J2

The second satellite to be discovered in the Voyager images of Jupiter has been tentatively named 1979 J2. It was discovered by Stephen P. Synnott of JPL and is the fifteenth satellite of Jupiter. It is 80 km in diameter as seen against the Jupiter disc, and it may be longer on its major axis (normal to the disc). 1979 J2 lies at 222,400 km from Jupiter's center, or 151 thousand km above the cloud tops, and circles Jupiter every 16 hr, 11 min, 21.3 ± 0.5 sec. It has an albedo similar to Amalthea (0.05) and appears to be carbonaceous condrite material augmented with sulphur, possibly transported from Io [7A-6].

7A.9 AMALTHEA

When discovered by Barnard in 1892, Amalthea became the fifth known satellite. It has a diamond or facet shape and is in synchronous rotation, keeping its major axis pointed toward Jupiter as expected from Euler dynamical theory [7A-12]. From Voyager photos it measures 270 ± 15 km along its major axis, 170 ± 15 km on its intermediate axis, and 155 ± 10 km on its polar axis [7A-8]. It is difficult to observe from Earth because it is so close to Jupiter (3.5 arc sec or 109,900 km above the cloud tops). Mean distance to Jupiter's center of mass is 181,300 km [7A-5].

7A.9.1 Appearance

Amalthea's color is dark and very red (590:410 nm about 1.5:1) with an average geometric albedo of 0.04 to 0.06 [7A-12]. There are also some bright spots with albedo 0.15 including a gray spot [7A-12]. It is possible that some of the sulphur compounds lost from Io are responsible for Amalthea's red color [7A-27].

When observed in the infrared, Amalthea appears warmer than if it were totally absorbing and obtained all of its heat from the Sun and Jupiter. It may derive additional energy from the Jovian radiation belt and from Joule heating [7A-11].

7A.10 1979 J1

The fourteenth satellite of Jupiter was discovered by David C. Jewitt in the navigation pictures taken by Voyager 2. It is tentatively called 1979 J1 and is located at the outer edge of the Jupiter ring system at 129 thousand kilometers. It has a circular orbit and a period of 7 hr, 9 ± 1 min, which is faster than the rotation rate of Jupiter itself (9 hr, 55 min, 29.71 sec). Its diameter is approximately 25 to 30 km, and it has an albedo of about 0.05 [7A-6, 7A-44].

7A.11 1979 J3

The sixteenth satellite of Jupiter was found in the Voyager images by Stephen P. Synnott. It orbits Jupiter once every 7 hr, 4 min, 30 ± 3 sec at a mean distance of 56,200 km above the Jovian cloud tops (127,600 km from Jupiter's center). It is probably inside the outer edge of Jupiter's ring system, discovered by Voyager 1, and may pass within 1400 km of 1979 J1 [7A-6]. With an orbital velocity of more than 113,600 km/sec, it is the fastest moving moon known in the solar system.

7A.12 RING SYSTEM

A ring of material about Jupiter was discovered by Voyager 1. Its outer edge extends 129,000 km from the center of the planet or 57,600 km above the cloud tops [7A-14]. Its thickness is $\leqslant$30 km, and it consists of a bright outer segment about 800-km wide, surrounded by a broader, dimmer, inner segment about 5200-km wide [7A-8]. The interior of the ring is filled with a much fainter material that may extend down to the top of Jupiter's atmosphere. Upper limits on the optical depth of the ring material range from 3×10^{-4} to 3×10^{-3} in the thermal infrared [7A-5]. The orbits of 1979 J1 and 1979 J3 may lie at or inside the outer edge of the ring.

7A.13 TROJAN ASTEROIDS

Trojans are two unique groups of asteroids which lead and follow Jupiter in its orbit at fixed average distances. They are called the Achilles Group and the Patroclus Group, which respectively lead and follow Jupiter at the L4 and L5 LaGrangian points in the Sun-Jupiter system (the 1:1 resonance). The L4 and L5 points form equilateral triangles with the Sun and Jupiter, but the Trojan satellites wander considerably from these equilibrium points because of perturbations by the outer planets and because the orbit of Jupiter is elliptical. The first Trojan asteroid, Achilles, was discovered in 1906. The Trojan asteroid, Hector, number 624, is unusual because of its elongated shape, estimated to be 50 x 50 x 210 km, which suggests it is either a strong iron cylinder or a twin system of two stony bodies revolving about their common center of gravity. Hector has an albedo of 0.028. The individual Trojans are named after the legendary combatants of the war between Greece and Troy. Surveys show that there are about 700 satellites brighter than mean opposition magnitude 20.9 in the Achilles group and about half that number in the Patroclus group. It has been postulated that the outer moons of Jupiter are possibly captured Trojan asteroids [7A-10, 7A-45].

Review Section 12 on Asteroids, paragraph 12.2.3.

REFERENCES

7A-1. Bronowski, J.: The Ascent of Man. Little, Brown and Company, Boston/Toronto, 1973, p. 189.

7A-2. Whyte, L. L.: The Next Development in Man. New American Library, New York, 1950, p. 106.

7A-3. Smoluchowski, R.: in Jupiter, T. Gehrels (ed.), University of Arizona Press, Tucson, Arizona, 1976.

7A-4. Morrison, D. and Burns, J. A.: The Jovian Satellites. Jupiter, T. Gehrels (ed.), University of Arizona Press, Tucson, Arizona, 1976, pp. 991-1034.

7A-5. Stone, E. C. and Lane, A. L.: Voyager 2 Encounter with the Jovian System. Science, vol. 206, 1979, p. 4421.

7A-6. Synnott, Stephen P.: personal communication.

7A-7. Morrison, D.: Four New Worlds, The Voyager Exploration of Jupiter's Satellites. Mercury, vol. IX-3, 1980.

7A-8. Smith, B. A., Soderblom, L. A., Beebe, R. F., Boyce, J., Briggs, G. A., Carr, M. H., Collins, S. A., Cook, A. F., II, Danielson, G. E., Davies, M. E., Hunt, G. E., Ingersoll, A. P., Johnson, T. V., Masursky, H., McCauley, J. F., Morrison, D., Owen, T., Sagan, C., Shoemaker, E. M., Strom, R. G., Soumi, V. E., and Veverka, J.: The Galilean Satellites and Jupiter: Voyager 2 Imaging Science Results. Science, vol. 206, 1979, p. 927.

7A-9. Satellites of Jupiter. A compendium reference work in the University of Arizona Press series, is in press, expected release date: July, 1982.

7A-10. Mitton, S. (ed.): The Cambridge Encyclopedia of Astronomy. Crown Publishers, Inc., New York, New York, 1977, p. 237.

7A-11. Hanel, R., Conrath, B., Flasar, M., Kunde, V., Lowman, P., Maguire, W., Pearl, J., Pirraglia, J., Samuelson, R., Gautier, D., Gierasch, P., Kumar, K., and Ponnamperuma, C.: Infrared Observations of the Jovian System from Voyager 1. Science, vol. 204, 1979, p. 972.

7A-12. Smith, B. A., Soderblom, L. A., Johnson, T. V., Ingersoll, A. P., Collins, S. A., Shoemaker, E. M., Hunt, G. E., Masursky, H., Carr, M. H., Davies, M. E., Cook, A. F., II, Boyce, J., Danielson, G. E., Owen, T., Sagan, C., Beebe, R. F., Veverka, J., Strom, R. G., McCauley, J. F., Morrison, D., Briggs, G. A., and Soumi, V. E.: The Jupiter System Through the Eyes of Voyager. Science, vol. 204, 1979, p. 951.

7A-13. Hanel, R., Conrath, B., Flasar, M., Herath, L., Kunde, V., Lowman, P., Maguire, W., Pearl, J., Pirraglia, J., Samuelson, R., Gautier, D., Gierasch, P., Horn, L., Kumar, S., and Ponnamperuma, C.: Infrared Observations of the Jovian System from Voyager 2. Science, vol. 206, 1979, p. 952.

7A-14. Stone, E. C. and Lane, A. L.: Voyager 1 Encounter with the Jovian System. Science, vol. 204, 1979, p. 4396.

7A-15. Davies, M. and Katayama, F. Y.: Coordinates of Features on the Galilean Satellites. J. Geophys. Res., vol. 86, 1981, pp. 8635-8657.

7A-16. Strom, R. G., Woronow, A., and Gurnis, M.: Crater Populations on Ganymede and Callisto. J. Geophys. Res., vol. 86, pp. 8659-8674.

7A-17. Pang, K., Hord, C. W., West, R. A., Simmons, K. E., Coffeen, D. L., Bergstralh, J. T., and Lane, A. L.: Voyager 1 Photopolarimeter Experiment and the Phase Curve and Surface Microstructure of Ganymede. Nature, vol. 280, 1979, p. 804.

7A-18. Science News, vol. 117, 1980, p. 315.

7A-19. Science News, vol. 117, 1980, p. 325.

7A-20. Peale, S. J., Cassen, P., and Reynolds, R. T.: Melting of Io by Tidal Dissipation. Science, vol. 203, 1979, p. 893.

7A-21. Finale, F. P., et al.: Planetary Satellites. J. A. Burns (ed.), University of Arizona Press, Tucson, Arizona, 1977, p. 379.

7A-22. Pilcher, C. B., Ridgeway, T. S., and McCord, T. B.: Science, vol. 178, 1972, p. 1087.

7A-23. Johnson, T. V. and McGetchin, T. R.: Icarus, vol. 18, 1973, p. 612.

7A-24. Brown, R. A. and Yung, Y. L.: Io, Its Atmosphere and Optical Emissions. Jupiter, T. Gehrels (ed.), University of Arizona Press, Tucson, Arizona, 1976, pp. 1102-1145.

7A-25. Masursky, H., Schaber, G. G., Soderblom, L. A., and Strom, R. G.: Preliminary Geological Mapping of Io. Nature, vol. 280, 1979, p. 725.

7A-26. McCauley, J. F., Smith, B. A., Soderblom, L. A.: Erosional Scarps on Io. Nature, vol. 280, 1979, p. 736.

7A-27. Sagan, Carl: Sulphur Flows on Io. Nature, vol. 280, 1979, p. 750.

7A-28. Peale, S. J., Cassen, P., and Reynolds, R. T.: Melting of Io by Tidal Dissipation. Science, vol. 203, 1979, p. 892.

7A-29. Smith, B. A., Shoemaker, E. M., Kieffer, S. W., and Cook, A. F., II: The Role of SO_2 in Volcanism on Io. Nature, vol. 280, 1979, p. 738.

7A-30. Carr, M. H., Masursky, H., Strom, R. G., and Terrile, R. J.: Volcanic Features of Io. Nature, vol. 280, 1979, p. 729.

7A-31. Fanale, F. P., Brown, R. H., Cruikshank, D. P., and Clark, R. N.: Significance of Absorption Features in Io's IR Reflectance Spectrum. Nature, vol. 280, 1979, p. 761.

7A-32. Smythe, W. D., Nelson, R. M., and Nash, D. B.: Spectral Evidence for SO_2 Frost or Absorbate on Io's Surface. Nature, vol. 280, 1979, p. 766.

7A-33. Nash, D. B., and Nelson, R. M.: Spectral Evidence for Sublimates and Absorbates on Io. Nature, vol. 280, 1979, p. 763.

7A-34. Morrison, D., Pieri, D., Veverka, J., and Johnson, T. V.: Photometric Evidence on Long-term Stability of Albedo and Color Markings on Io. Nature, vol. 280, 1979, p. 753.

7A-35. Morabito, L. A., Synnott, S. P., Kupferman, P. N., and Collins, S. A.: Discovery of Currently Active Extraterrestrial Volcanism. Science, vol. 204, 1979, p. 972.

7A-36. Strom, R. G., Terrile, R. J., Masursky, H., and Hansen, Candice: Volcanic Eruption Plumes on Io. Nature, vol. 280, 1979, p. 733.

7A-37. Cook, A. F., Shoemaker, E. M., and Smith, B. A.: Dynamics of Volcanic Plumes on Io. Nature, vol. 280, 1979, p. 743.

7A-38. Johnson, T. V., Cook, A. F., II, Sagan, C., and Soderblom, L. A.: Volcanic Resurfacing Rates and Implications for Volatiles on Io. Nature, vol. 280, 1979, p. 746.

7A-39. Pearl, J., Hanel, R., Kunde, V., Maguire, W., Fox, K., Gupta, S., Ponnamperuma, C., and Raulin, F.: Identification of Gaseous SO_2 and New Upper Limits for Other Gases on Io. Nature, vol. 280, 1979, p. 755.

7A-40. Smith, B. A. and Smith, S. A.: Icarus, vol. 17, 1972, p. 218.

7A-41. Kumar, S.: The Stability of an SO_2 Atmosphere on Io. Nature, vol. 280, 1979, p. 758.

7A-42. Ness, N. F., Acuna, M. H., Lepping, R. P., Burlaga, L. F., Behannon, K. W. and Neubauer, F. M.: Magnetic Field Studies at Jupiter by Voyager 1: Preliminary Results. Science, vol. 204, 1979, p. 982.

7A-43. Gurnett, D. A., Kurth, W. S., and Scarf, F. L.: Auroral Hiss Observed Near the Io Plasma Torus, Nature, vol. 280, 1979, p. 767.

7A-44. Jewitt, D. C., Danielson, G. E., and Synnott, S. P.: Discovery of a New Jupiter Satellite. Science, vol. 206, 1979, p. 951.

7A-45. Ridpath, Ian (ed.): The Illustrated Encyclopedia of Astronomy. Thomas Crowell Company, New York, New York, 1976, p. 20,212.

SECTION 8. SATURN

8.1 INTRODUCTION

To the naked eye the planet Saturn is yellowish in color and, because of its great distance from Earth, it appears least bright and moves most slowly through the Zodiac of all the planets visible without a telescope. But even though it is outshown by the nearer planets, its great size – second only to the other gas giant Jupiter – and its high albedo contribute to a visual magnitude in opposition which is greater than all but two stars, Sirius and Canopus. It was not until 1781, over 170 years after the invention of the telescope, that a more remote planet was discovered; it was in that year that Herschel discovered the planet Uranus.

The Rings of Saturn were seen by Galileo in July 1610 in the early observations made with his newly invented "spy glass." He, however, mistook the rings to be large moons, one on either side of the planet. In 1655, Christian Huygens determined that these were not satellites but a ring (he saw only one with no divisions) which encircled the planet. Huygens also is credited with the discovery, in the same year, of Saturn's giant satellite, Titan. Saturn soon became identified with its aesthetically pleasing ring system and it was not until the late 1970s that Uranus and Jupiter were discovered to also possess ring systems.

Largely because of its great distance from Earth, there was relatively little information about Saturn, its satellites, and rings until the recent observations by the interplanetary spacecraft Pioneer and Voyagers 1 and 2. Each of these, after observing Jupiter, made a close encounter with Saturn:

	Date	Distance of Closest Approach
Pioneer	September 1, 1979	81,000 km
Voyager 1	November 12, 1980	186,000 km
Voyager 2	August 26, 1981	100,800 km

Early summaries of results from Pioneer and Voyager 1 have been published in Science 207 (1980) [8-1] and Science 212 (1981) [8-2], respectively. Verbal reports of Voyager 2 data were given at the Fall Annual Meeting of AGU, December 1981 [8-3]. This section includes data from Pioneer and Voyager 1. As these data are rather new, the derived numerical results will likely be refined during the next few years.

Tables 8-1 through 8-4 summarize numerical data on the Saturn system, various aspects of which are discussed in the following paragraphs. Figure 8-1 shows the ring and satellite system schematically and is derived from Tables 8-3 and 8-4. References 8-1 and 8-2 show the geometry of the planetary flybys.

8.2 INTERNAL PROPERTIES

Deductions about the interior of Saturn are based on the measured magnetic and gravitational fields and remote observations of surface properties.

TABLE 8-1. DYNAMIC PROPERTIES

Parameter	Value	Comments
Semi-major axis	1427.0×10^6 km	9.539 AU
Perihelion distance[a] (January 1974)	1.35×10^9 km	9.015 AU
Aphelion distance[a] (May 1959)	1.51×10^9 km	10.066 AU
Eccentricity (e)	0.056	
Inclination of orbit (i)[b]	2.490 deg	
Mean orbital velocity		
Linear[b]	9.7 km/sec	
Angular	0.0337667 deg/day	
Sidereal year	29.46 years	
Sidereal day[c]	10 hr 39.4 m ± 0.3 min	from magnetic field
Synodic year[b]	378.09 days	
Earth-planet distance		
Apogee (September 1980)	1.571×10^9 km	10.50 AU
Perigee (March 1980)	1.264×10^9 km	8.448 AU
Orbital angular momentum	2.306×10^{38} kg km^2 sec^{-1}	
Longitude of node	113.3 deg	
Longitude of perihelion	92.3 deg	
Mean longitude at epoch 1960	280.7 deg	

Data from Observers' Handbook, 1980 [8-4] except as noted.

a. The American Ephemeris and Nautical Almanac for year given [8-5].

b. Abel, George, Exploration of the Universe, Holt, Rinehart and Winston, New York, 1975 [8-6].

c. Science 212 [8-2], p. 160.

TABLE 8-2. PHYSICAL DATA

Parameter	Value	Comments
Radius, equatorial	60,000 km[a] at 1 bar 60,330 km[b] at top of clouds	9.41 Earth
Oblateness[a]	0.912 ± 0.006	cf. Earth = 0.003
Mass[a]	5.684×10^{26} kg	95.17 Earth
Mean density	0.71 g cm^{-3}	0.127 Earth
Acceleration due to gravity at surface	12.9 m sec^{-2}	1.32 Earth
Escape velocity	39.4 km sec^{-1}	3.52 Earth
Polarity of magnetic field at equator[a,b]	southward	cf. Earth = northward
Magnetic field intensity at equator[a,b]	0.2 gauss	cf. Earth: slightly weaker, at surface, than Earth's
Magnetic dipole moment[a]	4.3×10^{28} gauss cm^3	5.3×10^2 Earth
Magnetic axis tilt[a]	less than 1 degree	
Mean distance to magnetospheric subsolar point[a]	30 R_S	cf. Earth = 10 R_E
Albedo[a]	0.45 ± 0.15	cf. Earth = 0.39
Visual magnitude at maximum light	–0.4	
Moment of inertia	1.158×10^{45} kg km^2	
Obliquity of axis	26.7 deg	cf. Earth = 23.4 deg
Internal heat flux, average[a]	2.4 ± 0.8 W m^{-2}	
Ratio of total planetary emission to absorbed sunlight[a]	2.2 ± 0.7	
Temperature, effective[a]	94.4 ±3 K	

Data from Reference 8-4 except as noted.

a. Science 207, 400ff [8-1].

b. Science 212 [8-2].

TABLE 8-3. SATELLITE DATA[a]

Satellite	Diameter (km)	Distance (km)	Distance (R_S)[b]	Period (hours)	Closest Approach (km)	
					Voyager 1	Voyager 2
1980S28	30[c]	137,300[c]	2.276[c]	14.446[c]	219,000	287,000
1980S27	220[c]	139,400[c]	2.310[c]	14.712[c]	300,000	247,000
1980S26	200[c]	141,700[c]	2.349[c]	15.085[c]	270,000	107,000
1980S3	90x40[c]	151,422[c]	2.510[c]	16.664[c]	121,000	147,000
1980S1	100x90[c]	151,472[c]	2.511[c]	16.672[c]	297,000	223,000
Mimas	390[c]	188,224	3.120	23.139	88,440	309,990
Enceladus	500[c]	240,192	3.981	33.356	202,040	87,140
Tethys	1050[c]	296,563	4.916	45.762	415,670	93,000
1980S6	~160	378,600[c]	6.275[c]	65.738[c]	230,000	270,000
Dione	1120[c]	379,074	6.283	66.133	161,520	502,250
Rhea	1530[c]	527,828	8.749	108.660	73,980	645,280
Titan	5140[c]	1,221,432	20.246	382.504	6,490	665,960
Hyperion	290[c]	1,502,275	24.901	521.743	880,440	470,840
Iapetus	1440[c]	3,559,400	58.999	1901.820	2,470,000	909,070
Phoebe	~160	10,583,200	175.422	9755.679	13,537,000	1,473,000

a. From Reference 8-2.

b. Here 1 R_S is defined as 60,330 km (37,490 miles).

c. From Voyager 1 data in Reference 8-2; distances and periods are for October 1, 1980. The remaining entries were provided by the Voyager navigation team.

TABLE 8-4. RING DATA[a]

Feature	Distance (km)	Distance (R_S)[b]	Period (hours)	Comments
Cloud tops[c]	60,330	1.000	10.657	Near 100-mbar level
D ring inner edge	~67,000	1.11	4.91	Extremely small optical depth
C ring inner edge	73,200[d]	1.21	5.61	
B ring inner edge	92,200[d]	1.53	7.93	
B ring outer edge	117,500[d]	1.95	11.41	Inner edge of Cassini division
A ring inner edge	121,000[d]	2.01	11.93	Outer edge of Cassini division
Encke division	133,500[d]	2.21	13.82	About 200-km wide
A ring outer edge	136,200[d]	2.26	14.24	
F ring	~140,600	2.33	14.94	Three narrow components
G ring	~170,000	2.8	19.9	Seen only in forward-scattered light
E ring inner edge	~210,000	3.5	27.3	
E ring maximum	~230,000	3.8	31.3	Near orbit of Enceladus
E ring outer edge	~300,000	5.0	46.6	

a. From Reference 8-2, p. 161.

b. Here 1 R_S is defined as 60,330 km (37,490 miles).

c. Distance at equator from Saturn's center; the period is the rotation rate of the planet.

d. From S. A. Collins, et al., NATURE, vol. 288, 1980, p. 439.

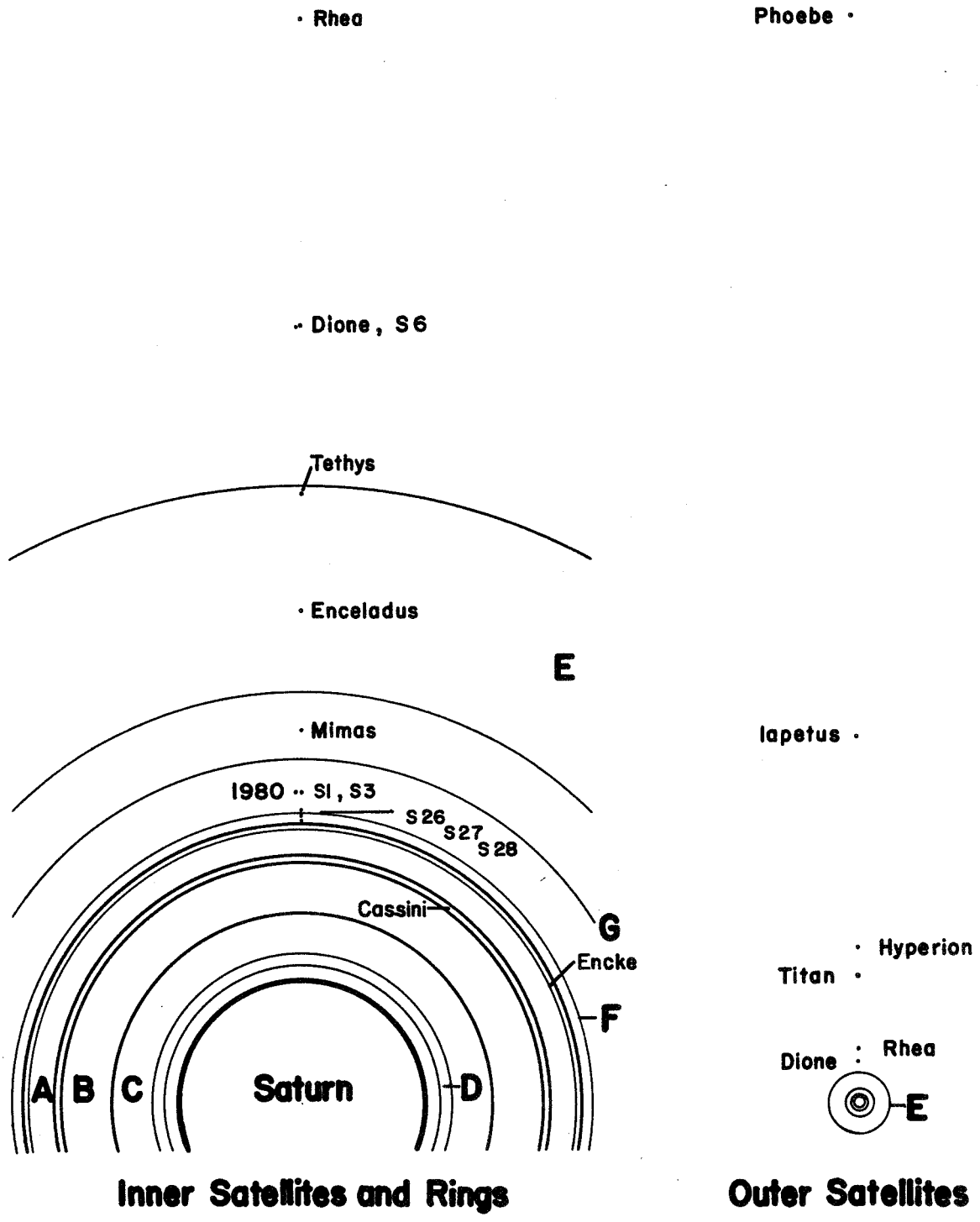

Figure 8-1. Rings, inner satellites, and outer satellites of Saturn.

8.2.1 Magnetic Field

The field of internal origin, as well as the magnetospheric field, were measured by magnetometers on both Pioneer and Voyager. The field inside $6R_S$ was fit with the usual spherical harmonic function series; using only first order internal and external terms. The following Schmidt normalized coefficients were obtained with an RMS residual of 2.7 nT:

Internal:

$$g_1^0 = 0.209 \text{ gauss}$$

$$g_1^1 = 0.00220 \text{ gauss}, \; h_1^1 = 0.00124 \text{ gauss}$$

External:

$$G_1^0 = -8.8 \text{ nT}$$

$$G_1^1 = -4.2 \text{ nT}, \; H_1^1 = 3.3 \text{ nT}$$

(where 1 nT = 10^{-5} gauss).

Use of internal second order (quadrupole) terms instead of external terms does not reduce the RMS residual. That is, the internal field is equivalent to a northward pointed magnetic dipole (opposite direction to Earth's) inclined only 0.7 deg to Saturn's rotation axis. The offset from the planet's center, corresponding to maximum possible quadrupole term, is less than 0.02 R_S.

8.2.2 Gravitational Field

The higher order gravitational data (expressed by J_n) currently available are derived from the measured orbit of Pioneer as perturbed by encounter with Saturn. The planet's mass is derived from perturbations on the orbit of Jupiter:

$$M_S = 3497.99 \; M_\oplus - \text{masses of satellites}$$

$$= 5.684 \times 10^{29} \text{ g} \quad .$$

The mass of the rings is $0 \pm 3 \times 10^{-6} \; M_S$. The harmonic coefficients were determined by a least squares fit to the trajectory data and are:

$$J_2 = (1.646 \pm 0.005) \times 10^{-2}$$

$$J_4 = (-0.99 \pm 0.08) \times 10^{-3}$$

using the assumed values:

$J_6 = 0.84 \times 10^{-4}$

$J_8 = 0.11 \times 10^{-4}$

Ring mass = 10^{-7} M_S .

8.2.3 Internal Models

The magnetic data suggest a smaller than expected conducting core. A metallic hydrogen core of radius 0.2 to 0.5 R_S is suggested based on internal dynamo models. However, these mechanisms generally require an inclination of approximately 10 deg between the rotation and magnetic axes. Inferences based on existing models may be wrong.

The Pioneer celestial mechanics experimenters [8-1] have used the gravitational data, the measured temperature of 140°K at the 1 bar level and the observed rotation rate and size to construct the following model.

An inner core consists of liquid H_2O and perhaps NH_3, CH_4 mixed with rock in solar proportions and has about 20 Earth masses and therefore a radius of 0.2 R_S. This is surrounded by liquid hydrogen to approximately 0.5 R_S, admixed with some helium. A gaseous envelope surrounds this composed of H_2 with 10 percent mass fraction of He (less than solar abundance), in agreement with the infrared observations by Voyager [8-2] and Pioneer [8-1].

The preliminary Voyager IR data agree with the Pioneer observation in giving an effective temperature of approximately 95°K. Combined with the albedo of 0.45 ± 0.15 it appears that Saturn radiates approximately 2.2 ± 0.7 times the energy it absorbs, requiring an average internal heat flux of 2.4 ± 0.8 W/m^2. In order to sustain this energy loss over the life of the solar system, it is conjectured that gravitational energy is released by radial fractionation of He from H_2.

8.3 SURFACE AND ATMOSPHERIC PROPERTIES

Saturn is gaseous outside its core and so there is no surface. Atmospheric properties as a function of depth have been determined by the ultraviolet, infrared and radio (S band telemetry) occultation experiments on both Pioneer and Voyager, and additionally by the imager on Voyager [8-1,8-2].

Table 8-5 shows atmospheric composition, necessarily above the clouds, inferred from the Voyager IR data [8-2]. The clouds are probably NH_3 and PH_3. Atmospheric temperature profiles as derived from Pioneer data are presented in Figures 8-2 and 8-3 which also show the pressure variation with altitude over a limited range. The data do not extend much below the tropopause. Figure 8-4 shows profiles to greater depths derived from the Voyager IR data, and Figure 8-5 shows a profile obtained by the Voyager radio occultation experimenters. The results agree.

TABLE 8-5. ATMOSPHERIC COMPOSITION [8-2]

Gas	Band	Wave Number (cm^{-1})	Approximate Mole Fraction
Positively identified:			
Hydrogen (H_2)	S_0,S_1	300 to 700	0.94
Helium (He)		200 to 600	0.06
Ammonia (NH_3)	Rotational	~200	2×10^{-4}[a]
Phosphine (PH_3)	ν_2	990	1×10^{-6}
Methane (CH_4)	ν_4	1304	8×10^{-4}[a]
Ethane (C_2H_6)	ν_9	821	5×10^{-6}
Acetylene (C_2H_2)	ν_5	729	2×10^{-8}
Tentatively identified:			
Methylacetylene (C_3H_4)	ν_9	633	
Propane (C_3H_8)	ν_{26}	748	

a. Assumed value.

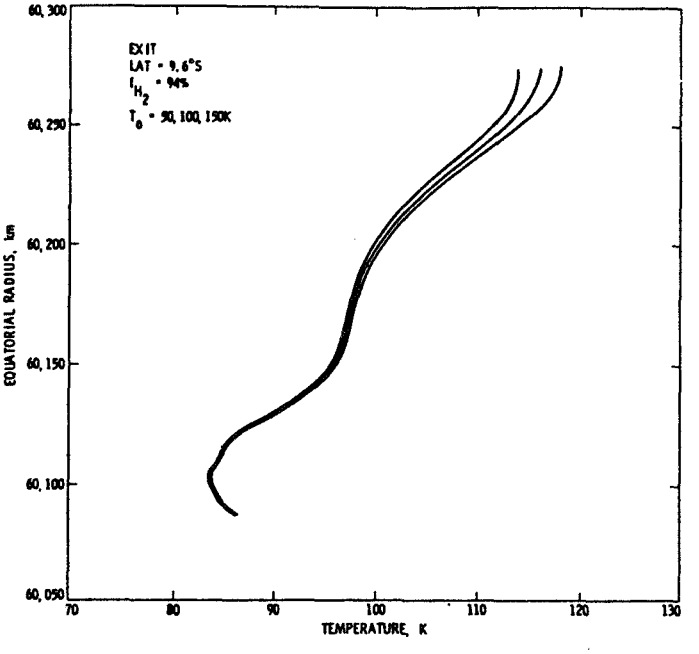

Temperature structure in the upper neutral atmosphere of Saturn, from a pressure level of about 1 to 120 mbar plotted against the equatorial radius. The measurement level just barely penetrates below the tropopause and into the convective region of the atmosphere.

Figure 8-2. Upper neutral atmosphere temperature structure. [8-1]

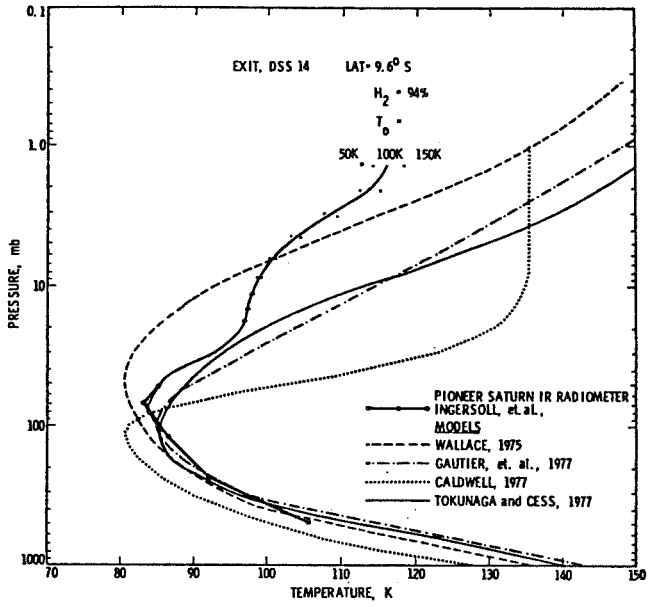

Pioneer 11 Saturn radio occultation results (heavy line with surrounding dots) shown with other data and models. The heavy line connecting the black dots represents the temperature structure derived from the Pioneer 11 Saturn infrared radiometer experiment. The four lighter curves represent models derived from ground-based observations. The radio occultation temperature profile shown here is for an assumed composition of 94 percent hydrogen and 6 percent helium by number. (The radio occultation curve stops at about 1.20 mbar.)

Figure 8-3. Neutral atmosphere temperature structure. [8-1]

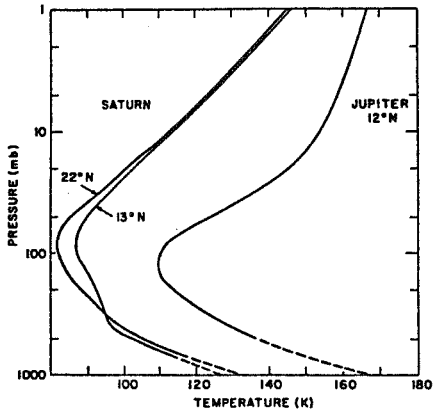

Vertical temperature profiles for Saturn and Jupiter, as retrieved by inversion of Voyager IRIS spectra. The dashed portions of the curves represent extrapolations along adiabats.

Figure 8-4. Atmospheric temperature structures of Saturn and Jupiter. [8-2]

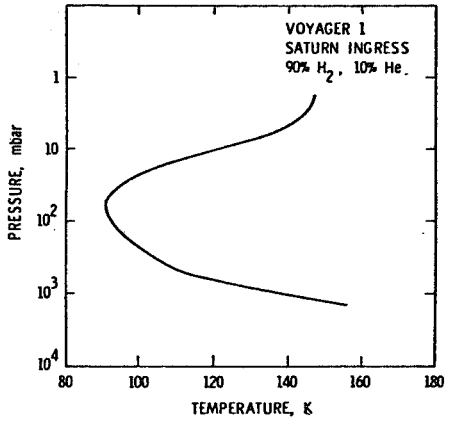

Atmospheric temperature as a function of pressure for a south polar area of Saturn, assuming an atmosphere of 90 percent H_2 and 10 percent He by volume.

Figure 8-5. South polar area atmospheric temperature structure. [8-2]

Temperature was also measured by the IR instruments as a function of latitude, as shown in Figure 8-6. The generally higher temperature in the southern hemisphere corresponds to the recent season of austral summer on Saturn before the Voyager encounter. It is natural to try to associate such variations in temperature with the banded features observed in the clouds by the Voyager imager and with the winds inferred from the clouds' motions. Unlike the situation on Jupiter, there appears to be little correlation. The color and albedo contrast on Saturn is much lower than on Jupiter, possibly because Saturn's lower temperature has produced more condensed aerosols above the cloud tops. The equatorial eastward wind on Saturn is much stronger than on Jupiter.

Figure 8-7 shows the winds, measured with respect to the core rotation speed of 810.76 deg per 24 hr (10 hr 39.4 min period) inferred from periodicities in planetary radio noise. The lower winds of Jupiter are shown as well. Figure 8-8 shows the surface features and winds on Saturn and Jupiter. There are presently no models to explain the atmosphere circulation on the two planets.

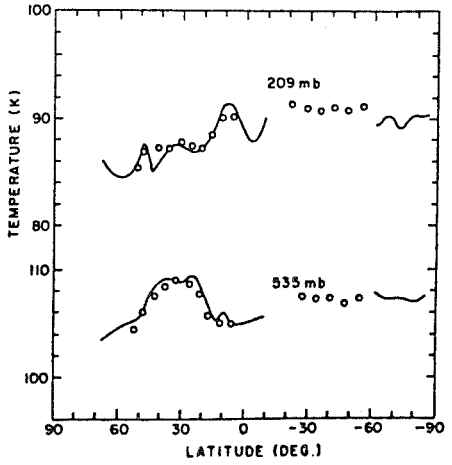

Figure 8-6. Latitudinal temperatures at 209 and 535 mb. [8-2]

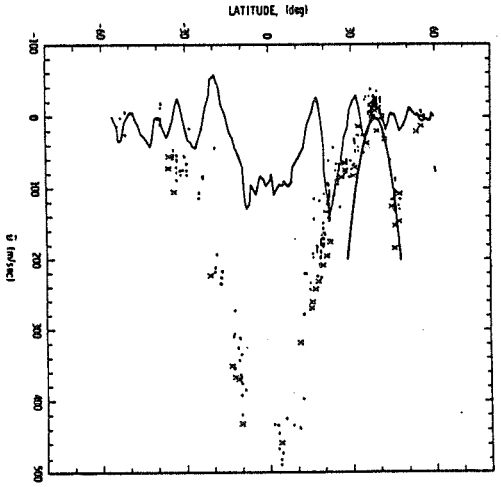

Figure 8-7. Zonal winds on Saturn and Jupiter. [8-2]

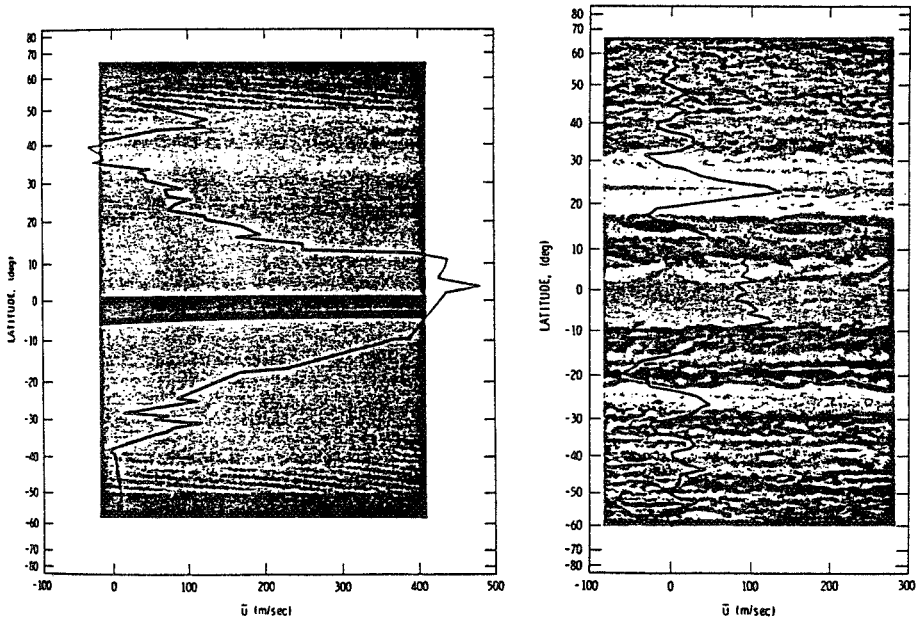

Figure 8-8. Saturn's mean eastward winds. [8-2]

The UV experiment [8-2] detected resonantly scattered sunlight in Ly α from which the existence of a hydrogen torus is inferred. The cloud of H lies in the equatorial plane between 8 and 25 R_S and is less than 6 R_S thick perpendicular to the plane. The brightness of 100 Rayleighs implies a density of approximately $10/cm^3$. The hydrogen is thought to be generated by photolysis of CH_4 in Titan's atmosphere; the hydrogen escapes Titan but remains captured by Saturn.

8.4 IONOSPHERE AND MAGNETOSPHERE

Models of Saturn's plasma environment are derived from in-situ measurements along the orbits of Pioneer and Voyager and are based on our extensive knowledge of the Earth's magnetosphere and ionosphere. Section 2, Vol. 1, on Terrestrial Space should be consulted for definitions and descriptions of major processes.

8.4.1 Ionosphere

Electron density as a function of altitude was derived from the radio occultation experiments on Pioneer [8-1] and Voyager [8-2] using the two-way telemetry link as the spacecraft were occulted by Saturn as seen from the Earth. Figure 8-9 shows results obtained by Voyager; they are in substantial agreement with Pioneer results.

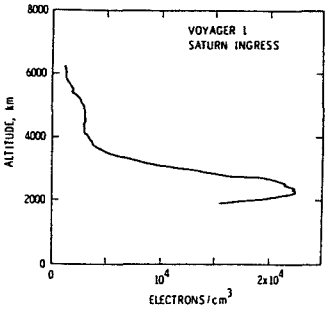

Concentration of electrons as a function of altitude above the 1-bar level for the ionosphere of Saturn. Curve is for south polar latitudes near the evening terminator. The solar zenith angle was about 89°. The topside plasma scale height was about 560 km.

Figure 8-9. South polar area electron density structure. [8-2]

The other observed effect of magnetospheric activity at low altitude is the aurorae, observed by the UVS in both northern and southern hemispheres at latitude 78°81.5', with a dark polar cap. H Lyα and $_2$H Lyα and Werner bands were observed with intensities of approximately 1 to 20 kR. The brightness varies with time, and implies an average precipitated electron energy of 2×10^{11} W.

8.4.2 Magnetosphere

8.4.2.1 Plasma

Data were obtained in-situ by magnetometers, plasma detectors, low and high energy charged particle detectors, and plasma wave detectors. Data from Pioneer and Voyager are in general agreement, with some differences readily attributable to the stronger solar wind flow at the time of Pioneer.

Both spacecraft approached Saturn from the direction of the sun; Pioneer exited near the local down meridian, while Voyager exited in the meridian plane of approximately 0300 local time.

Voyager encountered the bow shock at 26.1 R_S inbound and crossed it at 77.9 R_S outbound. The magnetopause was crossed at approximately 23 R_S inbound and approximately 45 R_S outbound, multiple crossings being due, presumably, to motion of the magnetopause back and forth past the spacecraft. Geometry is shown in Figure 8-10a and field strength in Figure 8-10b. The direction of the field is consistent with a dipole and a magnetotail as at the Earth.

The plasma detector [8-2] on Voyager sensed various boundary crossings. Total plasma density was calculated from the electron sensor while bulk flow was inferred from the ion detectors, which measured energy per unit charge. From 18 R_S to 7 R_S the flow velocity is consistent with rigid corotation (10 hr, 39 min period) to within 20 percent in velocity, provided that the double-peaked energy spectra are interpreted as indicating hydrogen (A/Z = 1) and a heavier component with A/Z ≅ 14. At 18 R_S the energy of the H is approximately 90 eV. The density distribution measured by Voyager and Pioneer suggests classification of the plasma as belonging to either a central or extended plasma sheet as shown in Figure 8-11. The farthest extent of the sheet is unmeasured. Equatorial densities in the central sheet are 7 to 20/cm^3 and 0.3 to 1.0/cm^3 in the extended sheet with flux tube content of approximately 4 x 10^3 R_S/cm^3 in each. The sources are unknown but the inner sheet may result in part from sputtering off the rings.

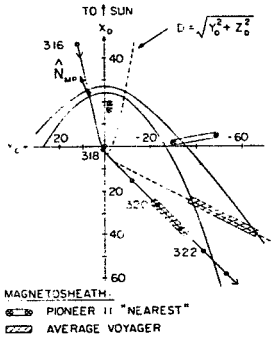

Voyager 1's trajectory near Saturn in orbital (solid curve) and cylindrical coordinates (dashed curve). Also shown are model bow shock and magnetopause boundaries, projected into the orbital ($X_0 = Y_0$) plane. Distances in Saturn radii (1 R_S = 60330 km).

Figure 8-10a. Bow shock and magnetopause configurations.

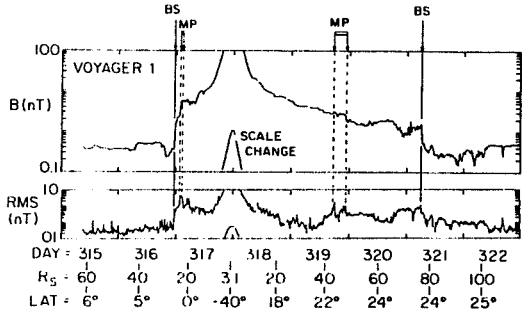

An overview of the magnitude and Pythagorean mean RMS of the magnetic field for 8 days around closest approach to Saturn. Shown are 16-min averages. The bottom two scales denote R_S, the planetocentric radial distance of the spacecraft in units of Saturnian radii and latitude (LAT) with respect to Saturn's equator.

Figure 8-10b. Magnetic field overview.

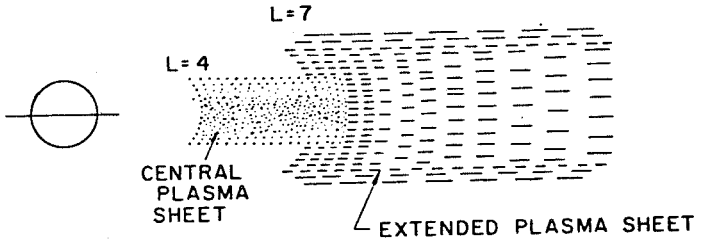

Figure 8-11. Schematic model of the plasma sheet configuration.

8.4.2.2 Energetic Charged Particles

Energetic particle data were obtained by a variety of instruments on both Pioneer and Voyager. Pioneer covered a greater range of radial distance because of its closer approach; Voyager, however, sampled the magnetotail.

Saturn's magnetosphere, as evidenced in particle intensities, is between Jupiter and Earth in general character, resembling Earth the more, as shown in Figure 8-12. The energetic particles may be classified into five regions (see Figure 8-13 for some of them). Outermost in the sunward hemisphere the mantle extends from the magnetopause (approximately 17 R_S for Pioneer, approximately 26 R_S for Voyager) to about 17 R_S. Particles in it do not drift completely around Saturn, but enter or exit to the tail or through the flanks of the magnetosphere. Intensities are highly variable and the region may essentially disappear when solar wind compresses the magnetosphere as at the time of the Pioneer encounter.

Inside of approximately 17 R_S the region of durable trapping extends inward to the outer edge of the A ring at 2.26 R_S. The average energy of particles increases with decreasing radius. The outer trapping region extends from approximately 17 R_S to L = 7. From L = 7 to L = 4 the ion intensity was greatly depressed and this volume was called the slot region. The satellites Enceladus, Tethys, 1980SG, and Dione move in this region, but absorption by them does not appear to account for the low intensities. Either additional absorbing matter is present, undetected optically, or wave-particle interactions scatter particles into the loss cone. The inner trapping reigon, inside the slot, has the highest intensities and most energetic particles. It is terminated sharply by the A ring, which has sufficient mass density to totally absorb all trapped particles. Figures 8-14a and 8-14b show intensity contours of various energies and Figures 8-15a and 8-15b show some energy spectra.

In the fifth region, the magnetotail, the intensities are variable, the ions generally being low, except for bursts streaming away from the planet, and the electrons higher (Fig. 8-16).

The inner trapping region is quite axisymmetric, consistent with Saturn's dipolar field. Saturn's rotation is not seen in the particle intensity. In contrast, the radial profile shows not only the major features outlined above but several narrow absorption features corresponding to the satellites inside approximately 4 R_S. The depth of depletion depends upon both energy and type of particle, being generally greater for ions and for particle mirroring near the equator. The trapped radiation profiles at the time of Pioneer confirmed the influence of some small satellites on the F ring with some evidence of E ring effects.

This evidence is consistent with a model in which the particles are initially accelerated in the magnetosheath and tail, and then diffuse inward through the trapping region gaining energy as the first and second adiabatic invariants remain constant. As they diffuse across L shells containing absorbing material the intensity is depleted in a wake whose size and direction depend upon the relative velocities of the absorber and longitudinal particle drift, the size of the absorber, the radial diffusion rate, and the time spent at the latitude of the absorber. No particles appear inside a region of complete removal. There is some evidence that a few particles result from CRAND (cosmic ray albedo neutron decay). Generally, few particles are accelerated to about 2 MeV.

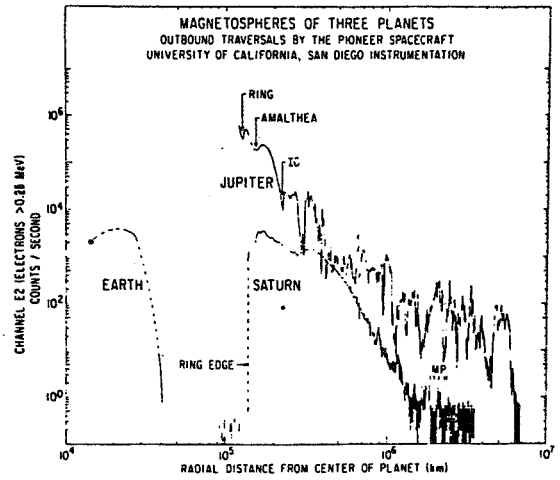

Magnetospheres of three planets. These profiles of the radiation belts of Earth, Jupiter, and Saturn were made by University of California instrumentation on two Pioneer spacecraft. The profile of Earth's radiation belt was made in the dawn sector by Pioneer 10; those of Jupiter and Saturn were made by identical instrumentation on Pioneer 11 outbound in the noon and dawn sectors, respectively. The data shown are from an electron scatter detector with a geometric factor of 1.04×10^3 cm^2 sr^{-1} for electrons > 0.255 MeV. In the Jupiter magnetosphere inside Io, this detector responded mainly to omnidirectional electrons penetrating the shielding. For these particles the energy threshhold is 35 MeV and the geometric factor 0.038 cm^2. Note that the abscissa is in kilometers. To normalize to planetary radii, divide by 6371 km for Earth, 71,372 km for Jupiter, and 60,000 km for Saturn.

Figure 8-12. Magnetospheres of Earth, Jupiter, and Saturn. [8-1]

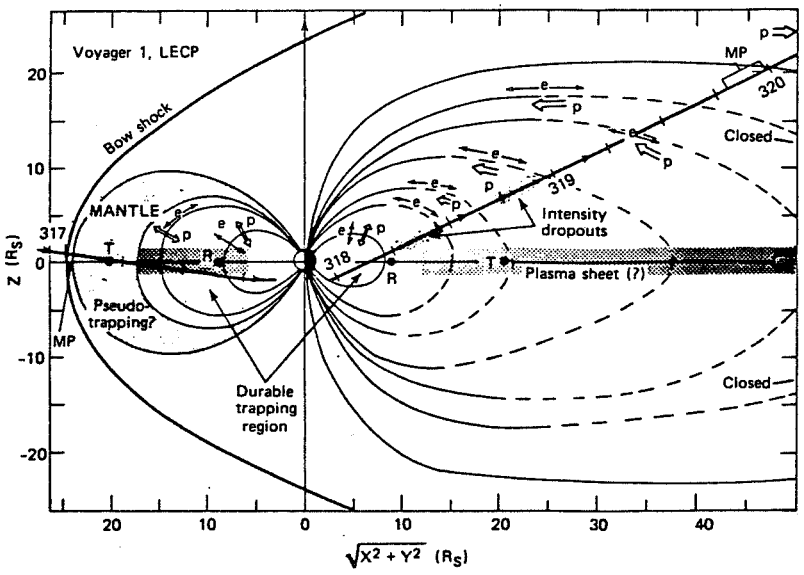

A schematic representation of Saturn's magnetosphere in the rz (trajectory) plane as revealed by the LECP data. Tick marks on the trajectory are at 6-hr intervals from day 318 to 320. Note the Titan-associated mantle region outside ~ 17 R_S, and the presence of closed field lines in the tail lobe region. The phase of the second-order anisotropies relative to the magnetic field (B) is shown for both electrons (e) and protons (p). R, Rhea; T, Titan; MP, magnetopause.

Figure 8-13. Schematic representation of Saturn's magnetosphere. [8-2]

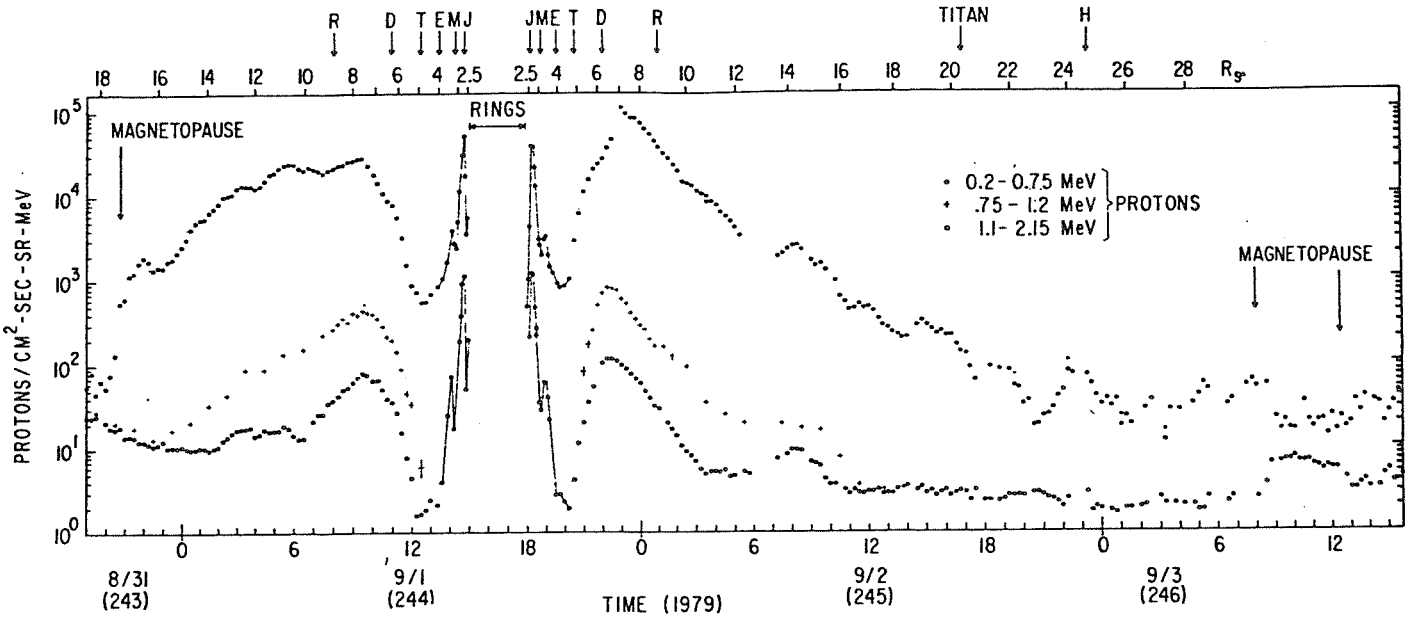

Proton fluxes during the inbound and outbound passes of Pioneer 11. Arrows indicate the position of Rhea (R), Dione (D), Tethys (T), Enceladus (E), Mimas (M), Janus (J), Titan, and Hyperion (H). The object J 11 is located near the orbit of Janus.

Figure 8-14a. Proton fluxes from Pioneer II. [8-1]

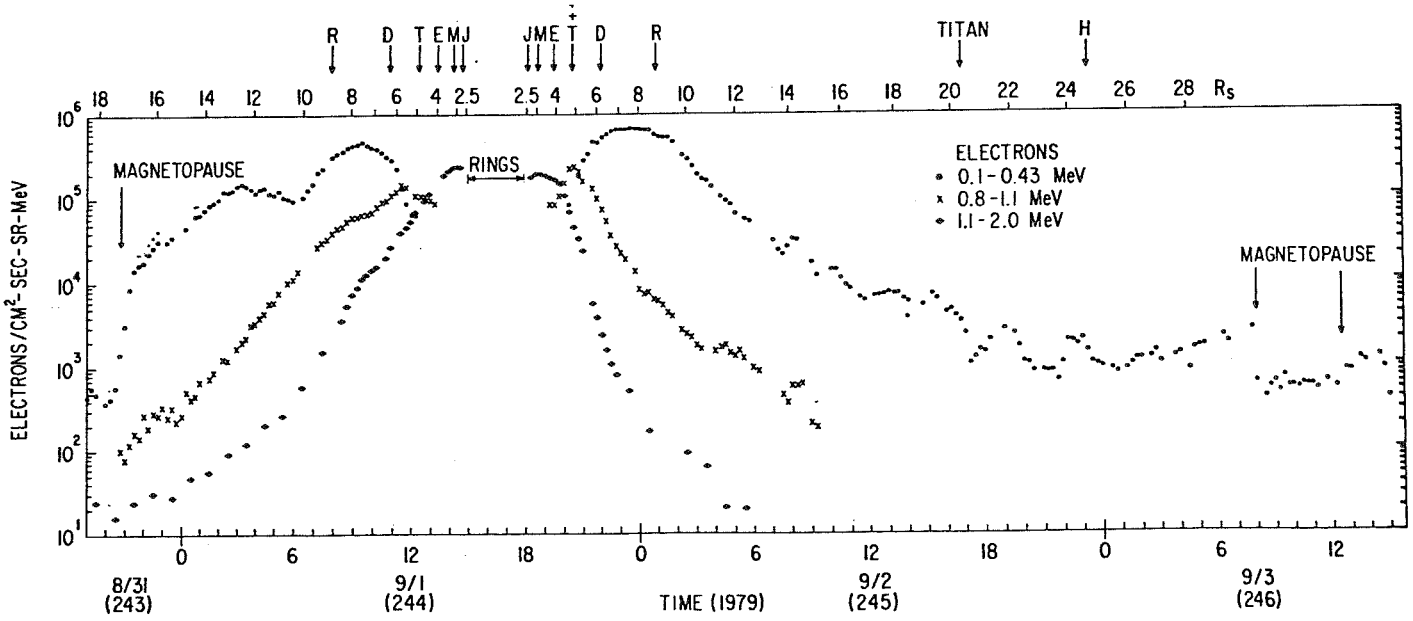

Figure 8-14b. Electron fluxes observed with Pioneer II. [8-1]

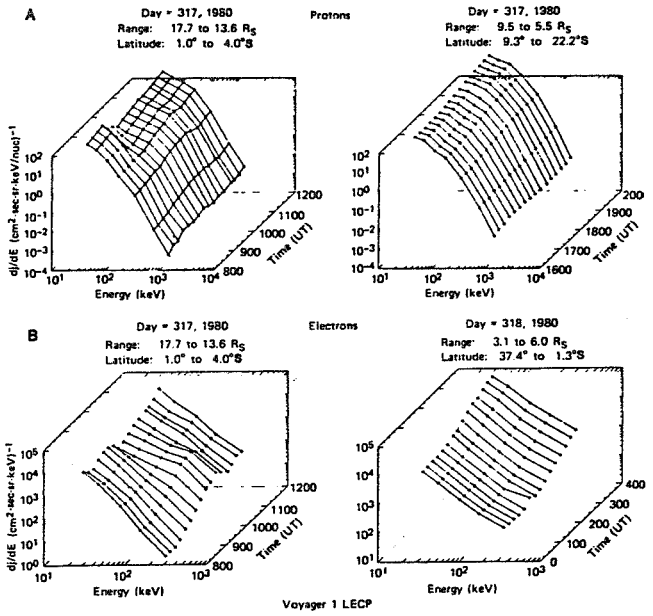

Time evolution (15-minute averages) of ion spectra. The highest energy point (~ 3 MeV) remains generally at background. Note the substantial evolution in the shape of the spectra. (B) Time evolution of electron spectra. In contrast to the ion spectra, the electron spectra can be described well by a power law in energy, except during spectrum evolution (for example, ~ 1000 to 1100, day 317).

Figure 8-15a. Ion spectra evolution. [8-2]

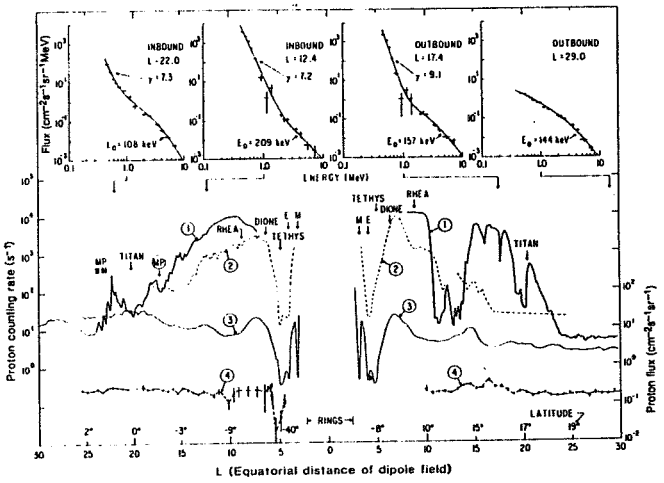

Proton intensities versus L and proton spectra in Saturn's magnetosphere. Curve 1 gives the counting rate of > 0.43-MeV protons from Voyager 1 and curve 2 gives a similar rate (> 0.55 MeV) as obtained by Pioneer 11, normalized to the geometric factor of the Voyager instrument. Curve 3 shows the Pioneer 11 1.6- to 5-MeV proton flux and curve 4 shows the Voyager 1 flux of 1.8- to 8-MeV protons (right-hand scale). On the inbound pass, the magnetosheath extends to L ~ 24 and is indicated by shaded areas near the magnetopause (MP) crossings. Voyager 1 latitudes are shown above the distance scale. Pioneer 11 remained within 5° of the equator equator. Proton spectra are shown in the insets. The power law index γ for the low-energy end is given as well as the characteristic energy E_0 for the high-energy end. Pre-encounter spectra were almost indistinguishable from the tail spectrum at L = 29.

Figure 8-15b. Proton intensities and spectra. [8-2]

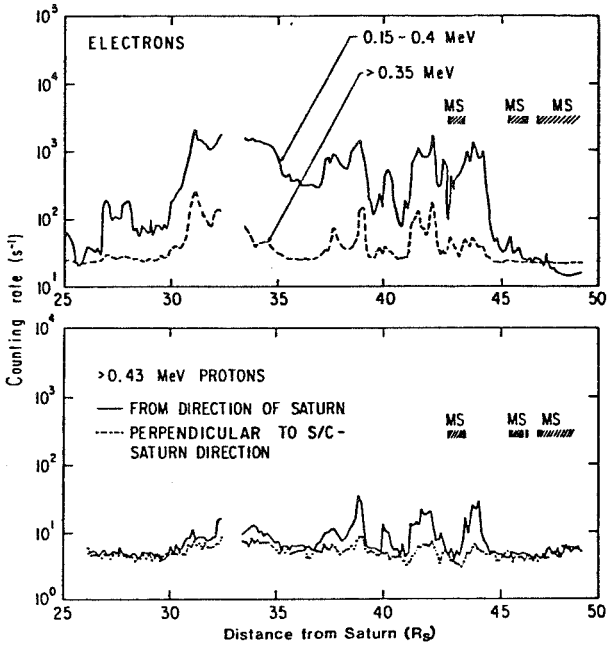

Voyager I electron and proton intensities in the magnetotail at northern latitudes between 20 and 23 deg versus distance from Saturn.

Figure 8-16. Voyager I electron and proton intensities. [8-2]

8.4.2.3 Electric and Magnetic Waves

Numerous plasma emissions were detected during encounter in the frequency range 0.1 to approximately 60 kHz. Field strengths are tens of micro-volts per meter. Modes include ion acoustic, electron plasma, chorus, hiss, electron cyclotron, and UHR. There was noise associated with plasma near the major satellites as well. Both the plasma wave and the planetary radio astronomy experiments (which observed up to 40 MHz frequencies) also detected waves from near the planet as opposed to the magnetosphere. As first reported by Kaiser et al. (1980) [8-7] and again discussed in Reference 8-2, kilometric radiation was observed at several AU from Saturn, but not 1 MHz noise as reported several years earlier by IMP-6 experimenters. The radiation is circularly polarized, RH from the northern hemisphere and LH from the southern. It also shows periodic amplitude modulation, which is interpreted as due to a weak higher order multipole of the magnetic field, not detected in situ by magnetometers. The period is 10 hr, 39.4 ± 0.15 min and this is defined as the core rotation period against which cloud motions are calculated. Measurements before and after encounter show that the phase of this modulation is independent of azimuth about Saturn. Hence the modulation is "clocklike" not like a "searchlight."

In addition, evidence for electrostatic discharges was observed as bursts of noise hundreds of microseconds long seen as short streaks in the dynamic spectral scans over the entire frequency range of 100 kHz to 40 MHz. These are shorter than the time for a frequency scan, but occur uniformly throughout the scans. Hence they are presumed to be broadband. About 10^4 bursts were recorded during the 48 hr centered on encounter; they have been attributed to an interaction of plasma with the rings.

8.5 SATELLITES AND RINGS

The best known and most impressive feature of Saturn is surely its rings, which the Voyager imager showed to have an enormously detailed structure, consisting of hundreds of ringlets. Of course the rings consist of many small satellites, and there is probably a continuum of body sizes from the resolved satellites down through the ring particles. Some spatial data are given in Tables 8-3 and 8-4; Figure 8-1 diagrams the orbital distance of the various objects.

8.5.1 Rings

Figure 8-1 shows a Voyager photograph of the rings. (Editorial comment: picture would be nice but not essential for text.) The rings are lettered in order of their discovery. Voyager was able to view the rings under three different illumination conditions: forward scattered sunlight, back scattered sunlight, and transmitted light when the spacecraft was on the dark side. In addition to the imaging and photometric observations, telemetry signal strength propagated and scattered through the rings was also measured. Table 8-6 lists physical data on the rings.

The cause of the fine structure in the rings is not known. Orbital resonances with the satellites could produce some of it. Two "shepherd" satellites (1980 S26 and S27) orbit just within and outside the F ring and may account for its structure.

8.5.2 Spokes

Among many interesting new observations the occurrence of narrow radial markings, spokes, in the B ring is perhaps most surprising. These are bright in forward scattered and dark in back scattered, indicating that they are comprised of small particles, probably levitated above the ring plane by electric forces. An explanation of the effect is not yet available.

8.5.3 Satellites

The 15 presently known satellites are listed in Table 8-3, all but Phoebe having been observed by Voyager. The inner five and 1980S6 are small and some are of non-spherical shape. They are thought to be composed of mixed water ice and rock. The larger satellites excepting Titan are probably water ice. Table 8-7 shows some properties of these icy satellites.

Titan is the second largest satellite in our solar system, after Jupiter's Ganymede, and has an atmosphere. It is discussed separately below. The other icy satellites show a variety of colors and markings, including heavy cratering, with the exception of Enceladus, which is the brightest but featureless. Evidently its surface has been remelted since the early period of cratering. One possibility is tidal heating by resonance interaction with Dione.

8.5.3.1 Titan

Titan has a substantial atmosphere comprised mainly of N_2 and supporting various haze layers, most prominent over the north polar cap, and clouds of methane. Figure 8-17 shows a profile of temperature versus pressure and altitude, and derived from IR and radio occultation measurements. The surface is obscured in visible light.

TABLE 8-6. RING OPTICAL DEPTHS [8-2]

Ring	Radial Zone[a]	Optical Depth		Particle Size, m (from S Band scattering)	Comment
		Visible	S Band		
D	–	–	–	–	Faint, with narrow features; few micron size particles
C	central	0.10 ± 0.02	0.02 to 0.28	2	Broad bands with embedded optically thick ringlets; regularly ordered
B	inner third	>1.0	>1.0	–	Many wide and narrow ringlets down to resolution limit (approximately 10 km); optically thin gaps between
Cassini Division	4 inner bands	0.08 ± 0.02 0.07 ± 0.02 0.07 ± 0.02 0.10 ± 0.02	0.15 to 0.65	8	Actually has narrow bands of matter, evenly spaced
A	central half	0.40 ± 0.08	0.65 to 0.80	10	Small scale structure only; some azimuthal asymmetry
F	–	–	–	–	Very narrow and shows a braided structure
G	–	–	–	–	Very narrow and faint
E	–	–	–	–	Broad but faint; has primarily very small particles

a. Refers to optical depths in visible.

TABLE 8-7. BULK PROPERTIES OF THE LARGEST SATURNIAN SATELLITES[a]

Satellite	Orbit Radius (R_s)	Radius[b] (km)	Density[c] (g cm^{-3})	Geometric[d] Albedo
Mimas (S1)	3.08	195 ± 5	1.2 ± 0.1	0.6 ± 0.1
Enceladus (S2)	3.97	250 ± 10	1.1 ± 0.6	1.0 ± 0.1
Tethys (S3)	4.91	525 ± 10	1.0 ± 0.1	0.8 ± 0.1
Dione (S4)	6.29	560 ± 10	1.4 ± 0.1	0.6 ± 0.1
Rhea (S5)	8.78	765 ± 10	1.3 ± 0.1	0.6 ± 0.1
Titan (S6)	20.4	2560 ± 26	1.9 ± 0.06	–
Hyperion (S7)	24.7	145 ± 20	–	0.3 ± 0.1
Iapetus (S8)	59.3	720 ± 20	1.2 ± 0.5	0.5 ± 0.3 (bright side)

a. Reference 8-2.

b. Average from several independent limb-fitting routines to Voyager 1 images, except Titan, which is from Tyler, et al., SCIENCE, vol. 212, 1981, p. 201.

c. Masses for Rhea and Titan are from Tyler, et al.; others are from ground-based and Pioneer measurements.

d. Albedos derived from telescopic visual magnitudes and Voyager 1 radii determination.

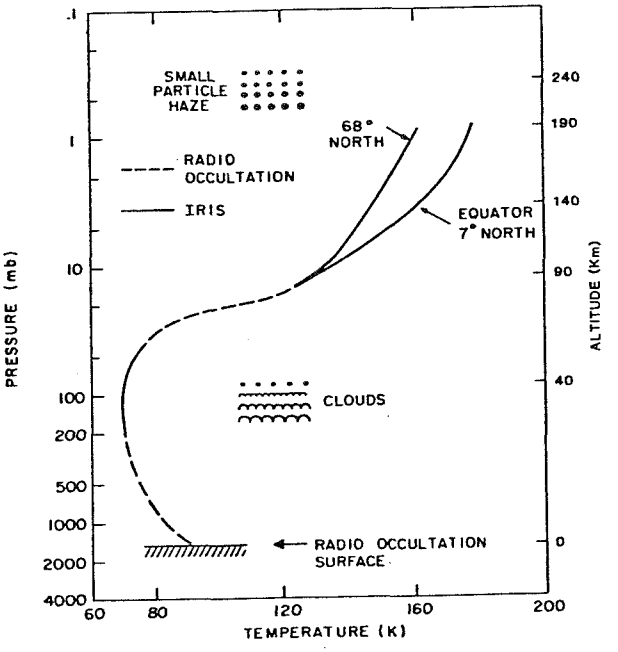

Figure 8-17. Temperature profile of Titan. [8-2]

Table 8-8 shows the trace composition of Titan's atmosphere as inferred from the Voyager IR spectrometer. As some Voyager investigators remark, the chemical processes leading to organic molecules, precursors of life, have occurred on Titan.

TABLE 8-8. ATMOSPHERIC COMPOSITION OF TITAN [8-2]

Gas	Band	Wave Number (cm^{-1})	Approximate Mole Fraction
Positively identified:			
Methane (CH_4)	ν_4	1304	1×10^{-2}
Ethane (C_2H_6)	ν_9	821	2×10^{-5}
Acetylene (C_2H_2)	ν_5	729	3×10^{-6}
Ethylene (C_2H_4)	ν_7	950	1×10^{-6}
Hydrogen cyanide (HCN)	ν_2	712	2×10^{-7}
Tentatively identified:			
Methylacetylene (C_3H_4)	ν_9,ν_{10}	633,328	–
Propane (C_3H_8)	ν_{26}	748	–

8.6 SUMMARY REMARKS

Saturn has a rich variety of satellites, showing us the variety of objects that can be formed. The planet itself and its planet-sized satellite Titan have interesting chemistries and the dynamics of the ring system continues to offer challenges. Knowledge of Saturn and its system is still in its infancy.

REFERENCES

8-1. Science, vol. 207, January 25, 1980: Dyer, J. W., "Pioneer Saturn," pp. 400-401; Opp. A. G., "Scientific Results from the Pioneer Saturn Encounter: Summary," pp. 401-403; Wolfe, J. H., et al., "Preliminary Results on the Plasma Environment of Saturn from the Pioneer 11 Plasma Analyzer Experiment," pp. 403-407; Smith, E. J., et al., "Saturn's Magnetic Field and Magnetosphere," pp. 407-410; Simpson, J. A., et al., "Saturnian Trapped Radiation and its Absorption by Satellites and Rings: The First Results from Pioneer 11," pp. 411-415; Van Allen, J. A., et al., "Saturn's Magnetosphere, Rings and Inner Satellites," pp. 415-421; Trainor, J. H., McDonald, F. B., and Schardt, A. W., "Observations of Energetic Ions and Electrons in Saturn's Magnetosphere," pp. 421-425; Fillius, W., Ip, W. H., and McIlwain, C. E., "Trapped Radiation Belts of Saturn: First Look," pp. 425-431; Judge, D. L., Wu, F.-M., and Carlson, R. W., "Ultraviolet Photometer Observations of the Saturnian System," pp. 431-434; Gehrels, T., et al., "Imaging Photopolarimeter on Pioneer Saturn," pp. 434-439; Ingersoll, A. P., et al., "Pioneer Saturn Infrared Radiometer: Preliminary Results," pp. 439-443; Humes, D. H., et al., "Impact of Saturn Ring Particles on Pioneer 11," pp. 443-444; Acuna, M. H. and Ness, N. F., "The Magnetic Field of Saturn: Pioneer 11 Observations," pp. 444-446; Kliore, A. J., et al., "Vertical Structure of the Ionosphere and Upper Neutral Atmosphere of Saturn from the Pioneer Radio Occultation," pp. 446-449; Anderson, J. D., "Pioneer Saturn Celestial Mechanics Experiment," pp. 449-453.

8-2. Science 212, April 10, 1981: Stone, E. C. and Miner, E. D., "Voyager 1 Encounter with the Saturnian System," pp. 159-163; Smith, B. A., et al., "Encounter with Saturn: Voyager 1 Imaging Science Results," pp. 163-191; Synnott, S. P., et al., "Orbits of the Small Satellites of Saturn," pp. 191-192; Hanel, R., et al., "Infrared Observations of the Saturnian System from Voyager 1," pp. 192-200; Tyler, G. L., et al., "Radio Science Investigations of the Saturn System with Voyager 1: Preliminary Results," pp. 201-206; Broadfoot, A. L., et al., "Extreme Ultraviolet Observations from Voyager 1 Encounter with Saturn," pp. 206-211; Ness, N. F., et al., "Magnetic Field Studies by Voyager 1: Preliminary Results at Saturn," pp. 211-217; Bridge, H. S., et al., "Plasma Observations Near Saturn: Initial Results from Voyager 1," pp. 217-224; Krimigis, S. M., et al., "Low-Energy Charged Particles in Saturn's Magnetosphere: Results from Voyager 1," pp. 225-231; Vogt, R. E., et al., "Energetic Charged Particles in Saturn's Magnetosphere: Voyager 1 Results," pp. 231-234; Gurnett, D. A., Kurth, W. S., and Scarf, F. L., "Plasma Waves Near Saturn: Initial Results from Voyager 1," pp. 235-238; Warwich, J. W., et al., "Planetary Radio Astronomy Observations from Voyager 1 Near Saturn," pp. 239-243.

8-3. Trans. Am. Geophys. Union, EOS62, 1981.

8-4. Observers Handbook, 1980.

8-5. The American Ephemeris and Nautical Almanac, 1959 and 1974.

8-6. Abell, G.: Exploration of the Universe. Holt, Rinehart and Winston, New York, 1975.

8-7. Kaiser, M. L., Desch, M. D., Warwich, J. W., and Pearce, J. B.: Voyager Detection of Non-Thermal Radio Emission from Saturn. Science 209, 1980, pp. 1238-1240.

SECTION 9. URANUS

9.1 INTRODUCTION

Uranus was discovered in 1789 by William Herschel. Unknown to the ancients, and barely visible to the naked eye, Uranus' magnitude is about 5.7. At first called the "Georgium Sidus" or "Herschel," it was not until much later that the name "Uranus" (the sky personified as a god in Greek mythology) gained acceptance.

Although Jupiter, Saturn, Uranus, and Neptune (the giant or Jovian planets) are frequently grouped together for discussion purposes, each has unique characteristics. Jupiter and Saturn are predominantly composed of hydrogen and helium, while Uranus and Neptune are believed to be made up mostly of heavier elements. Uranus is the only member of this group that lacks an internal heat source. Uranus' equator is inclined 98 deg to its orbital plane. (Greater than 90 deg means retrograde rotation.) Each pole points in a nearly sunward direction once each Uranian year. The planet must have extremely accentuated seasons. The interaction of solar wind with the pole-on planetary magnetosphere, which has intriguing possibilities, will be investigated by the Voyager 2 spacecraft. Scheduled arrival at Uranus by Voyager 2 is 1986, the year after its rotation axis is roughly aligned with the Sun (Fig. 9-1) [9-1]. The next optimum pole-on situation will be in 2027.

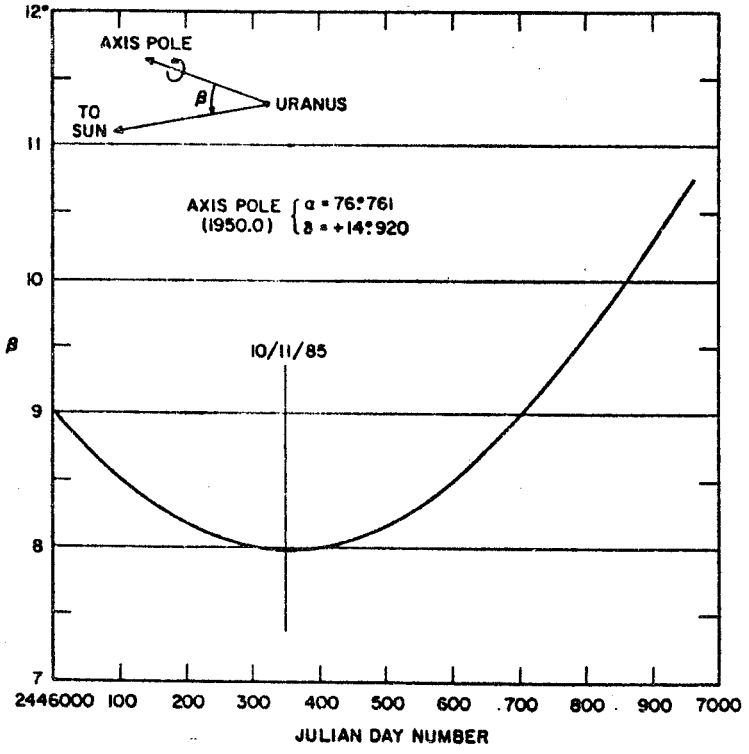

Figure 9-1. The time dependence of the angle β between the rotational axis of Uranus and the planet-Sun line, showing the especially interesting relationship that will exist during late 1985 [9-1].

Uranus is so distant from the Earth that telescopic imaging of its features has not been possible, although limb darkening can be detected from the Earth. The planet presents a green-blue disc caused by strong red absorption by methane. Uranus' small angular diameter (about 4 arc sec at opposition) has also led to difficulties in determining its rotation rate and oblateness.

Uranus has five optically identified moons which form a highly regular system. In 1977, numerous observers of an impending occulation reported subsidiary occultations. It soon became apparent that this was due to an extensive ring system about Uranus (paragraph 9.9). Later observations of the rings in occulation have led to the calculation of their orbital parameters and to new values of the harmonics of Uranus' gravity field.

9.2 DYNAMIC PROPERTIES

The dynamic properties in Table 9-1, for the mean equinox and ecliptic of 1950.0, at Julian Date 2444600.5, are adapted from References 9-2 through 904.

TABLE 9-1. DYNAMIC PROPERTIES

Parameter	Value	Comments
Mean Distance	2.884×10^9 km	19.28 AU
Eccentricity	0.05051	
Inclination of Orbit to the Ecliptic	0.771 deg	
Mean Orbital Velocity:		
Linear	6.8 km sec^{-1}	
Angular	0.0116 deg/day	
Orbital Angular Momentum	1.711×10^{42} kg m^2 sec^{-1}	
Sidereal Year	84.013 tropical years	
Synodic Period	369.66 days	
Inclination of Equator to the Orbit	97.88 deg	
Rotation Period	11 to 24 hr Retrograde	Review paragraph 9.2.1 and Table 9-2.

9.2.1 Comments

Perturbations to second order of the orbit of Uranus due to the three other Jovian planets have been investigated [9-5], as have the perturbations due to Pluto [9-6].

The orientation of Uranus' polar axis was first deduced assuming that its satellites are in orbits close to the equatorial plane of the planet. This has been confirmed by observations of the tilts of spectral lines in the Uranian absorption spectrum. However, there is a wide variation among different

determinations of Uranus' rotation period (Table 9-2), even where similar techniques have been used and it has not been possible to reconcile the various values. Photometric observations have not been helpful [9-7].

TABLE 9-2. THE ROTATION PERIOD OF URANUS

Period	Reference	Notes
12.8 ± 1.7 hr	[9-8]	From measurements of the geometric oblateness.
13.0 ± 1.3 hr	[9-9]	Whole-disk value calculated from the Doppler broadening of a reflected solar Fraunhofer line.
15.0 + 4.0 hr - 2.6	[9-10]	Similar to the above.
15.57 ± 0.80 hr	[9-11]	Tilts of reflected Fraunhofer lines, value for northern mid-latitudes. Some evidence for equatorial acceleration.
16.16 ± 0.33 hr	[9-5]	Similar method to the above. Evidence for latitudinal acceleration not present.
16.6 ± 0.5 hr	[9-12]	From measurements of the geometric oblateness.
23 + 5 hr - 2	[9-13]	Novel spectroscopic techniques.
24 ± 3 hr	[9-14]	Spectral line tilts.

*We wish to acknowledge our appreciation to J. L. Elliot of M.I.T./Cambridge for his advice and contributions.

Accurate determination of the rotation period will soon be possible from measurements during the impending Voyager 2 encounter. Measurements of the oblateness of Uranus suggest a period of approximately 16 hr.

9.3 PHYSICAL DATA

9.3.1 Mass, Figure, and Other Physical Properties

Table 9-3 summarizes Uranus's physical data.

9.3.2 Gravity Field

Analysis of precession rates of the elliptical rings of Uranus (paragraph 9.9) has made possible the calculation of the acceptable lead terms in the gravity field:

$J_2 = (3.352 \pm 0.006) \times 10^{-3}$ and $J_4 = (-2.9 \pm 1.3) \times 10^{-5}$ [9-16].

TABLE 9-3. PHYSICAL DATA

Parameter	Value	Comments/References
Equatorial Radius	26,145 km	[9-16] $n = 8 \times 10^{13}$ cm^{-3} number density level
Polar Radius	25,518 km	[9-16]
Mass	8.7268×10^{25} kg	14.6 Earth [9-15]
"Surface" Gravity	8.3 $msec^{-2}$	0.85 Earth [9-4]
Mean Density	1.2 g cm^{-3}	Estimated
Bolometric Bond Albedo	0.37 ± 0.05	[9-17]
Effective Temperature	58 ± 2°K	Paragraph 9.4 [9-18]
Equilibrium Temperature	$58 \begin{matrix} + 0.3 \\ - 0.6 \end{matrix}$ °K	[9-19]
Magnetic Field	Expected to be small; a polar field of intensity 0.6 to 0.9 gauss has been inferred from radio bursts, although the observations were ambiguous.	Paragraph 9.7 [9-20]

9.4 INTERIOR

Any solid surface Uranus may have is hidden well below atmospheric cloud cover. No precise information exists on the gross composition of the planet, except for the identification of hydrogen, methane, and a few trace constituents in the atmosphere. Interior modeling so far has been based on the following assumptions [9-21 through 9-23].

a) Uranus's mean density is intermediate between that of Jupiter or Saturn and that of Neptune. It has been assumed that the fraction of "volatile elements" (hydrogen and helium) declines through the Jovian planets and amounts to about 12 percent for Uranus. This does not include the hydrogen locked up as methane, ammonia, and water [9-24]. The fraction of these volatile elements is assumed to be depleted by a factor of at least 3 compared to "solar" abundances, although the depletion factor may be as high as 20 [9-25].

b) It is assumed that the relative amounts of "ices" (water, methane, and ammonia) and "rocks" (elements heavier than carbon and oxygen) follow solar abundance ratios: However, there is an uncertainty in the solar ice-to-rock ratio of 50 percent [9-21, 9-22]. Some modeling has also assumed superabundances of ammonium (NH_4^+) or neon [9-4].

Volatile elements, about 12 percent of total planetary mass, form an atmosphere above a thick mantle made up of the "ices." "Rocks" form a dense central core. The Uranian internal density distribution may follow such a curve as shown in Figure 9-2.

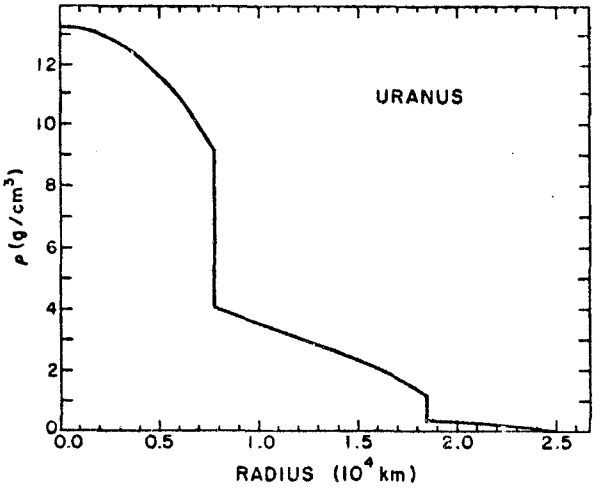

Figure 9-2. Density distribution in Uranus, calculated for a model with solar abundances of "ice" and "rock." The temperature distribution corresponds to the present epoch. [9-21]

The observed effective temperature of Uranus and its expected equilibrium temperature show no significant difference, indicating that the planet is in equilibrium with solar heating. In this respect it is different from the other three Jovian planets, each of which has an internal heat source [9-25 through 9-30]. Any internal heat source for Uranus must be less than 34 percent of the solar flux, based upon present data [9-29] and is probably less than 10 percent [9-19].

9.5 ATMOSPHERE

Observations of Uranus from the Earth show a featureless blue-green disk with some limb-darkening. The planet's coloration is due to strong absorptions by methane at the red end of the spectrum (methane being the major atmospheric component after molecular hydrogen and helium). Uranus' atmosphere is thought to have a total mass between one and two Earth masses, with the majority of this being hydrogen and helium [9-21].

In the mid-1970s, there were a number of reviews of Uranus' atmosphere [9-4, 9-31, 9-32] which, though superceded to a certain extent by more up-to-date data, contain useful information.

9.5.1 Composition of the Atmosphere

Hydrogen was first identified in the spectrum of Uranus in 1952 as the major atmospheric constituent. Although there is no spectroscopic evidence for helium [9-4], it is generally assumed to exist in the same ratio to hydrogen as occurs in the Sun [9-25]. The fraction of total atmosphere consisting of hydrogen is then around 85 percent [9-29], with approximately 10 percent helium. Only 5 to 10 percent consists of other gases such as methane.

Calculations of the abundance of hydrogen are highly model-dependent, but generally show the Uranian cloud layer to be overlain by 240 to 700 km-amagat of H_2 [9-33].[1]

Methane is the next most abundant atmospheric constituent. Analysis of spectra in the visible, thermal infrared, and microwave regions, although limited by the lack of good laboratory spectra, show that there is between a hundredth and a tenth as much methane as molecular hydrogen in the atmosphere [9-34]. From the methane-to-molecular hydrogen ratio, the C/H ratio for Uranus is deduced to be at least 0.005, 12 times the solar value and similar to that of Neptune [9-25, 9-35].

Another major constituent of the atmosphere is likely to be ammonia. Although an upper limit of about 2.5 m-amagat above the clouds has been set [9-19, 9-32]; ammonia ice crystals are the prime candidate for these clouds. Radio observations appear to show the existence of ammonia at lower levels [9-24, 9-32]. Other candidates for the cloud layer are solid methane [9-36] and solid hydrogen sulfide, possibly underlying NH_4HS [9-37].

Studies of the near infrared spectrum of Uranus have allowed upper limits to be put on the abundances of some expected constituents (assuming an H_2 abundance of 400 km-amagat) as shown in Table 9-4 [9-24].

TABLE 9-4. UPPER LIMITS FOR VARIOUS ATMOSPHERIC CONSTITUENTS [9-24]

Molecule	cm-amagat	Mixing Ratio
NH_3	5	1.2×10^{-7}
H_2S	30	8×10^{-7}
C_2H_2	2	5×10^{-8}
C_2H_4	20	5×10^{-7}
CH_3NH_2	10	3×10^{-7}

9.5.2 Structure of the Atmosphere

Unlike Jupiter and Saturn which have high thick cloud-decks, Uranus has a transparent atmosphere with the clouds down deeper [9-24]. There is, however, some evidence to suggest a high-level haze of aerosols or methane crystals.

1. km-amagat is equivalent to 2.69×10^{28} mol/m^2.

Figure 9-3 shows schematically the inferred methane haze and main cloud deck. Note that this is model-dependent and ammonia has not yet positively been identified as the predominant constituent of the clouds.

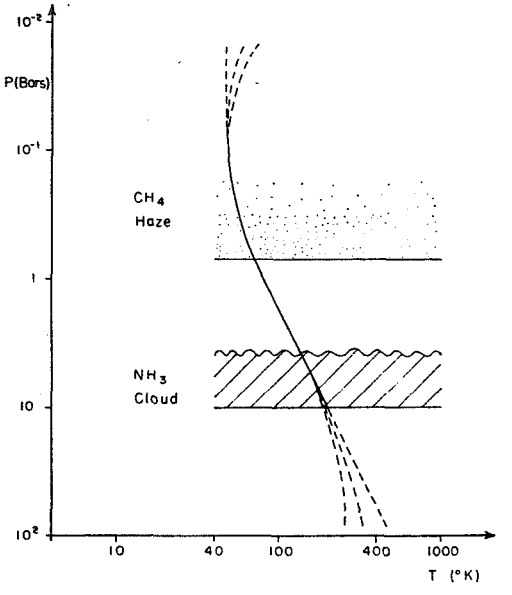

Figure 9-3. Inferred temperature profile and cloud layers as a function of pressure in the Uranus atmosphere [9-31].

The atmosphere of Uranus has been thought to be extremely constant until recently when the visible albedo, the infrared albedo, and the microwave brightness temperature were all found to vary (review Reference 9-38 and its references). At wavelengths from 3 to 13 cm, the brightness temperature of the planet varies by nearly 40 percent [9-39, 9-40]. (The majority of this thermal emission originates deep in the atmosphere below the clouds at pressures of a few bars to tens of bars and a temperature near 250°K.) Variations in flux are thought to represent climatic or seasonal changes.

9.5.2.1 Methane Haze Layer

Since few parameters of Uranus' atmosphere can be derived by ordinary telescopic observations from the Earth, the present most efficient tool for investigating the upper atmosphere is the use of occultation data. However, telescopic observations have indicated the presence of a high-level methane haze on Uranus from limb-brightening in the methane bands to the red end of the visible spectrum, with limb-darkening in the continuum at slightly shorter wavelengths [9-41, 9-42]. Polarization measurements also indicate the presence of an aerosol [9-43], as does the ultraviolet albedo of the planet [9-44].

Below the methane haze, if it exists, is a thick region with negligible aerosol scattering, reaching down to the dense cloud deck below [9-45], at a pressure level of 4 to 10 bars. Observations of continuum absorption in the blue, as well as the red, have shown that there is probably also some form of dust in the atmosphere [9-36].

9.5.3 Temperature Structure

The upper atmosphere is nonisothermal, with contrasts of 35 to 40°K compared to a mean temperature of 90 to 100°K [9-46]. A temperature inversion must occur between the altitude range covered ($T \cong 100°K$, $p \cong 10^{-3}$ mbar) and the region of the thermal infrared observations ($T \cong 60°K$, $p \cong 100$ mbar) [9-46, 9-47]. Figure 9-4 compares the occultation measurements [9-48] of the upper atmosphere with the infrared measurements deeper down [9-29, 9-49].

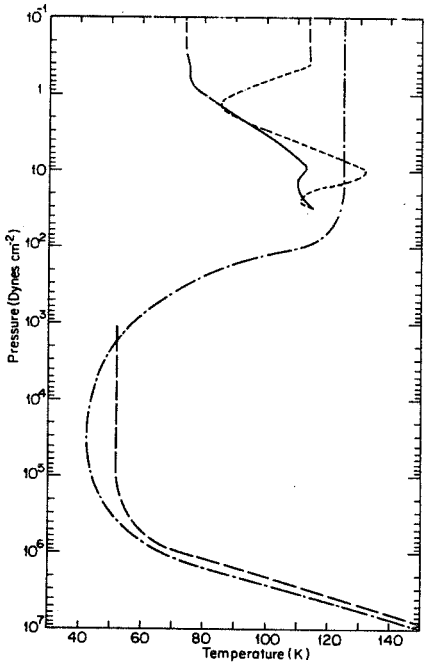

Figure 9-4. Comparison of occultation measurements of upper atmosphere with infrared measurements [9-48].

Diurnal and seasonal effects, despite the long duration of the seasons, are believed to be minimal. Calculations of expected dynamical drivers on Uranus show them to be very weak [9-31]. Direct observations of cloud movements have not been possible because of the large Earth-Uranus distance.

Modeling of the radiative and dynamical state of the atmosphere leads to an expectation of latitudinal temperature contrasts of the order 1°K per 10^4 km and typical meridional velocities of about 1 m/sec [9-31, 9-50].

Uranus' rapid rotation and large inclination imply that in the course of one orbit equatorial regions receive less integrated solar heat than do the poles. Stone [9-50] infers a high Richardson number (2800); also an atmosphere that is very insensitive to external parameters, is free from small-scale convection and possesses only nonsymmetrical features. Atmospheric turbulence is expected to be very weak compared to Jupiter and Saturn and even weak compared to the Earth.

9.6 IONOSPHERE

Analysis of the ionosphere of Uranus is hampered by the lack of any believable models or observations of the upper atmospheric structure and composition above the region probed by occultation techniques (paragraph 9.5). The recent evidence for a planetary magnetic field [9-20] will have

implications for the ionosphere, especially in view of the planet's obliquity, although a Jupiter-like ionosphere is not expected. Some of the problems of constructing model ionospheres for Uranus are discussed in Reference 9-44.

Early models of the ionosphere which were based on an assumption of photochemical equilibrium with solar extreme ultraviolet flux have been extended to take into account the effects of cosmic ray ionization (Fig. 9-5) [9-51, 9-52], which may be appreciable if the planetary magnetic field is relatively small, as suggested by the radio bursts [9-20]. The ionization effects of cosmic rays may be a useful diagnostic of the upper atmosphere's thermal structure. Models which neglect the effects of cosmic rays are now outdated.

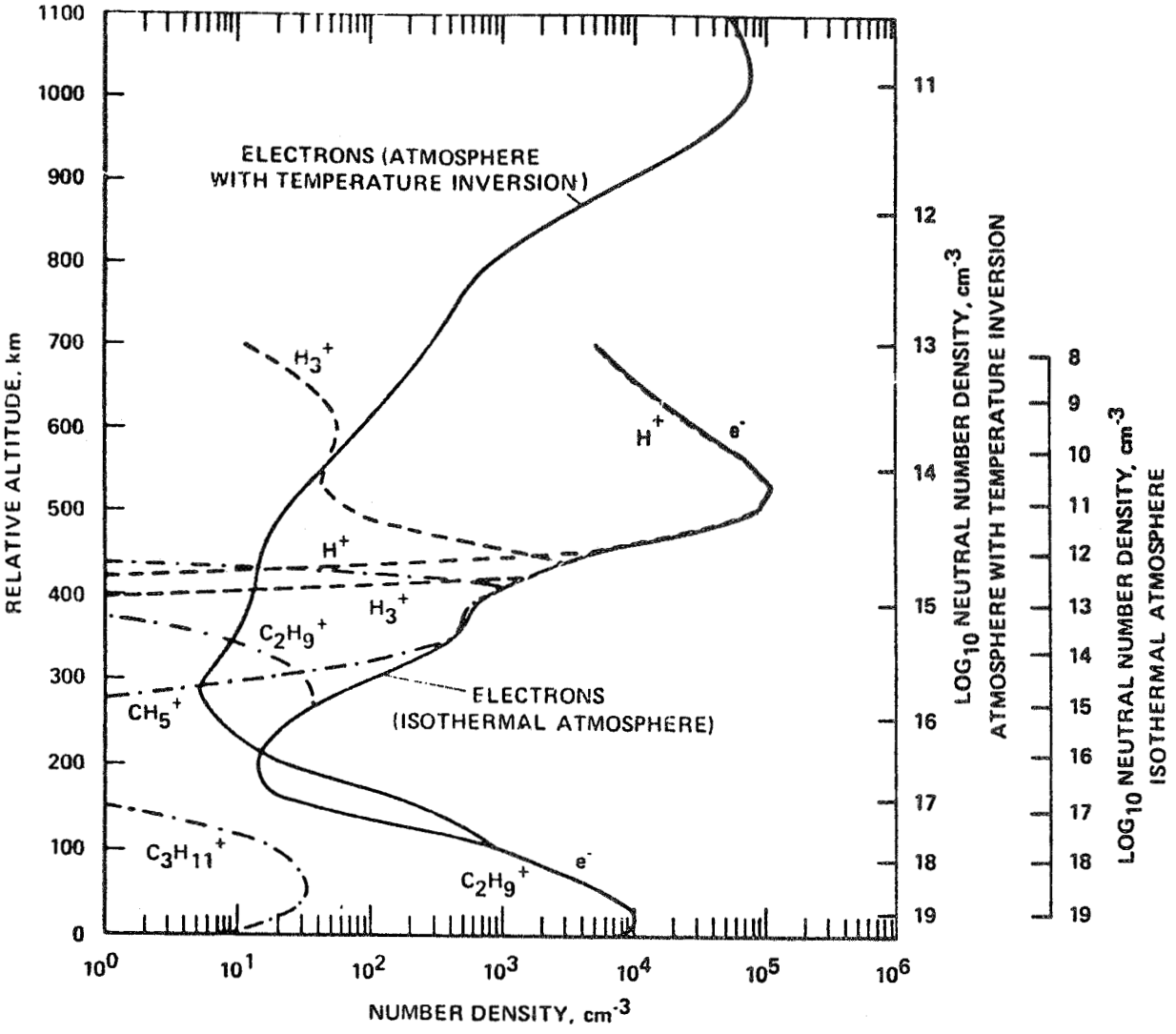

Figure 9-5. Tentative electron and ion number densities for Uranus. For purposes of clarity, the ion number densities are shown for the isothermal atmosphere only [9-52].

Two models are plotted. The isothermal model takes the temperature to be 56°K in all regions above the 10^{19} mol cm^{-3} density level, while the other model uses lower level thermal inversion. For both models the peak electron density is around 10^5 cm^{-3}, and protons are the dominant ions. The altitude scale is relative, zero being arbitrarily associated with a neutral number density of $5 \times 10^{19}/cm^3$.

9.7 MAGNETOSPHERE

Radio bursts from Uranus indicate the presence of some form of magnetosphere and, hence, a magnetic field. The "surface" magnetic field has been estimated to be 0.6 to 0.9 gauss [9-20]. Uranus' magnetosphere should be especially interesting since it is the only example in the Solar System that twice a year exhibits a pole-on orientation to the solar wind. The morphology of the magnetosphere during those times is expected to be as shown in Figure 9-6.

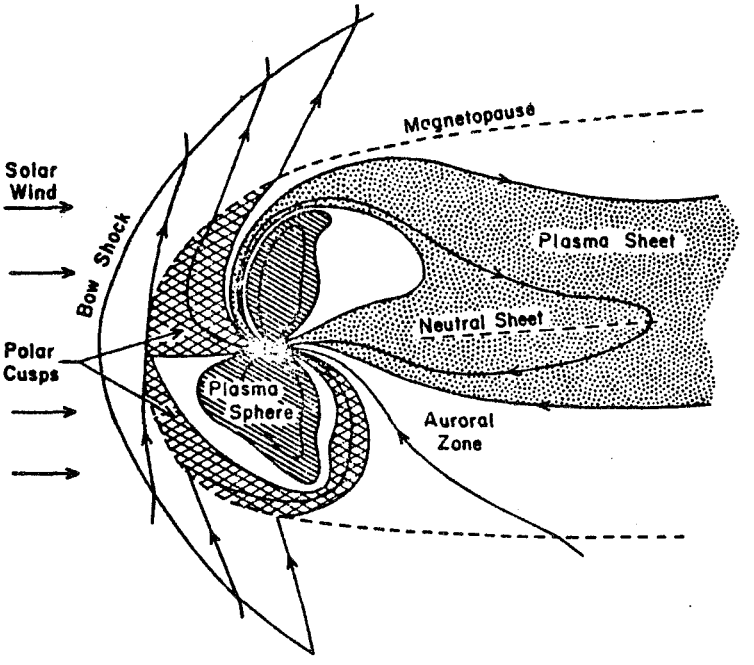

Figure 9-6. Hypothetical physical structure of a Uranian magnetosphere during the epoch of pole-on presentation to the solar wind. [9-1] Adapted from [9-53].

9.8 SATELLITES

Dynamically, Uranus' satellites form a very regular system. The four larger satellites all orbit in Uranus's equatorial plane. It is thought possible that they all [and possibly the rings as well (paragraph 9.9)] share a common origin in the breakup of some hypothetical larger body in the past [9-54].

The five Uranian moons are numbered from I through V as follows, with the year of discovery in parentheses:

Miranda	V	(1948)
Ariel	I	(1851)
Umbriel	II	(1851)
Titania	III	(1787)
Oberon	IV	(1787)

Tentative orbital parameters are given in Table 9-5. All five satellites revolve in a direct sense compared to the planet's spin; their orbits are retrograde compared to Uranus' orbit around the Sun. Synchronous rotation is expected for the satellites [9-54].

Recent infrared observations have led to the identification of water ice on the surfaces of Ariel, Umbriel, Titania, and Oberon [9-56, 9-57]. These four satellites show significant differences in reflectivity from other ice-covered satellites in the Solar System which may be due either to surface structure or a difference in the fraction of the surface covered by the ice [9-57]. The existence of ice or frost on the surface implies a higher mean albedo than a purely rocky surface, and the radii given may be too high (a rocky surface albedo was assumed).

9.9 RINGS

The discovery in 1977 of a ring system about Uranus has led to the refinement of knowledge of the planet's gravitational field and much speculation as to its origin. The discovery of a ring about Jupiter in 1979 shows that the existence of rings is a common feature of the Jovian planets (only Neptune lacks a known ring system). The comparative properties of the three sets of rings are reviewed in Reference 9-58.

There are three main ways in which rings are thought to form about a planet:

a) Meteoroidal bombardment of a large body, so that the fragments inside the planet's Roche limit form a ring;

b) Condensation of material inside the Roche limit as the planet was forming, which neither joins the planet nor can form a satellite;

c) The breakup of a satellite, or other body, which came within the planet's Roche limit.

Since Uranus' rings lie within a small range of orbital distances, all have a low albedo and show various eccentricities and inclinations, c) is favored as the explanation. It has been speculated that the large tilt of Uranus' spin axis might be due to a disruption caused by the close passage of a large body at some time in the past [9-59]; the rings might have been formed in the same event [9-60]. Knowledge of the physical nature of the rings of Uranus to late 1979 has been reviewed in References 9-61 and 9-62.

Accurate timings of occultation sequences from several observation points on the Earth have enabled accurate orbits to be calculated for the nine identified rings. The first six positively identified were labeled by the first six letters of the Greek alphabet; subsequently, three internal rings were found which have been labeled 4, 5, and 6. The orbital elements are shown in Table 9-6 [9-16].

The Uranian rings are notable for their thinness as deduced from the duration of the occulation event for each. Typical widths are shown in Table 9-7.

During numerous observed occultations, the rings never show a total loss of light signal, which allows an upper limit of about 4 km to be put on the ring particles. The optical thickness of the rings varies from about 0.2 to 0.7 for the inner rings to 2.3 for the ϵ-ring [9-61]. The majority of the ring particles are thought to be somewhat smaller than 4 km, although the presence of larger bodies cannot be ruled out.

TABLE 9-6. URANIAN RINGS: ORBITAL ELEMENTS [9-16]

Ring	Semimajor axis, a (km)	Eccentricity ($e \times 10^3$)	Azimuth of periapse, ω_0 (deg)	Precession rate from fitted J_2 and J_4 (deg/day)	Precession rate fitted individually (deg/day)
6	41 863.8 ± 32.6	1.36 ± 0.07	235.9 ± 2.9	2.7600	2.7706 ± 0.0034
5	42 270.3 ± 32.6	1.77 ± 0.06	181.8 ± 2.5	2.6678	2.6614 ± 0.0030
4	42 598.3 ± 32.7	1.24 ± 0.09	120.1 ± 2.7	2.5963	2.5957 ± 0.0031
α	44 750.5 ± 32.8	0.72 ± 0.03	331.4 ± 2.8	2.1832	2.1785 ± 0.0043
β	45 693.8 ± 32.8	0.45 ± 0.03	231.3 ± 4.0	2.0288	2.0272 ± 0.0064
η	47 207.1 ± 32.9	(0.03 ± 0.04)	(291.7 ± 88.3)	1.8094	—
γ	47 655.4 ± 32.9	(0.04 ± 0.04)	(301.6 ± 49.1)	1.7503	—
δ	48 332.0 ± 33.0	0.054 ± 0.035	139.0 ± 30.2	1.6657	—
ϵ	51 179.7 ± 33.8	7.92 ± 0.04	215.6 ± 0.5	1.3625	1.3625 ± 0.0004

TABLE 9-7. URANIAN RINGS: WIDTHS

6, 5, 4	$\sim$ 0.5 to 6.0 km	[9-63]
α γ δ	$\sim$ 2.0 to 5.0 km	[9-63]
β	$\sim$ 15 km	[9-63]
η	$\sim$ 60 km	[9-16]
ϵ	20 to 100 km	[9-64]

Immediately following the discovery of the rings, an optical search for them was initiated using previously exposed plates [9-61]. The results were negative, leading to an upper limit for their albedo of 0.05 [9-61, 9-65, 9-66]. This extremely low albedo suggests that the ring particles are fundamentally different from those of Saturn which are ice-covered and probably more stony in composition.

Comparison of the orbital distances of the Uranian rings with the Roche limit for various densities of material show the rings to be within the limit for any body with a density of less than 2.2 g cm^{-3} [9-67]. The Roche limit as a function of density of the satellite is shown in Figure 9-7 [9-68].

9.10 SPACE IN THE VICINITY OF URANUS

The only spacecraft to attain solar distances comparable to the orbit of Uranus (19 AU) has been Pioneer 10, which did not pass near the planet. At such large distances, the solar wind merges into the interstellar medium. Typical solar wind parameters at about 19 AU are believed to be as shown in Table 9-8 [9-1]. Siscoe [9-53] estimates the properties of the interstellar medium in the vicinity of Uranus to be as shown in Table 9-9 [9-53].

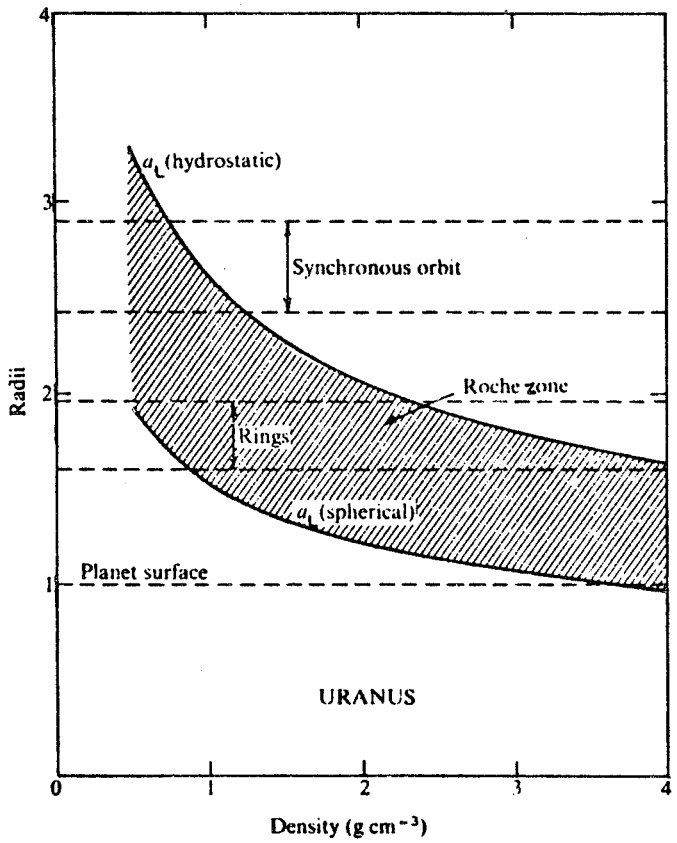

Figure 9-7. Roche limit a_L for Uranus as a function of satellite density [9-68]. a_L (hydrostatic) applies to a satellite that can relax to hydrostatic equilibrium and a_L (spherical) applies to a spherical satellite. It is in this Roche zone that a satellite is expected to lose solid particles from its surface. Location of the synchronous orbit shown above is based on a rotational period of 12.8 ± 1.7 hr.

TABLE 9-8. MEAN SOLAR WIND AT URANUS' ORBIT (EXTRAPOLATED)

Velocity	400 km sec^{-1}
Proton and electron number density	0.014 cm^{-3}
Azimuthal component of magnetic field	0.22 γ
Radial component of magnetic field	0.12 γ

TABLE 9-9. PROPERTIES OF THE INTERSTELLAR MEDIUM IN THE VICINITY OF URANUS (SPECULATIVE)

Neutral hydrogen density	0.1 cm^{-3}
Neutral helium density	0.008 cm^{-3}
Electron density	0.03 to 0.12 cm^{-3}
Kinetic temperature	100 to 10,000 K
Relative velocity	20 km sec^{-1}
Interstellar H flux	2×10^5 cm^{-2} sec^{-1}
Solar wind charge exchange H flux	$\sim 10^4$ cm^{-2} sec^{-1}

The solar flux at the distance of Uranus is about 3.8 W m^{-2}.

REFERENCES

9-1. Van Allen, J. A.: On the Magnetospheres of Jupiter, Saturn, and Uranus. Highlights of Astronomy. vol. 4, Part 1, 1977, pp. 195-224.

9-2. U. S. Government: Explanatory Supplement to the Astronomical Ephemeris and the American Ephemeris and Nautical Almanac. 1961.

9-3. U. S. Government: The Astronomical Almanac for the Year 1981. U. S. Government Printing Office, Washington, D.C.

9-4. Newburn, R. L. and Gulkis, S.: A Survey of the Outer Planets Jupiter, Saturn, Uranus, Neptune, Pluto and Their Satellites. Space Sci. Rev., vol. 14, 1973, pp. 179-271.

9-5. Brown, R. A. and Goody, R. M.: The Rotation of Uranus II. Astrophys. J., vol. 235, 1980, pp. 1066-1070.

9-6. Pireaux, J.: Representations des perturbations des grosses planetes dues a la presence de Pluton. Astron. Astrophys., vol. 79, 1979, pp. 132-137.

9-7. Lockwood, G. W. and Thompson, D. T.: A Photometric Test of Rotation Periods for Uranus and Time Variations of Methane-Band Strengths. Astrophys. J., vol. 221, 1978, pp. 689-693.

9-8. Elliot, J. L., Dunham, E., Mink, D. J., and Churms, J.: The Radius and Ellipticity of Uranus from Its Occultation of SAO 158687. Astrophys. J., vol. 236, 1980, pp. 1026-1030.

9-9. Tranger, J. T., Roesler, F. L., and Munch, G.: A Redetermination of the Uranus Rotation Period. Astrophys. J., vol. 219, 1978, pp. 1079-1083.

9-10. Munch, G. and Hippelein, H.: The Effects of Seeing on the Reflected Spectrum of Uranus and Neptune. Astron. Astrophys., vol. 81, 1980, pp. 189-197.

9-11. Brown, R. A. and Goody, R. M.: The Rotation of Uranus. Astrophys. J., vol. 217, 1977, pp. 680-687.

9-12. Franklin, F. A., Avis, C. C., Colombo, G., and Shapiro, I. I.: The Geometric Oblateness of Uranus. Astrophys. J., vol. 236, 1980, pp. 1031-1034.

9-13. Trafton, L.: Uranus' Rotational Period. Icarus, vol. 32, 1977, pp. 402-412.

9-14. Hayes, S. H. and Belton, M. J. S.: The Rotational Periods of Uranus and Neptune. Icarus, vol. 32, 1977, pp. 383-401.

9-15. Klepczynski, W. J., Seidelmann, P. K., and Duncomb, R. L.: The Masses of the Principal Planets. Celestial Mech., vol. 4, 1971, pp. 253-272.

9-16. Elliot, J. L., French, R. G., Frogel, J. A., Elias, J. H., Mink, D. J., and Liller, W.: Orbits of Nine Uranian Rings. Astronom. J., vol. 86, 1981, pp. 444-455.

9-17. Dlugach, M. and Yanovitskij, E. G.: The Optical Properties of Venus and the Jovian Planets II. Icarus, vol. 22, 1974, pp. 66-81.

9-18. Loewenstein, R. F., Harper, D. A., Moseley, S. H., Telesco, C. M., Thronson, H. A., Hildebrand, R. H., Whitcomb, S. E., Winston, R., and Stiening, R. F.: Far-Infrared and Submillimeter Observations of the Planets. Icarus, vol. 31, 1977, pp. 315-324.

9-19. Danielson, R. E.: The Structure of the Atmosphere of Uranus. Icarus, vol. 30, 1977, pp. 462-478.

9-20. Brown, L. W.: Possible Radio Emission from Uranus at 0-5 MHz. Astrophys. J., vol. 207, 1976, pp. L209-L212.

9-21. Hubbard, W. B. and MacFarlane, J. J.: Structure and Evolution of Uranus and Neptune. J. Geophys. Res., vol. 85, 1980, pp. 225-234.

9-22. Podalak, M. and Reynolds, R. T.: On the Structure and Composition of Uranus and Neptune. Icarus, vol. 46, 1981, pp. 40-50.

9-23. Hubbard, W. B.: Interiors of the Giant Planets. Science, vol. 214, 1981, pp. 145-149.

9-24. Fink, U. and Larson, H. P.: The Infrared Spectra of Uranus, Neptune, and Titan from 0.8 to 2.5 Microns. Astrophys. J., vol. 233, 1979, pp. 1021-1040.

9-25. Encrenaz, Th.: Infrared Radiation of the Planets. Infrared Phys., vol. 19, 1979, pp. 353-373.

9-26. Hubbard, W. B.: Intrinsic Luminosities of the Jovian Planets. Reviews of Geophys. and Space Phys., vol. 18, 1980, pp. 1-9.

9-27. Stier, M. T., Traub, A., Fazio, G. G., Wright, E. L., and Low, F. J.: Far-Infrared Observations of Uranus, Neptune, and Ceres. Astrophysical Journal, vol. 226, 1978, pp. 347-349.

9-28. Morrison, D. and Cruikshank, D. P.: Temperatures of Uranus and Neptune at 24 Microns. Astrophys. J., vol. 179, 1973, pp. 329-331.

9-29. Courtin, R., Gautier, D., and Lacombe, A.: On the Thermal Structure of Uranus from Infrared Measurements. Astron. Astrophys., vol. 63, 1978, pp. 97-101.

9-30. Hubbard, W. B.: Comparative Thermal Evolution of Uranus and Neptune. Icarus, vol. 35, 1978, pp. 177-181.

9-31. Stone, P. H.: The Atmosphere of Uranus. Icarus, vol. 24, 1975, pp. 292-298.

9-32. Hunt, G. E.: The Atmospheres of the Outer Planets. Advances in Physics, vol. 25, 1976, pp. 455-487.

9-33. Smith, W. H., Macy, W., and Pilcher, C. B.: Measurements of the H_2 4-0 Quadrupole Bands of Uranus and Neptune. Icarus, vol. 43, 1980, pp. 153-160.

9-34. Wallace, L.: The Structure of the Uranus Atmosphere. Icarus, vol. 43, 1980, pp. 231-259.

9-35. Macy, W., Gelfand, J., and Smith, W. H.: Interpretation of the 6818.9 Å Methane Line in Terms of Inhomogeneous Scattering Models for Uranus and Neptune. Icarus, vol. 34, 1978, pp. 20-27.

9-36. Danielson, R. E., Cochran, W. D., Wannier, P. G., and Light, E. S.: A Saturation Model of the Atmosphere of Uranus. Icarus, vol. 31, 1977, pp. 97-109.

9-37. Macy, W.: On the Clouds of Uranus. Icarus, vol. 40, 1979, pp. 213-222.

9-38. Lockwood, G. W.: Analysis of Photometric Variations of Uranus and Neptune Since 1953. Icarus, vol. 35, 1978, pp. 79-92.

9-39. Batty, M. J., Jauncey, D. L., Rayner, P. T., and Gulkis, S.: Evidence for Changes in the Microwave Brightness Temperature and Spectrum of Uranus. Astrophys. J., vol. 243, 1981, pp. 1058-1061.

9-40. Turegano, J. A. and Klein, M. J.: Precision Flux Density Measurements of the Giant Planets at 8420 MHz. Astron. Astrophys., vol. 94, 1981, pp. 91-94.

9-41. Prinn, R. G. and Lewis, J. S.: Uranus Atmosphere: Structure and Composition. Astrophys. J., vol. 179, 1973, pp. 333-342.

9-42. Pilcher, C. B., Morgan, J. S., Macy, W. W., and Kunkle, T. D.: Methane Band Limb-Brightening on Uranus. Icarus, vol. 39, 1979, pp. 54-64.

9-43. Michalsky, J. J. and Stokes, R. A.: Whole-disk Polarization Measurements of Uranus at Visible Wavelengths. Astrophysical Journal, vol. 213, 1977, pp. L135-L137.

9-44. Savage, B. D., Cochran, W. D., and Wesselins, P. R.: Ultraviolet Albedos of Uranus and Neptune. Astrophys. J., vol. 237, 1980, pp. 627-632.

9-45. Trafton, L.: The Aerosol Distribution in Uranus' Atmosphere: Interpretation of the Hydrogen Spectrum. Astrophysical Journal, vol. 207, 1976, pp. 1007-1024.

9-46. Elliot, J. L. and Dunham, E.: Temperature Structure of the Uranian Upper Atmosphere. Nature, vol. 279, 1979, pp. 307-308.

9-47. Gillett, F. C. and Rieke, G. H.: 5 to 20 Micron Observations of Uranus and Neptune. Astrophys. J., vol. 218, 1977, pp. L141-L144.

9-48. Dunham, E., Elliot, J. L., and Gierasch, P. J.: The Upper Atmosphere of Uranus: Mean Temperature and Temperature Variations. Astrophys. J., vol. 235, 1980, pp. 274-284.

9-49. Wallace, L.: On the Thermal Structure of Uranus. Icarus, vol. 25, 1975, pp. 538-544.

9-50. Stone, P. H.: The Dynamics of the Atmospheres of the Major Planets. Space Sci. Rev., vol. 4, 1973, pp. 444-459.

9-51. Atreya, S. K. and Donahue, T. M.: Ionospheric Models of Saturn, Uranus, and Neptune. Icarus, vol. 24, 1975, pp. 358-362.

9-52. Capone, L. A., Whitten, R. C., Prasad, S. S., and Dubach, J.: The Ionospheres of Saturn, Uranus, and Neptune. Astrophys. J., vol. 215, 1977, pp. 977-983.

9-53. Siscoe, G. L.: Particle and Field Environment of Uranus. Icarus, vol. 24, 1975, pp. 311-324.

9-54. Greenberg, R.: The Dynamics of Uranus Satellites. Icarus, vol. 24, 1975, pp. 325-332.

9-55. Veillet, C.: New Determination of the Orbit of Miranda. Astron. Astrophys., vol. 98, 1981, pp. 218-222.

9-56. Cruikshank, D. P. and Brown, R. H.: The Uranian Satellites: Water and Ice on Ariel and Umbriel. Icarus, vol. 45, 1981, pp. 607-611.

9-57. Cruikshank, D. P.: New-Infrared Studies of the Satellites of Saturn and Uranus. Icarus, vol. 41, 1980, pp. 246-258.

9-58. Pollack, J. and Cuzzi, J.: Rings in the Solar System. Scientific American, vol. 245, 1981, pp. 104-129.

9-59. Greenberg, R.: Outcomes of Tidal Evolution for Orbits with Arbitrary Inclination. Icarus, vol. 23, 1974, pp. 51-58.

9-60. Smoluchowski, R.: Planetary Rings. Comments on Astrophysics, vol. 8, 1979, pp. 69-78.

9-61. Ip, W. H.: Physical Studies of the Planetary Rings. Space Sci. Rev., vol. 26, 1980, pp. 39-96.

9-62. Ip, W. H.: New Progress in the Physical Studies of the Planetary Rings. Space Sci. Rev., vol. 26, 1980, pp. 97-109.

9-63. Nicholson, P. D., Person, S. E., Matthews, K., Goldreich, P., and Neugebauer, G.: The Rings of Uranus: Results of the 10 April 1978 Occultation. Astronom. J., vol. 83, 1978, pp. 1240-1248.

9-64. Nicholson, P. D., Matthews, K., and Goldreich, P.: The Uranus Occultation of 10 June 1979. I. The Rings. Astron. J., vol. 86, 1981, pp. 596-606.

9-65. Sinton, W. M.: Uranus: The Rings are Black. Science, vol. 198, 1977, pp. 503-504.

9-66. Smith, B. A.: Uranus Rings: An Optical Search. Nature, vol. 268, 1977, p. 32.

9-67. Smoluchowski, R.: The Ring Systems of Jupiter, Saturn and Uranus. Nature, vol. 280, 1979, pp. 377-378.

9-68. Dermott, S. F., Murray, C. D., and Sinclair, A. T.: The Narrow Rings of Jupiter, Saturn and Uranus. Nature, vol. 284, 1980, pp. 309-313.

SECTION 10. NEPTUNE

10.1 INTRODUCTION

Neptune is the first planet to be discovered as the basis of a prediction from orbital perturbations of other planets, and its discovery was one of the triumphs of nineteenth-century theoretical astronomy. Independent analyses by the French and British astronomers, LeVerrier and Adams, led Galle at the Berlin Observatory to find it in 1846.

Although often thought of as a twin of Uranus, Neptune is as dissimilar to that planet as Saturn is to Jupiter. Neptune is more massive and has a higher mean density. Although both planets have hydrogen as their major atmospheric component and telescopically show the blue-green coloration of methane, they must be different in structure since Neptune has an internal heat source, while Uranus does not. (Neptune radiates about twice the energy that is receives from the Sun.)

With an orbital period of about 165 years, Neptune has still not been tracked over one complete revolution. However, prediscovery observations of what was assumed at the time to be a star have allowed the time-base over which its position has been charted to be considerably extended. In particular, recently discovered observations by Galileo [10-1], soon after the invention of the telescope, may have astrometric value. Since Neptune cannot be seen by the naked eye, no earlier observations exist.

Because of its extreme distance from the Earth and small angular size, information on atmospheric structure, rotation rate, oblateness, etc., is vague and inaccurate. The best values for diameter and flattening, as well as upper atmospheric structure, have been derived from stellar occultation data. The planned encounter by Voyager 2 spacecraft in 1989 should revolutionize our knowledge of this planet.

10.2 DYNAMIC PROPERTIES

The following properties for the mean equinox and ecliptic of 1970 at Julian Date 2440588 are shown in Table 10-1 [10-2].

TABLE 10-1. DYNAMIC PROPERTIES

Parameter	Value	Comments
Semi-major Axis	4.50×10^9 km	30.06 AU
Eccentricity	0.0086	
Inclination of Orbit to the Ecliptic	1.776 deg	
Mean Orbital Velocity:		
Linear	5.4 km sec^{-1}	
Angular	0.006 deg day^{-1}	
Orbital Angular Momentum	2.52×10^{42} kg m^2 sec^{-1}	
Sidereal Year	164.79 years	
Synodic Period	367.48 days	
Rotation Period	approximately 18 hr	Uncertain, See Text
Inclination of Equator to the Orbit	28.8 deg	

10.2.1 Comments

At the present time, and until 1999, Neptune is the most distant planet from the Sun. Pluto's eccentric orbit has brought it within the orbit of Neptune for a period of 20 years (there is no chance of a planetary collision; Section 11, Pluto).

Neptune's orbit is highly circular; its spin axis is, however, considerably inclined to the orbit plane so seasons occur. Uncertainty in the rotation period is discussed in paragraph 10.3.2.

The orbits of Neptune and Pluto show a resonance: their mean motions are in the ratio 3:2 [10-3, 10-4]. The perturbations of Neptune by the other large planets have been computed [10-5] as well as perturbations due to Pluto [10-6].

10.3 PHYSICAL DATA

10.3.1 Mass, Figure, and Other Physical Properties

Table 10-2 summarizes Neptune's physical data.

TABLE 10-2. PHYSICAL DATA

Parameter	Value	Comments
Radius, mean	24,700 ± 60 km [10-7,10-8]	3.88 Earth
Mass	1.0296×10^{26} kg [10-9]	17.23 Earth
"Surface" Gravity	13.8 $msec^{-2}$ [10-2]	1.4 Earth
Mean Density	1.66 g cm^{-3}	Earth = 5.41
J_2	0.0041 ± 0.0004 [10-10]	
Geometrical Flattening	0.026 ± 0.008 [10-7]	
Bolometric Bond Albedo (estimated)	0.33 [10-8]	
Visual Magnitude	approximately 7.8 [10-11]	
Effective Temperature	59.7 ± 4.0°K [10-12]	
Equilibrium Temperature	46 ± 2°K [10-8]	
Magnetic Field	None observed; Internal field is probably small or absent [10-13]	

10.3.2 Comments

With an angular diameter of about 2 arcsec when viewed from the Earth, Neptune is too small for accurate determinations of its size by imaging techniques; interferometric and occultation methods are more useful. Little information is available on cloud markings and rotation period. With only two satellites, precise determination of Neptune's mass has also been difficult. Neptune's mean density is the highest of the Jovian planets, suggesting a different composition and internal structure.

Over the past few years there has been much controversy over the planet's rotation period. Derived rotation periods range from 11.2 hr [10-14] to around 22 hr [10-15] (a variation much greater than could be attributed to differential zonal rotation). Both photometric light curve data analyses of possible zonal atmospheric winds and theoretical study of the planet's figure lead to a "most probable" rotation period near 18 hr [10-16 through 10-19]. A review of the plausibility of the recent spin period values [10-20] has shown that a period of the order 19 hr or less is needed to explain the observed flattening.

Neptune's albedo appears to change by several hundredths of a magnitude over periods of months or years. Observations over almost three decades [10-21] showed a secular increase in brightness from 1972 to 1976, with a following decline [10-22]. The variations may be linked to solar activity [10-11, 10-23]; they are also observed for Saturn's moon Titan and for Uranus [10-21, 10-22].

10.4 INTERIOR

Neptune has no visible solid surface. Present modeling of the interior has many uncertainties due to lack of information on the chemical composition and inaccuracies in values for oblateness and rotation period [10-20].

In 1973, it was discovered that Neptune radiates more energy than it receives from the Sun (like Jupiter and Saturn, but unlike Uranus). The source of this heating cannot be tidal effects due to the satellite Triton [10-8], so an internal source is implied [10-24]. The observed effective temperature of the planet is 1°K [10-8, 10-12, 10-25], whereas the equilibrium temperature for solar heating is 46 ± 2°K [10-8], depending upon the albedo adopted. Radiated energy is at least twice the incident solar flux [10-25].

A number of theories have been put forward to explain Neptune's internal source of energy [10-26]. Neptune, like all the Jovian planets, once had a considerably higher temperature than at present and is cooling towards a state of equilibrium with solar radiation. This cooling is controlled to a large extent by the atmosphere and is not strongly dependent upon internal conductivity. The present heat excess arises either from a central reservoir or from separation of the planet's chemical constituents as a core is formed [10-26]. Possible thermal histories of Uranus and Neptune are compared in Reference 10-27.

Models of the structure of Neptune are highly speculative. Depletion of hydrogen and helium is implied by the general trend toward higher concentrations of heavier elements moving outwards from Jupiter to Neptune [10-28]. Models of Neptune's interior have been based on the assumption that the relative amounts of "ices" (water, methane, and ammonia) and "rocks" (elements heavier than carbon and oxygen) follow solar abundancies [10-29, 10-30]. The general picture suggested is of a central "rocky" core surrounded by ices, with a total mass of about 15 Earth masses, and a gaseous envelope of hydrogen and helium, with some inpurities, of one to two Earth masses [10-29]. According to this model, the dependence of density upon radius would exhibit the trend shown in Figure 10-1 with three distinct domains.

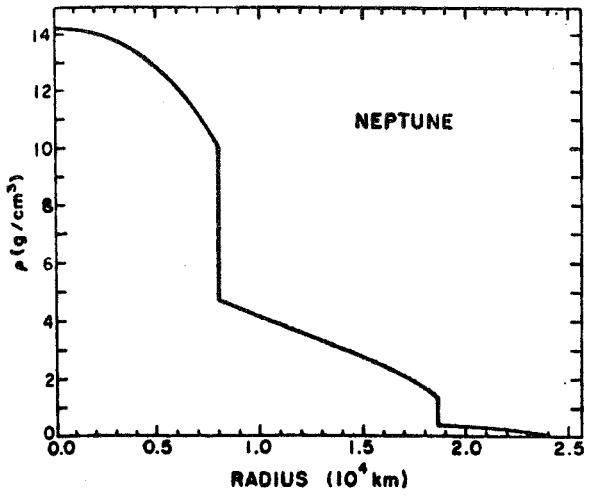

Figure 10-1. Neptune's density distribution for a model with solar abundances of "ices" and "rocks." Temperature structure as for the present time [10-29].

10.5 ATMOSPHERE

Neptune presents a featureless disk when telescopically viewed from the Earth. Improved understanding of atmospheric motions awaits observations of atmospheric albedo and color markings which will be possible with the launching of the Space Telescope in the mid-1980s and the expected arrival of Voyager 2 at Neptune in 1989.

As noted, visual observations show a blue-green coloration caused by methane. Knowledge of Neptune's atmosphere up to 1976 is reviewed in Reference 10-31.

10.5.1 Composition

The predominant constituents of Neptune's atmosphere are hydrogen and helium. Hydrogen was first detected in 1952. Recent observations have shown the hydrogen abundance to be in excess of 200 km-amagat (5.5×10^{30} mol/m^2) and may be twice that. More hydrogen exists in Neptune's atmosphere than the sum of all other constituents [10-31 through 10-33].

Spectroscopic evidence for the presence of methane in Neptune's atmosphere was found in 1967 [10-31]. Abundance is estimated to be near 6 km-amagat [10-34]. The derived C/H ratio of 5×10^{-3} is about 12 times the solar ratio [10-35]. Other trace constituents, detected in stratospheric spectra, are acetylene and ethane. The following approximate mixing ratios have been derived (ratios of partial pressures) [10-36]:

$CH_4/H_2 \sim 10^{-3}$ to 10^{-2}

$C_2H_6/H_2 \sim 10^{-6}$

$C_2H_2/H_2 \sim 10^{-8}$

Ammonia has yet to be detected [10-14], but remains expected as a minor constituent. Numerous other trace constituents are strongly suspected to exist in the atmosphere which have so far escaped identification. They include phosphine (PH_3) and monodeuterated methane (CH_3D) [10-37]. The presence of such constituents is inferred from observation of them on Jupiter and Saturn, and the requirements for absorbers to explain Neptune's low infrared albedo at 5 μm [10-37].

Observations in the near-infrared have led to the upper limits for expected trace constituents as shown in Table 10-3.

TABLE 10-3. UPPER LIMITS FOR NEPTUNE'S ATMOSPHERE [10-38]

Molecule	cm-amagat	Mixing Ratio
NH_3	20	5×10^{-7}
H_2S	100	3×10^{-6}
N_2O	30	8×10^{-7}
COS	20	5×10^{-7}
C_2H_2	10	3×10^{-7}
C_2H_4	20	5×10^{-7}
C_2H_6	50	1×10^{-7}
CH_3OH	20	5×10^{-7}
CH_3NH_2	10	3×10^{-7}

10.5.2 Structure

Little information is presently available on the structure of Neptune's atmosphere [10-31]. The upper atmosphere has been investigated by occultation techniques [10-7, 10-39, 10-40]. Apart from their use in determining planetary dimensions, light curves for different observation positions at the Earth give temperature profiles for different positions on Neptune. Diurnal temperature variations are 10°K or less, and latitudinal variations (equator to 55 deg latitude) are 15°K or less; both at an altitude typical of particle density approximately 5×10^{14} cm^{-3}. At this altitude the temperature is about 140°K, so that thermal contrasts are 10 percent or less. Scale height is about 55 km, although the region is not isothermal with height, and distinct layering is seen [10-40]. Infrared observations have led to thermal profiles shown in Figure 10-2 [10-35].

The model N_1 shown in Figure 10-2, which gives the best fit to infrared data uses as parameters:

$H_2/(H_2 + H_e) \sim 0.8$

$CH_4/H_2 \sim 2 \times 10^{-3}$

Effective Temperature ~ 58.4°K

An implication is that there is a strong super-saturation of methane in Neptune's upper atmosphere [10-41].

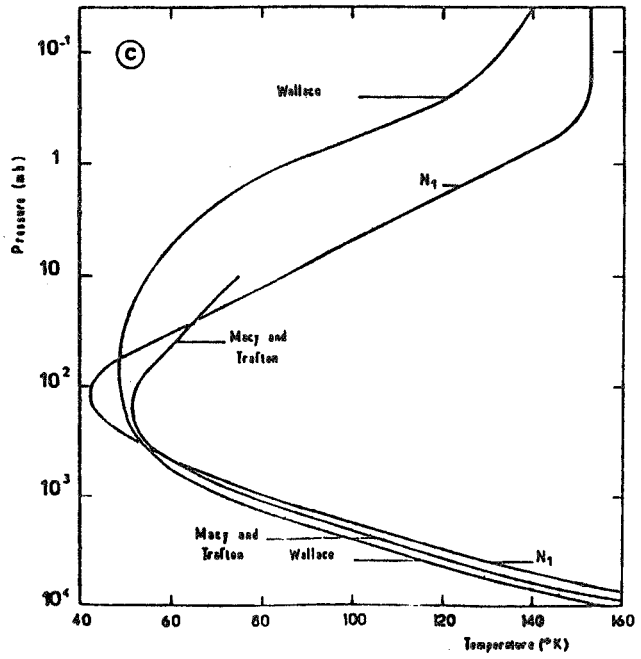

Figure 10-2. Neptune's atmospheric thermal profile.

10.5.3 High Cloud Layer

The presence of a high scattering cloud layer has been inferred [10-38]. This layer must be of small optical depth since observations of methane and hydrogen visible spectra would otherwise not be possible. The layer is thought to be at a pressure level of about 0.7 bar, from the fact that it is overlain by about 50 km-amagat of H_2. (Some researchers locate the cloud layer higher in the atmosphere [10-42, 10-43]. The cloud oscillates in height, with a variation in altitude of the order of 6 km [10-38]. Thus, most of the atmosphere of Neptune may be obscured under a tenuous cloud layer.

Until recently, it was thought that Uranus and Neptune had atmospheres which were unchanging, and they were used in the mid-1970s as photometric standards to trace possible changes in the solar constant. It is now known, however, that Neptune shows considerable changes in infrared albedo [10-42, 10-44, 10-45], presumably caused by changes in the high cloud layer. These changes may be related in turn to solar activity [10-11, 10-21, 10-23, 10-46]. The high cloud appears to form and partially disperse over a period of 1 year and may appear and disappear repetitively over periods of a few years [10-44]. Changes over periods of a few days have also been noted [10-19].

Parameters of the high cloud include:

a) An average optical thickness of about unity

b) Particle sizes greater than 1 μm.

The most probable constituents are methane and/or argon crystals [10-44].

10.5.4 Atmospheric Dynamics

No observational information exists that applies to the lower atmmosphere. Derivation of multiple rotation periods by spectroscopic and photometric means may imply the existence of zonal flow [10-15, 10-17, 10-18, 10-19, 10-47]. The equatorial jets expected to exist in Neptune's atmosphere have been modeled and lead to an expectation that, reflecting differential zonal flows, the atmosphere at the equator rotates 25 to 40 percent faster than at the poles [10-48].

10.6 IONOSPHERE

Ionospheric models have been constructed using the assumption of photochemical equilibrium with the solar extreme ultraviolet flux [10-49]. This treatment has been extended to include the ionization effects of cosmic rays, the effect of which may be comparable to the solar EUV [10-50]. If Neptune does not possess an intrinsic magnetic field, cosmic rays become especially important.

The curves in Figure 10-3 show tentative electron and ion densities for the ionosphere, from two different models. The "isothermal" model assumes a constant temperature of 50°K above the 10^{19} mol cm^{-3} density level. The other model is for a lower level thermal inversion and uses temperature values from Reference 10-51. The ion densities for this latter model are not shown. Huge uncertainties are apparent. The altitude scale is relative; "zero" altitude is set at an arbitrary number-density level.

10.7 SATELLITE SYSTEM

Compared to the satellite systems of the other Jovian planets, Neptune's system can best be described as chaotic. The largest of Neptune's two moons, Triton (also one of the largest satellites in the solar system) was discovered in 1846 soon after the discovery of Neptune itself. It is peculiar for having a decaying, retrograde orbit, with a low eccentricity. The other moon, tiny Nereid, was not discovered until 1949. Its orbit is the most eccentric of all planetary satellites. Discoveries have been reported of third and fourth satellites of Neptune [10-52] but remain unconfirmed.

As noted, the orbits of Neptune's two known satellites are peculiar. Recent modeling has led to the suggestion of a disruption caused by the near passage of another body of 2 to 5 Earth masses. Pluto is a possible candidate [10-53].

Present figures for the dimensions of Triton and Nereid are extremely tentative and are based on an assumed albedo of 0.5. Table 10-4 summarizes the physical data of Neptune's two moons, Triton and Nereid.

10.7.1 Triton

Recent spectra of Triton show it to be similar to various terrestrial, meteoritic, and lunar minerals [10-54]; "rocky" rather than "icy."

Recent high-resolution spectral data have shown absorption features at 8900 Å and at 2.3 μm which have been ascribed to gaseous methane [10-55, 10-56]. Initial estimates of methane abundance gave a value of 50 m-amagat and a surface pressure of approximately 1 mbar [10-55], close to the value

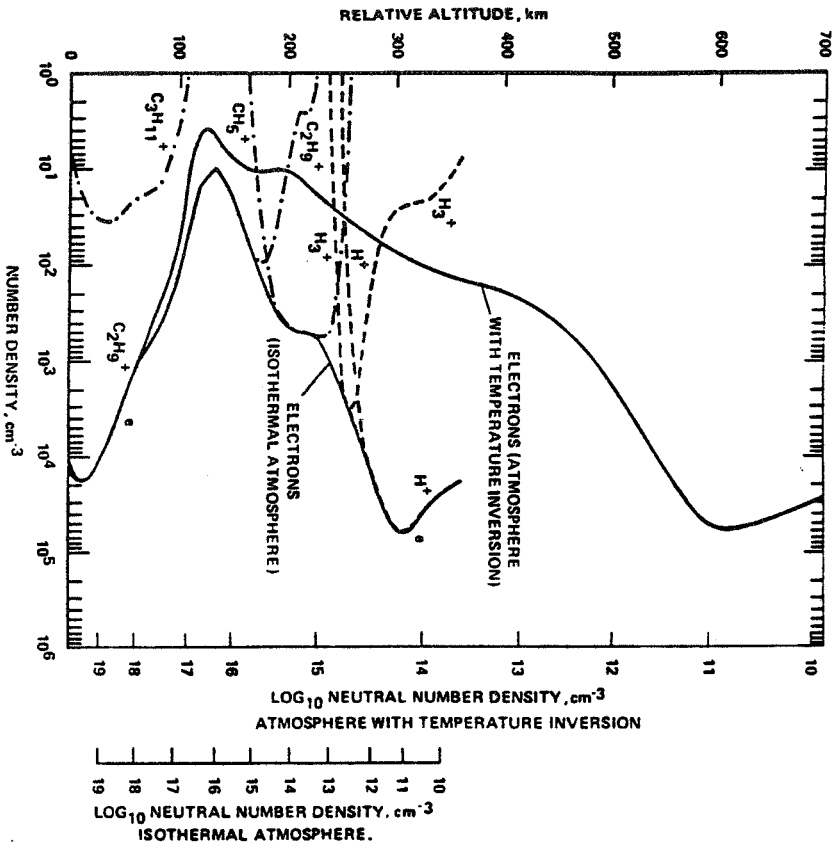

Figure 10-3. Tentative electron and ion number densities for Neptune. [10-50]

TABLE 10-4. PHYSICAL DATA OF NEPTUNE'S MOONS, TRITON AND NEREID

Parameter	Triton	Nereid
Orbital Period [10-57]	5.8768 days	359.88 days
Semi-major axis [10-43]	355.25×10^3	5567.0×10^3 km
Eccentricity [10-57]	< 0.01	0.7483
Inclination of Orbit to Neptune's Equator [10-57]	160 deg	27.6 deg
Mass (calculated from below)	1.34×10^{23} kg	2.1×10^{19} kg
Mass (Moon) / Mass (Neptune) [10-57]	0.0013	2×10^{-7}[a]
Radius [10-57]	∿ 1900 km	∿ 150 km[a]
Mean Density	∿ 4.9 g cm^{-3}	--
Subsolar Temperature [10-58]	62°K	62°K
Average Temperature [10-58]	44°K	44°K
Albedo (extremely tentative) [10-55]	∿ 0.21	--

a. Very uncertain.

expected for the equilibrium vapor pressure of surface methane frost. Triton may thus have a dusty, rocky surface, with patches of methane frost in the low temperature regions (away from the subsolar point) [10-56].

Triton's orbit is decaying rapidly, and Triton will be destroyed in 10 to 100 million years when it falls into Neptune [10-43, 10-59]. Photometric observations have shown that it is locked in synchronous rotation about Neptune, with its leading side appearing brighter than the trailing side.

10.7.2 Nereid

Because of its faintness when observed from the Earth, little is known of the physical parameters of Nereid. It is thought to be asteroidal in nature.

10.8 RINGS

The discovery of rings about Uranus and Jupiter in 1977 and 1979, respectively, leaves Neptune the only Jovian planet without a known ring system. A recent study [10-60] showed that stable rings could exist close to the plane of Neptune's equator, or perpendicular to it, but occultation observations have not led to detection of a ring system.

10.9 SPACE IN THE VICINITY OF NEPTUNE

Solar flux at the distance of Neptune is about 1.55 W m^{-2}, assuming no interplanetary extinction [10-61]. For information on other parameters, review Section 9.0, Uranus.

REFERENCES

10-1. Kowal, C. and Drake, S.: Galileo's Observations of Neptune. Nature, vol. 287, 1980, pp. 311-313.

10-2. Explanatory Supplement to the Astronomical Ephemeris and the American Ephemeris and Nautical Almanac, HMSO, London, 1961.

10-3. Peale, S.: Orbital Resonances in the Solar System. Ann. Rev. Astron. Astrophys., vol. 14, 1976, p. 215-246.

10-4. Greenberg, R.: Orbit-Orbit Resonances in the Solar System: Varieties and Similarities. Vistas in Astron., vol. 21, 1977, pp. 209-239.

10-5. Simon, J. and Bretagnon, P.: Perturbations due deuxieme ordre des quatre grosses planetes. Variations seculaires dun demi-grand axe. Astron. Astrophy., vol. 69, 1978, pp. 369-372.

10-6. Pireaux, J.: Representations des perturbations des grosses planétes dues a la presence de Pluton. Astron. Astrophys., vol. 79, 1979, pp. 132-137.

10-7. Freeman, K. C. and Lynga, G.: Data for Neptune from Occultation Observations. Astrophy. J., vol. 160, 1970, pp. 767-780.

10-8. Trafton, L.: The Source of Neptune's Internal Heat and the Value of Neptune's Tidal Dissipation Factor. Astrophys. J., vol. 193, 1974, pp. 477-480.

10-9. Klepczynski, W. J., Seidelmann, P. K., and Duncomb, R. L.: The Masses of the Principal Planets. Celest. Mech., vol. 4, 1971, pp. 253-272.

10-10. Peale, S. J.: The Gravitational Fields of the Major Planets. Space Science Rev., vol. 14, 1973, pp. 412-423.

10-11. Lockwood, G. and Thompson, D.: A Relationship Between Solar Activity and Planetary Albedos. Nature, vol. 280, 1979, pp. 43-45.

10-12. Stier, M., Traub, W., Fazio, G. J., Wright, E., and Low, F.: Far-Infrared Observations of Uranus, Neptune and Ceres. Astrophys. J., vol. 226, 1978, pp. 347-349.

10-13. Torbett, M. and Smoluchowski, R.: Hydrodynamic Dynamo in the Cores of Uranus and Neptune. Nature, vol. 286, 1980, pp. 237-239.

10-14. Munch, G. and Hippelein, H.: The Effects of Seeing on the Reflected Spectrum of Uranus and Neptune. Astron. Astrophys., vol. 81, 1980, pp. 189-197.

10-15. Hayes, S. and Belton, M.: The Rotation Periods of Uranus and Neptune. Icarus, vol. 32, 1977, pp. 383-401.

10-16. Belton, M., Wallace, L., Hayes, S., and Price, M.: Neptune's Rotation Period: A Correction and a Speculation on the Difference Between Photometric and Spectroscopic Results. Icarus, vol. 42, 1980, pp. 71-78.

10-17. Belton, M., Wallace, L., and Howard, S.: The Periods of Neptune: Evidence for Atmospheric Motions. Icarus, vol. 46, 1981, pp. 263-274.

10-18. Slavsky, D. and Smith, H.: The Rotation Period of Neptune. Astrophys. J., vol. 226, 1978, pp. L-49-L-52.

10-19. Cruikshank, D.: On the Rotation Period of Neptune. J. Astrophys. Lett., vol. 220, 1978, pp. L57-L59.

10-20. Cook, A.: A Note on the Flattening of Uranus and Neptune. Monthly Notices Roy. Astron. Soc., vol. 187, 1979, pp. 39P-43P.

10-21. Lockwood, G.: Analysis of Photometric Variations of Uranus and Neptune Since 1953. Icarus, vol. 35, 1978, pp. 79-92.

10-22. Lockwood, G.: Secular Brightness Increases of Titan, Uranus and Neptune, 1972-1976. Icarus, vol. 32, 1977, pp. 413-430.

10-23. Suess, S. and G. W. Lockwood: Correlated Variations of Planetary Aledos and Coincident Solar-Interplanetary Variations. Solar Phys., vol. 68, 1980, pp. 393-409.

10-24. Murphy, R. and Trafton, L.: Evidence for an Internal Heat Source in Neptune. Astrophys. J., vol. 193, 1974, pp. 253-255.

10-25. Loewenstein, R., Harper, D., and Moseley, H.: The Effective Temperature of Neptune. Astrophys. J., vol. 218, 1977, pp. L145-L146.

10-26. Hubbard, W.: Intrinsic Luminosities of the Jovian Planets. Rev. Geophys. Space Phys., vol. 18, 1980, pp. 1-9.

10-27. Hubbard, W.: Comparative Thermal Evolution of Uranus and Neptune. Icarus, vol. 35, 1978, pp. 177-181.

10-28. Encrenaz, Th.: Infrared Radiation of the Giant Planets. Infrared Phys., vol. 19, 1979, pp. 353-373.

10-29. Hubbard, W. and MacFarlane, J.: Structure and Evolution of Uranus and Neptune. J. Geophys. Res., vol. 85, 1980, pp. 225-234.

10-30. Podolak, M. and Reynolds, R. T.: On the Structure and Composition of Uranus and Neptune. Icarus, vol. 46, 1981, pp. 40-50.

10-31. Hunt, G.: The Atmospheres of the Outer Planets. Advances in Phys., vol. 25, 1976, pp. 455-487.

10-32. Smith, W., Macy, W., and Pilcher, C.: Measurements of the H_2 4-0 Quadrupole Bands of Uranus and Neptune. Icarus, vol. 43, 1980, pp. 153-160J.

10-33. Trafton, L.: Neptune Observations of the H_2 Quadrupole Lines in the (4-0) Band. Exploration of the Planetary System, edited by Woszcylzyk and Iwaniszewka, Reidel Publishing Co., 1974, p. 497.

10-34. Macy, M., Gelfand, J., and Smith, W.: Interpretation of the 6818.9-Å A Methane Line in Terms of Inhomogeneous Scattering Models for Uranus and Neptune. Icarus, vol. 34, 1978, pp. 20-27.

10-35. Courtin, R., Gautier, D., and Lacombe, A.: Indications of Supersaturated Stratospheric Methane on Neptune from Its Atmospheric Thermal Profile. Icarus, vol. 37, 1979, pp. 236-248.

10-36. Macy, W.: Mixing Ratios of Methane, Ethane, and Acetylene in Neptune's Stratosphere. Icarus, vol. 41, 1980, pp. 153-158.

10-37. Macy, W., Sinton, W., and Biechman, C.: Five-Micrometer Measurements of Uranus and Neptune. Icarus, vol. 42, 1980, pp. 68-70.

10-38. Fink, U. and Larson, H.: The Infrared Spectra of Uranus, Neptune and Titan from 0.8 to 2.5 Microns. Astrophys. Jour., vol. 233, 1979, pp. 1021-1040.

10-39. Kovalevsky, J. and Link, F.: Diametre aplatissement et proprietes optiques de la haute atmosphere de Neptune d'apres l'occultation de l'etoile BD-17° 4388. Astron. Astrophys., vol. 2, 1969, pp. 398-412.

10-40. Rages, K., Veverka, J., Wasserman, L., and Freeman, K.: The Upper Atmosphere of Neptune: An Analysis of Occultation Observations. Icarus, vol. 23, 1974, pp. 59-65.

10-41. Macy, W. and Trafton, L.: Neptune's Atmosphere: The Source of the Thermal Inversion. Icarus, vol. 26, 1975, pp. 428-436.

10-42. Joyce, R., Pilcher, C., Cruikshank, D., and Morrison, D.: Evidence for Weather on Neptune. I. Astrophys. J., vol. 214, 1977, pp. 657-662.

10-43. Newburn, R. and Gulkis, S.: A Survey of the Outer Planets: Jupiter, Saturn, Uranus, Neptune, Pluto and Their Satellites. Space Science Rev., vol. 14, 1973, pp. 179-271.

10-44. Pilcher, C.: Evidence for Weather on Neptune. II. Astrophys. J., vol. 214, 1977, pp. 663-666.

10-45. Savage, B. D., Cochran, W. D., and Wesselius, P. R.: Ultraviolet Albedos of Uranus and Neptune. Astrophy. J., vol. 237, 1980, pp. 627-632.

10-46. Hardorp, J.: The Sun Among the Stars – IV. Albedos of Uranus and Neptune and the Solar Color. Astron. Astrophy., vol. 96, 1981, pp. 123-126.

10-47. Belton, M., Wallace, L., Hayes, S., and Price, M.: Neptune's Rotation Period: A Correction and a Speculation on the Difference Between Photometric and Spectroscopic Results. Icarus, vol. 42, 1980, pp. 71-78.

10-48. Drobyshevskii, E.: On the Equatorial Flows on Uranus and Neptune. Sov. Astron., vol. 23, 1979, pp. 598-604.

10-49. Atreya, S., and Donahue, T.: Ionospheric Models of Saturn, Uranus, and Neptune. Icarus, vol. 24, 1975, pp. 358-362.

10-50. Capone, L., Whitten, R., Prasad, S., and Dubach, J.: The Ionospheres of Saturn, Uranus and Neptune. Astrophys. J., vol. 215, 1977, pp. 977-983.

10-51. Wallace, L.: On the Thermal Structure of Uranus. Icarus, vol. 25, 1975, pp. 538-544.

10-52. IAU Circular Number 3608: Neptune's Third Satellite. Sky and Telescope, vol. 62, May 29, 1981, p. 317.

10-53. Harrington, R. and Van Flandern, T.: The Satellites of Neptune and the Origin of Pluto. Icarus, vol. 39, 1979, pp. 131-136.

10-54. Cruikshank, D., Stockton, A., Dyck, H., Becklin, E., and Macy, W.: The Diameter and Reflectance of Triton. Icarus, vol. 40, 1979, pp. 104-114.

10-55. Benner, D., Fink, U., and Cromwell, R.: Image Tube Spectra of Pluto and Triton from 6800 to 9000 Å. Icarus, vol. 36, 1978, pp. 82-91.

10-56. Cruikshank, D. and Silvaggio, P.: Triton: A Satellite With an Atmosphere. Astrophy. J., vol. 233, 1979, pp. 1016-1020.

10-57. The Astronomical Almanac for 1981, U. S. Government Printing Office, Washington, D.C.

10-58. Gaffney, E. and Matson, D.: Water Ice Polymorphs and Their Significance on Planetary Surfaces. Icarus, vol. 44, 1980, pp. 511-519.

10-59. McCord, T.: Dynamical Evolution of the Neptunian System. Astron. J., vol. 71, 1966, pp. 585-590.

10-60. Dobrovolskis, A.: Where are the Rings of Neptune? Icarus, vol. 43, 1980, pp. 222-226.

10-61. Levine, J., Kraemer, D., and Kuhn, W.: Solar Radiation Incident on Mars and the Outer Planets: Latitudinal, Seasonal and Atmospheric Effects. Icarus, vol. 31, 1977, pp. 136-145.

SECTION II. PLUTO

11.1 INTRODUCTION

Pluto is believed to have about the same radius as the Earth's Moon, but only one-fifth its mass. It is the smallest of all the known planets and is dwarfed by the major satellites of Jupiter and Saturn. For most of its orbit it is the outermost planet, though at present and until 1999 it is closer to the Sun than Neptune.

Pluto was discovered in 1930 as the result of a deliberate search for a planet beyond Neptune whose presence was predicted from orbital perturbations of Neptune and Uranus. The new planet was found in just about the expected location, but because of its tiny mass, Pluto cannot be the real source of the perturbations and its discovery has to be regarded as fortuitous. For accounts of the events leading up to the discovery of Pluto review References 11-1 and 11-2.

Interest in Pluto received an unexpected impulse in 1978 with the discovery of an "elongation" of photographic images of the Planet [11-3]. This elongation has been ascribed to the presence of a satellite, christened "Charon" [11-4]. In this discussion, the position is adopted that Charon is real, although its existence has not yet been established beyond question [11-5].

11.2 DYNAMIC PROPERTIES

Since Pluto was discovered only 52 years ago, it has been observed only over about one-fifth of its orbital period of 247.7 years. For this reason, differences exist in dynamic parameters for the planet derived by various workers. A recent study by Seidelmann, et al., [11-6] gives the parameters (future observations will doubtless lead to refinements) shown in Table 11-1.

TABLE 11-1. DYNAMIC PROPERTIES

Parameters	Value	Comments
Semi-Major Axis	5.94173×10^9 km	39.718 AU
Eccentricity	0.25235	
Orbit Inclination	17.139 deg	
Longitude of Ascending Node	109.513 deg	
Longitude of Perihelion	112.986 deg	
Mean Anomaly	345.503 deg	
All of the above are for Epoch 1979 May 7.0; Ecliptic and Equinox of 1950.0. Further approximate parameters follow:		
Mean Orbital Velocity	4.74 km sec^{-1}	
Mean Motion	0.0039181 deg/day	
Perihelion Distance	4.425×10^9 km	29.5 AU
Aphelion Distance	7.375×10^9 km	49.2 AU
Orbital Period	247.687 years	
Additional Ephemerides are References 11-7 through 11-9.		

Pluto's approximate positions for the next 40 years are shown in Table 11-2 [11-10].

TABLE 11-2. POSITIONS OF PLUTO (1990 to 2030) [11-10] (By permission.)

Year	Distance from Sun (AU)	Right Ascension (deg)	Declination (deg)
1990	29.58	227.03	1.37
1995	29.72	238.51	6.30
2000	30.12	249.98	10.89
2005	30.78	261.39	14.92
2010	31.64	272.61	18.20
2015	32.67	283.53	20.69
2020	33.81	294.02	22.37
2025	35.04	304.00	23.32
2030	36.31	313.37	23.63

Although Pluto passes inside the orbit of Neptune, it never approaches closer than about 18 AU [11-11], so there is no likelihood of collision. The orbit is stable; mutual gravitational effects of the three outermost planets have recently been studied in detail, both numerically and analytically [11-12 through 11-17], and resonances have been noted both with Neptune and Uranus. Precise positions have recently been charted [11-18, 11-19]. (It was in the course of this investigation that Charon was discovered.)

The perturbations that were the original impetus for the search for a planet father out from the Sun than Neptune have proved to be largely erroneous – the result of imperfect knowledge of Neptune's orbit. In any case, Pluto is so small that it could not have been responsible. Recent and more precise orbit determinations for Neptune and Uranus have revealed unexplained perturbations, and although Pluto is definitely not responsible, at the present time it is unclear what the source might be. The hypothesis of yet another undiscovered planet does not seem to match the observations, and the question remains open at the time of this writing. (The actual perturbations caused by Pluto have been investigated [11-12].)

11.3 PHYSICAL DATA

11.3.1 Mass, Figure, and Other Physical Properties

Table 11-3 summarizes Pluto's physical data.

The discovery of Pluto's satellite Charon has led to the first reliable estimate of the planet's mass. The current value continues the downward trend in mass values derived since the planet's discovery [11-27]. (See Reference 11-25 for an amusing commentary.) Many of the values of phsyical constants are speculative at best, since they rely on estimates of other quantities that are presently uncertain. Table 11-4 shows the dependence of estimated physical parameters for Pluto and Charon on the albedo adopted [11-28].

TABLE 11-3. PHYSICAL DATA

Parameter	Value	Comments
Radius	1600 ± 300 km	Less than one-third of the Earth
Mass	1.4 to 2.0 × 10^{22} kg	[11-21, 11-23 through 11-25]
Mean Density	0.55 to 1.75	Earth = 5.52 [11-22]
Geometric Albedo	0.25 to 0.50	
Apparent Visual Magnitude	15.3	[11-21]
Surface Temperature	∿ 50°K	[11-26]
Surface Atmospheric Pressure	<50 mbar	[11-26]

TABLE 11-4. PHYSICAL PARAMETERS OF PLUTO AND CHARON [11-28]

Pluto Diameter (km)	Charon Diameter (km)	Density (g cm^{-3})	Albedo (2 μm)
2600	1200	$1.3^{+1.0}_{-0.7}$	0.55 ± 0.2
3000	1350	$0.8^{+0.6}_{-0.3}$	0.40 ± 0.15
3600	1650	$0.5^{+0.3}_{-0.2}$	0.25 ± 0.1
4000	1800	$0.35^{+0.2}_{-0.1}$	0.20 ± 0.1

11.4 INTERIOR

The new estimates for mass and radius of Pluto indicate that the planet has a very low specific gravity, less than unity, suggesting that Pluto and presumably Charon are made up of frozen volatiles [11-20]. The pair have been described as "snowballs," unlike the rocky terrestrial planets. Lupo and Lewis [11-22, 11-24] have attempted a model for the planet based on a composition of methane, rock, and water-ice. Figure 11-1 shows their results. The model suggests a relatively thin methane layer (<5 percent) over a silicate rock (20 percent) and water-ice interior. At the present stage of knowledge, this modeling is highly speculative.

11.5 SURFACE

Pluto is at the limit of resolution by ground-based telescopes. It will be an interesting object for study by the Space Telescope from near-Earth orbit. Earth-based spectrophometry in the near infrared shows strong absorption at 1.7 μ, perhaps caused by methane gas over methane frost, though discrepancies exist between the planetary absorption feature and laboratory spectroscopic studies.

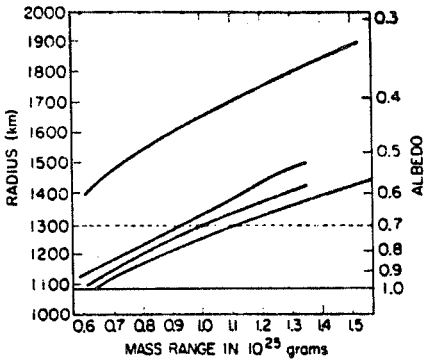

Top to Bottom: 100% methane; 49% water, 27% rock, 24% methane; 97% water, 3% methane; and 65% water, 32% rock, 3% methane. The albedo-radius relationship is plotted on the vertical axes.

Figure 11-1. Mass-radius curves for four compositions. [11-22]

At optical wavelengths the reflectance of Pluto increases from 3600 to 8600 Å, resembling some asteroids [11-29]. A speculative interpretation is that the planet's surface has outcrops of rocky materials in addition to methane frost [11-30].

Conflicting evidence exists on the roughness of the surface. Speckle interferometric studies [11-20] indicate limb darkening and a central enhancement that could be due to the surface acting like a semi-specular reflector. A frost surface, on the other hand, would be expected to be grainy, and polarimetric studies imply microscopic roughness [11-29].

11.6 ATMOSPHERE

Since Pluto is both very small and very cold, there are few possibilities for noncondensable atmospheric gases. A possible candidate is neon [11-31]; a gas which unfortunately is not accessible by Earth-based spectroscopy. An upper limit can be set for any atmosphere of about 50-mb surface pressure, based upon the lack of an observable ultraviolet "upturn" in scattered radiation [11-26]. The actual surface pressure is probably much smaller.

A finite vapor pressure of methane must always exist above the frost layer and because of the large difference between perihelion and aphelion distances, this vapor pressure must vary by at least two orders of magnitude during a planetary year. If there is a stable atmosphere at all, other heavier gases are needed, and some (thin) atmosphere is implied to account for the presence of methane (which would otherwise be expected to have totally evaporated during the lifetime of the planet).

11.7 SATELLITE

Although the reality of Pluto's satellite Charon is not unequivocally established at the present time, the confirming evidence is strong. Based on recent astronomical observations, Table 11-5 shows inferred parameters of Charon.

TABLE 11-5. PHYSICAL PARAMETERS OF CHARON

Parameter	Value	Comments
Semi-Major Axis	19,700 ± 300 km	[11-32]
Angular Separation from Pluto (July 8.17, 1978)	0.84 ± 0.03 arcsec	[11-33]
Period	6.3871 ± 0.0002 days	[11-32]
Inclination to the Eliptic (May 7.8, 1978)	115 ± 5 deg	[11-23]
Inclination to Pluto's Orbit (May 7.8, 1978)	120 ± 5 deg	[11-23]
Inclination to the Equator	94 ± 3 deg	Celestial Equator and Equinox of 1950 [11-32]
Node on Equator	221 ± 3 deg	[11-32]
Nodal Position Angle (May 7.8, 1978)	170 ± 5 deg	[11-23]
True Anomaly (January 31, 1982)	75 ± 8 deg	[11-32]
Radius	600 to 1000 km	[11-21,11-23, 11-28]
Mass	$\sim 1.3 \times 10^{21}$ kg ± 10 percent	0.09 Pluto [11-23]
Apparent Visual Magnitude	16.9	
Magnitude Difference from Pluto	1.7 ± 0.1	[11-33]

Prior to the discovery of Charon, a periodicity of 6.387 days had been noted in the photometric light-curve of Pluto [11-34], which was believed to be due to the rotation of the planet, together with surface albedo features. Although now thought to be partially due to the movement of Charon in its orbit, surface features may also contribute, provided the satellite's orbital period is synchronous with the rotation period of the planet.

Pluto and Charon appear to form a "double-planet" system with the mass of Charon nearly one-tenth that of Pluto. (For comparison, this ratio for the Moon-Earth system is near one-eightieth.)

11.8 IONOSPHERE AND MAGNETOSPHERE

No information yet exists about any possible ionosphere or about the interaction between Pluto and the solar plasma. It is very unlikely that Pluto possesses an intrinsic magnetic field, since its low density implies lack of a conducting core.

11.9 ORIGIN

For some time it has been thought possible that Pluto is an escaped satellite of Neptune [11-35]. Recent studies indicate that this suggestion is still viable, though obviously speculative [11-36, 11-37].

11.10 SPACE IN THE VICINITY OF PLUTO

The mean solar flux at 30 AU amounts to less than 1.5 W m^{-2}. No direct information exists as yet on solar plasma at these great distances (review Section 9.10 of Uranus for some estimates).

REFERENCES

11-1. Hoyt, W. G.: Planets X and Pluto. University of Arizona Press, Tucson, Arizona, 1980.

11-2. Whyte, A. J.: The Planet Pluto. Pergamon Press, 1980.

11-3. Icarus, Special Pluto Issue, vol. 44, No. 1, October 1980.

11-4. Christy, J. W. and Harrington, R. S.: The Satellite of Pluto. Astronom. J., vol. 83, 1978, pp. 1005-1008.

11-5. Marsden, B. G.: Planets and Satellites Galore. Icarus, vol. 44, No. 1, October 1980, pp. 29-37.

11-6. Seidelmann, P. K., Kaplan, G. H., Pulkkiner, K. F., Santoro, E. J., and Van Flandern, T. C.: Ephemeris of Pluto. Icarus, vol. 44, 1980, pp. 19-28.

11-7. Cohen, C. J., Hubbard, E. C., and Oesterwinter, C.: Elements of the Outer Planets for One Million Years. Astronomical Papers of the American Ephemeris, vol. 22, part 1, 1972.

11-8. Kaplan, G. H., Seidelmann, P. K., and Smith, E.: Astrometric Ephemeris of Pluto 1970-1990. U.S. Naval Observatory Circular No. 139, 1972.

11-9. Duncombe, R. L., Klepczynski, W. J., and Seidelmann, P. K.: Astronautics and Aeronautics. August issue, 1972, pp. 63-65.

11-10. Jaffe, L. D. and Ivie, C. V.: Science Aspects of a Mission Beyond the Planets. Icarus, vol. 39, 1979, pp. 486-494.

11-11. Cohen, C. J. and Hubbard, E. C.: Liberation of the Close Approaches of Pluto to Neptune. Astronom. J., vol. 70, 1965, pp. 10-13.

11-12. Pireaux, J.: Representations des Perturbations des Grosses Planetes dues a la Presence de Pluton. (In French), Astronomy and Astrophysics, vol. 79, 1979, pp. 132-137.

11-13. Nacozy, P. E.: A Review of the Motion of Pluto. Celest. Mech., vol. 22, 1980, pp. 19-23.

11-14. Williams, J. G. and Benson, G. S.: Resonances in the Neptune-Pluto System. Astronom. J., vol. 76, 1971, pp. 167-177.

11-15. Nacozy, P. E. and Diehl, R. E.: On the Long-Term Motion of Pluto. Celest. Mech., vol. 8, 1974, pp. 445-454.

11-16. Nacozy, P. E. and Diehl, R. E.: A Discussion of the Solution for the Motion of Pluto. Celest. Mech., vol. 17, 1978, pp. 405-421.

11-17. Nacozy, P. E., and Diehl, R. E.: A Semianalytical Theory for the Long-Term Motion of Pluto. Astronom. J., vol. 83, 1978, pp. 522-530.

11-18. Barbieri, C., Benacchio, L., Capaccioli, M., Pinto, G., and Schoenmaker, A. A.: Accurate Positions of the Planet Pluto from 1974 to 1978. Astronom. J., vol. 84, 1979, pp. 1890-1893.

11-19. Zappala, V., DeSanctis, G., and Ferreri, W.: Astrometric Positions of Pluto from 1973 to 1979. Astronomy and Astrophysics Supplement Series, vol. 41, 1980, pp. 29-31.

11-20. Arnold, S. J., Boksenberg, A., and Sargent, W. L. W.: Measurement of the Diameter of Pluto by Speckle Interferometry. Astrophys. J. Lett., vol. 234, 1979, pp. L159-L163.

11-21. Bonneau, D., and Foy, R.: Interferometrie au 3.60m Resolution due Systeme Pluton-Charon. Astronomy and Astrophys., vol. 92, in French, 1980, pp. L1-L4.

11-22. Lupo, M. J. and Lewis, J. S.: Mass-Radius Relationships and Constraints on the Composition of Pluto. Icarus, vol. 42, 1980, pp. 29-34.

11-23. Christy, J. W. and Harrington, R. S.: The Discovery and Orbit of Charon. Icarus, Special Pluto Edition, vol. 44, No. 1, October 1980, pp. 38-40.

11-24. Lupo, M. J. and Lewis, J. S.: Mass-Radius Relationships and Constraints on the Composition of Pluto, II. Icarus, Special Pluto Edition, vol. 44, No. 1, October 1980, pp. 41-42.

11-25. Dessler, A. J. and Russell, C. T.: From the Ridiculous to the Sublime: The Pending Disappearance of Pluto. EOS, vol. 61, No. 44, 1980.

11-26. Fink, V., Smith, B. A., Benner, D. C., Johnson, J. R., and Reitsema, H. J.: Detection of a CH_4 Atmosphere on Pluto. Icarus, Special Pluto Edition, vol. 44, No. 1, October 1980, pp. 62-71.

11-27. Duncombe, R. L. and Seidelmann, P. K.: A History of the Determination of Pluto's Mass. Icarus, Special Pluto Edition, vol. 44, No. 1, October 1980, pp. 12-18.

11-28. Walker, A. R.: An Occultation by Charon. Month. Not. Roy. Astron. Soc., vol. 192, 1980, pp. 47P-50P.

11-29. Lane, W. A., Neff, J. S., and Fix, J. D.: A Measurement of the Relative Reflectance of Pluto at 0.86 Micron. Publications of the Astronomical Society of the Pacific, vol. 38, 1976, pp. 77-79.

11-30. Cruikshank, D. P., Pilcher, C. B., and Morrison, D.: Pluto: Evidence for Methane Frost. Science, vol. 194, 1976, pp. 835-837.

11-31. Hart, M. H.: A Possible Atmosphere for Pluto. Icarus, vol. 21, 1976, pp. 455-487.

11-32. Harrington, R. S. and Christy, J. W.: The Satellite of Pluto, III. Astronom. J., vol. 86, 1981, pp. 442-443.

11-33. Thomsen, B. and Ables, H. D.: Abstract in the Bull. Amer. Astron. Soc., vol. 10, 1978, p. 586.

11-34. Neff, J. S., Lane, W. A., and Fix, J. D.: An Investigation of the Rotational Period of the Planet Pluto. Publications of the Astronomical Society of the Pacific, vol. 86, 1974, pp. 225-230.

11-35. Harrington, R. S. and Van Flandern, T. C.: The Satellites of Neptune, and the Origin of Pluto. Icarus, vol. 39, 1979, pp. 131-136.

11-36. Dormand, J. R. and Woolfson, M. M.: The Origin of Pluto. Month. Not. Roy. Astron. Soc., vol. 193, 1980, pp. 171-174.

11-37. Farnella, P., Milani, A., Nobili, A. M., and Valsecchi, G. B.: Tidal Evolution and the Pluto-Charon System. In The Moon and the Planets, vol. 20, 1979, pp. 415-421. Also in Icarus, Special Pluto Edition, vol. 44, No. 1, October 1980, pp. 810-812.

SECTION 12. ASTEROIDS

12.1 INTRODUCTION

The asteroids, sometimes called "minor planets," are small rocky bodies that mainly orbit the Sun between Mars and Jupiter. The largest, Ceres, was the first to be discovered (by Piazzi in 1801). Since then over 2000 have been observed and catalogued. The main information source is the Tucson Revised Index of Asteroid Data (TRIAD) computer file which is maintained at the University of Arizona. A major conference on asteroids was held at the University of Arizona in March, 1979, and most of the information contained in this section was adapted from the collection of invited papers to that conference, edited by T. Gehrels [12-1]. Other recent reviews are References 12-2 through 12-5. For a discussion of the potential for human exploration and utilization of the asteroids, review Reference 12-6.

12.1 Asteroids As Objects of Study

Study of asteroid orbits by the methods of celestial mechanics has led to improved knowledge of astrodynamic constants. Another compelling reason for present research interest in asteroids arises from their relatively undisturbed history. They provide a potential window back in time to the early period of the origin and development of the Solar System. Detailed imaging studies from spacecraft and sample return will provide unique information. From the standpoint of human utilization, asteroids have been seriously suggested as natural space-stations, as sources for materials for the construction of large structures in space, and even as sources for strategic minerals for use on the Earth. Close flybys of asteroids will probably be a frequent event in the next few years of space exploration.

Future space missions will include docking operations and sample return to the Earth. The most accessible asteroids for sample return from a propulsion standpoint are the Earth-crossers, and of them the most favorable discovered to date is 1943 Anteros [12-7]. Launch opportunities for the most accessible objects, those with orbits similar to the Earth's orbit, might, on first consideration, be assumed to occur frequently. In fact, for any particular object, they are spaced many years apart, so such opportunities should not be allowed to pass unnoticed.

Table 12-1 lists data for the largest asteroids and others of particular interest.

12.2 ORBITS

By convention, asteroid orbits are divided into zones based upon semi-major axis, eccentricity, and inclination, some of which represent true dynamical families (viz. Eos and Koronis) (Table 12-2) [12-8].

The distribution of semi-major axes is shown in Figure 12-1. Gaps which correspond to orbital periods that are harmonics of Jupiter's period are called "Kirkwood gaps" after their discoverer [12-9].

TABLE 12-1. DYNAMIC PROPERTIES AND OTHER DATA FOR SELECTED ASTEROIDS

Number	Name	Year of Discovery	Approximate Diameter (km)	Opposition Magnitude	a	Orbital Period (year)	e	i	Type
1	Ceres	1801	102	7.79	2.767	4.6	0.0802	10.60	C
2	Pallas	1802	583	8.46	2.773	4.61	0.2394	34.82	U
3	Juno	1804	249	9.0	2.671	4.36	0.2574	13.02	S
4	Vesta	1807	555	6.5	2.361	3.63	0.0889	7.14	U
5	Astraea	1845	116	11.3	2.577	4.13	0.1862	5.33	S
6	Hebe	1847	206	9.5	2.424	3.77	0.2019	11.65	S
7	Iris	1847	222	9.2	2.386	3.69	0.2309	5.47	S
8	Flora	1847	160	9.7	2.201	3.27	0.1567	5.88	S
9	Metis	1848	168	10.0	2.387	3.69	0.1233	5.60	S
12	Victoria	1850	135	10.8	2.334	3.57	0.2190	8.38	S
15	Eunomia	1851	261	9.5	2.642	4.30	0.1870	11.76	S
18	Melpomene	1852	164	9.8	2.296	3.48	0.2176	10.15	S
20	Massalia	8152	140	10.2	2.409	3.74	0.1426	0.68	S
192	Nausikaa	1879	99	11.0	2.403	3.72	0.2445	6.87	S
324	Bamberga	1892	256	11.3	2.685	4.39	0.3346	11.30	C
387	Aquitania	1894	113	10.7	2.74	4.53	0.2383	17.97	S
433	Eros	1898	20	7.2	1.458	1.76	0.2230	10.83	S

TABLE 12-1. (Concluded)

Number	Name	Year of Discovery	Approximate Diameter (km)	Opposition Magnitude	a	Orbital Period (year)	e	i	Type
588	Achilles[a]	1906	70	16.3	5.174	11.77	0.149	10.334	U
944	Hidalgo	1920	28.6	18.8	5.86	14.18	0.656	42.4	
1036	Ganymede	1924	39.8	13.6	2.666	4.34	0.536	26.4	S
1221	Amor[b]	1932		20.5	1.972	2.77	0.436	11.9	
1566	Icarus[b]	1949	1.9	12.2	1.078	1.12	0.826	22.94	U
1620	Geographos[b]	1951	2.2	14.2	1.244	1.387	0.335	13.33	S
1685	Toro[b]	1948	4.7	13.6	1.367	1.598	0.435	9.37	S
1862	Apollo[b]	1932		16.1	1.469	1.78	0.559	6.36	
2060	Chiron	1977		17.2	13.695	50.68	0.378	6.925	
2062	Aten[b]	1976	1.1	10.1	0.966	0.95	0.237	17.9	S
2101	Adonis[b]	1936		20.5	1.873	2.56	0.764	1.37	
	Hermes[b]	1937		18.0	1.639	2.10	0.622	5.62	

a. Trojan

b. Earth-crosser

Note: Elements taken from different Tables often differ considerably. These are from Reference 12-11.

TABLE 12-2. ORBITAL ELEMENT ZONES [12-9] (By permission.)

Zone	Description	Criteria			Number in TRIAD[b]
A	Apollo-Amor		$q = a(1-e) \leq 1.65$		55
HU	Hungarias	$1.82 \leq a \leq 2.00$	$e \leq 0.15$	$i \geq 16°$	17
PH	Phocaeas	$2.25 \leq a < 2.50$	$e \leq 0.35$	$i \geq 17°$	42
FL	Floras	$2.06 \leq a \leq 2.295$	$0.08 \leq e \leq 0.20$	$i \leq 10°$	201
NY	Nysa family	$a = 2.43$	$e = 0.17$	$i = 3°$	13
I	Main-belt I	$2.06 \leq a \leq 2.50$	$e \leq 0.35$	$i \leq 30°$	283
II	Main-belt II	$2.50 < a \leq 2.82$	$e \leq 0.35$	$i \leq 30°$	578
Eos	Eos family	$a = 3.01$	$e = 0.17$	$i = 10°$	86
Ko	Koronis family	$a = 2.85$	$e = 0.05$	$i = 2°$	50
Th	Themis family	$a = 3.13$	$e = 0.15$	$i = 1°$	83
III	Main-belt III	$2.82 < a \leq 3.27$	$e \leq 0.35$	$i \leq 30°$	557
IV	Main-belt IV	$3.27 < a \leq 3.65$	$e \leq 0.35$	$i \leq 30°$	46
HI	Hildas	$3.80 \leq a \leq 4.20$	$e \leq 0.35$	$i \leq 30°$	28
T	Trojans	$5.06 \leq a \leq 5.30$	– No test –	–	21
Z	Exceptional	– None of the above –			18

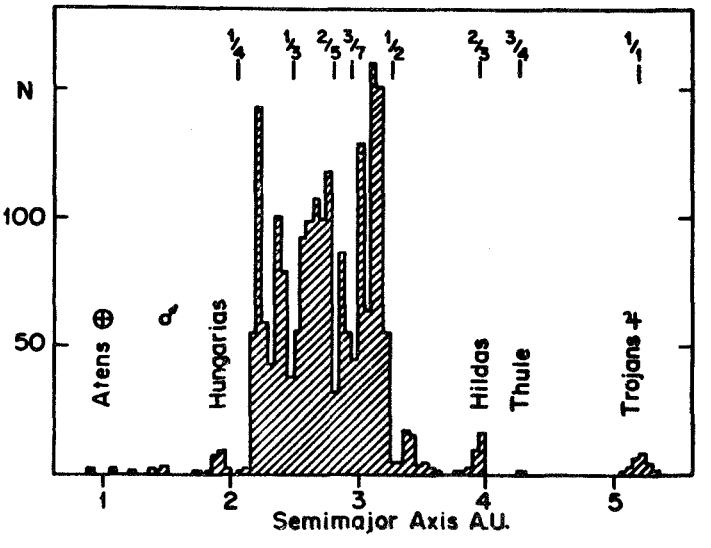

Figure 12-1. The helocentric distribution of minor planets in increments of 0.05 AU. The positions of some of the important asteroid groups are indicated. Fractions indicate ratio of orbital periods for the principal dynamical resonances with Jupiter [12-8]. (By permission.)

12.2.1 Earth-Crossers

The Earth-crossers are of particular interest since they would be easiest to visit and either return with samples or exploit for mining and other purposes. Known examples are shown in Table 12-3.

TABLE 12-3. EARTH-CROSSERS (Adapted from [12-10])

Class	TRIAD Number	Name	a	e	i	Diameter (km)	Part/ Cont.
Aten	--	1976 UA	0.844	0.424	6.27	(0.2)	C
	2100	Ra-Shalom	0.832	0.465	13.1	3.4	C
	2062	Aten	0.966	0.237	17.9	0.9	C
Apollo	--	1978 SB	2.164	0.888	10.5	(10.4)	C
	1566	Icarus	1.078	0.828	20.2	1.4	C
	--	1974 MA	1.757	--	--	--	P
	2101	Adonis	1.873	0.732	1.96	--	C
	1864	Daedalus	1.461	0.640	15.9	3.3	C
	1865	Cerberus	1.080	0.513	14.9	--	C
	--	Hermes	1.639	0.622	5.62	--	C
	1981	Midas	1.776	--	--	--	P
	1862	Apollo	1.470	0.505	6.14	--	C
	2063	Bacchus	1.077	0.320	8.78	--	C
	--	1959 LM	(1.34)[i]	(0.379)[i]	(3.3)	--	?
	1685	Toro	1.368	0.438	9.15	6.0	C
	2135	1977 HA	1.600	(0.490)	(23.3)	--	P
	--	6743 P-L	1.620	0.476	6.81	--	C
	1620	Geographos	1.245	0.351	14.2	2.0	C
	--	1976 WA	2.407	--	--	--	P
	--	1950 DA	1.683	0.535	10.7	--	C
	1866	Sisyphus	--	--	--	--	P
	--	1973 NA	2.447	--	--	--	P
	--	1978 CA	1.125	0.278	25.3	1.9	C
	1863	Antinous	--	--	--	--	P

TABLE 12-3. (Concluded)

Class	TRIAD Number	Name	a	e	i	Diameter (km)	Part/ Cont.
	2102	Tantalus	1.290	--	--	--	P
	--	6344 P-L	--	--	--	--	P
Amor	--	1978 DA	--	--	--	0.9	P
	2061	Anza	--	--	--	(9.5)	P
	1915	Quetzalcoatl	(2.49)	(0.60)	(19.7)	--	P
	1917	Cuyo	--	--	--	--	P
	1943	Anteros	--	--	--	--	P
	1221	Amor	--	--	--	--	P
	1580	Betulia	2.196	--	--	6.4	P
	--	1972 RA	--	--	--	--	P
	1627	Ivar	--	--	--	(7.0)	P
	887	Alinda	--	--	--	4.1	P

The Earth-crossers are divided into three classes: Aten, Apollo, and Amor according to the following scheme [12-10].

Name	Number Known	Criterion
Aten	3	a <1 AU and orbit overlaps Earth orbit at aphelion.
Apollo	23	a $\geqslant 1$ AU and orbit overlaps Earth orbit at perihelion.
Amor	10	Perihelion between 1.017 AU (Earth aphelion) and an arbitrary cut-off between 1 and 2 AU. (Review Reference 12-10.)

A question of interest: "How probable is a collision between an Earth-crosser and the Earth?" Collision rates are estimated at about one collision to absolute magnitude 18 (diameter around 1 km) per 300,000 years. On the average, the colliders will be from the classes Aten, Apollo, and Amor in the proportions 2:4:1 [12-10].

12.2.2 Mars-Crossers

The Mars-crossers are also a class of particular interest to the space mission planner, and known members are shown in Table 12-4.

TABLE 12-4. MARS-CROSSERS (Adapted from References 12-11 through 12-13].)

TRIAD Number	Name	A	E	I	Albedo	Diam	(AU) ToMars	ToJup
228	Agathe	2.201	0.241	2.543			0.049	2.382
313	Chaldaea	2.376	0.181	11.620	.033	122.0	0.039	2.078
391	Ingeborg	2.321	0.307	23.124		17.5	0.039	1.984
433	Eros	1.458	0.223	10.828	.180	22.0	0.439	3.095
475	Occllo	2.595	0.380	18.800			0.102	1.630
512	Taurinensis	2.189	0.254	8.759		23.9	0.145	2.320
574	Reginhild	2.252	0.239	5.691		8.7	0.118	2.226
699	Hela	2.613	0.408	15.304			0.072	1.623
719	Albert	2.584	0.540	10.821			0.561	1.208
730	Athanasia	2.244	0.177	4.228			0.053	2.297
749	Malzovia	2.243	0.174	5.386		12.6	0.014	2.337
753	Tiflis	2.329	0.220	10.114		24.9	0.015	2.182
865	Zubaida	2.416	0.197	13.310			0.050	1.992
870	Manto	2.322	0.265	6.198			0.032	2.170
898	Hildegard	2.725	0.374	10.199			0.079	1.352
985	Rosina	2.300	0.277	4.070			0.058	2.197
1009	Sirene	2.628	0.454	15.752			0.418	1.269
1011	Laddamia	2.394	0.350	5.469	.222	7.4	0.356	1.709
1034	Mozartia	2.292	0.263	3.994			0.044	2.223
1036	Ganymed	2.666	0.536	26.415		39.8	0.445	1.210
1037	Davidweilla	2.181	0.181	5.380			0.023	2.454
1065	Amundsenia	2.361	0.297	8.366			0.085	2.061
1078	Mentha	2.270	0.139	7.371			0.004	2.307
1088	Mitaka	2.201	0.196	7.650		19.4	0.024	2.414
1104	Syringa	2.631	0.343	6.438			0.077	1.524
1110	Jaroslawa	2.218	0.241	5.855			0.038	2.368
1126	Otero	2.272	0.147	6.505			0.020	2.286
1131	Porzia	2.229	0.286	3.236			0.126	2.253
1134	Kepler	2.685	0.466	15.030			0.323	1.245
1139	Atami	1.947	0.255	13.099			0.221	2.502
1147	Stavropolis	2.270	0.232	3.880			0.040	2.262
1195	Orangia	2.257	0.201	7.178			0.055	2.274
1198	Atlantis	2.249	0.335	2.724			0.222	2.123

TABLE 12-4. (Concluded)

TRIAD Number	Name	A	E	I	Albedo	Diam	(AU) ToMars	ToJup
1204	Renzia	2.263	0.294	1.887			0.127	2.190
1221	Amor	1.921	0.436	11.913			0.697	2.095
1250	Galanthus	2.555	0.268	15.115			0.166	1.647
1293	Sonja	2.227	0.275	5.358			0.097	2.293
1316	Kasan	2.410	0.321	23.835			0.036	1.858
1355	Magoeba	1.853	0.045	22.825			0.003	2.930
1374	Isora	2.250	0.279	5.307			0.108	2.239
1386	Storeria	2.364	0.288	11.790			0.051	2.089
1429	Pemba	2.548	0.342	7.704			0.050	1.712
1468	Zomba	2.195	0.271	9.956			0.151	2.301
1480	Aunus	2.202	0.110	4.871			0.015	2.415
1492	Oppolzer	2.173	0.117	6.052			0.063	2.422
1513	1940EB	2.193	0.099	3.973			0.013	2.435
1543	Bourgeois	2.628	0.325	11.170			0.002	1.610
1563	Noel	2.192	0.085	5.988			0.002	2.453
1593	Fagnes	2.225	0.281	9.977			0.151	2.245
1620	Geographos	1.245	0.335	13.327		2.2	0.309	3.243
1627	Ivar	1.864	0.397	8.430		7.0	0.674	2.213
1629	Pecker	2.239	0.154	9.705			0.039	2.328
1640	1951QA	2.289	0.343	7.113			0.234	2.048
1648	Shajna	2.237	0.206	4.557			0.036	2.328
1653	Yakhontovia	2.611	0.322	4.078			0.002	1.631
1656	Suomi	1.877	0.124	25.066		9.4	0.015	2.871
1664	1929CD	2.339	0.223	6.121			0.110	2.062
1676	1939LC	2.236	0.186	6.146			0.014	2.355
1706	Dieckvoss	2.126	0.115	1.872			0.008	2.564
1710	1941UF	2.323	0.267	8.459			0.032	2.183
1715	1938GK	2.398	0.241	11.514			0.045	2.029
1717	1954AC	2.196	0.129	6.187		11.8	0.084	2.366
1718	1942RX	2.366	0.276	7.673			0.010	2.125
1727	1965BA	1.854	0.102	22.895		7.1	0.010	2.905
1747	Wright	1.709	0.110	21.412			0.222	2.988
1750	Eckert	1.927	0.173	19.075		5.8	0.033	2.756

12.2.3 Other Orbits

Beyond the main asteroid belt are the Trojan asteroids, that cluster near two of the Lagrangian points of three-body stability of the Sun-Jupiter system (the points in space preceding and following Jupiter in orbit, equidistant from the Sun and Jupiter). Their number is estimated at around a thousand [12-14].

Certain asteroids move in exceptional orbits. Chiron is the farthest-out minor planet discovered so far, with perihelion far beyond the orbit of Jupiter (a = 13.7 AU) [12-15]. (Chiron is known to be a highly perturbed "chaotic" orbit that will eventually lead either to collision with a planet or hyperbolic ejection from the Solar System.) While most asteroids orbit the Sun with relatively small orbital inclinations, there are some exceptions. Notable is Pallas, with i = 34.8 deg.

12.3 MASS, DENSITY, AND DYNAMICAL PROPERTIES

The masses of the asteroids range from the largest, Ceres, whose mass is of the order 10^{21} kg down. The mass of the entire asteroid belt is estimated to be of the order 3×10^{21} kg (about one-twentieth the mass of the Moon).

Diameters (largest) [12-16]		Densities [12-17]
1 Ceres	987 ± 150 km	2.3 ± 1.1
2 Pallas	538 ± 50 km	2.6 ± 0.9
4 Vesta	544 ± 80 km	3.3 ± 1.5

Pole orientations have been published for around 15 asteroids based upon ground-based photometry [12-18]. Rotation periods of several hundred asteroids have been determined. There is a tendency for smaller objects to spin faster. (Typical periods are in the range 5 to 20 hr [12-19].) Several cases have been documented of possible satellites of asteroids, based on stellar occulation data [12-20].

12.4 ASTEROID CLASSES (SPECTRUM, ALBEDO, AND INFERRED MINEROLOGY)

Most asteroids can be put into one of two broad categories: the C type, akin to the carbonaceous chondride meteorites, and the S type, possibly akin to the stony-iron meteorites.

Table 12-5, from Zellner [12-9], describes the scheme used in the TRIAD file, which adds classes M, E, R, and U (a catch-all for objects otherwise unclassified).

Within the main asteroid belt, the estimated percentage population of class C asteroids rises from 47 percent in Zone I to 96 percent in Zone IV; while the percentage of class S declines from 43 percent in Zone I to none in Zone IV. Only a few E and R objects are known; some 10 percent are classified "U" [12-13]. IN Figure 12-2, the lower albedo peak is for C asteroids, the higher is for S.

TABLE 12-5. DESCRIPTION OF THE ASTEROID TYPES [12-9] (By permission.)

Type	Albedo	Spectrum	Mineralogy	Meteoritic Analogues[a]
C	low	relatively flat, weak features	silicates plus opaques (carbon)	carbonaceous chondrites
S	moderate	reddish Fe^{2+} absorptions	silicates plus metal	stony irons (H chondrites?)
M	moderate	slightly reddish, featureless	metal, or metal plus neutral silicates	nickel-irons enstatite chondrites
E	high	flat featureless	neutral silicates	enstatite achondrites
R	moderate to high	red, strong features	Fe^{2+} silicates	various or unknown (ordinary chondrites?)
U	various	unusual	various	various or unknown (certain achondrites)

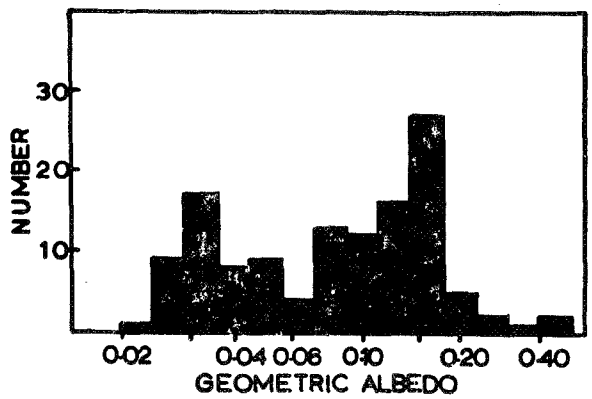

Figure 12-2. Histogram of measured asteroid albedos [12-21]. (By permission.)

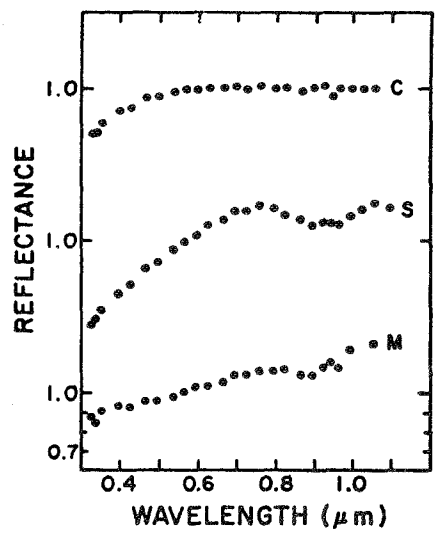

Figure 12-3. Average reflectance spectra in the visible for S, C, and M asteroids [12-22]. (By permission.)

12.5 ORIGIN [12-23]

The origin of the asteroids and, indeed, the general question of the origin and early development of the entire Solar System are research topics of great interest. The earliest idea about the asteroids was that they are remnants of the explosion of the "missing planet" between Mars and Jupiter. More recently, the tendency has been to favor theories that assert that the asteroids accreted in the same way as larger planets, then suffered many subsequent collisions among themselves, along with large orbital perturbations from close approaches with massive bodies catapulted through the asteroid belt by Jupiter. Such gravitational stirring could explain the peculiar features of some orbits, such as the large inclination of Pallas. However, the concept of a large planet that exploded into fragments has not been ruled out. The issue remains one of lively debate. It has been suggested that some of the dark asteroids with perihelia within the Mars orbit may be extinct cometary nuclei.

REFERENCES

12-1. Gehrels, T. (ed.): Asteroids. University of Arizona Press, Tucson, 1979, p. 1181.

12-2. Zellner, B. (ed.): Icarus, vol. 40, No. 3, 1979.

12-3. Chapman, C. R., Williams, J. G., and Hartmann, W. K.: The Asteroids. Ann. Rev. Astron. Astrophys., vol. 16, 1978, pp. 33-75.

12-4. Gaffey, M. J. and McCord, T. B.: Asteroid Surface Materials: Mineralogical Characterizations from Reflectance Spectra. Space Sci. Rev., vol. 21, 1978, pp. 555-628.

12-5. Delsemme, A. H. (ed.): Comets, Asteroids, Meteorites – Interrelations, Evolution and Origins. University of Toledo Press, 1977, p. 587.

12-6. Morrison, D. and Wells, W. C.: Asteroids: An Exploration Assessment. NASA Conf. Publication 2053, 1978.

(NOTE: References 12-7 through 12-23 are taken from Reference 12-1 above.)

12-7. Morrison, D. and Niehoff, J.: Future Exploration of the Asteroids, pp. 227-250.

12-8. Gradie, J. E., Chapman, C. R., and Williams, J. G.: Families of Minor Planets, pp. 359-390.

12-9. Zellner, B.: Asteroid Taxonomy and the Distribution of the Compositional Types, pp. 783-806.

12-10. Shoemaker, E. M., Williams, J. G., Helin, E. F., and Wolfe, R. F.: Earth-Crossing Asteroids: Orbital Classes, Collision Rates With Earth and Origin, pp. 253-282.

12-11. Bender, D. F.: Osculating Orbital Elements of the Asteroids, Table p. 1014 ff.

12-12. Bowell, E., Gehrels, T., and Zellner, B.: Magnitudes, Colors, Types and Adopted Diameters of the Asteroids, pp. 1108-1129.

12-13. Williams, J. G.: Proper Elements and Family Memberships of the Asteroids, Table, 1040 ff.

12-14. Gehrels, T.: The Asteroids: History, Surveys, Techniques and Future Work, pp. 3-24.

12-15. Kowal, C. T.: Chiron, pp. 436-439.

12-16. Millis, R. L. and Elliott, J. L.: Direct Determination of Asteroid Diameters From Occultation Observations, pp. 98-118.

12-17. Schubart, J. and Matson, D. L.: Masses and Densities of Asteroids, pp. 84-97.

12-18. Taylor, R. C.: Pole Orientations of Asteroids, pp. 480-493.

12-19. Burns, J. A. and Tedesco, E. F.: Asteroid Lightcurves: Results for Rotations and Shapes, pp. 494-527.

12-20. VanFlandern, T. C., Tedesco, E. F., and Binzel, R. P.: Satellites of Asteroids, pp. 443-465.

12-21. Morrison, D. and Lebofsky, L.: Radiometry of Asteroids, pp. 184-205.

12-22. Chapman, C. R. and Gaffey, M. J.: Reflectance Spectra for 277 Asteroids, pp. 655-687.

12-23. Chapman, C. R.: The Asteroids: Nature, Interrelations, Origin and Evolution, pp. 25-60.

SECTION 13. COMETS

13.1 INTRODUCTION

Comets are the most distinctive and peculiar members of the Solar System family. They have always been regarded with awe since, unlike the planets and stars, they appear unexpectedly, and then disappear after what is sometimes an impressive display. It is conceivable that the Star of Bethlehem was a comet. It is known from present day orbit calculations that Halley's Comet appeared in the sky in 11 BC Most scholars believe that this date is too early to be correct for the birth of Christ. It is interesting, however, that Giotto di Bondone (1267-1337), who probably witnessed the appearance of Halley's Comet in 1301, chose to depict the Star as a comet in his fresco "The Adoration of the Magi" in the Arena Chapel of Padua, which was completed in 1304. Halley's Comet, the brightest of the periodic comets, also figured in history in 1066. Its appearance that year coincided with the campaigns of William the Conqueror and a comet appears in the Bayeux Tapestry that chronicles those events. Reference 13-1 presents an interesting and lively account of comets through history.

Comets move around the Sun in elliptical orbits that often are nearly parabolic. Though a few are "trapped" within the Solar System on smaller periodic orbits, most come from enormous distances with aphelia near 5×10^4 AU. At the present time, about 100 short-period comets have been discovered (period less than 200 years), together with about 600 long-period comets. Reference 13-2 quotes the present rate of discovery as about four long-periods and one short-period per year. Comets are often first seen at a distance from the Sun of 3 to 4 AU. They are usually discovered either by astronomers studying the sky for some other reason or by amateur enthusiasts. Although the comet nucleus is small, typically 1 or 2 km in radius, volatiles produce an enormous gas cloud around the nucleus, the coma, and a tail develops in the anti-solar direction which can be as much as 1 AU in length. (The word "comet" means "long hair.") Actually, most comets have two tails, one which extends straight outwards from the Sun, the ion tail; the other which is shorter and curved, the dust tail. The coma and ion tail are self-luminous, with radiation from excited atomic and molecular species; the dust tail shines with scattered sunlight.

A comet is most spectacular when close to the Sun, and brighter comets have perihelia within the orbits of the inner planets. Comets that are visible from Earth are believed to be only a tiny fraction of those that remain at great distances from the Solar System or are on orbits whose perihelia are outside the orbit of Jupiter and never become active.

Close study of comets, along with asteroids and other small bodies in the Solar System, will reveal important information on the early stages of the development of the solar nebula into the Solar System.

Comet Kohoutek (1973 XII), a "new comet," was subjected to intensive study from the ground and from space platforms. It was observed by the astronauts on SKYLAB. This coordinated program contributed enormously to scientific understanding of cometary physics. The possibilities for exploration of comets by space vehicles have been considered by NASA committees, as discussed briefly in paragraph 13.10. Many of the theories of cometary physics currently accepted are based upon indirect evidence, and a mission to study a comet at close range seems essential.

13.1.1 Comet Naming

Except for P/Encke and P/Halley, and a few "great comets," comets are named for their discoverer(s) with a maximum of three names. Appearances are identified in tables as "1972 II" or "1974 g." A comet so designated might be new or might be a periodic comet that was previously known: 1835 II and 1910 II were both appearances of Halley's Comet. (Periodic comets are designated "P.")

13.2 ORBITS

All comets originate far from the Solar System in Oort's Cloud, which is believed to extend out to the boundary of the influence of the Sun's gravitational attraction; a sphere of radius about 50,000 AU [13-3, 13-4]. Oort postulated that the Cloud must contain some 10^{11} comets, by arguments based upon rate of appearance. (The total mass of all comets is estimated to be roughly equal to the Earth's mass [13-4].) Once a comet approaches the Solar System, it is subject to perturbations by the major planets, particularly Jupiter. A possible outcome, particularly if its initial perihelion is near Jupiter's orbit, is that it will gradually lose orbital energy through interactions with Jupiter on many orbital passages and eventually will achieve a quasi-stable orbit within the Solar System [13-5]. (It is dynamically possible for a comet initially on a near-parabolic orbit to achieve a periodic orbit within the Solar System through one fortuitous encounter with Jupiter, but numerical experimentation has shown that this is extremely unlikely and is definitely not the explanation for the periodic comets observed [13-4].)

Even on a periodic orbit within the Solar System, a comet must be regarded as a brief visitor. Most orbits are unstable and end up with hyperbolic ejection from the Solar System. Everhart's computer simulation of comet orbits [13-5] revealed a $N^{-1/2}$ law of survival: out of 500 comets that reach the Solar System on near-parabolic orbits, after N=100 returns, only about 50 remain. Those that do survive may eventually reach quasi-stable or stable orbits within the Solar System. But even in a stable orbit, eventually all volatiles will be used up and the comet will "die."

Comet orbital periods are divided into two classes: long, greater than 200 years, and short, less than 200 years. This division corresponds roughly to a semi-major axis the size of the Solar System (34 AU, compared to Pluto, with semi-major axis of 39.8 AU). Those with long periods are randomly distributed in orbital plane inclination, while those with short periods mostly move in orbital planes fairly near the plane of the ecliptic. (Comet Halley, with retrograde motion, is an exception.) This difference lends credence to the idea that those within the Solar System have been strongly perturbed by interactions with Jupiter.

Nearly 700 cometary orbits have been studied and the elements determined; 102 are periodic and 67 have been observed two or more times [13-6]. P/Encke was first seen in 1886 and has appeared every 3.3 years since. It has the shortest period of any known comet. P/Halley was noted by the Chinese in 86 BC and has been seen 27 times; last in 1910. Its next appearance will be in 1985 to 1986.

13.2.1 Dynamic Properties

The dynamic properties of the known periodic comets have been determined with high precision (Table 13-1). The Keplerian osculating elements change with time caused by planetary perturbations. But other changes are also known to occur, under the influence of nongravitational forces, which will be discussed in a later paragraph.

TABLE 13-1. DYNAMIC PROPERTIES FOR SELECTED COMETS [13-6]

Name	Time of Recent Perihelion	Period (year)	q (AU)	Q (AU)	e	Arg. of Perihelion	Node	i	No. of Appearances
Encke	1974.32	3.30	0.338	4.09	0.847	185.9	334.2	12.0	51
Grigg-Skjellerup	1972.17	5.12	1.001	4.94	0.663	359.3	212.7	21.0	13
Tempel-2	1972.87	5.26	1.364	4.68	0.549	190.9	119.3	12.5	16
Giacobini-Zinner	1972.59	6.52	0.994	5.98	0.715	171.9	195.1	31.7	10
Borelly	1974.36	6.76	1.316	5.84	0.632	352.7	75.1	30.2	10
Halley	1910.30	76.09	0.587	35.33	0.967	111.7	57.8	162.2	27
Tempel-Tuttle	1965.33	32.91	0.982	19.56	0.904	174.6	234.4	162.7	4
Swift-Tuttle	1862.64	119.98	0.963	47.69	0.960	152.8	138.7	113.6	1
Bennett (1970 II)	Mar 20.0446 1970		0.537		0.99619	354.15	223.96	90.04	1
Kohoutek (1973 XII)	Dec 28.4307 1973		0.142425		1.0000	37.82	257.76	14.30	1

Orbital speed at 1 AU: nearly the same for all comets.

Encke — 37.050 m/sec

Halley — 41.531 m/sec

Parabolic Orbit — 42,112 m/sec

New comets, those on extremely large orbits, may appear at any time. Examples are Comet Bennett of 1970 and Comet Kohoutek of 1973. Since their computed orbital periods are extremely long, even if such comets survive their swing around the Sun, they effectively leave for good. Short period comets return every few years or decades, unless they are ejected from the Solar System (as happened to Comet Lexel in 1770), or unless they break up. P/Biela, discovered in 1772, split into two components in 1846 on its tenth return and disappeared.

The largest recorded perihelion distance (q) is 6.02 AU for Comet 1974 g. There is no reason to believe that there are not great numbers of comets with larger perihelia that cannot be observed because they never become active. The smallest recorded q is for Comet 1887 I, which was sun-grazing: q = 0.0048 AU [13-6].

Osculating eccentricities of 1.0 (parabolic) or slightly greater (hyperbolic) have been computed for 283 comets. Everhart and Raghavan carried out an extensive study of the interaction of comets having near-parabolic orbits with the planets in the Solar System [13-7].

The orbital speed of all comets is about the same at the same distance from the Sun, since

$$v = 29{,}785\ (2/r - 1/a)^{1/2}\ \text{m/sec}$$

with r and a measured in AU, and a is large.

13.3 COMET MORPHOLOGY

What is seen when a comet appears is a very large envelope of luminous gas, the coma, which surrounds the central core nucleus and the long antisolar tail. In the ultravilet the coma is much larger, since surrounding it is a huge overlaying corona of neutral hydrogen (Fig. 13-1).

Comets have two types of tails called "Type I" and "Type II." Type I is straight and extends radially outwards from the Sun as far as 10^8 km. Type II is shorter (up to 10^7 km) and curved in the opposite direction to the orbital movement of the comet. It is now known that Type I tails are composed of ionized gas molecules and Type II dust particles (Figs. 13-2 and 13-3).

13.4 NONGRAVITATIONAL FORCES

Encke first noticed in 1819 that the period of P/Encke deviated from the prediction of Newtonian theory. Its period shortened about 2.5 hr with each perihelion passage.

A satisfactory explanation only came in 1950 when Whipple [13-10] proposed his "dirty snowball" model for the cometary nucleus. His explanation for the observed orbital deceleration of P/Encke is that the cometary nucleus is rotating in such a direction that evaporating material on the sunlit side is ejected slightly in the forward direction. As a consequence, the orbital motion of the body is retarded, causing the orbital period to decrease [Fig. 13-4). (Rotation in the opposite direction would lead to an acceleration and an increase in orbital period.) For a full discussion, review Reference 13-11. In his review article of 1978 [13-4], Whipple lists acceleration parameters for 37 comets (which include Tempel-2 and Halley). He notes that 13 periodic comets are known for which there is no measurable deviation from Newtonian motion.

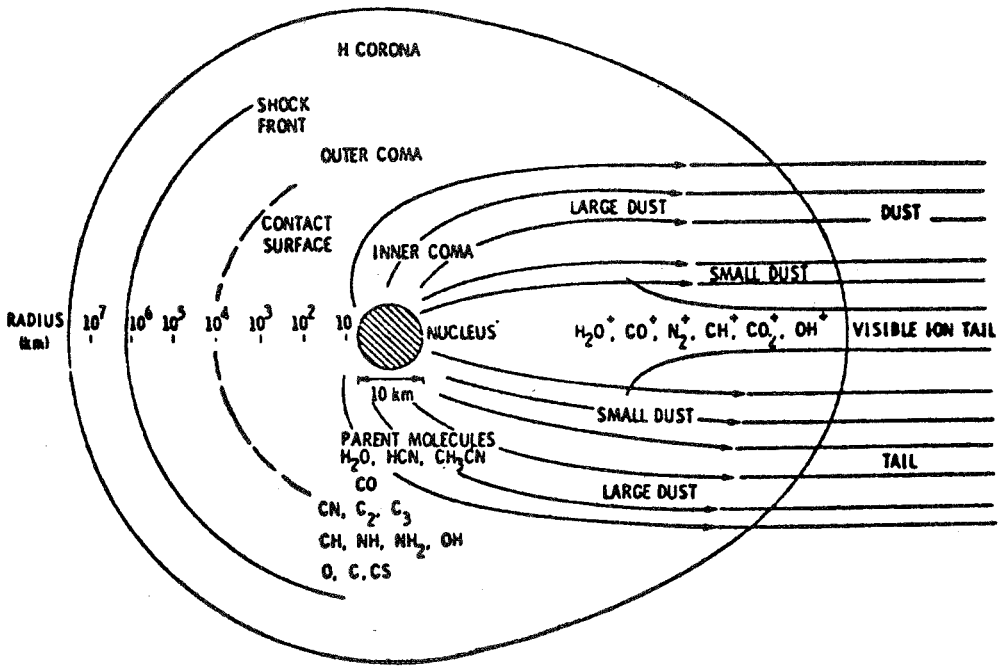

Figure 13-1. Sketch of principal features of a comet on a logarithmic scale [13-8].

13.5 THE NUCLEUS

Two models have been proposed for the cometary nucleus:

a) That it is a swarm of ice-coated dust grains, held together by self-gravitation [13-12] (Lyttleton's "sandbank" model);

b) That it is a fragile solid structure, a conglomerate of ice (predominantly water-ice), with dust grains embedded in it [13-10] (Whipple's "dirty snow-ball" model).

Comets frequently survive grazing encounters with the Sun which subject them to strong tidal forces, which favors Whipple's solid nucleus model. Moreover, the solid nucleus model has been successful in explaining the observed nongravitational forces experienced by many periodic comets. The recent radar detection of the nucleus of Comet Encke [13-13] adds confirmation that the comet nucleus is a solid structure [13-14].

Estimates of both the cohesive and tensile strength of the comet nucleus, based on estimates of the gravitational compressive force and the tidal force at Sun-grazing distance, suggest a value of about 10^5 dyne/cm^2 [13-14].

There is great variability among comets [13-15]. The surface of the nucleus is known to be nonuniform, since vaporization rates are observed to vary with time. Nonuniformities are probably the result of the collection of nonvolatile dust from the nucleus itself and collection of meteoroidal material as the comet passes through the Solar System (particularly true for old periodic comets) [13-4]. The dust layer then acts to inhibit volatilization and shields volatiles from solar radiation. Models are discussed in Reference 13-16. Released dust goes into the coma and ultimately into the dust tail and into interplanetary space.

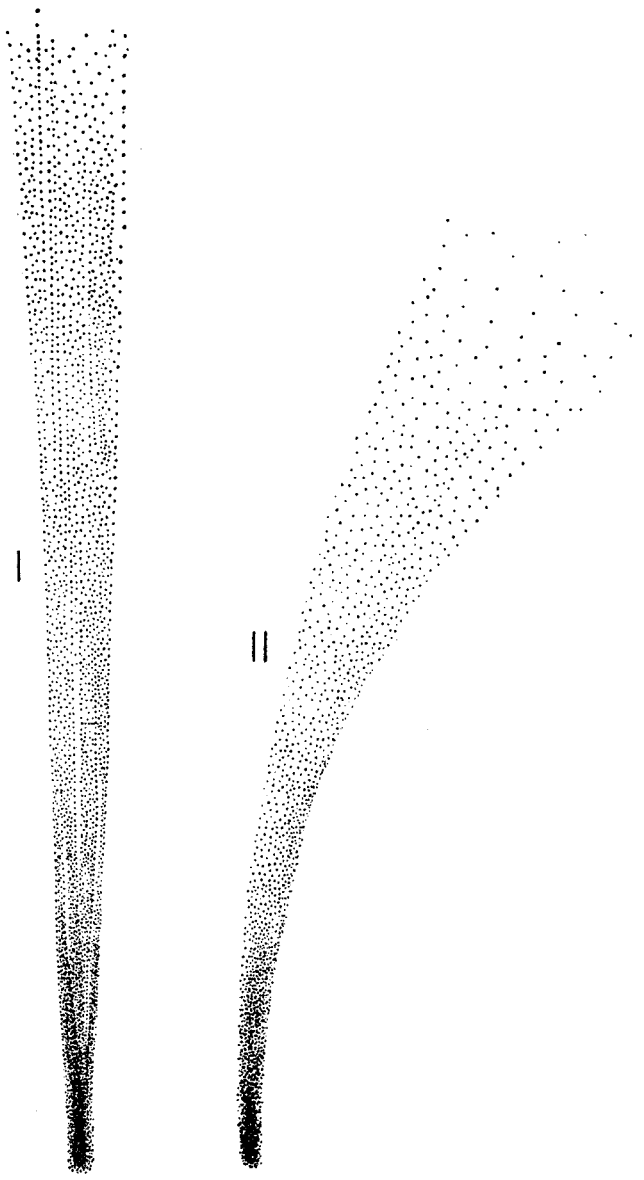

Figure 13-2. Types of comet tail are depicted in these schematic drawings. Type I tails are long and straight; Type II tails are curved [13-9].

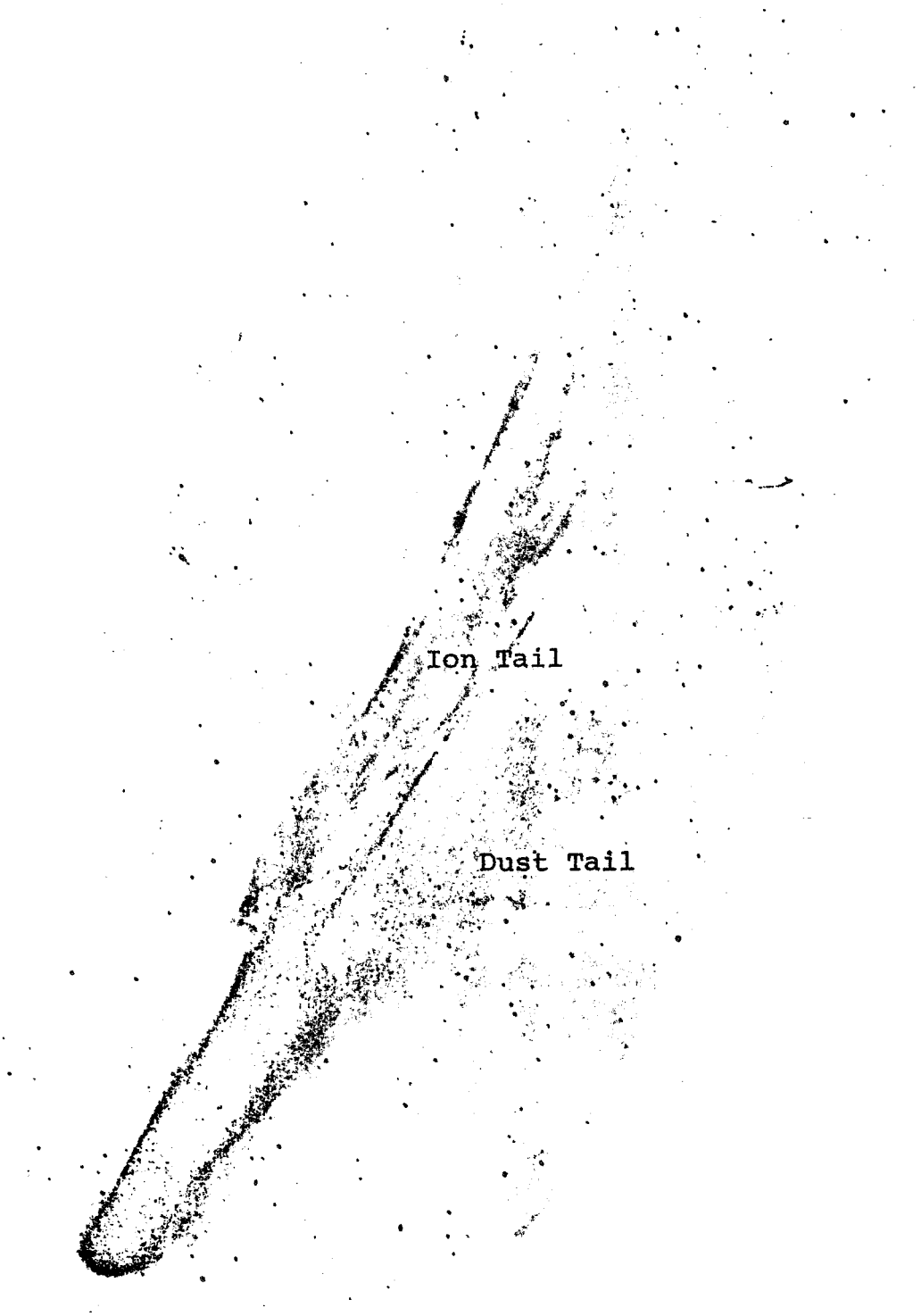

Figure 13-3. Comet Mrkos was photographed on August 23, 1957, with the 48-in. Schmidt telescope on Palomar Mountain. In this negative print the light areas are dark and vice versa [13-9].

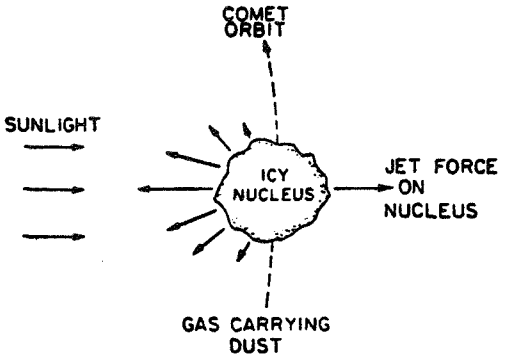

a) Nonrotating nucleus

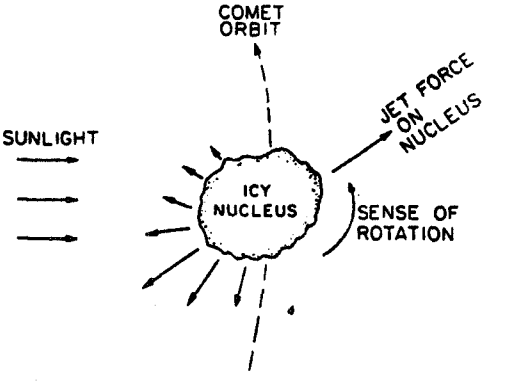

b) Rotating nucleus

Figure 13-4. Jet force on icy comet nucleus by sublimating ices: (a) nonrotating nucleus; force away from Sun: (b) rotating nucleus; lag produces force component normal to comet-Sun line [13-4].

13.5.1 Size

There has been one successful observation of a radar echo from a comet: P/Encke in 1980 by the Arecibo radio telescope [13-13], leading to the radius of 2 ± 1 km for an assumed albedo of 0.15. Present estimates are that cometary nuclei are 1 to 10 km in radius [13-14].

13.5.1 Mass

No direct mass determination has been made, since no perturbations of another body during close encounters has been noted. For an assumed mean density of 1.3 g cm^{-3} and a radius of 2 km, the mass would be about 4×10^6 g. Cometary masses are probably in the range of 10^{15} to 10^{20} g.

13.5.3 Mass Loads

Mass loss per perihelion passage obviously depends upon perihelion distance. An estimate for P/Encke is 0.1 percent per perihelion passage [13-17].

13.5.4 Escape Velocity

Considering the range of estimated radii and masses, escape velocities from the surface of the comet nucleus will be in the approximate range 30 to 200 cm/sec.

13.5.5 Rotation

As discussed in paragraph 13.4, rotation of the nucleus is the best explanation for the small non-gravitational forces which have been often noted (Fig. 13-4). The photographic images of many comets exhibit a series of concentric halos, and with assumptions concerning the velocity of ejected gas, rotation rates have been computed for about 50 periodic comets. Axis orientations have been deduced for about seven [13-14]. Whipple [13-18] reports a median rotation period of about 15 hr. The directions of rotation and axis orientation appear to be random. In the case of P/Encke, a further refinement has been necessary to explain the observed decrease in the nongravitational decelleration over the past 200 years. This effect has been explained [13-19] by assuming that the comet nucleus is ellipsoidal and that the axis of rotation precesses in direction referred to the celestial sphere.

13.5.6 Composition

H_2O ice is believed to be the principal volatile material in comet nuclei. Evidence comes not only from the observed spectra of the coma, but also by noting that most comets first appear at 3 to 4 AU distance from the Sun. This is the distance where the vapor pressure of water-ice would first become appreciable under solar heating (Fig. 13-5) [13-20]. However, new arrivals sometimes first appear much farther out. (Comet Kohoutek was discovered at a distance of 4.9 AU.) Hence more volatile molecules must be present, perhaps trapped in the H_2O ice as hydrates or clathrates [13-4].

Spectroscopic evidence for water-ice includes observations of neutral hydrogen (Lyman α), OH, and H_2O^+. As the comet approaches the Sun, temperatures get high enough in individual dust grains, so the spectroscopic lines of more refractory elements appear. The ion-tail shows emission spectra of various molecular species.

13.6 COMA

The coma is the luminous head of the comet, the expanding envelope of gas and dust around the nucleus that develops as the comet approaches the Sun and solar radiation volatilizes material from the sunlit side of the nucleus. It is composed of gas molecules, ions, and dust grains (Fig. 13-1). Within the coma, complex interactions take place between the solar wind and solar radiation and atoms, molecules, and dust particles emitted from the nucleus. The schematic diagram is shown in Figure 13-6.

13.6.1 Coma: Characteristic Distances and Other Parameters

At 1 AU, gas production rates for bright comets are of the order 10^{29} mol/sec. Gas expansion velocities are of the order of 1 km/sec. Dust-to-gas ratios are 0.1 to 1 (by mass) [13-14]. Collisional mean free path equals photodissociation scale-length typically at about 10^4 km [13-15]. Visible coma extends out to 10^5 km. Bow shock interaction between cometary ions and solar wind is at 10^5 to 10^6 km on sunward side.

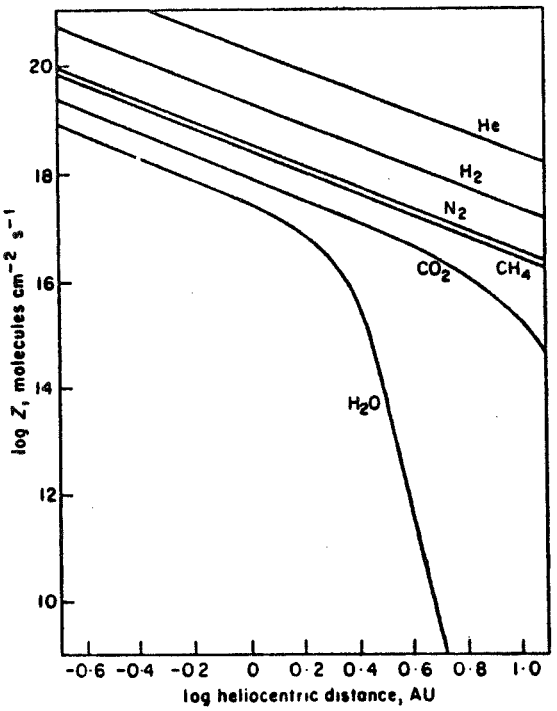

Figure 13-5. Vaporization rate Z, of various snows as a function of solar distance [13-4].

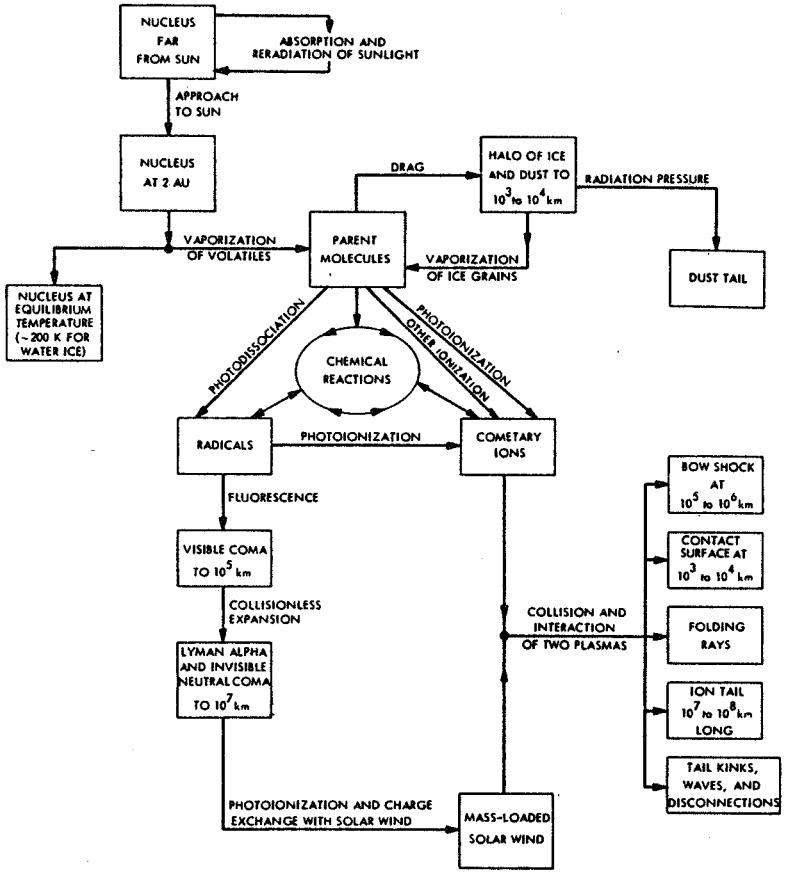

Figure 13-6. Features and processes involved in a comet's interaction with sunlight and the solar wind [13-21].

13.6.2 Composition and Spectroscopic

Table 13-2 lists the atomic and molecular species that have been observed in comet heads in emission. It must be emphasized that individual comets vary considerably.

TABLE 13-2. OBSERVED COMPOSITION OF COMETS (COMA) [13-4]

H, C, C_2, C_3, CH, CN, $^{12}C^{13}C$, HCN, CH_3CN, NH, NH_2,
O, OH, H_2O, Na, K, Ca, V, Cr, Mn, Fe, Co, Ni, Cu

13.6.3 Hydrogen Corona

Surrounding the visible coma and extending out to a great distance is an envelope of hydrogen, first discovered by rocket observations of Lyman α radiation at 1216 Å in 1970. Figure 13-7 shows Lyman α isophotes for Comet Kohoutek.

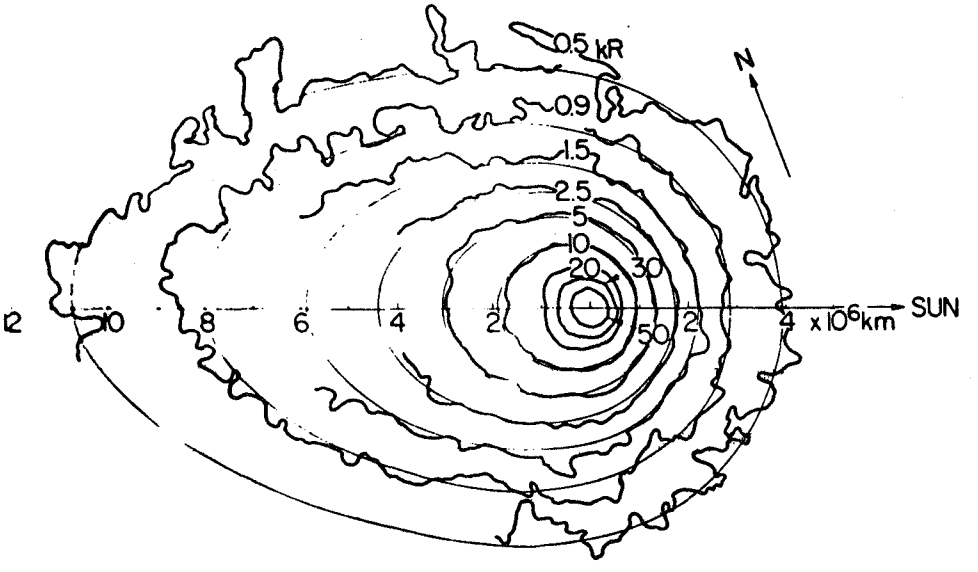

Figure 13-7. Isodensity tracings of a 15-sec Lyman α image of Comet Kohoutek (1973 XII) taken by an electrographic camera on January 8, 1974 (r = 0.43 AU). The light curves represent model isophotes [13-22].

13.7 DUST

Many comets show the characteristic curved dust tails. The luminosity of the dust tail comes from scattered sunlight. When dust is released from the surface of the comet on the sunward side, it is first carried radially outward from the nucleus by the flow of gases. Eventually it is pushed by solar radiation pressure toward the anti-solar direction. Away from the nucleus dust grains move in orbits under the combined forces of solar radiation pressure and gravity and so spread into a curved tail which may lag the comet-Sun line by as much as 60 deg [13-14].

When released into the coma, the dust particles are initially accelerated by drag forces due to the expanding gas to velocities of the order 1 km/sec, which is in excess of escape velocity from the comet nucleus (paragraph 13.5.4). Dust grains are then entrained up to distances of 10 to 100 km where they decouple from the expanding gas envelope and the ions. (Apparently there is some initial interaction between dust near the nucleus and the forming ion tail.) After decoupling, the dust is influenced by solar radiation pressure and solar gravity.

Some comets have strongly dominant dust tails, others have predominantly ion tails. No reason is known at present for such differences.

Sometimes a so-called anti-tail is observed. This is a spike that looks as if it extends in the sunward direction. The cause of this phenomenon is that a sharply curved dust tail is observed edge-on and the geometry causes it to appear to extend in the sunward direction due to projection effects. Such sharply curved dust tails are further evidence for the existence of relatively large particles (greater than 30 μm) which leave the coma at relatively low velocity.

13.7.1 Quantitative Estimates of Cometary Dust Parameters

Spectra: Weak infrared emission features of 10 and 18 μ have been observed from some dust tails. These are attributed to silicates.

Length: Some dust tails are as much as 10^7 km long [13-4].

Particle Size: Dust particles are believed to be in the 0.1 to 1-μm size range, with near 1 μm dominating [13-14]. There is evidence for larger particles; 30 μm or more, at least in some comets.

Velocity of emission from nucleus: estimated about 1 km/sec.

Dust production rate at 1 AU: 4×10^6 g/sec long-period comets; 2×10^4 g/sec P/Encke [13-23].

13.8 ION TAILS

The mechanism by which ion tails are "pushed" in the anti-solar direction was a mystery until the hypothesis of an outflow of solar plasma (the solar wind). The existence of the solar wind was inferred from a study of comet tails [13-24] years before its direct measurement by space probes. Ion tails exhibit a great variety of forms and complexities described as kinks, waves, knots, rays, etc. All of these phemonena must be due to complex interactions between solar wind with its trapped magnetic field and ionized gases from the comet, though detailed explanations have so far not been very successful [13-14]. In particular, no correlation between solar activity and ion tail morphology has yet been established [13-14].

Observed motions of material (or possibly hydromagnetic waves) in ion tails have velocities in the range 20 to 250 km sec^{-1}.

The spectra of light from comet tails is dominated by CO^+ (which accounts for the blue color: 3800 to 4800 A) and H_2O^+ (5600 to 7000A). The exact mechanism of ionization is not certain [13-14], though it presumably results from photoionization by solar UV and interactions with the solar

wind plasma. Excitation is through resonance fluorescence [13-15]. Species observed spectroscopically: CH^-, CO^-, CO_2^+, N_2^+, OH^+, H_2O^+, and CA^+.

13.9 WHAT EVENTUALLY HAPPENS TO A COMET?

As already remarked, comets are transients in the Solar System. The chance of any particular "new" comet being captured in a short-period orbit within the Solar System is very small. Most simply return to Oort's Cloud, presumably to loop back eons later, or are ejected in hyperbolic orbits.

Other fates include falling into the Sun, an event actually observed by chance by a spacecraft-borne solar coronagraph on August 31, 1979 [13-26], and breaking up as the result of tidal forces or for unknown reasons (presumably because of out-bursts of gas) [13-4]. When volatiles are eventually exhausted, or the comet nucleus is totally covered with nonvolatile material, the comet becomes inactive. Then some experts believe it becomes a dark asteroid, such as those of the Apollo group, or it may disintegrate into meteoroids. Scenarios are uncertain [13-27]. However, periodic comets are known to be associated with meteor streams. Some examples are:

Perseids with P/Swift-Tuttle

Taurids with P/Encke

October Draconids with P/Giacobini-Zinner

Leonids with P/Tempel-Tuttle

Also, several meteor streams are associated with P/Halley. Review Paragraph 14.4 of the section on Interplanetary Dust.

13.10 PROSPECTS FOR SPACE PROBE EXPLORATION OF COMETS

Many aspects of cometary physics will be put on a firm footing only when a comet is visited by a space probe and measurements are made in situ. Early missions will, of necessity, be ballistic encounters. Eventually, missions using ion propulsion or solar sail propulsion will give much greater flexibility. Measurements will be performed both by remote sensing techniques from a distance of around 10^5 km and by probes to within 100 to 1500 km of the nucleus and closer if the dust hazard permits. Analyses of proposed missions to P/Encke, P/Tempel-2, and P/Halley appear in References 13-8 and 13-28. P/Encke, because of its short-period orbit, presents fairly frequent launch opportunities, while P/Halley with a period fo 76 years is a once-in-a-lifetime proposition. (For the ESA plans for the 1985 to 1986 Giotto Mission to P/Halley, review Reference 13-29.)

REFERENCES

13-1. Calder, N.: The Comet is Coming! The Viking Press, New York, NY, 1980.

13-2. Mendis, A. and Alfven, H.: On the Origin of Comets. The Study of Comets, Part 1, Proc., IAU Colloquium No. 25, Goddard Space Flight Center, NASA SP-393, 1974, pp. 638-657.

13-3. Oort, J. H.: The Structure of the Cloud of Comets Surrounding the Solar System and a Hypothesis Concerning Its Origin. Bull. Astr. Neth. V., vol. 408, 1950, pp. 91-110.

13-4. Whipple, F. L.: Comets. Cosmic Dust, J.A.M. McDonnell (ed), Wiley, New York, 1978, pp. 1-73.

13-5. Everhart, E.: The Evolution of Comet Orbits. The Study of Comets, Part 1, Proc. IAU Colloquium No. 25, Goddard Space Flight Center, NASA SP-393, 1974, pp. 445-460.

13-6. Marsden, B. G.: Catalogue of Cometary Orbits. Second Edition, IAU, Smithsonian Astrophysical Observatory, Cambridge, Mass., 1975.

13-7. Everhart, E. and Raghavan, N.: Changes in Total Energy for 392 Long-Period Comets, 1800-1970. Astronom. J., vol. 75, 1970, pp. 258-272.

13-8. NASA/Jet Propulsion Laboratory: A Strategy for the Space Exploration of Comets. Report of the Comet Science Working Group, NASA/JPL, July 1978.

13-9. Biermann, L. F. and Lust, R.: The Tails of Comets. Comets, Reprints from Scientific American, J. D. Brant (ed), W. H. Freeman and Co., San Francisco, 1981, pp. 39-45.

13-10. Whipple, F. L.: A Comet Model, I. The Acceleration of Comet Encke. Astrophys. J., vol. 111, 1950, pp. 375-394.

13-11. Marsden, B. G., Sekanina, Z., and Yeomans, D. K.: Comets and Nongravitational Forces V. Astronom. J., vol. 78, 1973, pp. 211-225.

13-12. Lyttleton, R. A.: The Comets and Their Origin. Cambridge University Press, 1953.

13-13. Kamoun, P. G., Campbell, D. B., Ostro, S. J., Pettengill, G. H., and Shapiro, I. I.: Comet Encke: Radar Detection of Nucleus. Science, vol. 216, 1982, pp. 293-295.

13-14. Wykoff, S.: Overview of Comet Observations. To appear in Comets, L. L. Wilkening (ed.), University of Arizona Press (in press 1982). NOTE: The editor is greatly indebted to Dr. Wykoff for making a preprint available.

13-15. Whipple, F. L. and Huebner, W. F.: Physical Processes in Comets. Ann. Rev. Astron. Astrophys., vol. 14, 1976, pp. 143-172.

13-16. Brin, G. D.: Three Models of Dust Layers on Cometary Nuclei. Astrophys. J., vol. 237, 1980, pp. 1-15.

13-17. Whipple, F. L. and Sekanina, Z.: Comet Encke: Precessrion of the Spin Axis, Nongravitational Motion, and Sublimation. Astronom. J., vol. 84, 1979, pp. 1894-1909.

13-18. Whipple, F. L.: Rotation of Comet Nuclei. In Comets: Gases, Ices, Grains, and Plasma, IAU Colloquium No. 61, L. L. Wilkening (ed.), 1981.

13-19. Whipple, F. L.: The Spin of Comets. Comets, Reprints from Scientific American, J. D. Brant (ed.), W. H. Freeman and Co., San Francisco, 1981, pp. 56-63.

13-20. Delsemme, A. H. and Miller, D. C.: Physico-Chemical Phenomena in Comets-III. Plan. Sp. Sci., vol. 19, 1971, pp. 1229-1257.

13-21. Brant, J. D. (ed.): Comets, Reprints from Scientific American. W. H. Freeman and Co., San Francisco, 1981.

13-22. Keller, H. U.: The Interpretations of Ultraviolet Observations of Comets. Space Sci. Rev., vol. 18, 1976, pp. 641-684.

13-23. Ney, E. P.: Optical and Infrared Observations of Bright Comets. Comets: Gases, Ices, Grains, and Plasmas, IAU Colloquim No. 61, L. L. Wilkening (ed.), 1981.

13-24. Michels, D. J., Sheeley, N. R., Jr., Howard, R. A., and Koomen, M. J.: Observations of a Comet on Collision Course with the Sun. Science, vol. 215, 1982, pp. 1097-1102.

13-25. Arpigny, C.: Spectra of Comets and Their Interpretation. Ann. Rev. Astr. Astrophys., vol. 3, 1965, pp. 351-376.

13-26. Discover, vol. 2, No. 2, December 1981, p. 26. (Note at end of ref.)

13-27. Hughes, D. W.: Can Comets become Asteroids? Nature, vol. 286, 1980, pp. 10-11.

13-28. Farquhar, R. W.: Mission Strategy for Cometary Exploration in the 1980's. The Study of Comets, Part 1, Proc. IAU Colloquium No. 25, Goddard Space Flight Center, NASA SP-393, 1974, pp. 1033-1057.

13-29. Battrick, B. and Mort, J.: Scientific and Experimental Aspects of the Giotto Mission. European Space Agency, SP-169, 1981.

SECTION 14. INTERPLANETARY DUST

14.1 INTRODUCTION

This section reviews present knowledge of the interplanetary dust (IPD) environment of the Solar System. IPD means all solid bodies ranging in diameter from sub-micron to tens of centimeters (masses from less than 10^{-17} g to approximately 10 kg). The total mass of the PID cloud is only 10^{19} to 10^{20} g (10^{-14} of the total mass of the solar system). The flux close to the Earth is approximately 10^{-13} to 10^{-12} g $m^{-2}sec^{-1}$.

In recent years there have been a number of useful collections of papers and books on the IPD [14-1 through 14-5]. There is also useful information in Reference 14-6. The recent review paper by Millman [14-7] makes an excellent introduction.

14.2 DYNAMIC PROPERTIES OF THE IPD CLOUD

Table 14-1 shows the dynamic properties of the IPD cloud.

TABLE 14-1. DYNAMIC PROPERTIES

Total Mass	10^{19} to 10^{20} g		10^{-9} Earth Mass
Flux near 1 AU	$(0.5 \text{ to } 1) \times 10^{-12}$ g m^{-2} sec^{-1} $(2\pi \text{ sterad})^{-1}$		
Spatial Mass Density	$> 4 \times 10^{-23}$ g cm^{-3} $< 1.5 \times 10^{-22}$ g cm^{-3}		[14-5]
	Population 1	Population 2	
Mass	$> 10^{-7}$ g	$< 10^{-6}$ g	See text; division into two populations is still speculative.
Diameter	> 2 μm	< 2 μm	
Density	2 to 3 g cm^{-3}	Up to 8 g cm^{-3}	
Composition	Silicates	Iron + Silicates	
Velocity	Near 10 km sec^{-1}	Near 50 km sec^{-1}	
Orbits	Low Eccentricity	Hyperbolic	
Albedo	~ 0.24		Inferred [14-8]
	< 0.1		From collected samples [14-5]

14.3 RESEARCH TECHNIQUES FOR STUDYING THE INTERPLANETARY DUST

In the following paragraphs the basic methods by which the parameters of the IPD can be investigated are outlined. References 14-1 through 14-8 give additional details of the techniques.

14.3.1 Zodiacal Light

The Zodiacal Light is the cone of light that extends along the ecliptic for a few tens of degrees just before sunrise and just after sunset. It is caused by sunlight scattered by the IPD. The distribution of the Zodiacal Light in the sky indicates that the IPD is restricted to a discoid distribution close to the plane of the ecliptic.

The major scatterers are particles in the range 5 to 100 μm. Smaller particles, with diameters less than the wavelength of visible light, are inefficient Mie scatterers. Larger particles have a much smaller spatial density and do not contribute appreciably to the Zodiacal Light. Particles within these size limits are often referred to as the "Zodiacal Cloud" [14-9] and form a distinct component of the interplanetary dust cloud. Although it is often assumed that the Zodiacal Cloud is diagnostic of all the IPD, there are reasons to expect that smaller and larger particles may be distributed differently (paragraph 14.6).

There are two additional components of the sunlight scattered by the IPD. The first is the F Corona, the innermost part of the Zodiacal Light, resulting from the IPD closest to the line-of-sight to the Sun. From the ground under normal conditions solar radiation renders its observation impossible except during solar eclipses.

The second is the Gegenschein (counterflow) in the night sky, approximately 20 deg about the antisolar point. The Gegenschein is caused by backscatter of solar radiation by the IPD.

Observations of the Zodiacal Light are useful in studies of the IPD since a very large sample of particles contribute. The advent of spacecraft measurements has meant that observations can be made at any time of day, undisturbed by atmospheric scattering and airglow.

The visual brightness of the Zodiacal Light is normally expressed in units of S_{10}. One S_{10} is defined as equivalent to one-tenth visual magnitude Sun-type star per square degree. Thus one S_{10} = 1.261×10^{-9} erg cm^{-2} sec^{-1} sterad $^{-1}$ $Å^{-1}$ over the visible region. Values of S_{10} at specific wavelengths are given in Reference 14-9. In addition to the general references, a review of the Zodiacal Light is given in Reference 14-10.

14.3.2 IPD Entering the Atmosphere

Even though the majority of dust particles entering the Earth's atmosphere have very small mass, their velocities are high (12 to 72 km sec^{-1}), and they have sufficient kinetic energy to produce visible emission, along with ion trails which can be detected by radar. Visible meteors have mass greater than 10^{-2} g while radar meteors range down to 10^{-5} g and less [14-7]. Observation programs of a few months can sample thousands of meteors visually and tens of thousands by radar. Thus, statistically significant numbers of IPD particles are accessible, although there is an important sampling bias: only particles crossing the Earth's orbit are observed.

Both visible and radar observations give the space density of the IPD from count rates along with orbits of individual particles from the direction cosines. The presence of recurrent meteor showers at certain times of year implies that the majority of the observed IPD originated as cometary debris (paragraph 14.4).

14.3.3 Lunar Microcraters

Earth-crossing IPD produce the microcratering seen on the surfaces of lunar material returned by the Apollo program. The dimensions of these microcraters allow constraints to be put on the mass, density, and velocity of the impacting IPD. The trace element composition of the lunar soil is also modified by the incoming flux of IPD [14-7].

14.3.4 Terrestrial Sampling

Samples of the IPD, although in minute quantities, are also available on the Earth. Sources include the deep ocean beds and polar ice-caps where a gradual build-up has been occurring over geological time. Recent in-fall material can be sampled using high-flying aircraft [14-11 through 14-16].

14.3.5 Spacecraft Sampling

Micrometeoroid detectors on various spacecraft (e.g., Pioneers 8, 9, 10, and 11; Helios 1 and 2; and HEOS 2) have led to investigations of the IPD environment from inside the orbit of Mercury out to Saturn and beyond. Although sample numbers are small (hundreds of particles or less), the data have been particularly useful in confirming the extent of IPD and in studying the gravitational influence of the planets, especially Jupiter. The results are discussed in paragraph 14.6. The best data still are for the close-Earth environment.

14.4 ORIGIN OF THE IPD

The association of 15 to 20 meteor streams with known comets is evidence that at least part of the IPD is cometary debris. Until recently it was thought that additional contributions were due to the disintegration of asteroids and to the injection of dust from a cloud or reservoir at the outer limits of the solar system. However, it is now believed that the predominant source is material that results from the gradual decay of short- and long-period comets [14-17]. No meteor orbits have been observed that appear to originate outside the Solar System, and no association has been found between a meteor stream and any known asteroid.

It is now customary to assume that the entire IPD Cloud is of cometary origin. Estimates of the total mass of this cloud (10^{19} to 10^{20} g) [14-7] along with a mean lifetime for the particles (10^4 to 10^6 years) indicate that short-period comets cannot supply sufficient material to maintain the cloud, requiring a significant contribution from long-period comets. Estimates are of the order of 10^7 g sec^{-1} [14-18] or even 3×10^8 g sec^{-1} [14-19]. Several bright, long-period comets per century plus two or three outstanding new comets per thousand years appear to be necessary [14-7].

The orbits of meteoroids gradually decay due to the influence of the Poynting-Robertson effect, solar radiation pressure, and collisions. Therefore, the mean orbit for any meteor shower will differ somewhat from the parent comet, and the association is sometimes difficult to establish. Tables 14-2 and 14-3 are taken from Reference 14-8. Table 14-2 shows the accepted comet/shower and shower/shower associations. The parameters D_{SH} and D^1 used in attempts to establish an association are discussed in Reference 14-8. The other parameters in Table 14-2 are:

π The difference in perihelion longitudes of the shower and the shower/comet

θ The angle between the lines of apsides

I The difference in the inclinations of the shower and the shower/comet.

TABLE 14-2. COMET/SHOWER AND SHOWER/SHOWER ASSOCIATIONS [14-8]

	Π	Θ	I	D_{SH}	D'
Comet associations					
Daytime β Taurids/S. Taurids	9°.4	13°.6	9°.9	0.226	0.101
Daytime β Taurids/N. Taurids	0.0	3.3	4.7	0.085	0.041
S. Taurids/N. Taurids	9.1	11.4	7.6	0.196	0.069
Daytime β Taurids/Encke (1971 II)	2.7	4.8	10.1	0.181	0.061
S. Taurids/Encke (1971 II)	7.4	9.0	10.9	0.226	0.092
N. Taurids/Encke (1971 II)	2.4	2.5	12.8	0.227	0.078
η Aquarids/Orionids	1.1	1.2	4.1	0.074	0.026
η Aquarids/Halley (1835 III)	1.7	1.7	4.5	0.089	0.036
Orionids/Halley (1835 III)	0.6	0.8	8.4	0.148	0.049
Annual Andromedids/Andromedids[a]	2.6	3.2	4.2	0.107	0.050
Annual Andromedids/Biela (1972 predicted)[a]	2.2	3.4	4.7	0.094	0.036
Andromedids/Biela (1852 III)	1.5	1.5	0.4	0.022	0.007
April Lyrids/Thatcher (1861 I)	1.0	1.3	0.9	0.028	0.012
τ Herculids/Schwassmann-Wachmann 3(1930 VI)	6.9	7.1	2.3	0.106	0.049
June Bootids/Pons-Winnecke (1915 III)	5.9	5.9	0.6	0.089	0.035
o Draconids/Metcalf (1919 V)	1.7	5.6	6.8	0.161	0.069
Perseids/Swift-Tuttle (1862 III)	1.3	1.5	0.3	0.025	0.010
Aurigids/Kiess (1911 II)	11.3	11.4	2.0	0.231	0.102
October Draconids/Giacobini-Zinner (1946 V)	0	0	0	0	0
ϵ Geminids/Ikeya (1964 VIII)[b]	6.1	6.3	7.6	0.177	0.064
Leo Minorids/(1739)	0.5	0.8	0.7	0.029	0.019
December Phoenicids/Blanpain (1819 IV)[c]	3.7	3.8	5.5	0.145	0.063
Leonids/Tempel-Tuttle (1965 IV)	2.1	2.2	0.6	0.037	0.013
Monocerotids/Mellish (1917 I)[d]	5.4	10.7	9.3	0.194	0.171
Ursids/Tuttle (1939 X)	0.6	1.2	1.2	0.092	0.047
Meteor shower associations					
Daytime ζ Perseids/N. Piscids	7.0	7.5	3.0	0.126	0.089
N. χ Orionids/S. χ Orionids	1.0	8.9	9.0	0.158	0.064

[a] The second set of elements from Cook (1973) for the Annual Andromedids was used.
[b] A newly recognized association.
[c] The average of the two sets of elements for the December Phoenicids was used.
[d] The only questionable association in this table according to the D criteria. See text.

Table 14-3 shows those comets known to be producing meteor streams and, hence, contributing significantly to the IPD cloud. The first six columns show the orbital elements of each of the comets; λ^i and β^i are the heliocentric longitude and latitude of the comet at periapsis passage. The final column names the meteor showers believed to originate from that comet.

TABLE 14-3. COMETS KNOWN TO BE PRODUCING METEOR SHOWERS [14-8]

Comet	P (yr)	q (AU)	e	ω	Ω	i	λ'	β'	Meteor showers
Encke (1971 II)	3.3	0.339	0.847	185°9	334°2	12°0	160°0	−1°2	β Taurids, N. Taurids, S. Taurids
Blanpain (1819 IV)	5.1	0.892	0.699	350.2	79.2	9.1	69.5	−1.5	December Phoenicids
Schwassmann–Wachmann 3 (1930 VI)	5.4	1.011	0.673	192.3	77.1	17.4	268.8	−3.7	τ Herculids
Pons–Winnecke (1915 III)	5.9	0.971	0.702	172.4	99.8	18.3	272.6	+2.4	June Bootids
Giacobini–Zinner (1946 V)	6.6	0.996	0.717	171.8	196.3	30.7	9.2	+4.2	October Draconids
Biela (1852 III)	6.6	0.861	0.756	223.2	247.3	12.6	109.8	−8.6	Andromedids, Annual Andromedids
Tuttle (1939 X)	13.6	1.023	0.821	207.0	269.8	54.6	106.2	−21.7	Ursids
Tempel–Tuttle (1965 IV)	32.9	0.982	0.904	172.6	234.4	162.7	61.5	+2.2	Leonids
Halley (1835 III)	76.3	0.587	0.967	110.7	56.8	162.3	305.2	+16.6	η Aquarids, Orionids
Swift–Tuttle (1862 III)	120	0.963	0.960	152.8	138.7	113.6	330.3	+24.8	Perseids
Mellish (1917 I)	145	0.190	0.993	121.3	88.0	32.7	213.8	+27.5	Monocerotids
Ikeya (1964 VIII)	391	0.822	0.985	290.8	269.3	171.9	338.3	−7.6	ε Geminids
Thatcher (1861 I)	415	0.921	0.983	213.4	31.2	79.8	217.9	−32.8	April Lyrids
Kress (1911 I)	2509	0.684	0.996	110.4	158.0	148.4	44.4	+29.4	Aurigids
(1739)	—	0.674	1	104.8	210.3	124.3	95.3	+53.1	Leo Minorids
Metcalf (1919 V)	—	1.115	>1	185.7	121.4	46.4	305.4	−4.2	υ Draconids

14.4.1 Two Population Methods

Models of the origin of the IPD cloud have been somewhat confused by the discovery in 1973 from the Pioneer 8 and 9 space probes of a distinct and separate component of the IPD. Members of the component, termed the β meteoroids, move outward from the Sun on hyperbolic orbits.

The β-meteoroids are thought to be one of the two independent populations of the IPD. Their relative properties are shown in Table 14-1 [14-20 through 14-23].

Although the identification of two populations with totally different properties is still tentative, there is much supporting evidence. For instance, particles collected in the stratosphere tend to be either large and chondritic in nature or small and metallic. The β-meteoroid population has also been identified in the data from the Helios I spacecraft between 0.3 and 1.0 AU [14-24]. This is discussed more fully in paragraph 14.6. The genesis of the two populations in the IPD cloud remains a major topic for research.

14.5 COMPOSITION OF THE IPD

Meteoritic samples of the IPD have been collected from permanent ice-packs, the stratosphere, and ocean sediments. Problems associated with the analysis of these samples include: (a) the small particle sizes: 10^{-8} to 10^{-11} g, 2 to 30 μm diameter for stratospheric grains [14-15]; a little larger for oceanic grains, 30 to 200 μm [14-12]; (b) the selection effect since highly volatile grains are lost during atmospheric entry; and (c) the small number of individual particles which are available – only about

400 grains have been recovered from the stratosphere [14-14]. Nevertheless, IPD samples provide a third source of extraterrestrial material after lunar samples and meteorities and are therefore of extreme interest to cosmogonists.

While much of the IPD is found to be similar to chrondritic meteorites, it appears to be a distinct third classification of extraterrestrial material [14-11]. Trace element analysis of some grains has shown the presence of both volatile and nonvolatile components in abundances believed to be typical of the primitive presolar nebula [14-14].

Table 14-4 shows the average composition of 13 stratospheric particles analysed by Brownlee [14-6]. Compositional differences from this average have been isolated for Mafic grains (single-mineral grains) and also spherules (spherical grains collected in the stratosphere, apparently formed in a melt process) [14-13].

TABLE 14-4. CHEMICAL COMPOSITION OF IPD PARTICLES BY WEIGHT' NORMALISED TO SILICON [14-6]

Element	Fraction
Na	0.04
Mg	0.74
Al	0.06
Si	1.00
S	0.40
K	0.01
Ca	0.07
Cr	0.02
Mn	0.03
Fe	1.25
Ni	0.08

Isotopic analysis of IPD samples has also been carried out, but only to a limited extent. Magnesium and calcium isotopic abundances are close to the terrestrial ratios [14-13]. Isotopic ratios of the noble gases confirm that the "chondritic" IPD is extraterrestrial [14-25].

14.6 SIZE AND MASS DISTRIBUTION OF THE IPD

Approximately two-thirds of the total mass of the IPD exists as particles between 10^{-3} and 10^{-6} g [14-7]. The identification of lunar microcraters with diameters as small as 0.01 μm implies the existence of dust particles as small as 10^{-18} g [14-21]. Figure 14-1 shows the mass distribution of the IPD

cloud calculated in two different ways. The "meteoritic particles" curve results from terrestrial meteor observations for the larger masses and lunar microcraters for the smaller masses. The "Zodiacal Light particles" curve is calculated from the scattering of radiation between 2000 Å and 20 μm. Although the curves obtained by these two methods are clearly different, this does not necessarily indicate an error, since the meteoritic particles are only sampled at 1 AU. The "cumulative particle flux" curve is discussed in the following paragraphs.

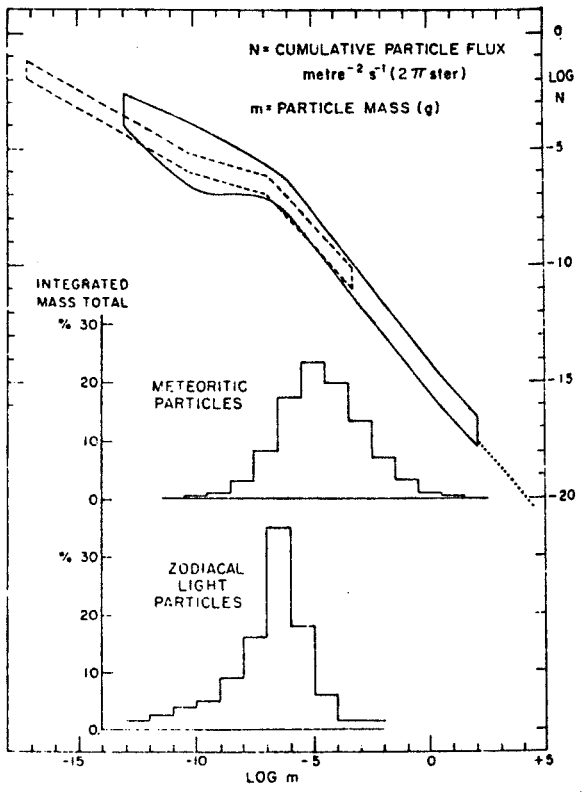

Figure 14-1. Mass distribution and particle flux of interplanetary dust [14-7].

The size distribution of meteoroids could be calculated from the mass distribution, if their density were constant. However, this is known not to be the case, since various distinct density classes have been identified.

From the cometary origin of IPD it may be inferred that initially the grains were made up of ices mixed with iron silicates. Comparison of lunar microcrater morphologies shows that the impacting material is biased towards three different densities: 1, 3, and 8 g cm^{-3} (i.e., ices, silicates, and iron) [14-7]. Polarization curves of the Zodiacal Light suggest that the surface structure of the scattering grains is fluffy or rough [14-7]. Fluffy or icy grains would be altered or destroyed during atmospheric entry.

The intensity and spectral distribution of the Zodiacal Light allows the size distribution of the IPD to be inferred. Derived size distributions are of the form

$$N(a) \sim a^{-x}$$

where n is the number of grains of radius a. Values of x range from 2 to 4 with a bias towards the lower figure [14-9].

14.7 SPATIAL DISTRIBUTION OF THE IPD

14.7.1 Perturbations

Population 2 particles, the β-meteoroids, leave the inner Solar System along hyperbolic paths. Their acceleration is thought to be due to solar radiation pressure which dominates the gravitational attraction of the Sun in the case of very small particles. Radiation pressure dominates when $a\rho \leqslant 1$; for a in μm, ρ in g cm^{-3} [14-9].

For larger particles (Population 1) the net effect of the solar radiation impinging on the particles acts in the opposite direction due to the relativistic Poynting-Robertson effect [14-26]. There is a retarding force on the particle, in the solar reference frame, produced by the absorption of solar radiation and subsequent emission of thermal radiation. The way in which the Poynting-Robertson effect causes the gradual dispersion of the meteoric debris ejected by a comet along the orbital path of the comet is elegantly discussed in Reference 14-27. Equations of motion for a particle under the influence of this effect are also given in References 14-5 and 14-28. The loss time (t) for a particle to spiral into the Sun under the influence of the Poynting-Robertson effect is approximately

$$t = a\rho\ r^2$$

where a is the radius of the particle in "μm," "ρ" is its density in g cm^{-3}, and r is the radius of its (assumed circular) orbit in AU. Time, t, is then in thousands of years. A 1-μm silicate grain at 2 AU falls into the Sun in about 10^4 years [14-9, 14-26].

The relative importance of the Poynting-Robertson effect and collisional processes as loss mechanisms for the IPD is discussed in References 14-5 and 14-29. Collisions are thought to be a major source of the β-meteoroids in the innermost regions of the Solar System. These particles may originate from the destruction of the larger Population 1 grains. Gradual sublimation of the Population 1 grains as they approach the Sun could also be a source.

The effect of incident solar wind particles upon IPD grains is negligible in terms of the pressure exerted, amounting to only approximately 10^{-3} of the radiation pressure [14-9]. The solar wind does however cause a tangential drag of about 25 percent of the value of the Poynting-Robertson effect and may also cause sputtering of the dust grains.

Another drag force results from Lorentz scattering [14-30, 14-31]. Each IPD grain presumably carries an electric charge, and the varying magnetic field carried by the solar wind exerts a force. Electrodynamic forces are important only for dust grains smaller than about 1 μm [14-5, 15-32].

14.7.2 Flux

The upper part of Figure 14-1 shows the cumulative particle flux for all masses from 10^{-17} g to 100 kg. Two envelopes are shown. The dashed line curve was deduced from lunar microcrater counts and extends only up to masses of 10^{-3} g. The solid line combines results from all other techniques. The dotted line at 100 g to 100 kg shows the flux of massive particles, as determined from Apollo seismometers on the lunar surface. All data pertains to 1 AU [14-7, 14-9].

The total mass flux at 1 AU probably lies between 5×10^{-13} and 1×10^{-12} g m^{-2} sec^{-1} $(2\pi$ sterad$)^{-1}$ [14-7]. Both of the envelopes in Figure 14-1 show inflections at 10^{-7} and 10^{-10} g. This is additional evidence for the existence of two distinct populations of IPD, as discussed in paragraph 14.4 [14-20 through 14-22].

14.7.3 Spatial Density

From the intensity distribution of the Zodiacal Light the mass density of the Zodiacal Cloud is estimated to be 4×10^{-23} g cm^{-3} [14-9]. However, since the Zodiacal Cloud is only a subset of the IPD cloud, this is only a lower limit for the IPD mass density. An upper limit has been set of 1.5×10^{-22} g cm^{-3} [14-33]. Inferred values at 1 AU are close to this upper limit [14-21].

The IPD has now been sampled by spacecraft from 0.3 AU out to beyond 18 AU. The data for 0.3 to 3.3 AU show a gradual dropoff of density as r^{-v}, where v is about 1.3. There is evidence for a slight enhancement between 2.0 and 3.5 AU, close to the asteroid belt, although the rise in space density is much smaller than had been expected [14-7, 14-34, 14-35]. There is no great variation in the spatial density of meteoroids in the 10^{-8} to 10^{-9} range from 1 to 18 AU [14-35]. Prior to spacecraft sampling it was not certain that any appreciable IPD extended beyond approximately 5 AU. A significant population is now known to exist beyond this distance into the outer Solar System.

14.7.4 Symmetry of the IPD Cloud

Observations of the Zodiacal Light indicate a disc-shaped distribution of the IPD close to the ecliptic plane of the Solar System. Observations from space probes Helios 1 and 2 suggest that the Zodiacal Cloud between 0.3 and 1.0 AU lies close to the orbital plane of Venus [14-36]. Beyond 1 AU the cloud appears to be closer to the invariable plane of the Solar System. Planetary influences are discussed in References 14-37 and 14-38.

14.7.5 Concentration of the IPD Close to Planets

Gravitational focusing increases the flux of IPD close to a planet. The flux enhancement near Jupiter is at least 10 times interplanetary space, and the factor may be closer to 100. At Saturn the observed enhancement factor is even higher, around 1000x, although this may be partly due to the existence of ring particles. (Some of the enhancement at both planets could be due to particles in orbit. Review Reference 14-35 for a full discussion.) Other data from Pioneer 10 and 11 show a general enhancement in the spatial density of IPD beyond 5 AU [14-34].

Near the Earth the total particle flux is greatly enhanced over interplanetary space at 1 AU [14-39]. Measurements were made by the HEOS-2 space probe of altitudes 20,000 to 60,000 km. Three distinct types of events were noted: "Random Particles," "Groups," which were made up of particle impacts closer than 6.5 hr apart, and "Swarms" which were events less than 40 min apart. Physically, random particles are thought to be the general IPD background, groups are thought to be lunar ejecta, and swarms to be the fragments of larger bodies. The enhancement of the IPD flux (random events) is only a factor of about 3. The total flux of all particles (randoms, groups, and swarms) is given in Table 14-5.

TABLE 14-5. TOTAL PARTICLE FLUX AT THE EARTH
(Particles m^{-2} sec^{-1} $(2\pi$ sterad$)^{-1}$) [14-39]

Altitudes (10^3 km)	$\Phi(m > 10^{-14}$ g)	$\Phi(m > 10^{-13}$ g)	$\Phi(m > 10^{-12}$ g)	$\Phi(m > 10^{-11}$ g)	$\Phi(m > 10^{-10}$ g)
50–60	$(1.1–6.2)\times10^{-3}$	$(1.0–5.7)\times10^{-3}$	$(0.7–1.7)\times10^{-3}$	$(3.3–5.8)\times10^{-4}$	$(3.3–5.8)\times10^{-4}$
40–50	$(2.4–7.4)\times10^{-3}$	$(0.6–5.6)\times10^{-3}$	$(0.4–4.4)\times10^{-3}$	$(2.7–9.8)\times10^{-4}$	$(1.8–3.6)\times10^{-4}$
30–40	$(2.4–5.1)\times10^{-3}$	$(1.2–3.7)\times10^{-3}$	$(0.8–3.3)\times10^{-3}$	4.9×10^{-4}	9.7×10^{-5}
20–30	$(3.0–5.5)\times10^{-3}$	$(1.4–3.6)\times10^{-3}$	$(1.0–3.2)\times10^{-3}$	3.2×10^{-4}	3.2×10^{-4}
average	$(2.2–6.1)\times10^{-3}$	$(1.1–4.7)\times10^{-3}$	$(0.7–3.2)\times10^{-3}$	$(3.5–5.9)\times10^{-4}$	$(2.3–3.4)\times10^{-4}$

The influx of IPD to the Earth is important in aeronomy and other atmospheric sciences [14-16]. The total amount of interplanetary matter collected by the Earth is thought to amount to about 16,000 tons per year, to within a factor of two [14-12, 14-33]. Processes involved in planetary capture of particles are modeled in References 14-37 and 14-38.

14.8 CONCLUDING REMARKS

This discussion of the IPD has been restricted to the smaller solid particles in the Solar System. Little is known about the solid objects from 10 cm up to a few kilometers in size since they are too small to be seen telescopically and rarely encounter the Earth.

REFERENCES

14-1. Fernandez, J. A.: The Role of Collisions with Interplanetary Particles in the Physical Evolution of Comets. The Moon and the Planets, vol. 25, 1981, pp. 507-519.

14-2. Elsasser, H. and Fechtig, H. (eds.): Interplanetary Dust and Zodiacal Light. IAU Colloquium No. 31, Springer-Verlag, Berlin and New York, 1976. (Volume 48 of "Lecture Notes in Physics.")

14-3. Delsemme, A. H. (ed.): Comets, Asteroids, Meteorites: Interrelations, Evolution, and Origin. The University of Toledo Press, 1977.

14-4. McDonnell, J. A. M. (ed.): Cosmic Dust. Wiley, New York, 1978.

14-5. Halliday, I. and McIntosh, B. (eds.): Solid Particles in the Solar System. IAU Symposium Number 90, D. Reidel Publishing, Dordrecht, 1980.

14-6. Brownlee, D. E.: Astronomy and Astrophysics, vol. 92, 1980, p. 295; and in Protostars and Planets, T. Gehrels (ed.), University of Arizona Press, Tucson, 1978, p. 135.

14-7. Millman, P. M.: Interplanetary Dust. Naturwissenschaften, vol. 66, 1979, pp. 134-139.

14-8. Drummond, J. D.: A Test of Comet and Meteor Shower Associations. Icarus, vol. 45, 1981, pp. 545-553.

14-9. Leinert, C.: Zodiacal Light – A Measure of the Interplanetary Environment. Space Science Reviews, vol. 18, 1975, pp. 281-339.

14-10. Leinert, C.: Zodiakallicht-Beobachtungen. Naturwissenschaften, vol. 66, 1979, pp. 221-227. (In German).

14-11. Pillinger, C.: Small Minded – The Characterization of Interplanetary Dust by Electron Microscopy. Nature, vol. 294, 1981, pp. 517-518.

14-12. Hughes, D. W.: Cosmic Spherules. Nature, vol. 294, 1980, pp. 778-779.

14-13. Esat, T. M., Brownlee, D. E., Papanastassiou, D. A., and Wasserburg, G. J.: Magnesium Isotope Composition of Interplanetary Dust Particles. Science, vol. 206, 1979, pp. 190-197.

14-14. Ganapathy, R. and Brownlee, D. E.: Interplanetary Dust: Trace Element Analysis of Individual Particles by Neutron Activation. Science, vol. 206, 1979, pp. 1075-1077.

14-15. Fraundorf, P., Patel, R. I., Shirck, J., Walker, R. M., and Freeman, J. J.: Optical Spectroscopy of Interplanetary Dust Collected in the Earth's Stratosphere. Nature, vol. 286, 1980, pp. 866-868.

14-16. Toon, O. B. and Farlow, N. H.: Particles Above the Tropopause. Annual Review of Earth and Planetary Sciences, vol. 9, 1981, pp. 19-58.

14-17. Lebedinets, V. N.: Problems in Constructing a Genetic Model of the Interplanetary Dust Cloud. Solar System Research, vol. 13, 1979, pp. 122-128.

14-18. Whipple, F. L.: NASA SP-150, 1967, p. 49.

14-19. Parthasarathy, R.: Cometary Origin of Interplanetary Submicron Dust. Astronomical Journal, vol. 84, 1979, pp. 143-147.

14-20. LeSergeant D'Hendecourt, L. B. and Lamy, P. L.: Interplanetary Dust: Are There Two Independent Populations? Nature, vol. 276, 1978, pp. 800-802.

14-21. LeSergeant D'Hendecourt, L. B. and Lamy, P. L.: On the Size Distribution and Physical Properties of Interplanetary Dust Grains. Icarus, vol. 43, 1980, pp. 350-372.

14-22. LeSergeant D'Hendecourt, L. B. and Lamy, P. L.: Collision Processes among Interplanetary Dust Grains: An Unlikely Origin of the Beta Meteoroids. Icarus, vol. 47, 1981, pp. 270-281.

14-23. Lamy, P. L. and Perrin, J. M.: Zodiacal Light Models with a Bimodal Distribution. Solid Particles in the Solar System, I. Halliday and B. McIntosh (eds.), IAU Symposium No. 90, D. Reidel Publishing of Dordrecht, 1980, pp. 75-80.

14-24. Grun, E., Pailer, N., Fechtig, H., and Kissel, J.: Orbital and Physical Characteristics of Micrometeoroids in the Inner Solar System as Observed by HELIOS 1. Planetary and Space Science, vol. 28, 1980, pp. 333-349.

14-25. Rajan, R. S., Brownlee, D. E., Tomandl, D., Hodge, P. W., Farrar, H., IV., and Britten, R. A.: Detection of ^{4}He in Stratospheric Particles Gives Evidence of Extraterrestrial Origin. Nature, vol. 267, 1977, pp. 133-134.

14-26. Wyatt, S. P., Jr. and Whipple, F. L.: The Poynting-Robertson Effect on Meteor Orbits. Astrophysical Journal, vol. 111, 1950, pp. 134-141.

14-27. Lyttleton, R. A.: Effect of Solar Radiation on a Swarm of Meteoric Particles. The Moon and the Planets, vol. 23, 1980, pp. 27-39.

14-28. Burns, J. A., Lamy, P. L., and Soter, S.: Radiation Forces on Small Particles in the Solar System. Icarus, vol. 40, 1979, pp. 1-48.

14-29. Trulsen, J. and Wikan, A.: Numerical Simulation of Poynting-Robertson and Collision Effects in the Interplanetary Dust Cloud. Astronomy and Astrophysics, vol. 91, 1980, pp. 155-160.

14-30. Consolmagno, G.: Lorentz Scattering of Interplanetary Dust. Icarus, vol. 38, 1979, pp. 398-410.

14-31. Consolmagno, G.: Influence of the Interplanetary Magnetic Field on Cometary and Primordial Dust Orbits: Applications of Lorentz Scattering. Icarus, vol. 43, 1980, pp. 203-214.

14-32. Millet, J., Lafon, J. P. L., and Lamy, P. L.: On the Electrostatic Potential of Interplanetary Grains: Influence of the Thermionic Effect. Astronomy and Astrophysics, vol. 92, 1980, pp. 6-12.

14-33. Hughes, D. W.: Cosmic Dust Influx to the Earth. COSPAR 17th Meeting, Brazil. Space Research, vol. 15, Akademie Verlag, Berlin, 1975, pp. 531-539.

14-34. Stanley, J. E., Singer, S. F., and Alvarez, J. M.: Interplanetary Dust Between 1 and 5 A.U. Icarus, vol. 37, 1979, pp. 457-466.

14-35. Humes, D. H.: Results of Pioneer 10 and 11 Meteoroid Experiments: Interplanetary and Near-Saturn. Journal of Geophysical Research, vol. 85, 1980, pp. 5841-5852.

14-36. Leinert, C., Hanner, M., Richter, I., and Pitz, E.: The Plane of Symmetry of Interplanetary Dust in the Inner Solar System. Astronomy and Astrophysics, vol. 82, 1980, pp. 328-336.

14-37. Misconi, N. Y.: The Photometric Center of the Gegenschein. Icarus, vol. 47, 1981, pp. 265-269; also "The Symmetry Plane of the Zodiacal Cloud at 1 A.U.," Solid Particles in the Solar System, I. Halliday and B. McIntosh (eds.), IAU Symposium No. 90, D. Reidel Publishing, Dordrecht, 1980, pp. 49-54.

14-38. Misconi, N. Y. and Weinberg, J. L.: Is Venus Concentrating Interplanetary Dust Toward Its Orbital Plane? Science, vol. 200, 1978, pp. 1484-1485.

14-39. Fechtig, H., Grun, E., and Morfill, G.: Micrometeoroids within Ten Earth Radii. Planetary and Space Science, vol. 27, 1979, pp. 511-531; see also errata, p. 911.

☆U.S. GOVERNMENT PRINTING OFFICE: 1983-639-008/ 16

TECHNICAL REPORT STANDARD TITLE PAGE

1. REPORT NO.	2. GOVERNMENT ACCESSION NO.	3. RECIPIENT'S CATALOG NO.
NASA TM-82501		

4. TITLE AND SUBTITLE	5. REPORT DATE
Space and Planetary Environment Criteria Guidelines for Use in Space Vehicle Development, 1982 Revision (Volume II)	June 1983
	6. PERFORMING ORGANIZATION CODE
7. AUTHOR(S) Compiled by Robert E. Smith and George S. West	8. PERFORMING ORGANIZATION REPORT # ES83
9. PERFORMING ORGANIZATION NAME AND ADDRESS George C. Marshall Space Flight Center Marshall Space Flight Center, Alabama 35812	10. WORK UNIT NO. M-398
	11. CONTRACT OR GRANT NO.
	13. TYPE OF REPORT & PERIOD COVERED Technical Memorandum
12. SPONSORING AGENCY NAME AND ADDRESS National Aeronautics and Space Administration Washington, D.C. 20546	14. SPONSORING AGENCY CODE

15. SUPPLEMENTARY NOTES This document was prepared for the most part by various staff members of the Universities Space Research Association (USRA) and their associated scientists and scientific sources under sponsorship of the Marshall Space Flight Center's Atmospheric Science Division.

16. ABSTRACT

The two volumes of the document provide guidelines on space and planetary environment criteria for use in space vehicle development. Information is incorporated in the disciplinary areas of atmospheric and ionospheric properties, radiation, geomagnetic field, astrodynamic constants, and meteoroids for the Earth's atmosphere about 90 km, interplanetary space, and the atmosphere and surfaces (when available) of the Moon and the planets (other than Earth) of this solar system. Chapters on the Sun, Terrestrial Space, the Moon, Mercury, Venus, and Mars constitute Volume I, NASA TM-82478. Volume II contains chapters on Jupiter, Saturn, Uranus, Neptune, Pluto, Comets, Asteroids, and Interplanetary Dust.

This document, Volume II, TM-82501, is recommended as a tool for use in the development of space vehicles. However, an environment specialist should be consulted in critical design interface applications for the most current information and scientific interpretation.

NASA TM-82473, entitled "Terrestrial Environment (Climatic) Criteria Guidelines for Use in Aerospace Vehicle Development, 1982 Revision," provides natural environmental information for altitudes below 90 km for the Earth.

Further, there is no intent to automatically change any references to previous documents in contract Scopes of Work by the issuance and acquisition of either NASA TM-82473, NASA TM-82478, or NASA TM-82501.

17. KEY WORDS	18. DISTRIBUTION STATEMENT
Environment criteria Space environment Solar radiation Atmospheric models; upper atmosphere Astrodynamic constants Planetary environments	Unclassified - Unlimited STAR Category: 15

19. SECURITY CLASSIF. (of this report)	20. SECURITY CLASSIF. (of this page)	21. NO. OF PAGES	22. PRICE
Unclassified	Unclassified	177	A09

MSFC - Form 3292 (May 1969)

For sale by National Technical Information Service, Springfield, Virginia 22161